TRAFFICKING OF AMYLOID BETA PROTEIN AT THE BLOOD BRAIN BARRIER: NOVEL INSIGHTS IN ALZHEIMER'S DISEASE PATHOGENESIS

A DISSERTATION
SUBMITTED TO THE FACULTY OF THE
UNIVERSITY OF MINNESOTA

BY

NIDHI SHARDA

IN PARTIAL FULFILLMENT OF THE REQUIREMENTS
FOR THE DEGREE OF
DOCTOR OF PHILOSOPHY

KARUNYA KANDIMALLA

DECEMBER 2016

ACKNOWLEDGEMENTS

"*Creativity is intelligence having fun"- Albert Einstein*

There are several people and forces that made my journey of creativity and scientific discovery fun and worth all the effort. Firstly, I would like to acknowledge and thank my adviser and mentor- Dr. Karunya Kandimalla for his extended support throughout my graduate program. I am deeply grateful to him for introducing me to this invigorating and extremely relevant project question. As a brilliant mentor and teacher, he let me make mistakes; but at the same time guided and mentored me throughout, to be able to display courage and strength to overcome challenges. I am immensely grateful to have imbibed some of his positivity, passion and skills not just in science, but life in general.

Next, I sincerely acknowledge Dr. Willam Elmquist and Dr. Cheryl Zimmerman for being excellent Pharmacokinetics teachers and great mentors. I owe my love for pharmacokinetics to them- a field that I aspire to build my career in. Their extensive support- professionally and personally- is one of the several reasons I would value their positivity in my life forever. I would also like to thank Dr. Ling Li for being on my thesis committee and inspiring me to consider my research perspective from the big picture point of view. She encouraged me to ask and address the right questions clearly and concisely- a skill that I hope to have learnt well. I am also grateful to Dr. Ron Siegel for always finding time for my discussions to comprehend complicated mathematical equations. His love for science and numbers is inspiring.

Next, I would like to thank all the past and current Kandimalla lab members- Dr. Kristen Jaruszewski, Dr. Edward K. Agyare, Dr. Suresh K. Swaminathan, Dr. Rajesh S. Omtri, Vidur Sarma, Shail Panchamia, John Welby and Surabhi Talele; for their active discussions and lively ethos in the lab to nurture my growth as a scientist and human being. I would also like to thank the entire team at Mayo Clinic, Rochester- Geoff Curran, Tracy Decklever, Kevin Thompson, Dr. Krishna Kalari, Dr. Joseph Poduslo and Dr. Val Lowe for their effective collaboration and support throughout. Further, I would like to acknowledge the help received from the personnel and staff at Flow Core facility, University Imaging Center, particularly John Oja, Guillermo Marques and Dr. Thomas Pengo, who helped with the microscopy data analysis as well. I would also like to thank Isaac Angert, Dr. Jochen Mueller (Physics, UMN) and Antje Neubauer (Becker-Heckl) to help me understand fluorescence lifetime concepts.

Further, I do not think I would have been the person or scientist I am, for not the faculty, staff and both past and current students at Department of Pharmaceutics. I acknowledge to have learnt from my peers and colleagues as much as I have from the faculty. Particularly, I would like to thank Dr. Mehak Mehta, Dr. Karen Parrish and Dr. Shruthi Vaidhyanathan for being wonderful friends and inspiring scientists.

Next, I would also like to acknowledge the financial assistantship received from Kandimalla laboratory and Department of Pharmaceutics in the form or teaching and research assistantship to accomplish this work. Also, I am grateful to receive the monetary awards from Pharmacokinetics, Pharmacodynamics and Drug metabolism (PPDM) section at the American Association of Pharmaceutical Scientists (AAPS); American Association of Indian Pharmaceutical Scientists (AAiPS); Blood Brain barriers

section, Cold Spring Harbor Laboratory (CSHL); Council of Graduate Student (COGS), University of Minnesota, to provide encouragement to participate in several national conferences throughout the course of my graduate program.

At the personal front, I am grateful to have the unconditional love and support from my entire family and friends. I would like to thank my parents, Neera and Wg Cdr P.K. Sharda; sister Maansi Sharda and brother-in-law Rohit Singh; and Chachu (uncle) Harish Sharda; for always believing in my strengths, abilities and potential to realize my dreams. I am truly fortunate and blessed to be a part of Sharda family. I would also like to acknowledge the love and support from my aunt- Shyama and Mahender Mohllajee, cousin Dr. Anshu Mohllajee, her husband Dr. Samir Thadani and adorable niece Anamika Thadani.

Finally, I am blessed to have the friends who have stayed with me through all my highs and lows of this journey. I take this as an opportunity to thank and be grateful to them for their friendship. In particular, I thank Dr. Dimple Modi and Dr. Yash Jalundhwala- who had encouraged me to start this journey and have lived it through with me, in every way possible. I would also like to thank all my friends from Minneapolis, Los Angeles and Delhi; Dr. Isha Koonar, Sampada Koranne, Avani Gosalia, Dr. Mamta Kapoor Bhushan, Dr. Rashmi Kandwal, Vikrant Krishna, Ashank Sinha, Sudeepto Ganguly, Rushit Doshi, Keerti Jain, Ritu Jain, Sofina Jain, Aditya Bilagi, Pooja Jumani, Pooja Shah, Neha Luniya, Divya Malik and Manan Dhunna- who have showered me with their love and care as and when I needed it the most!

I am deeply grateful to have you all in my life and in this incredible journey of scientific and self-discoveries! Thank you!

DEDICATION

I dedicate this thesis to my grandmother, my Beeji- Smt. Kamla Devi Sharda (-2010),

who gave me the love, self-belief and wings to dream and fly!

Beeji, you love and live in all of us, forever!

ABSTRACT

Alzheimer's disease (AD) is the most common form of dementia in elderly population. Unfortunately, the current treatment approaches for AD are symptomatic and do not interfere with the disease progression at any stage. The risk of AD increases with age; from 12 %, above 70 years of age, to 50 % beyond 80 years of age. Due to an improvement in average life span in many regions across the globe, AD is being recognized as a major socio-economic health problem that is expected to worsen in the near future. Also, with 99.6 % of current clinical trials failing in AD due to insufficient knowledge of the disease targets and lack of early diagnostic methods; detailed investigations into AD pathogenesis is critically important.

Development of amyloid beta (Aβ) plaques in the brain is one of the primary pathological hallmarks of AD. Impaired clearance and not overproduction of toxic Aβ proteins leads to their accumulation and subsequent plaque formation in sporadic AD that accounts for more than 90 % of total AD cases. Blood brain barrier (BBB) is expected to be the primary clearance portal of Aβ from the brain. Being at the interface between brain and plasma, the BBB also maintains the dynamic equilibrium of brain and plasma Aβ pools. This equilibrium is believed to be perturbed in AD due to BBB dysfunction. However, the manifestations of BBB dysfunction and the precise mechanisms that may trigger it, are not clearly understood.

Two major Aβ isoforms, Aβ40 and Aβ42, play a predominant role in AD pathogenesis. Aβ42 is believed to be pathological whereas Aβ40 is constitutively expressed and believed to have protective properties against neurological anomalies.

Also, Aβ40 expression is 10- and 1.5- fold higher than Aβ42 in cerebral spinal fluid (CSF) and plasma, respectively. This ratio of Aβ42:Aβ40 increases in brain and decreases in plasma, respectively, during disease progression. However, the pathophysiological mechanisms driving this clinical observation is not known yet.

In my thesis, I demonstrate distinct age dependent changes in the BBB permeability and plasma exposure of Aβ40 and Aβ42 at the BBB endothelium in wild type (WT) and AD-transgenic (APP,PS1) mice. Further, to investigate the pathophysiological mechanisms driving these observations, I conducted *in-vitro* studies in polarized hCMEC/D3 monolayers, a widely used BBB model, and demonstrated that Aβ40 and Aβ42 are internalized at the BBB endothelium via clathrin- and lipid raft-mediated endocytosis, respectively. This mechanistic difference offers an opportunity to the BBB to independently handle and modulate the clearances of Aβ40 and Aβ42. Also, *in-vivo* investigations coupled with quantitative modeling, have indicated that Aβ40 may accumulate more than Aβ42 at the BBB endothelium. This may decrease Aβ40 transcytosis at the BBB and increase the exposure of the BBB endothelium to the vasculotropic Aβ40. To investigate the mechanisms driving this observation, I tested the hypothesis published by our lab previously that the impaired transcytosis of Aβ40 at the BBB endothelium is due to the perturbed vesicular exocytosis. Also, synaptic transmission involving SNARE exocytosis machinery is known to be impaired in AD. Thus, I investigated the ability of Aβ40 and Aβ42 to perturb the SNARE exocytosis machinery at the BBB endothelium and in neurons, in comparison with tetanus neurotoxin, a well-established disruptor of the VAMP-2 mediated exocytosis. My findings reveal that Aβ40 and Aβ42 isoforms use VAMP-2 (vesicular SNARE) to

exocytose at the BBB endothelium and neurons. Further, using fluorescence resonance energy transfer (FRET) and lifetime microscopy (FLIM), I have demonstrated that Aβ40 and Aβ42 interfere with the functioning of SNARE fusion between VAMP-2 and SNAP-25. Moreover, my findings suggest that Aβ40 may be more efficient than Aβ42 in perturbing this process, and consequently may interfere with its own exocytosis.

In summary, my work provides evidence for the presence of distinct clearance mechanisms of Aβ40 and Aβ42 isoforms at the BBB endothelium. This novel assertion provides a framework to explain the disrupted clearance of Aβ, perturbed Aβ42:Aβ40 ratios and dysregulated transport of Aβ and other endogenous proteins at the BBB endothelium observed in AD patients. These findings could be applied to identify new drug targets to ameliorate BBB dysfunction in AD.

TABLE OF CONTENTS

LIST OF TABLES

LIST OF FIGURES

CHAPTER FOUR

CHAPTER FIVE

CHAPTER ONE

1. INTRODUCTION

1.1. Global epidemic of Alzheimer's disease

Alzheimer's disease (AD) is the most common form of dementia in the elderly population (> 65 years). Currently, it affects nearly 5 million Americans. As per World Health Organization (WHO), there will be a global epidemic of AD by 2050. (Hebert et al., 2013) Apart from progressive decline in memory and cognition, other clinical symptoms of AD include depression, disorientation, agitation, anxiety and other behavioral anomalies that restrict the patient's ability to learn and in later stages perform routine everyday tasks. As a result, these patients become dependent on the families and caregivers for their social and economic needs. This multifaceted societal burden was estimated to be more than 2.5 billion dollars in 2012. Furthermore, due to lack of effective treatment options beyond symptomatic relief, AD has become the 6th leading cause of death, and the only one among top ten diseases that cannot be cured, prevented or even slowed. Needless to say, this complex situation indicates an urgent need towards meticulous and comprehensive understanding of the basic disease pathogenesis.

1.2. Alzheimer's disease: "graveyard for drug developers"

To address this unmet medical need, several drug companies are working towards discovering drugs to interfere with AD pathology. However, with 99 % of clinical trials failed or discontinued in just 2013-14, AD is increasingly being regarded as the "graveyard for drug developers". One possible reason for this situation is the recruitment

of patients who are in the lateral stages of the disease, well beyond the onset of mild cognitive impairment (MCI). The proposed cascade of pathological biomarkers **(Figure 1.1)**, are manifested in the AD patient, several years before any symptomatic changes in the cognition are noted. It is now believed that the therapeutic inventions are effective only during the early stages when the level of some biomarkers, particularly Aβ, show predominant alterations.

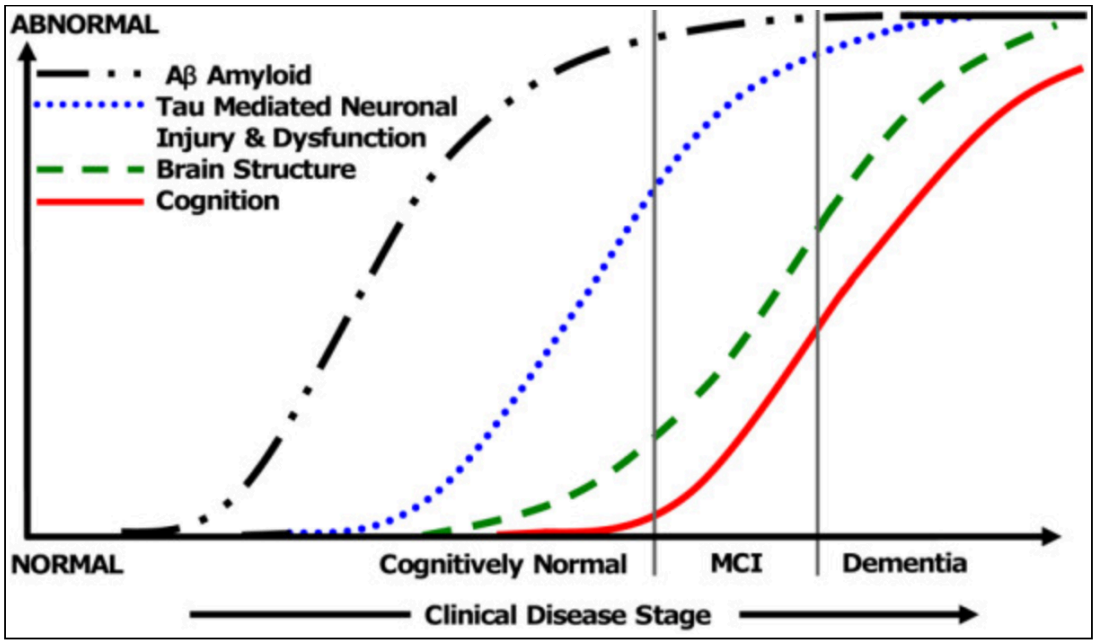

Figure 1.1 Proposed cascade of biomarker profiles in Alzheimer's disease (AD) pathology. Changes in amyloid beta (Aβ) protein and tau levels are evident many years before the onset of Mild Cognitive Impairment (MCI). Reused by acquiring license and permission (Jack et al., 2010).

1.3. Hallmarks of Alzheimer's disease

Since the time of Alois Alzheimer, the eminent scientist who diagnosed the first AD case (Stelzmann et al., 1995), the two characteristic hallmarks of AD brain have been identified: (1) amyloid plaques, composed of amyloid beta (Aβ) proteins, in the brain parenchyma, and (2) neurofibrillary tangles (NFT) in the neurons, composed of the tau protein **(Figure 1.2)**. These are known to initiate the synaptic neuronal dysfunction that leads to clinical symptoms of memory loss and dementia. Although, both Aβ or/and tau proteins competed for the spot of key trigger to AD pathogenesis, it was shown that Aβ peptides are capable of modulating taupathy (formation of NFT) and therefore work upstream of tau in AD pathogenesis **(Figure 1.2)**.

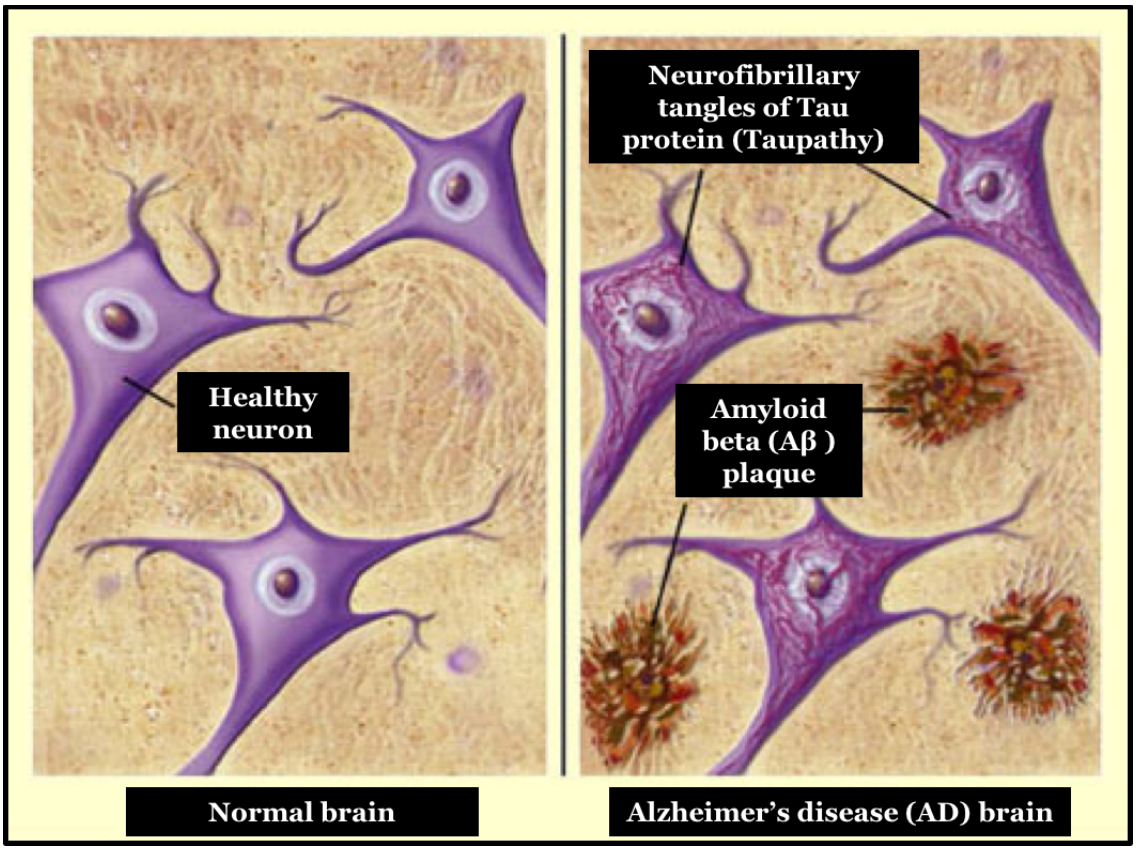

Figure 1.2 Hallmarks of Alzheimer's disease (AD). Comparing the brain of healthy individuals (normal brain) to that of AD patients, two characteristic hallmarks of AD have been identified: (1) Extracellular plaques of amyloid beta (Aβ) protein and (2) Neurofibrillary tangles (NFT) of tau protein. Image modified and reused from National Institute on aging and National Institute of Health (National Institute on Aging, 2015).

1.4. Production and clearance of amyloid beta (Aβ) protein

The accumulation of mass is imminent, if there is an imbalance between its production and/or clearance. Increased burden of Aβ in brain with AD progression is no exception. Production of Aβ has been well investigated **(Figure 1.3)** and is known to be generated from the proteolytic processing of parent precursor protein- Amyloid Precursor Protein (APP), expressed primarily in the brain. The APP, which is a transmembrane protein, can be cleaved sequentially by either of the two pathways:

(1) Normogenic or non-amyloid genic pathway. In this pathway, α-secretase cleaves the Aβ domain of APP and releases the non-toxic fragment sAPPα. This sAPPα is further cleaved by ϒ-secretase to generate small soluble peptide p3, another non-toxic peptide.

(2) Amyloidgenic or AD pathway. APP is first cleaved by β-secretase outside the Aβ domain to release soluble sAPPβ extracellularly. Finally, this sAPPβ is cleaved by ϒ-secretase to form the ~ 4 kD toxic protein Aβ.

Depending upon the cleavage site of ϒ-secretase, it can form either the short Aβ40 or slightly longer Aβ42 (Blennow et al., 2006; LaFerla et al., 2007; Selkoe and Podlisny, 2002) **(Figure 1.5)**. These two isoforms will be discussed in parallel in the subsequent sections. More than 90 % of the APP is processed in the normogenic pathway, and only 10 % is expected to participate in the amyloidogenic pathway. Furthermore, there are reports indicating that a negative feedback loop may exist to regulate the processing of APP via the amyloidogenic pathway by modulating the transcription and expression of either secretases.

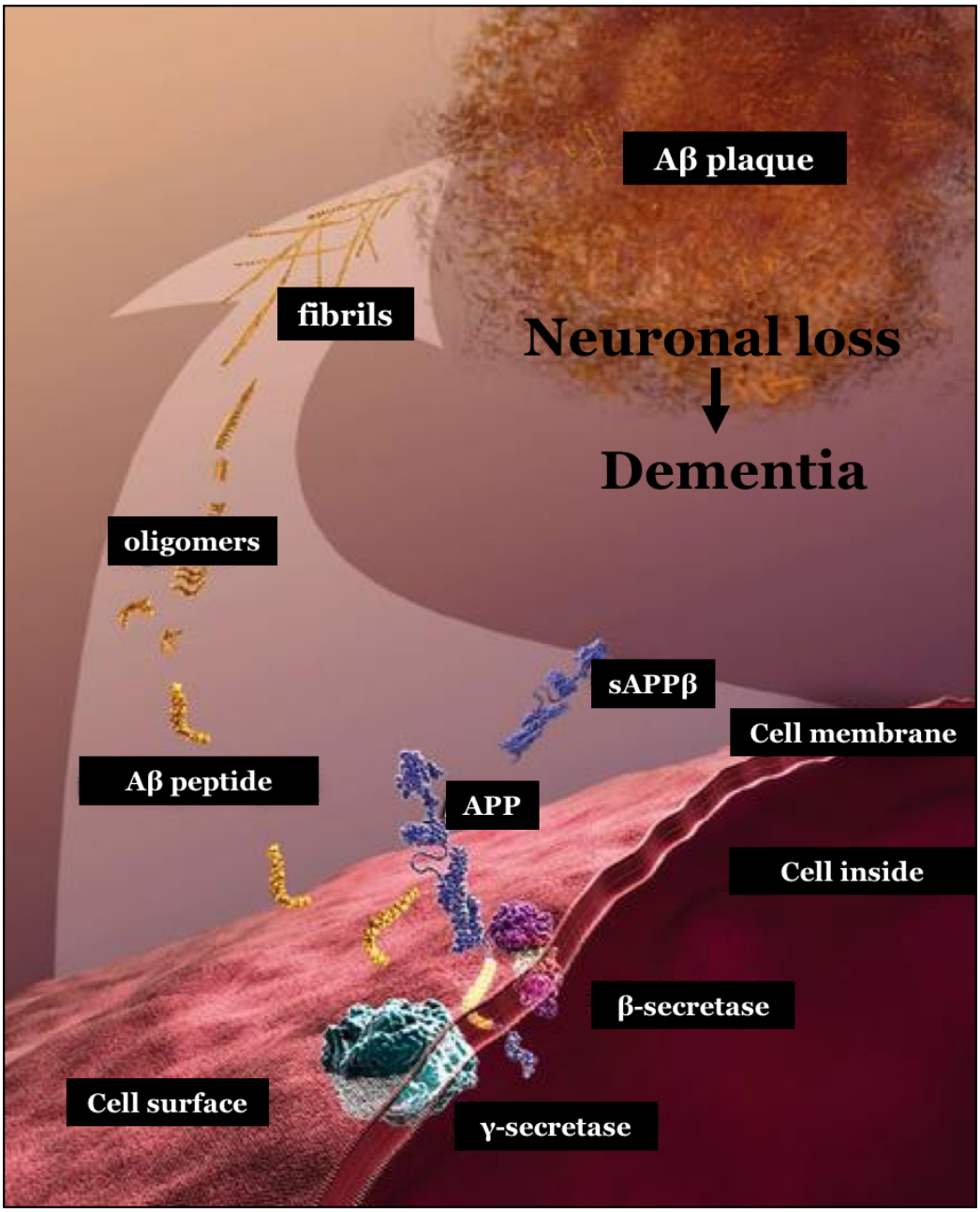

Figure 1.3 Generation of Amyloid beta (Aβ) peptides. Aβ is produced from the sequential cleavage of transmembrane, amyloid precursor protein (APP), by proteases β-secretase and γ-secretase. The Aβ peptide thus released extracellularly, forms oligomers followed by fibrils that eventually form plaque in combination with metals and other cellular debris. The soluble Aβ peptides and even more Aβ oligomers have been proposed to trigger neuronal loss leading to dementia. The increase in brain Aβ levels is believed to be due to impaired clearance and not due to the overproduction of Aβ. Image modified and reused from National Institute on Aging and National Institute of Health (National Institute on Aging, 2015).

1.5. Aβ is both physiological and pathological

Before we move onto the intricate details of Aβ clearance, the processing of APP will be discussed. Firstly, the production of Aβ has been shown to be important for the viability of neurons in the brain (Plant et al., 2003). Aβ was also found in the CSF of non-demented individuals (Mehta et al., 2000; Shoji et al., 1997) as well as in the medium of neuronal cell cultures (Haass et al., 1992). The systemic clearance of Aβ is fast with a short half-life of 2.5-3 minutes after primarily getting metabolized in liver and kidneys (Ghiso et al., 2004). Aβ is also a constituent of normal urine (Ghiso et al., 2004, 1997). In physiology, APP catabolism to form Aβ has been shown to modulate synaptic activity by several mechanisms. For example, a negative feedback loop has been proposed to inhibit APP transcription when Aβ is in excess (Kamenetz et al., 2003). Further, APP has also been demonstrated to have neuroprotective properties (Giuffrida et al., 2009) by triggering neuronal cell survival (Plant et al., 2003) and excitability (Parihar and Brewer, 2010; Plant et al., 2006). The proposed physiological roles of Aβ are reviewed in (Castellani et al., 2009; Pearson and Peers, 2006).

The idea that Aβ is toxic and gets accumulated as plaques in the brain and perpetrates AD pathophysiology has been long proposed. After the two isoforms were identified and characterized, it was established that Aβ42 is the more toxic and pathological form, whereas Aβ40 may have a physiological function that is not well understood. Studies in mice that overexpress Aβ40 or Aβ42 (BRI-mice), crossed with Tg2576 mouse model, which harbor Swedish mutation on APP showed that the overall higher levels of Aβ40 inhibited amyloid deposition by 60–90 % (McGowan et al., 2005). The ratio of Aβ42:Aβ40 in patient brain has been shown to increase with AD

progression. However, it is interesting that in familial AD cases, the change in ratio is due to a decrease in Aβ40 and not always due to an increase in Aβ42 (Tanzi, 2012). However, no such trend is yet clear in sporadic AD cases. Whether, it is the same or opposite rationale in sporadic AD cases as well is not known. An excellent review is put together in (Castellani et al., 2009; Tanzi, 2012) . The toxicity of Aβ is believed to be perpetrated by triggering apoptosis, promoting inflammation and enhancing oxidative stress. This ultimately results in disrupted synaptic neurotransmission and neuronal death. However, it is also noted that not all individuals manifesting increasing Aβ burden correlate with cognitive decline, and that large amounts of Aβ is also seen in cognitively normal elderly individuals. These ideas probably suggest that Aβ should be considered toxic only when there is an imbalance between its production and clearance. Further, there is evidence that Aβ interferes with exocytosis mechanisms in neurons (Uemura and Greenlee, 2001). Apart from neuronal synapses, this idea of Aβ directly modulating vesicular exocytosis becomes even more interesting when we consider that exocytosis is one of the basic components of simple cellular trafficking physiology and function (intracellular uptake or endocytosis, transit and exocytosis). More so, because Aβ, being a protein itself, would have to be transported via vesicular trafficking, and therefore, may impact its own transit. This idea would be elaborated in a separate section.

Along with Aβ, APP has also been ubiquitously expressed in neuronal as well as non-neuronal cells (Niederwolfsgruber et al., 1998) to promote cell growth, differentiation and carcinogenesis (Nalivaeva and Turner, 2013). Some studies suggest that the membrane localization and processing of APP may differ from neuronal and peripheral cells; and so, specific function and transducer properties of APP (or Aβ) might

be unique to its production site (Jung et al., 1996). Interestingly, abnormal APP metabolism in pancreas has been also seen in AD, such that it is referred as type 3 Diabetes by several investigators (de la Monte and Wands, 2008; Miklossy et al., 2010). Insulin degrading enzyme or IDE, one of the primary proteases involved in the catabolism of insulin, has been shown to directly regulate the activity of not just insulin but also of Aβ, and APP (Farris et al., 2003). Further, interleukin 1, estrogen hormone and GSK-3 alpha have been also shown to regulate Aβ metabolism. (Jaeger et al., 2009; Jaffe et al., 1994; Phiel et al., 2003) Further, whether this central insulin resistance is a cause or consequence of Aβ triggered AD pathology is not totally understood yet. Moreover, there is evidence that APP is involved in several normal brain functions including cell-cell interactions (Coulson et al., 2000), cell-surface adhesion (Soba et al., 2005), neuronal cell migration (Rice et al., 2012) and development (Joo et al., 2010) and maturation (Kirazov et al., 2001) of adult brain development and neuromuscular junctions (Akaaboune et al., 2000). It has also been shown to regulate calcium homeostasis (Octave et al., 2013) and have a functional role in neuronal network formation, synaptic vesicular exocytosis, finally affecting learning and memory.

1.6. Aβ clearance mechanisms- Blood Brain Barrier as the primary clearance portal

Predominantly, there are three ways by which excess Aβ can be removed or cleared from the brain parenchyma: (1) proteolytic degradation by enzymes such as neprilysin, insulin degrading enzyme, and angiotensin converting enzyme (ACE); (2) receptor mediated transport across the blood-brain barriers- that comprise of both: Blood-Brain Barrier (BBB) and Blood-Cerebral Spinal Fluid Barrier (BCSFB); (3) bulk flow or perivascular drainage from the brain interstitial fluid (ISF) to CSF and into the blood

stream via either the choroid plexus (CP) or via the 'glymphatic pathway' (Nedergaard, 2013). Once into the blood stream, Aβ is cleared almost instantaneously (within minutes) by liver and kidneys **(Figure 1.4).**

1.6.1. Proteolytic degradation of Aβ

Depending upon the amino acid site of cleavage, several proteases are implicated in the degradation of Aβ (Saido and Leissring, 2012) peptides. Two among them, neprilysin (NEP) and insulin degrading enzyme (IDE), appear to have the maximum contribution towards the degradation (Marr et al., 2003; Maruyama et al., 2005). Both have been independently shown to be inversely correlated with Aβ load in the brain and with disease progression. Particular links with the vascular deposits of Aβ in Cerebral Amyloid Angiopathy (CAA) have also been established where the expression of NEP has been shown to decline in the vasculature of AD patients with CAA (Carpentier et al., 2002). The levels of these enzymes have also been shown to decrease with age, thus substantiating that proteolytic degradation contributes to AD pathology. Recently, it was shown that APP-intracellular domain (AICD), one of the proteolytic cleaved products of APP, epigenetically upregulates the expression of NEP, as well as another enzyme that aids in Aβ clearance- transthyretin (Kerridge et al., 2014). Other proteases contributing to Aβ degradation include matrix metalloproteinases (Lorenzl et al., 2003; Yoshiyama et al., 2000), angiotensin converting enzyme (ACE) (Kugaevskaya, 2012), endothelin converting enzymes (ECEs) (Pacheco-Quinto, 2013; Tayler, 2013), plasmin and cathepsins (Baranello et al., 2015).

1.6.2. Bulk flow or perivascular glymphatic drainage of Aβ

Despite the high metabolic activity and the extreme sensitivity of neuronal function to its immediate milieu, brain lacks the lymphatic vasculature that is expected to clear out the byproducts of metabolism like in the rest of the body. This role is supposedly taken over the by the bulk flow of CSF that is formed in choroid plexus and flows through the ventricles and subarachnoid space. The solutes (or waste byproducts) are finally reabsorbed into the blood stream via arachnoid villi of the dural sinuses, cranial nerve sheaths or nasal lymphatics. The interstitial fluid (ISF) diffuses through the brain tissue without any discrete anatomical flow path. This convective bulk flow of ISF is instrumental in removing most interstitial solutes including Aβ (Iliff et al., 2012; Weller et al., 2008).

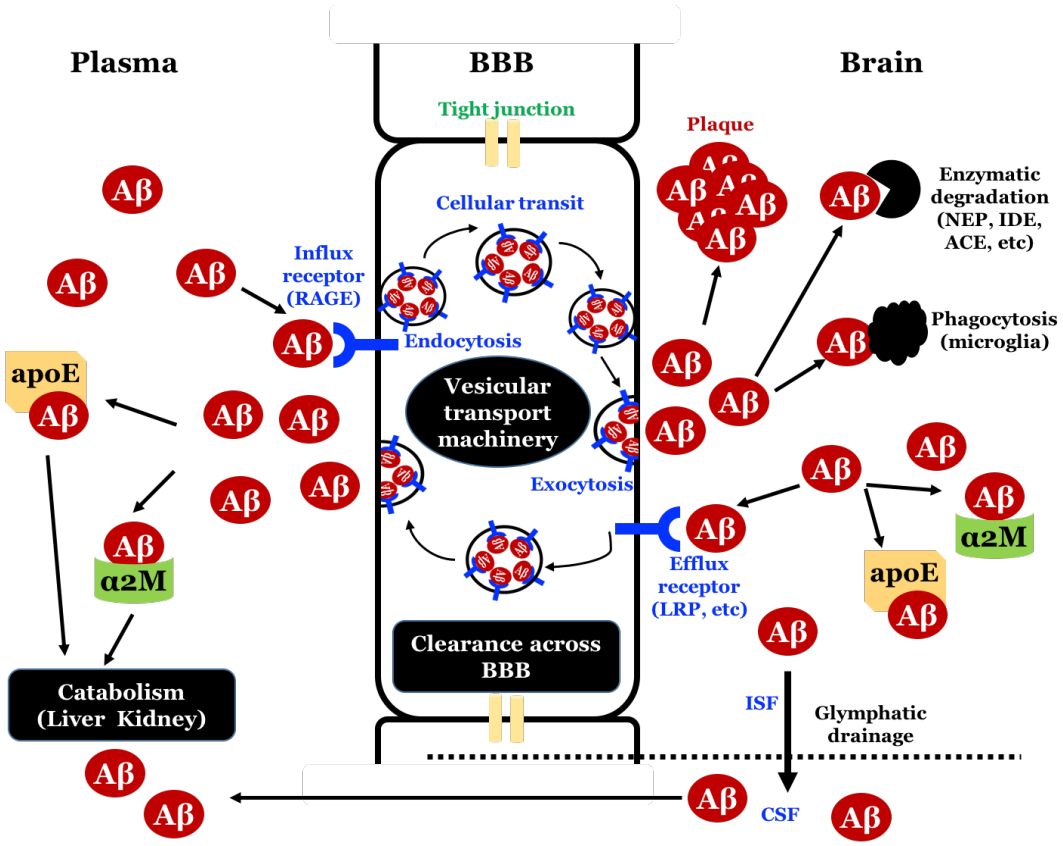

Figure 1.4 Clearance processes of amyloid beta (Aβ) protein. Predominantly, brain Aβ can be cleared by (1) enzymatic degradation by neprilysin (NEP), insulin degrading enzyme (IDE), etc.; (2) phagocytosis by microglia; (3) perivascular glymphatic drainage- that is via interstitial fluid (ISF) into the cerebral spinal fluid (CSF) or (4) transport across the BBB endothelium. Once in the plasma, it is cleared by catabolic processes in liver and kidney. The soluble Aβ is stabilized by chaperones α2M and apoE. BBB maintains this dynamic equilibrium of plasma and brain Aβ pools. Receptors such as RAGE (influx) and LRP (efflux) have been proposed to be involved in Aβ transcytosis. However, the precise vesicular transport machinery (endocytosis, cellular transit and exocytosis) of Aβ at the BBB endothelium is not known yet.

1.6.3. Aβ clearance across the brain barriers

There are two well-defined barriers between the brain and plasma milieu: (1) Blood-Brain Barrier (BBB) and (2) Blood-CSF Barrier (BCSFB). Transport across the BBB has been proposed to be one of the primary clearance portals for brain Aβ clearance. In fact, the large surface area of the BBB (20 m^2), along with BCSFB, are critical to maintaining the brain homeostasis (Marques et al., 2013). This clearly indicates that brain barriers directly hold the communication channel between plasma and brain homeostasis and respond to peripheral or brain parenchymal events with specific responses that are *not* independent of each other.

1.7. Blood-brain barrier: an integral component of the neurovascular unit

The Blood-Brain Barrier was first discovered in 1885 when Paul Ehrlich injected a water soluble dye in the periphery that could not enter and stain the brain. Subsequent follow up experiment by his student Edwin Goldmann in 1904, who injected trypan blue directly into the cerebrospinal fluid (CSF) stained all cell types in the brain but failed to penetrate into the periphery. These studies clearly demonstrated that a physical barrier exists between the brain and periphery that prevented the entry of even small molecules. However, it was not until 1990, that Lewandowsky formally used the term bluthirnschranke (Blood-Brain Barrier) to describe this barrier (Hawkins and Davis, 2005).

The sophistication in describing BBB characteristics has evolved over the years. Anatomically, it is represented as a single layer of endothelial cells that line the circumference of the brain capillary walls. These endothelial cells are distinguished from those in the periphery by increased mitochondrial content (Olden-dorf et al., 1977), a lack

of fenestrations (Fenstermacher et al., 1988), minimal pinocytotic activity (Sedlakova et al., 1999), and the presence of tight junction (TJ) (Kniesel and Wolburg, 2000). More recently, it is being realized that the abovementioned BBB endothelium is an integral part of the neurovascular unit (NVU) that consists of: (1) endothelium lining the cerebral vascular tree, pericytes covering the vascular capillaries, and vascular smooth muscle cells (VSMCs) enwrapping the cerebral arterioles and arteries; (2) glial cells such as astrocytes, microglia and oligodendrocytes; and (3) neurons. This close proximity of neurons with the NVU enables an effective functioning of the central nervous system to regulate cerebral blood flow, transport of oxygen and energy, and clearance of toxic and metabolic waste. It was shown that for Aβ40 (Shibata et al., 2000), about 75 % of the total clearance is via the BBB, 10 % is by ISF bulk flow and 15 % is retained due to enzymatic degradation or by macrophages (Lai and McLaurin, 2012). Using two-photon microscopy it was shown that neurons are usually within 13 μm of a capillary (Zhang and Murphy, 2007), and the neuronal cells are considerably away from CSF (Smith et al., 2004). Therefore, BBB, being relatively closer to the neurons, have an edge to control the brain solutes composition. This BBB is therefore expected to maintain the dynamic equilibrium between plasma and brain Aβ pools, as is discussed in the next section.

1.8. Plasma and brain Aβ pools

Theoretically, there are two distinguishable Aβ pools- (1) Brain Aβ pool, that is the combination of ISF and CSF Aβ pools; and (2) plasma or peripheral Aβ pool, also called as circulating Aβ pool. However, more emphasis has been placed on the changes in brain Aβ pool, because of the manifestation of characteristic plaques in the brain and consciously or unconsciously disregarded the contribution of circulating plasma or

peripheral Aβ pools that are not immediately apparent. The brain Aβ concentration increases from 0.3 nM (normal) to ~ 12 nM (AD) during the course of the disease (Deane et al., 2004). Interestingly, the same 40 fold increase in also seen in the plasma Aβ concentration that rises from 0.05 nM (normal) to ~ 2 nM (AD) (Deane et al., 2004). Also, the brain Aβ concentration is noted to be about 6 fold higher than the plasma Aβ concentration, in both physiological (normal) and pathological (AD) conditions (Cirrito et al., 2003; Deane et al., 2004). This circulating plasma Aβ reflects the contribution of Aβ from the peripheral tissues that produce Aβ constitutively, as well as Aβ that gets transported across the blood brain barriers from the CNS. The increase in plasma Aβ pool will probably expose BBB on the luminal side, which may affect the luminal signaling and functioning.

1.9. Aβ isoforms and the critical Aβ42:Aβ40 ratios

The ratio of Aβ42:Aβ40 has been noted to be perturbed in AD patients with the disease progression. Among the two isoforms, at physiological conditions, Aβ40 levels are 10- and 1.5- fold greater than that of Aβ42 in CSF and in plasma, respectively (Fagan et al., 2006). As the disease progresses from mild cognitive impairment (MCI) to cognitive decline, Aβ42:Aβ40 ratio decreases in plasma and increases in brain (Toledo et al., 2013). In familial AD, the increase in the ratio is due to overproduction of Aβ. However, in sporadic AD, it is attributed not to overproduction but impaired clearance (Mawuenyega et al., 2010). Also, interestingly, it is known that there are distinct sites of production for Aβ40 and Aβ42; Aβ40 is primarily produced in trans golgi network (TGN), whereas Aβ42 is primarily produced in endoplasmic reticulum (ER) (Hartmann

et al., 1997). Can the Aβ40 and Aβ42 clearance pathways also be any different? If they are different, then both Aβ40 and Aβ42 clearance pathways may have to be investigated separately to understand inefficient Aβ clearance in the AD brain.

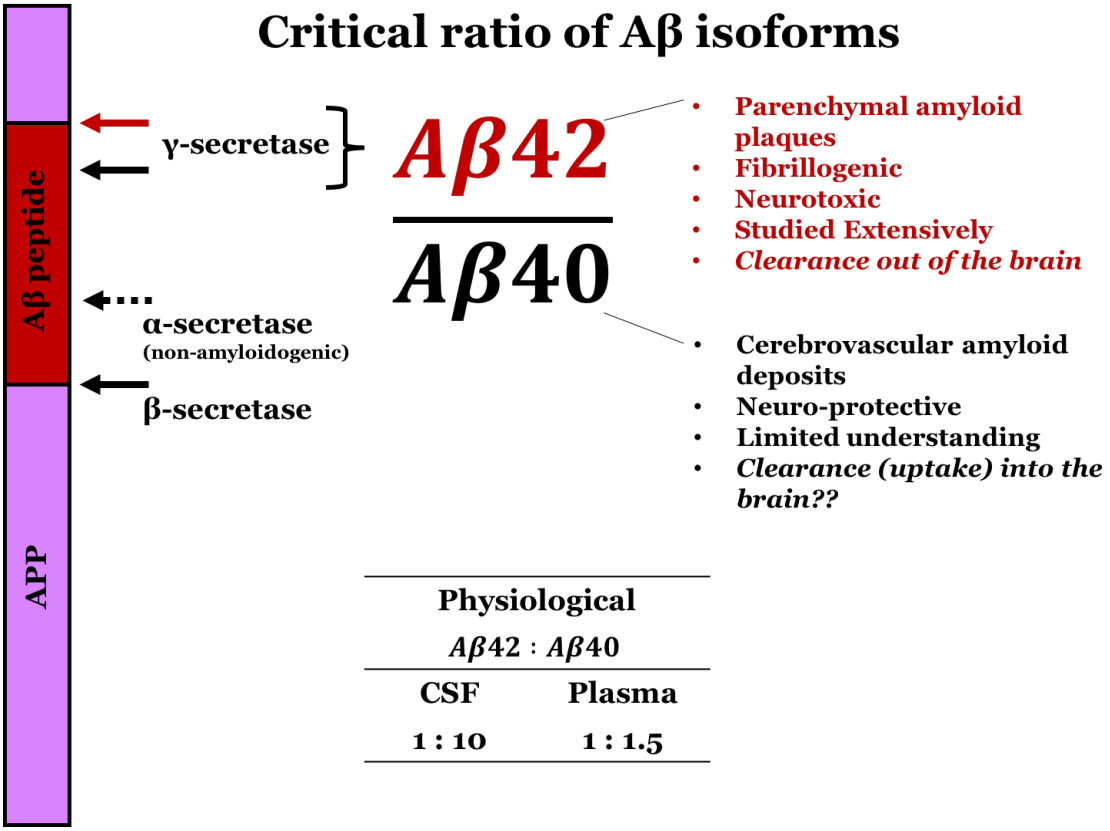

Figure 1.5 Critical ratio of Aβ isoforms is perturbed in AD. Amyloid beta (Aβ) peptide is formed from APP due to cleavage by protease β- and γ- secretases. In the non-amyloidogenic or normogenic pathway, α-secretase cleaves at the regions that are within the Aβ peptide sequence. Depending upon the site of γ- secretase, Aβ can be formed as long (Aβ42) or short (Aβ40). Moreover, physiological ratio of Aβ42:Aβ40 is changed during the course of disease progression in both CSF and plasma. Aβ42 is the primary component of most parenchymal plaques and is supposed to be more fibrillogenic and neurotoxic. Therefore, this isoform, is expected to be more toxic and is studied extensively. Whereas, Aβ40 is present in larger amounts and predominates cerebrovascular amyloid deposits. Further, there is evidence that Aβ40 is actually neuroprotective against Aβ42. Therefore, our hypothesis is that the impaired Aβ clearance, could mean the impairment of toxic Aβ42 clearance out of the brain, as well as impaired clearance (uptake) of relatively protective Aβ40 into the brain.

The association between the plasma Aβ levels and brain Aβ accumulation along with cognitive decline in familial AD or Down Syndrome patients have been well established (Matsuoka et al.; Schupf et al., 2001). The reports from the sporadic AD cases have been rather inconsistent. For example, cross sectional studies in sporadic AD patients have reported a decrease (Lui et al., 2010), or an increase (Mayeux et al., 2003, 1999) in Aβ42 or an increase (Mehta et al., 2000) in Aβ40 levels with no significant change in their ratios (Figurski et al., 2012; Fukumoto et al., 2003; Toledo et al., 2011). Similarly, longitudinal studies have been associated with an increased risk conversion to AD having a high baseline of Aβ40 (Hansson et al., 2012; van Oijen et al., 2006), or Aβ42 (Blasko et al., 2010; Mayeux et al., 2003; Schupf et al., 2008). Interestingly, there is consistency in the lower plasma levels of Aβ42:Aβ40 ratio in studies that accounted for them (Graff-Radford et al., 2007; Okereke et al., 2009; Schupf et al., 2008; van Oijen et al., 2006). These ideas further substantiate that Aβ should be considered toxic only when there is an imbalance between its production and clearance.

In plasma and CSF, Aβ peptides can exist as soluble free unbound forms or are bound to chaperones. There are several receptors that can play this role of chaperones including apoE, apoJ, transthyretin, and LRP (sLRP). (Deane et al., 2009) Aβ40 binds to LRP with a higher affinity (K_d = 0.6 - 1.2 nM) compared to Aβ42 (Deane et al., 2004). Interestingly, no differential effect of Aβ isoforms was seen on LRP internalization or synthesis, but just proteasome dependent LRP degradation was promoted at pathological levels of Aβ.

1.10. Impaired clearance, and not overproduction triggers Aβ accumulation

After several years of debate on what impacts AD pathology most, over production or impaired clearance, it was clarified that impaired clearance and not overproduction is responsible for the accumulation of Aβ in the brain (Mawuenyega et al., 2010). In this seminal study, the authors conducted stable isotope labeling kinetics (SILK) study of Aβ production versus clearance. Participants were infused with a stable isotope of $^{13}C_6$-leucine and cerebrospinal fluid samples were collected before, during and after labeling. Stable isotope labeling tandem mass spectrometry (SILT-MS) method was used to analyze samples. Finally, the increase in labeled Aβ during the production phase and the removal of labeled Aβ during the clearance phase reflected the relative production and clearance of Aβ in the CNS (Mawuenyega et al., 2010).

1.11. Amyloid as prions

A new dimension suggests AD progression may be similar to that of the infectious prion (or prionoids/ prion like) disease. As per this concept, amyloid state of protein refers to that state where proteins elongates to form fibers and spines consisting of many β sheets (Eisenberg and Jucker, 2012). As infectious prions in the microbial world, these self-aggregating prionoids or amyloids transmit or propagate the disease from one cell to another. However, several unanswered questions pertaining to this theory arise. For example, (1) what triggers these proteins to transition into amyloid state; (2) how do they transmit from one cell to another; and (3) does that mean extracellular amyloids have access to intracellular amyloids, and vice versa? Several theories have been proposed to support or oppose this ideology. However, overall, they all direct the rational

investigations to intracellular and transcellular trafficking and protein sorting in the cell (Aguzzi and Rajendran, 2009; Benilova et al., 2012).

1.12. BBB dysfunction in Alzheimer's disease: Are we still missing something?

1.12.1. Why do we have to investigate the vesicular transport of amyloid beta (Aβ) protein at the BBB?

(1) Alzheimer's disease is characterized by amyloid plaque deposition in the brain.

(2) Impaired clearance and not over production of Aβ likely drives the amyloid accumulation in AD brain.

(3) Blood brain barrier (BBB) is one of the primary clearance portals of Aβ from brain.

(4) A 40-fold increase in the total amount of Aβ is seen in both plasma and brain pools. Also, ratio of Aβ42:Aβ40 is disrupted in AD patients, both in brain (increases) and plasma (decreases).

(5) Plasma Aβ may contribute to the brain Aβ load by so far unclear mechanisms.

Therefore, the key question is: *How* is Aβ being cleared across the BBB? Owing to the existence of dynamic equilibrium between plasma and brain Aβ pools, does the problem (impaired clearance) lie in one or both directions, because the transport in either direction is *not* independent of each other (DeMattos et al., 2001; Eisele et al., 2014; Schupf et al., 2008; Sutcliffe et al., 2011)? Further, *what* causes the BBB to be 'dysfunctional'- a concept that will be elaborated more in the subsequent section? In AD, it is known that not just Aβ, but transport of other biomolecules such as insulin, transferrin, glucose, etc. is also disrupted. So the next question is, are these impaired

trafficking processes *linked* in any way? And finally, how can they be rectified?

1.13. Thesis proposal

My thesis work attempts to address the abovementioned questions. It is known that BBB plays a key role in brain homeostasis. Therefore, its dysfunction, will contribute to multiple diseases, including AD. The BBB dysfunction has been characterized in several reviews (Erickson and Banks, 2013) as (1) BBB disruption, which results in the leakage of peripherally circulating substances into the CNS that can be neurotoxic (Alafuzoff et al., 1983; Wada, 1998); (2) transporter dysfunction leading to consequences such as inadequate nutrient supply, buildup of toxic substances in the CNS, and increased presence of compounds that are normally prevented from entering the brain (De Reuck, 2012; Slemmon et al., 1994); and (3) altered protein expression and secretions by endothelial cells and other cell types of the NVU that can result in inflammatory activation, oxidative stress, and neuronal damage (Owen et al., 2010; Sultana et al., 2013). All three of these perturbations have been reported in AD. Consequently, BBB dysfunction has been postulated as a cause and consequence of AD (Erickson and Banks, 2013). Moreover, almost all AD cases, associated with vascular defects (such as high cholesterol, blood pressure, or cardiovascular disorders) have been shown to be directly correlating with BBB impairment (Erickson and Banks, 2013; Sagare et al., 2013).

Defects in the BBB transporters that influx or efflux Aβ has been an active field of research. It has been shown that Aβ in the brain parenchyma is primarily cleared across the BBB via the low-density lipoprotein receptor-related protein-1 (LRP-1), whose expression is reduced in the microvasculature of AD brain (Shibata et al., 2000). This assertion of decreased Aβ efflux has been validated by several other groups (Deane et al.,

2009, 2004; Jaeger et al., 2009; Pascale et al., 2011; Sagare et al., 2007, 2013). Other efflux transporters such as PGP are also implicated in Aβ efflux. It was postulated that both LRP and PGP may act together to efflux Aβ. However, it has now been shown that LRP can function independently as well (Deane et al., 2004; Shibata et al., 2000). Once in the plasma, Aβ is rapidly cleared by the liver, and to a lesser extent by the kidney and spleen. It's very short half-life (in minutes) further suggests the physiological necessity of maintaining low levels of circulating Aβ around the cerebrovascular milieu to prevent its influx into the brain, which can contribute to the plaque deposition, as has been shown recently. The influx transporter, receptor for advanced glycation end products (RAGE) has been identified as the primary transporter mediating luminal-to-abluminal Aβ transcytosis at the BBB endothelium (Candela et al., 2010; Deane et al., 2009; Fang et al., 2010; Mackic et al., 1998; Shi et al., 2009; Takuma et al., 2009). This assertion has been validated in several transgenic rodent AD models.

Another transporter that has been described in relation to AD is the glucose uptake transporter GLUT-1. Brain glucose consumption is known to be reduced in AD. A corresponding decrease in the expression of GLUT-1 on BBB has also been observed in AD patients (Harik, 2011; Horwood and Davies, 1994; Kalaria and Harik, 1989) However, whether the reduced glucose consumption is the cause or consequence of decreased transporter expression is yet to be deciphered. Although transporters provide critical information about Aβ transcytosis process, the rationale behind why the transporters become dysfunctional in the first place remain unresolved.

In addition to pathological changes at the receptor level, there may also be alterations in intracellular trafficking at the BBB. For example, changes in transport of

free and bound iron-transferrin (Deane et al., 2004; Qian and Wang, 1998), cholesterol (Chen et al., 2014) insulin (Mooradian, 1997), among others have been shown as a part of AD pathology. The vesicular trafficking disruptions could be manifested as: (1) perturbation in molecular pathways, and (2) alterations in vesicular trafficking. The occurrence and the impact of both these defects are addressed in my thesis.

1.14. Vesicular transcytosis of Aβ

Primary pathway by which Aβ can get across cellular plasma membrane is via the transcellular pathway. After binding to cell surface receptor, Aβ is endocytosed into the cell. There are several sub-steps that assist this vesicle formation and subsequent entry or endocytosis into the cell. It starts by the attachment or binding of Aβ to its receptor. This binding can result in either of the following effects (a) Aβ is taken up into the endothelial cell by endocytosis, sorted to the other end of the cell, and exocytosed. In other words, it is trafficked or transported across the BBB endothelium **(Figure 1.6)**. (b) Aβ is bound to the receptor (say efflux transporter in this case PGP from the luminal side or LRP from the abluminal side) and is effluxed out into the plasma without entering the endothelium, and so does not reach the opposite side; or (c) it enters the BBB endothelium (endocytosis), but fails to exocytose on the opposite side and accumulate in the endothelial cell.

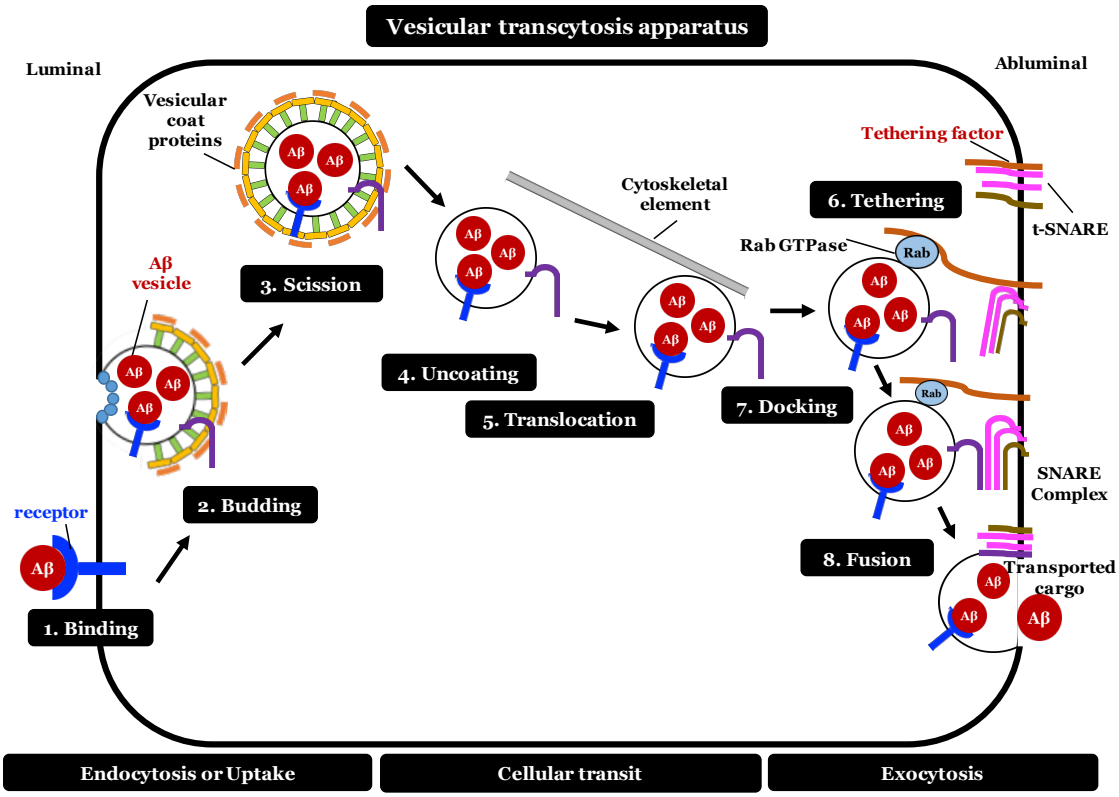

Figure 1.6 General vesicular transcytosis apparatus at the BBB endothelial cell. (1) Aβ cargo binds the receptor on the luminal side. (2) The membrane around the cargo-receptor complex begins to bud and form a vesicle by recruiting the coat proteins as well as targeting peptides (SNAREs). (3) The vesicle is now cleaved from the membrane by other proteins in a process called as scission. (4) The free vesicle in the cytosol is uncoated to expose the targeting peptide. (5) The uncoated vesicle is then translocated onto the other side of the cell or the acceptor organelle by microtubular cytoskeletal elements. (6) The vesicle is attached or tethered to the abluminal membrane by a tethering factor. This process usually employs Rab GTPases. (7) The tethered vesicle docks at the abluminal side of the membrane and the v-SNARE (targeting peptide on the vesicle) comes close to the t-SNARE (targeting peptide on the target membrane) by a process called as docking. (8) Finally, the two SNARE peptides, coil around each other to form the SNARE complex and bring the two membrane close to each other and eventually fuse, to release the transported cargo. As shown, this entire vesicular transport apparatus is divided into endocytosis or uptake, cellular transit and exocytosis.

Despite large amount of work conducted to understand the receptors-mediated endocytosis, the vesicular transport apparatus: comprising the endocytosis, intracellular transit and exocytosis still remains to be de-convoluted. In my thesis project, I specifically focused on the segments of this process occurring at the two plasma membrane extremities of the cell: endocytosis (uptake) and exocytosis (fusion, release). Interestingly, synaptic transmission processes, that involves the fusion or release of the neurotransmitters at the synaptic cleft is also impaired in AD **(Figure 1.7)**. However, little is known about the mechanistic players that are responsible for this loss. In our work, we investigated the contribution of the commonly employed SNARE exocytosis machinery in AD.

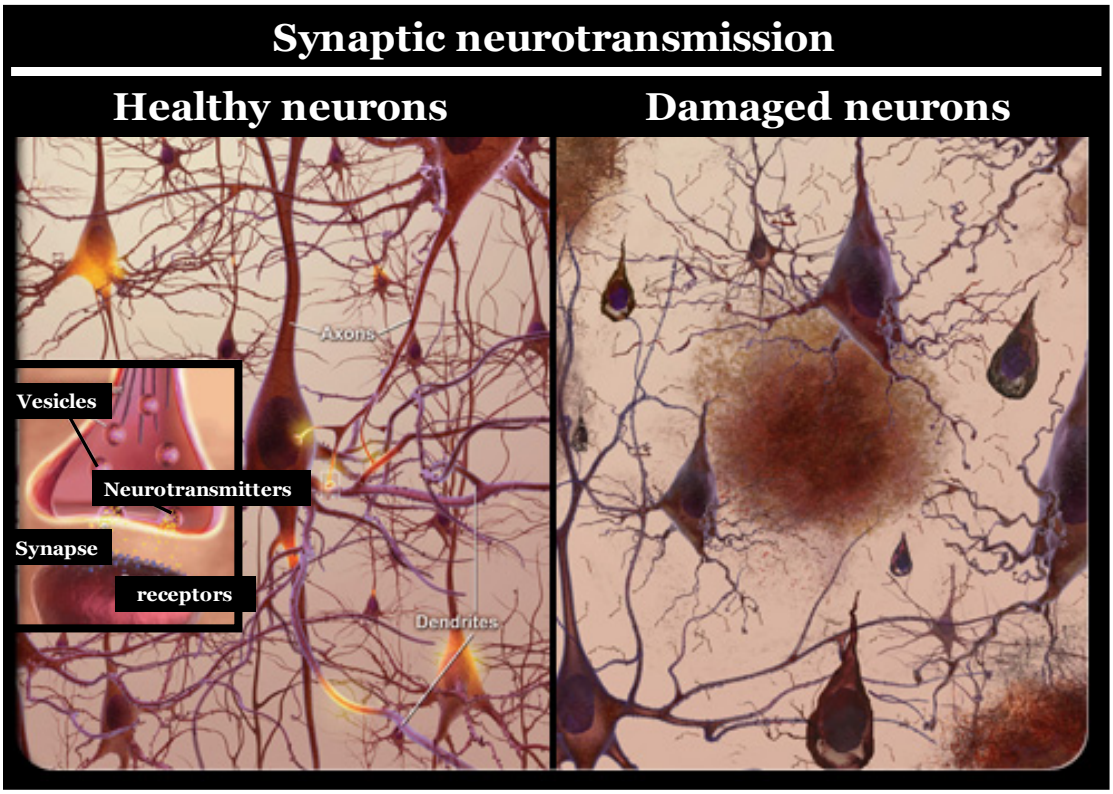

Figure 1.7 Synaptic neurotransmission is impaired in Alzheimer's disease (AD). Healthy neurons communicate with each other via synaptic neurotransmission involving the release of neurotransmitters in vesicles by presynaptic neurons into the synapse that are further taken up by the receptors on the post synaptic neuron. In damaged neuronal network in AD, extracellular Aβ plaques and neurofibrillary tangles may disrupt this synaptic neurotransmission. SNARE machinery is also involved in synaptic neurotransmitter release, as well as the vesicular trafficking at the BBB endothelium. Image modified and reused from National Institute on aging and National Institute of Health (National Institute on Aging, 2015).

1.14.1. Can AD be a trafficking disorder?

Now, as receptors cannot explain the problem completely, and we are aware that clearance or the transport of Aβ across the BBB endothelium may be the problem-nexus, finally leading to its accumulation as plaques; is there a possibility that AD is a trafficking disorder? It is difficult to provide a clear cut answer to this question, but that is certainly a possibility.

Interestingly, several disorders are known in literature where impaired trafficking is the issue. Very recently, a mutation in COPA genes disable the coat proteins to assemble and form the complex needed for the intracellular transport in hereditary auto-immune mediated lung disease and arthritis (Watkin et al., 2015). Earlier, chloride channel disease have been shown to result from impaired vesicular function (Jentsch et al., 2005). Clathrin mediated endocytosis has been shown to be impaired in multiple diseases including Type A-B Niemann-Pick disease. In AD as well, there is evidence that understanding trafficking might provide some critical clues. For example, the neuronal sortilin-related receptor (SORL1) that has roles in sorting and trafficking has been found to be associated with AD (Caglayan et al., 2014; Rogaeva et al., 2007). Disorders in trafficking of APP had already been suggested in the field earlier (Kim et al., 2015; Suzuki, 2006). However, the trafficking apparatus and possible issues in Aβ itself need further investigation. Trafficking disorders have been specifically common in neuropathological disorders: dynein dysfunction has been shown to synaptic vesicle docking and impair cognitive function (Kimura et al., 2012), impaired receptor mediated endocytosis contributes to alcohol-induced apoptosis (Casey et al., 2008), lysosomal dysfunction leading to Alzheimer-like neuritic dystrophy (Lee et al., 2011), lysosomal

and SNARE function are impaired in lysosomal storage disorders (Fraldi et al., 2010); as well as some rare ailments such as Hermansky-Pudlak Syndrome and Chediak-Higashi syndrome (Huizing et al., 2001).

What we do not know is how this cargo, Aβ is trafficked across the BBB endothelium. Is it the same or different process in either direction of luminal to abluminal (plasma to brain) or abluminal to luminal (brain to plasma)? What are the molecular players that are involved? Is there an impairment in the function of these molecular players that prevents them to shuttle Aβ normally? These are some of the questions that need critical investigation to discover the nexus of the impaired clearance of Aβ at BBB endothelium.

1.15. Thesis project

1.15.1. Objective

The primary objective of my thesis project was to identify key molecular and kinetic processes that are critical to Aβ transport at the BBB endothelium in Alzheimer's disease (AD).

This objective was built upon three simple ideas **(Figure 1.8)**:

(1) Detecting *early* is the key and changes in Aβ are earliest changed biomarker seen in AD.

(2) BBB maintains the equilibrium between plasma and brain Aβ pools. Although Aβ plaques are seen in brain, both plasma and brain Aβ levels increase 40-fold proportionately. Therefore, luminal exposure could affect the brain Aβ buildup as well.

(3) Characteristic ratio of Aβ42:Aβ40 increase in brain and decrease in plasma. This switch may be due to alterations in *either* isoform. So, investigations in parallel are critical.

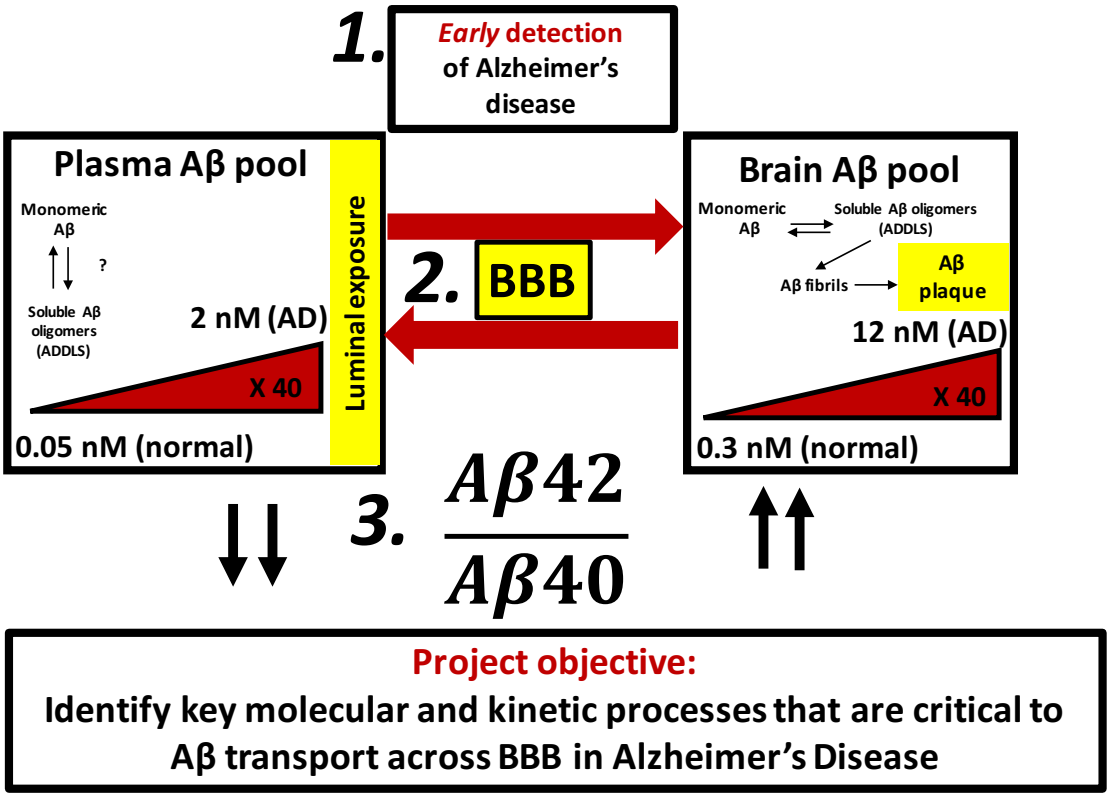

Figure 1.8 The three simple ideas used to build the thesis project objective.

1.15.2. Hypothesis

The primary hypothesis of my work is that over time, Aβ isoforms are accumulating at the BBB endothelium; thereby (1) impacting their transit or permeability across BBB; (2) perturbing the dynamic equilibrium of brain and plasma Aβ pools; and finally (3) triggering BBB dysfunction and worsening Aβ burden to transform into plaques.

This hypothesis is built upon earlier published work from our group demonstrating that mutant form Dutch-Aβ40 is accumulating in the BBB endothelium by interfering with its own exocytosis in cerebral amyloid angiopathy (CAA) (Agyare et al., 2013). Dutch-Aβ40, a vasculotropic mutant form, accumulated more than the regular Aβ40 isoform. Interestingly, more than 80 % of sporadic AD cases have CAA. Here, we hypothesize, that over several years, like the mutant form, Aβ isoforms are also accumulating at the BBB endothelium, probably to varying extents, and thereby impacting their clinical ratios, as well as clearance transport processes.

1.15.3. Specific Aims

1. Evaluate age dependent changes in luminal exposure of Aβ isoforms at the BBB endothelium (Chapter TWO)
2. Investigate key molecular players in the uptake or endocytosis of Aβ isoforms at the BBB endothelium (Chapter THREE)
3. Evaluate the initial kinetic interactions of Aβ isoforms with the BBB endothelium (Chapter FOUR)
4. Investigate the role of SNARE exocytosis machinery in the exocytosis of Aβ isoforms at the BBB endothelium and in the neurons in AD (Chapter FIVE)

1.15.4. Rationale

The rationale for this work is that differential interactions of Aβ isoforms with the BBB endothelium could resolve mechanistic reasons behind the perturbed ratio seen in AD and explain the dysregulated transcytosis leading to the impaired Aβ clearance.

1.15.5. Novelty

Our approach was novel as we investigated (1) early changes at BBB endothelium, rather than brain parenchyma, where the plaques are observed. We believe that changes at BBB endothelium could probably be the 'cause' to lead to the 'effect' of brain Aβ plaques; suggesting a possible paradigm shift in field. (2) We investigated not just pathological Aβ42, but both Aβ isoforms in parallel. (3) We employed sophisticated research tools for mechanistic (such as FLIM-FRET) and kinetic (such as SPECT-CT) techniques to elucidate initial Aβ interactions with BBB endothelium.

CHAPTER TWO

2. AGE DEPENDENT CHANGES IN AMYLOID BETA KINETICS IN WILD TYPE AND ALZHEIMER'S DISEASE TRANSGENIC MICE

2.1. SUMMARY

Age is the most common risk factor for Alzheimer's disease (AD). Amyloid beta (Aβ) proteins accumulate in the AD brain most likely due to their impaired clearance. The manner in which age causes BBB dysfunction, perturbs Aβ trafficking at the BBB, and brings dynamic changes in plasma and brain Aβ concentrations is not well understood. In this chapter, changes in plasma pharmacokinetics as well as luminal to abluminal (L-A) permeability of ^{125}I-Aβ with age in WT and AD transgenic (APP,PS1) mice are presented. We demonstrate that luminal exposure of BBB endothelium to Aβ40 isoform increases with age whereas Aβ42 isoform decreases in WT animals. This trend is lost in APP,PS1 animals. Surprisingly, the increased exposure of protective Aβ40 isoform is not translated into its higher BBB permeability; where, BBB permeability of Aβ40 decreases with age and is apparent in as early as 8 week WT animal, when compared to APP,PS1 mice. On the other hand, BBB permeability of Aβ42 increases with age in WT animal and is not significantly different from APP,PS1 animal even at 52 weeks. These findings suggest that over age, unknown mechanisms triggering BBB dysfunction prevent the protective isoform Aβ40 to reach the brain whereas toxic Aβ42 can permeate regardless. In the subsequent chapters, we discuss some of these mechanisms that might be implicated in triggering this BBB dysfunction.

2.2. INTRODUCTION

Age is the most common risk factor associated with Alzheimer's disease (AD). (Karran et al., 2011; Tanzi, 2012) Many of the common AD symptoms such as dementia or memory loss, confusion, apathy, depression and delusion are often misinterpreted as the consequences of normal aging (Selkoe, 1991; Selkoe and Podlisny, 2002; Selkoe and Schenk, 2003). However, there is a distinction between AD symptoms and physiological changes observed in normal aging. Typically, there are basic differences between normal aging, pathological aging and AD. For example, it has been demonstrated that brains of normal aging and AD have different numbers and volume of neurons, particularly in hippocampus region that is majorly affected in AD (Simić et al., 1997).

Moreover, the pathological hallmarks of AD, amyloid plaques and intraneuronal tangles are not consistently expressed during normal or pathological aging. Further, the extents of soluble and insoluble Aβ in circulation, may also distinguish AD, normal aging, and pathological aging (J Wang et al., 1999). It was shown that the increasing amount of insoluble Aβ40 is believed to shift the trend from normal aging, to pathological aging, to AD (Jun Wang et al., 1999).

Moreover, age dependent changes seen in the Aβ transporter expression at the BBB and blood-CSF-Barrier or Choroid plexus (CP) could contribute to BBB dysfunction leading to disequilibrium of plasma and brain Aβ pools. For example, at CP, there was an increase in the transcription of the Aβ efflux transporters, LRP-1 and PGP, no change in RAGE expression and a decrease in LRP-2, the CP epithelium influx transporter, with aging (Pascale et al., 2011). These changes are the reverse of that seen at the BBB, where the transcription of LRP-1 and PGP decreases and the expression of RAGE increases.

This indicates a compensatory mechanism for Aβ transporters at the brain barriers. However, what exactly drives this change or switch in the transcriptional expression of the transporters is not known yet.

The convenience and necessity of plasma biomarkers in AD have been very well accepted (Lui et al., 2010; Toledo et al., 2013; Yaffe et al., 2011). Although some controversies still exist, there is a reasonable acceptance that the two Aβ pools do not work independently of each other. That is to say, plasma Aβ levels might be able to directly or indirectly contribute to the brain Aβ load, leading to its accumulation. However, what role does age play in this orchestrated event is poorly understood.

The purpose of the following study was to precisely address some of these questions. Plasma pharmacokinetics and BBB permeability of Aβ isoforms in three different age groups (8 week, 24 week, and 52 week) of wild type and AD transgenic (APP,PS1) mice were compared and trends assessed. We propose that there are age dependent changes in the luminal exposure of BBB endothelium that may be able to define or provide clues to explain the alterations in clinical ratios of Aβ isoforms as well as the Aβ accumulation trends in AD. We hypothesize that age could trigger and accelerate several pathological features observed in AD.

2.3. MATERIALS AND METHODS

2.3.1. Aβ proteins

Aβ40 and Aβ42 were synthesized as described earlier (Kandimalla et al., 2005). The Aβ monomers were prepared according to the procedure described by Klein (Klein et al., 2004). Briefly, Aβ peptides were accurately weighed, dissolved in ice cold 1,1,1,3,3,3

hexafluoroisopropanol (HFIP) (MP Biomedicals, Santa Ana, CA), and incubated at room temperature for 60 min. The resultant solutions were chilled on ice, aliquoted appropriately, and allowed to dry overnight. The HFIP traces were further removed by vacuum evaporation, and the dried films were stored at -20 °C. Before each experiment, the Aβ films were dissolved in anhydrous dimethyl sulfoxide (DMSO), diluted in Hams F-12 medium (Mediatech, Manassas, VA), and centrifuged at 18,000 rpm to remove any insoluble Aβ aggregates.

2.3.2. Radio iodination of proteins

Carrier-free $Na^{125}I$ and $Na^{131}I$ were obtained from PerkinElmer Life and Analytical Sciences (Boston, MA). Human Aβ40 (500 μg), Aβ42 (500 μg) or BSA (500 μg) was labeled with either ^{125}I or ^{131}I, using the chloramine-T procedure (Kandimalla et al., 2005; Poduslo et al., 1997). Free radioactive iodine was separated from the radiolabeled protein by dialysis against 0.01 M phosphate-buffered saline at pH 7.4 (Sigma-Aldrich, St. Louis, MO). Purity of the radiolabeled proteins was determined by trichloroacetic acid (TCA) precipitation. The radioiodinated Aβ was deemed to be acceptable if the TCA perceptible counts were greater than 95 % of the total counts. The final radioactivity associated with ^{125}I labeled Aβ40 or Aβ42 was determined to be 4 mCi/mg protein.

2.3.3. Animals

All experiments conducted on animals were as per the National Institutes of Health Guide for Care and Use of Laboratory animals and approved by the Institution's Animal Care and Use Committee of the Mayo Clinic, Rochester, MN. The wild-type (WT) mice (B6/SJL strain) were housed in virus free barrier facility with 12-h light and dark cycle, and were provided with pellet food and purified water ad libitum.

2.3.4. Plasma pharmacokinetic studies

The plasma pharmacokinetic studies were conducted as explained schematically in **Figure 2.1**. Briefly, 8-, 24-, and 52- wild type or WT (C57B6/SJL) and AD transgenic (APP,PS1) mice weighing 25-30 g were anesthetized. The genetic background of these APP,PS1 mice was the C57B6/SJL mice. Femoral vein and femoral artery were catheterized under general anesthesia using 1.5 % isofluorane in oxygen at 4 L/min. 100 μCi/100μL single intravenous bolus dose of ^{125}I-Aβ40 or ^{125}I-Aβ42 was administered via the femoral vein and blood samples (20 μL) were collected from the femoral artery. Samples were collected at 0.25, 1, 3, 5, 10 and 15 minutes. At the end of the experiment, at 15th minute, an aliquot of ^{131}I-BSA (100 μCi, 100 μL) was injected to serve as a measure of residual plasma volume (V_p). One minute after the ^{131}I-BSA injection, the final blood sample was collected, and the animal was sacrificed. Blood samples were made up to a volume of 100 μL using saline, centrifuged, and the blood cells were separated. The resultant plasma, thus obtained, was subjected to TCA precipitation and radioactivity of both ^{125}I and ^{131}I in precipitate and supernatant was assayed using two channel gamma counter (Cobra II; PerkinElmer Life and Analytical Sciences, Boston, MA).

The plasma concentrations of ^{125}I-Aβ40 and ^{125}I-Aβ42 were described by bi-exponential disposition and the pharmacokinetic parameters were estimated by Phoenix WinNonlin® 6.4 by fitting the following equation:

$$C(t) = Ae^{-\alpha t} + Be^{-\beta t} \quad (1)$$

where, C(t) = ^{125}I-Aβ40 or ^{125}I-Aβ42 μCi/ml of plasma, A and B are intercepts and α and β are the bi-exponential rate constants.

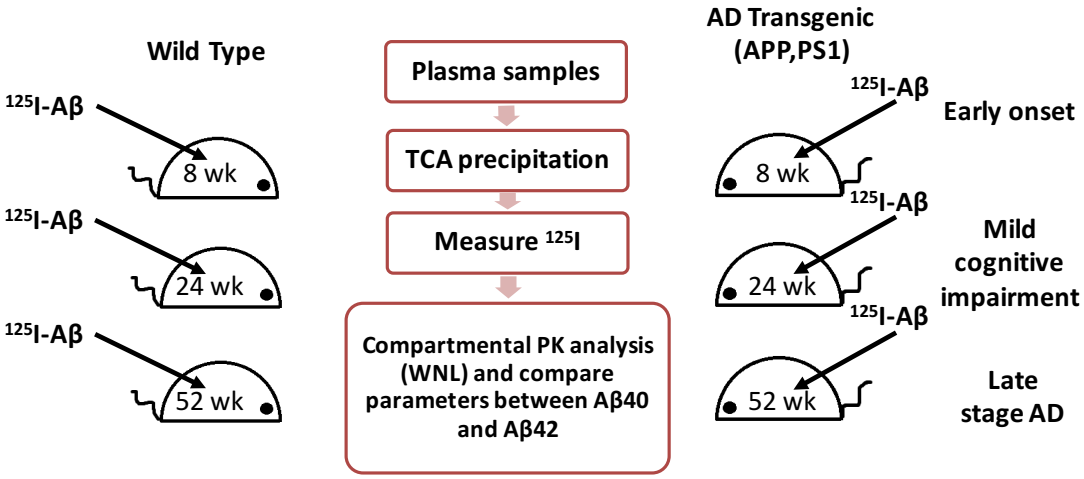

Figure 2.1 Experimental study design to predict ^{125}I-Aβ40 and ^{125}I-Aβ42 plasma pharmacokinetics. Plasma samples were collected at designated time points and the radioactivity associated with the intact peptide was determined by TCA precipitation. A two-compartment model was fitted to the data using WinNonlin® 6.4 and the parameters were estimated.

2.3.5. Blood brain barrier permeability studies

After the 15th minute blood sample was obtained from the femoral artery as described above, ^{131}I-BSA was injected via the femoral vein, and the final blood sample was withdrawn at the end of the 16th minute. Then, the animal was sacrificed, brain was removed from the cranial cavity; dissected into the anatomical regions: cortex, caudate putamen, hippocampus, thalamus, brain stem and cerebellum and assayed for ^{125}I and ^{131}I radioactivity.

The residual brain region plasma volume (V_p, microliters per gram) and the permeability surface area product (PS) values were calculated as described, using:

$$V_p = \frac{q_p \, X \, 10^3}{C_v \, X \, W} \qquad (2)$$

where, q_p is the ^{131}I-BSA content (cpm) of tissue, C_v is the ^{131}I-BSA concentration (cpm per milliliter) in plasma. W is the weight (grams) of the brain region.

From the total of ^{125}I-Aβ content (q_T) (cpm) of the brain region, the amount of ^{125}I-Aβ that enters the brain extravascular or parenchymal space (q) (cpm per gram) is calculated as follows:

$$q = \frac{q_T}{W} - \frac{V_p C_a}{10^3} \qquad (3)$$

where, C_a is the final ^{125}I-Aβ concentration (cpm per milliliter) in plasma. The PS (milliliters per gram per second) at the BBB is calculated as follows:

$$PS = \frac{q}{\int_0^t C_p \, dt} \quad (4)$$

where, t is the circulation time, q is the extravascular ^{125}I activity in the brain region at time t and $\int_0^t C_p \, dt$ is the plasma concentrations time integral of ^{125}I-Aβ.

2.3.6. Data analysis and statistics

Unless mentioned otherwise, the significance of difference in the mean values of controls and treatments were tested by Two-Way ANOVA followed by Bonferroni post hoc test for age and animal model (WT vs APP,PS1) as two factors in GraphPad Prism version 5.0 (GraphPad Software Inc, San Diego, CA).

2.4. RESULTS

2.4.1. ^{125}I-Aβ40 and ^{125}I-Aβ42 exhibit bi-exponential disposition in the plasma (Figures 2.2 and Table 2.1)

Like described before, (Agyare et al., 2013; Kandimalla et al., 2005), both ^{125}I-Aβ40 and ^{125}I-Aβ42 exhibited bi-exponential disposition in the plasma. Moreover, their plasma pharmacokinetic parameters altered with age and between WT and APP, PS1 mice.

Age dependent changes in predicted plasma pharmacokinetic parameters:

Aβ40 **(Figure 2.2 (A-B) and Table 2.1)**: In WT as well as in APP,PS1 mice, AUC increased and clearance decreased with age. A corresponding increase in the terminal half-life, ($t_{1/2,\beta}$) with age in both WT and APP,PS1 mice was also noted. In addition, the C_{max} values decreased with age in both WT and APP,PS1 animals.

Aβ42: **(Figure 2.2 (C-D) and Table 2.1)**: Unlike Aβ40, C_{max} decreased with age in WT animals. On the other hand, AUC and clearance trends demonstrated a decrease and an increase, respectively with age. Terminal half-life ($t_{1/2,\beta}$) also trended to decrease with age in WT mice. But there was no change in these parameters with age in APP,PS1 animals.

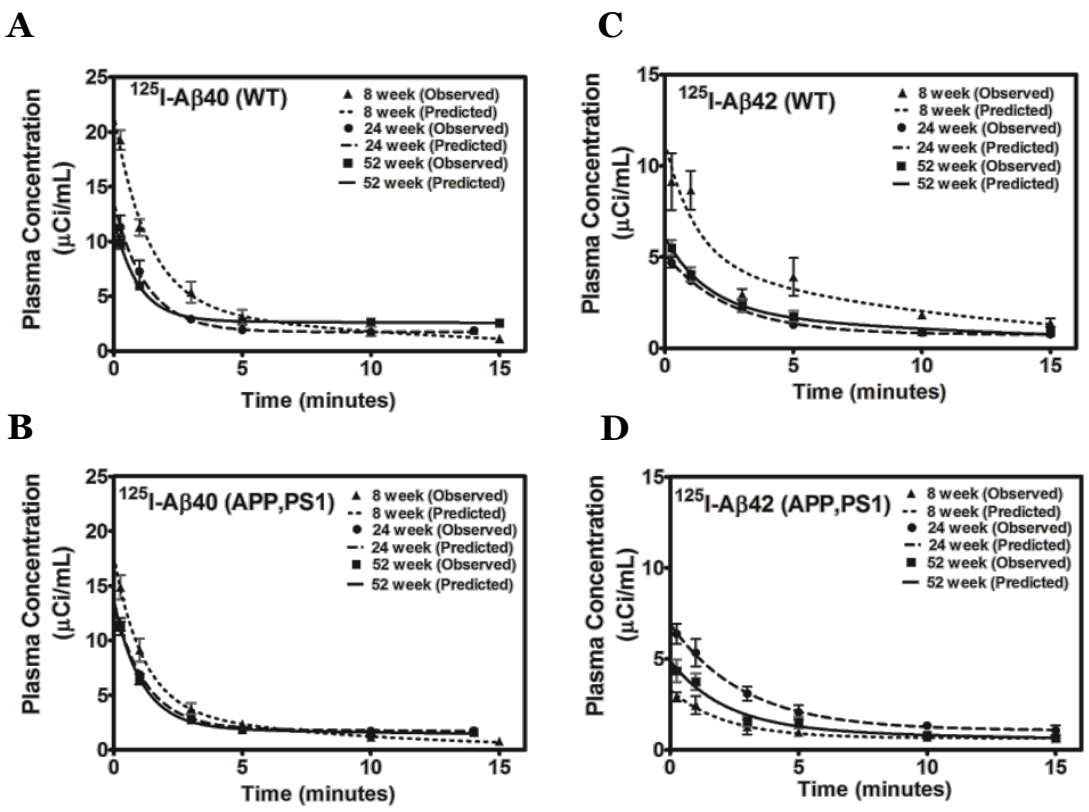

Figure 2.2 Plasma pharmacokinetics of ^{125}I-Aβ40 and ^{125}I-Aβ42 in WT and APP,PS1 mice at 8, 24, 52 weeks. Plasma pharmacokinetic profiles of ^{125}I-Aβ40 in **(A)** WT and **(B)** APP,PS1 animals. Plasma pharmacokinetic profiles of ^{125}I-Aβ42 in **(C)** WT and **(D)** APP,PS1 animals. Data are mean ± S.D. (n = 3-6); lines indicate the fit of two-compartment pharmacokinetic model to the plasma concentration time data.

Table 2.1 Predicted plasma pharmacokinetic parameters

	Aβ40				Aβ42			
	WT		APP,PS1		WT		APP,PS1	
Age (weeks)	AUC (μCi.min/mL)	CL (mL/min)	AUC (μCi.min/mL)	CL (mL/min)	AUC (μCi.min/mL)	CL (mL/min)	AUC (μCi.min/mL)	CL (mL/min)
8	63.51 ± 6.50	1.57 ± 0.16	49.65 ± 12.40	2.11 ± 0.5	78.87 ± 11.81	1.26 ± 0.19	27.64 ± 9.35 #	3.61 ± 1.22
24	43.47 ± 3.13	2.29 ± 0.16	103.04 ± 34.53	0.97 ± 0.32 #	40.13 ± 9.40	2.49 ± 0.28	72.19 ± 19.7	1.39 ± 0.3
52	372.67 ± 62.98 ***	0.26 ± 0.04 **	86.83 ± 22.76 ###	1.15 ± 0.31	31.15 ± 3.5	3.21 ± 0.3	30.89 ± 7.8	3.24 ± 0.8
Age (weeks)	C_{max} (μCi/mL)	β-half life (min)	C_{max} (μCi/mL)	β-half life (min)	C_{max} (μCi/mL)	β-half life (min)	C_{max} (μCi/mL)	β-half life (min)
8	23.22 ± 0.6	6.17 ± 1.9	17.74 ± 1.8 ###	5.98 ± 1.2	11.26 ± 0.51	16.32 ± 5.44	3.4 ± 0.29 ###	13.96 ± 7.72
24	16.35 ± 0.38	5.62 ± 1.22	12.53± 0.24 ##	28.65 ± 13.46	5.23 ± 0.29	17.58 ± 8.88	7.1 ± 0.2	25.38 ± 12.5
52	12.79 ± 0.13 ***	87.59 ± 16.92 **	13.71 ± 0.23	24.30 ± 9.52 ##	6.04 ± 0.3 *	6.8 ± 1.5	5.1 ± 1.0	10.74 ± 7.4

Table 2.1 Predicted plasma pharmacokinetic parameters of ^{125}I-Aβ40 and ^{125}I-Aβ42 in WT and APP,PS1 animals. Data are mean ± S.D. (n = 3-6) Significance determined by Two-Way ANOVA followed by Bonferroni post hoc tests between age (* $p < 0.05$, ** $p < 0.01$ and *** $p < 0.001$) and WT versus APP,PS1 (# $p < 0.05$) and ### $p < 0.001$).

Differences in plasma pharmacokinetic parameters between WT and APP,PS1 mice:

Aβ40: **(Figure 2.2 (A-B) and Table 2.1)**: In 52-week old APP,PS1 mice, AUC and terminal half-life values ($t_{1/2,\beta}$) were lower than it was in WT animals; no such difference in clearance was observed in WT and APP,PS1 mice. C_{max} in APP,PS1 animal was lower than that of WT in an 8 and 24-week old animal, but the trend was lost by 52-weeks.

Aβ42: **(Figure 2.2 (C-D) and Table 2.1)** There was a decrease in both AUC and C_{max} values in 8-week-old APP,PS1 mice compared to age-matched WT mice. However, no such differences were observed at later ages. Clearance and $t_{1/2,\beta}$ were not different between WT and APP,PS1 mice.

Interaction between the age and genotype factors (WT and APP,PS1)

Aβ40: Significant interaction was found between age and genotype factor in AUC***, clearance**, C_{max} *** and $t_{1/2,\beta}$ **.

Aβ42: Similar to Aβ40, significant interaction was found between age and genotype factor in AUC* and C_{max} ***; but not in $t_{1/2,\beta}$ and clearance.

2.4.2. Changes in the L-A BBB permeability of ^{125}I-Aβ40 and ^{125}I-Aβ42 with age and between WT and APP,PS1 mice (Figure 2.3)

Age dependent changes in L-A BBB permeability:

Aβ40: **(Figure 2.3 A-B)** BBB permeability of Aβ40 decreased with age in the cortex and hippocampus of WT mice. Although, similar trends were evident in APP,PS1 mice, they were not statistically significant.

Aβ42: **(Figure 2.3 C-D):** BBB permeability increases with age in WT animals in both cortex and hippocampus. Again, statistically significant trends were not seen in APP,PS1 animals with age.

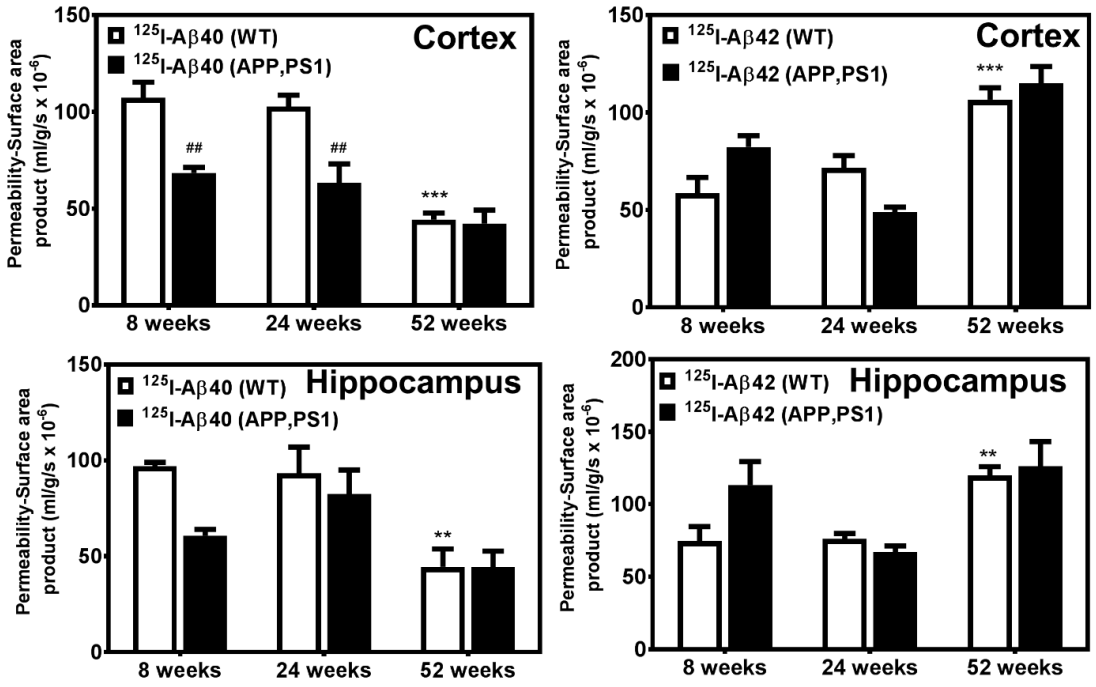

Figure 2.3 Blood brain barrier (BBB) permeability surface area (PS) product of ^{125}I-Aβ40 and ^{125}I-Aβ42 in WT and APP,PS1 mice at 8-, 24-, 52- weeks in two brain regions (cortex and hippocampus) that are severely implicated in AD. Luminal to abluminal (L-A) PS values of ^{125}I-Aβ40 in **(A)** cortex; **(B)** hippocampus. Similarly, luminal to abluminal (L-A) PS values of ^{125}I-Aβ42 in **(C)** cortex; **(D)** hippocampus. Data is mean ± S.D. (n = 3-6) Significance assessed over age (** $p < 0.01$ and *** $p < 0.001$) and WT versus APP,PS1 ($^{\#\#}$ $p< 0.01$) by Two-Way ANOVA followed by Bonferroni post hoc tests.

Differences in L-A BBB permeability between WT and APP,PS1 mice:

Aβ40 **Figure 2.3 (A-B):** Even at an early age of 8-weeks, the BBB permeability of Aβ40 in APP,PS1 mice was lower than that observed in WT mice. Similar trends were seen in 24-week mice as well. By 52 weeks, the permeability of Aβ40 in WT mice also decreased to the levels observed in APP.PS1 mice.

Aβ42 **Figure 2.3 (C-D)***:* No substantial difference in BBB permeability was seen between WT and APP,PS1 animals at any age group, not even by 52 weeks.

Interaction between the age and genotype factors (WT and APP,PS1)

Aβ40: Significant interaction was found between age and genotype factor in BBB permeability in cortex**; but not in hippocampus.

Aβ42: Similar to Aβ40, Significant interaction was found between age and genotype factor in BBB permeability in cortex*; but not in hippocampus

2.5. DISCUSSION

Age is the obvious risk factor of AD. Higher concentrations of Aβ isoforms and perturbations in Aβ42:Aβ40 ratios that are associated with AD progression, are believed to be a consequence of BBB dysfunction. However, the manner in which these three factors interplay with each other and perpetrate AD pathogenesis is not clearly understood. The objective of this study was to investigate changes in the plasma pharmacokinetics and BBB permeability of Aβ isoforms with age in WT and APP,PS1 mice.

The plasma pharmacokinetics of Aβ40 and Aβ42 in WT and APP,PS1 mice demonstrate distinct profiles (**Figures 2.1 and Table 2.1).** Increase in the plasma AUC and decrease in clearance for Aβ40 shows that this isoform accumulates in the plasma and Aβ42 does not. As significant interaction was seen between age and genotype (WT and APP,PS1) factors; to assess individual trends in the factors, One-Way ANOVA statistical analysis followed by Bonferroni's post hoc tests was also conducted **(Supplementary Figure S-2.2)** and the increase and decrease in plasma AUC and the opposite trends for clearance, for Aβ40 and Aβ42; respectively with age, were validated. This decreases the plasma Aβ42:Aβ40 ratio, which was previously shown to be associated with AD pathology. Interestingly, these indications of age dependent changes in Aβ profiles that are lost in AD model have been suggested earlier as well (Giedraitis et al., 2007; Sundelöf et al., 2008), where the normal equilibrium (correlation) between CSF and plasma Aβ levels was not seen in AD or MCI cases (Giedraitis et al., 2007). In Tg2576 AD transgenic mice model, there are age dependent changes in plasma, brain and CSF of both Aβ40 and Aβ42. Brain levels of Aβ40 and Aβ42 increase to that observed in

AD by 12-24 months, that is proportional to a decrease in CSF Aβ and a highly significant decrease in plasma Aβ levels (Kawarabayashi et al., 2001). Also, human plasma Aβ40 and Aβ42 have been shown to increase with age over 65 years and in late onset AD (Ertekin-Taner et al., 2008) and early onset AD. APP,PS1 is an animal model that overexpresses amyloid beta proteins. The kinetic changes observed in APP,PS1 mice might not be entirely due to the saturation of receptors Aβ by proteins, because the changes are evident at a very early age of 8-weeks, when the Aβ protein concentration is barely detectable in the plasma (Poduslo et al., 1999). This finding of accumulation of Aβ40 and not Aβ42 with age, also meant that over time, the luminal exposure of BBB endothelium to Aβ40 increases with age. Now instinctively, one would think that as the Aβ concentrations in the brain are almost 10 fold higher in normal as well as AD conditions, will this increased plasma (or luminal) exposure directly contribute to Aβ accumulation in the brain?

Surprisingly, our BBB permeability data (**Figure 2.2)** revealed that the increased exposure of Aβ40 does not translate to increase in its permeability. In fact, the permeability of Aβ40 decreases at an early age of 8 weeks in APP,PS1 mice compared to WT mice. However, no significant change in the permeability of Aβ42 was seen even by 52 weeks. Also, we could clearly see that over age, while the BBB permeability of Aβ40 decreases with age the permeability of Aβ42 increases with age in WT and APP,PS1 mice. This finding reemphasizes that BBB is far more than just a layer of tightly packed endothelial cell surrounding the cerebral blood vessels. It has an active signaling and trafficking apparatus and is directly and independently capable of modulating the brain homeostasis. Further, these results suggest that the increase in Aβ42 permeability is not

due to mere breakdown of the paracellular integrity of the BBB, but most likely due to the BBB dysfunction triggered by age.

In summary, the key finding from this chapter is as follows: a relatively early change in the course of disease progression; the decrease in Aβ40 uptake and increase in Aβ42 uptake at the BBB endothelium from the luminal to abluminal (L-A) direction could increase and decrease the Aβ42:Aβ40 ratios in the brain and plasma, respectively; that are associated with AD progression. In the subsequent chapters, we provide evidence that this BBB dysfunction is triggered by disrupted vesicular trafficking by Aβ isoforms.

CHAPTER THREE

3 DISTINCT UPTAKE MECHANISMS OF AMYLOID BETA ISOFORMS AT THE BLOOD BRAIN BARRIER ENDOTHELIUM IN ALZHEIMER'S DISEASE

3.1.SUMMARY

Blood brain barrier (BBB) is one of the primary clearance portals of Aβ proteins from the brain; and also is known to maintain the dynamic equilibrium between plasma and brain Aβ pools. It is widely known that Aβ42:Aβ40 ratios in plasma and brain are perturbed during AD progression. However, the mechanistic details on how these ratios are altered have not been clearly elucidated. In this chapter, using molecular interventions and kinetic assessments of Aβ proteins in two *in-vitro* BBB models, we demonstrate that the BBB endothelium handles Aβ40 and Aβ42, distinctly. While, Aβ40 is endocytosed via the clathrin-dependent endocytosis, Aβ42 is endocytosed by the lipid raft-mediated endocytosis. Our findings also suggest that the rate of uptake and permeability of Aβ isoforms are distinct, only in the luminal to abluminal or L-A direction. These mechanistic and kinetic differences provide the first direct evidence supporting the hypothesis that BBB dysfunction implicated in AD could differentially affect the trafficking of Aβ40 and Aβ42 between plasma and brain; and engender shifts in the Aβ42:Aβ40 ratios observed during AD progression. Further, Aβ isoforms utilizing the two canonically employed endocytosis machineries to varying extents, and probably

interfering with their function, also provide a mechanistic rationale to the impaired transport of other macromolecules such as insulin, transferrin, among others, that is seen in AD pathology.

3.2. INTRODUCTION

Most of the investigations on neurodegenerative disorders including Alzheimer's disease (AD) have been neurocentric. The involvement of the neurovascular unit (NVU) in neurodegenerative diseases has been relatively underexplored (Bell et al., 2007; Deane et al., 2009). The NVU comprises of BBB endothelium, astrocytes, pericytes, oligodendrocytes, and neurons, which work together as a cohesive communication and functional unit (Erickson and Banks, 2013; Zlokovic, 2010). This NVU is believed to be disrupted in AD (Zlokovic, 2010). The BBB endothelium, which is a critical component of the NVU, and is present at the interface of plasma and brain, is believed to maintain the dynamic equilibrium of Aβ in periphery and brain.

Recently, Mauwyenga et al (Kwasi G Mawuenyega et al., 2010) clearly demonstrated that it is the impaired clearance, and not overproduction of Aβ proteins that leads to their over accumulation and subsequent plaque formation in sporadic AD brain. Further, the BBB endothelium plays a critical role in Aβ clearance from the brain. In addition to degradation by proteolytic enzymes and removal by perivascular drainage, the BBB endothelium is suggested as one of the primary clearance pathways of Aβ (Bowman and Quinn, 2008; Deane et al., 2009). Hence, BBB dysfunction could impair Aβ clearance from the brain, and augment cerebral Aβ burden.

In non-demented individuals, the concentration of Aβ40 is about 10- fold and 1.5-fold higher than Aβ42 in cerebrospinal fluid (CSF) and plasma, respectively (Deane et al., 2009). These Aβ42:Aβ40 ratios were shown to increase in brain and decrease in plasma during AD progression (Toledo et al., 2013) Although not entirely clear, peripheral Aβ levels have been demonstrated to contribute to brain Aβ burden; directly

via the bi-directional transport of Aβ across BBB endothelium (DeMattos et al., 2001; Eisele et al., 2014; Marchi et al., 2004); or indirectly due to the dysfunction triggered by oxidative stress (Ascolani et al., 2012) or other mechanisms (Schupf et al., 2008; Sutcliffe et al., 2011). Although, dynamic equilibrium of plasma and brain Aβ levels are expected to be maintained by the BBB endothelium, the precise molecular mechanisms at the BBB endothelium that could discriminate Aβ40 and Aβ42 have not been deciphered.

Further, receptor for advanced glycation end products (RAGE) and low-density-lipoprotein receptor related protein (LRP) have been demonstrated to be involved in the influx and trafficking of Aβ proteins at the BBB endothelium. Interestingly, these receptors are proposed to be internalized by different mechanisms: LRP uses lipid rafts-mediated transport processes (Yoon et al., 2007) and RAGE may use clathrin-dependent or independent endocytotic processes (Ott et al., 2014). In addition, there may be other receptors involved in Aβ trafficking at the BBB (Roy and Rauk, 2005). Therefore, instead of focusing on the receptor identity and the associated mechanisms, in this study we focused on the global endocytosis mechanisms and kinetics that could differentially regulate Aβ trafficking at the BBB endothelium.

3.3. MATERIALS AND METHODS

3.3.1. Synthesis of native and fluorescein-labeled Aβ proteins

Aβ40, fluorescein labeled Aβ40 (F-Aβ40), Aβ42, and F-Aβ42 were synthesized as described in our earlier publications (Agyare et al., 2013; Kandimalla et al., 2005; Omtri et al., 2012) and Aβ monomers were prepared according to the procedure described by Klein (Klein et al., 2004) and characterized as soluble oligomers (Supplementary figure S-3.1). Fluorescein is attached to Aβ at the N-terminus, which does not participate in the secondary structure of the protein. Moreover, being a small molecule with a molecular weight of 332.32 g/mol; fluorescein is not expected to substantially alter the inherent biophysical properties and physiological interactions of Aβ40 and Aβ42 (molecular weight 4329.86 g/mol and 4514.04 g/mol, respectively).

3.3.2. Chemicals and materials

The $Na^{125}I$ was obtained from Perkin-Elmer Life and Analytical Sciences (Boston, MA). Plasticware was obtained from Corning Life Sciences (Tewksbury, MA), USA Scientific (Ocala, FL) or Denville Scientific Inc. (South Plainfield, NJ). Chlorpromazine was obtained from MP Biomedicals (Solon, OH) and methyl-β-cyclodextrin was purchased from Acros Organics (Morris, New Jersey). The K44-Dynamin plasmid was a kind gift from McNiven laboratory (Mayo Clinic, Rochester, MN) (Cao et al., 2007). The siRNA-clathrin was obtained from Dharmacon (Lafayette, CO). All other reagents were purchased from Sigma Aldrich (St. Louis, MO), unless stated otherwise.

3.3.3. Cell cultures

Human brain endothelial (hCMEC/D3) cells were a gift from Dr. Pierre-Oliver Couraud, INSERM U1016, Institut Cochin, Paris, France. The hCMEC/D3 cells were grown in EBM-2 medium (Lonza, NJ) supplemented with 1 ng/mL human basic fibroblast growth factor (PeproTech, NJ), 10 mM HEPES, 1 % chemically defined lipid concentrate (Gibco, NY), 5 µg/mL ascorbic acid, 1.4 µM hydrocortisone, 1 % penicillin-streptomycin (MP Biomaterials, OH) and 5 % of fetal bovine serum. Polarized hCMEC/D3 cell monolayers were cultured on collagen (Corning, MA) coated cover slip bottomed dishes (Mattek, MA), on 6 well plates, or on Transwell® filters (Corning Costar™, MA) at 5 % CO_2 and 37 °C. Bovine brain microvascular endothelial (BBME) cells were obtained from Cell Applications Inc., (San Diego, CA). The BBME cellular monolayers were grown as reported previously (Agyare et al., 2013). Formation of monolayers on Transwell® filters with good tight junctional integrity was confirmed by measuring the trans-endothelial electrical resistance (TEER) across the monolayers. All the monolayers were moved to low-serum (1 % serum) medium, one hour before the experiment.

3.3.4. Microscopy and cellular imaging

The hCMEC/D3 or BBME monolayers were treated with 3.1 µM of F-Aβ40, F-Aβ42, Sulforhodamine101 (SR101) labeled Aβ40, or SR101-Aβ42 for 60 min followed by 20 µg/mL of AlexaFluor®633 labeled transferrin (AF633-TRF) treatment for 30 min. In case of inhibitor experiments, the cells were pretreated with inhibitor for the designated time and then incubated with F-Aβ. Then the cells were washed with PBS and the nuclei were stained by incubating with Hoechst dye (0.5 µg/mL in PBS) for 5 min. At

the end, the dishes were fixed in 4 % para-formaldehyde (PFA) at 4 °C for 60 min; mounted with ProLong® gold antifade reagent (Life technologies, OR); and dried overnight before imaging by laser confocal microscopy.

3.3.5. Clathrin knockdowns and K44-negative dominant dynamin transfections

GFP and non-GFP K44-negative-dominant dynamin transfections of hCMEC/D3 cell monolayers were performed using Lipofectamine reagent (Invitrogen, CA) as per manufacturer's protocol. The cells were allowed to recover for 24 h in hCMEC/D3 medium (1 % FBS) and the experiment was performed the next day. Clathrin knockdown was performed on polarized hCMEC/D3 cell monolayers using siRNA kit containing RNAi mix (Invitrogen, CA) and reduced serum medium, Opti-MEM® (Gibco, NY). The cells were allowed to recover for 48 h in hCMEC/D3 medium (1 % FBS) before the uptake experiment were performed.

3.3.6. Flow cytometry

Following the treatment with various fluorophores, hCMEC/D3 cells were washed thoroughly with PBS and gently trypsinized with trypsin-EDTA for 30 sec and neutralized with FBS. The dislodged cells were washed twice using ice cold PBS, fixed with 4 % PFA solution and analyzed for intracellular fluorescence using BD FACSCalibur™ flow cytometer. The F-Aβ40 and F-Aβ42 intracellular fluorescence intensities were measured using 488 nm laser fitted with 530/30 filter. Data was acquired with BD CellQuest™ Pro and analyzed using FlowJo software. The F-Aβ uptake was represented as histograms of intracellular fluorescence intensities. All sample analyses were performed within one hour from the completion of the experiment.

3.3.7. Permeability across the BBB endothelium

Polarized BBME cell monolayers were incubated with ^{125}I-Aβ42 in tracer amounts on either luminal or on the abluminal side. Multiple samples were taken from the contralateral chamber (receiver compartment containing the blank medium) till 90 min to assay the radioactivity that transcytosed across the BBME endothelium. Flux of ^{125}I-Aβ42 across the BBME endothelium was calculated as the slope of cumulative amount of ^{125}I-Aβ42 accumulating in the receiver chamber versus time. The apparent permeability coefficients were calculated by normalizing the flux with the initial concentration of ^{125}I-Aβ42 protein added to the donor chamber and the surface area of the Transwell® filter used. The resultant value is the permeability coefficient with units of cm/min.

3.3.8. Uptake kinetics of F-Aβ40 and F-Aβ42 at BBB endothelium

Following experiments were conducted to elucidate the kinetics of F-Aβ40 and F-Aβ42 uptake at the BBB endothelium:

3.3.8.1. Total, specific, and non-specific uptake of F-Aβ as a function of donor concentration

Polarized hCMEC/D3 cells monolayers were incubated with various concentrations of F-Aβ40 or F-Aβ42 (0.19 μM to 3.1 μM) on the luminal side for 30 min and analyzed using flow cytometry as per the procedure previously described. The geometric means of intracellular fluorescence were obtained from the cytometer. The experiment was performed at both, 37 °C (total uptake: specific + non-specific uptake) and 4 °C (non-specific uptake). Intracellular fluorescence (geometric mean ± S.D.) was plotted against F-Aβ concentrations (μM).

Since the intracellular fluorescence was measured as geometric means, the specific uptake of F-Aβ was calculated as described below:

$$Uptake_{specific} = \frac{Geometric\ mean_{37°C}}{Geometric\ mean_{4°C}} \quad (1)$$

The ratio thus obtained was plotted over donor concentration and fitted to a Michaelis-Menten model (Equation 2) as described below using GraphPad Prism® software and the parameters were predicted.

$$Uptake\ Rate\ or\ V = \frac{V_{max}C}{K_m + C} \quad (2)$$

where, V = velocity or rate of uptake (unit less as ratio), V_{max}= maximum uptake rate (unit less), C = concentration (μM), K_m= Michaelis-Menten constant (μM).

3.3.8.2.Total uptake of F-Aβ as a function of time

Polarized hCMEC/D3 monolayer was incubated with 3.1 μM of F-Aβ40 or F-Aβ42 in either luminal (L) or abluminal (A) chambers for various lengths of time (15-60 min). Intracellular uptake from the luminal to abluminal (L-A) or abluminal to luminal (A-L) was assessed by flow cytometry as described above. The geometric means, thus obtained were then plotted over time and the rates of uptake were estimated by fitting the data to a linear regression model using GraphPad Prism® software.

3.3.9. Mechanism of F-Aβ40 and F-Aβ42 endocytosis at the BBB endothelium

Following studies were conducted to investigate the uptake mechanisms of F-Aβ40 and F-Aβ42 at the BBB endothelium:

3.3.9.1.Energy dependence of F-Aβ40 and F-Aβ42 uptake

The polarized hCMEC/D3 cell monolayers grown on Transwell® filters and 6-well culture plates were pre-incubated with glucose free DMEM supplemented with 50 mM 2-deoxy glucose and 0.1 % sodium azide (ATP depletion medium) for 30 min before start of the experiment. The control cells were incubated with regular DMEM medium containing glucose. Then, 3.1 μM of either F-Aβ40 or F-Aβ42 was added to the luminal side of the Transwell® filter and incubated for 30 min. The resultant intracellular fluorescence was assessed by flow cytometry.

3.3.9.2.Temperature dependence of F-Aβ40 and F-Aβ42 uptake

The hCMEC/D3 monolayers on Transwell® filters (and 6 well culture plates) were acclimatized to 37 °C or 4 °C for 60 min. Then the monolayers were treated with various concentrations (0.19 μM to 3.1 μM) of either F-Aβ40 or F-Aβ42 (luminal side for Transwell® filters) for 30 min at 37 °C or 4 °C. The cells were harvested and the intracellular fluorescence was assessed by flow cytometry. The geometric means obtained were analyzed as described in section 3.3.8.1**.**

3.3.9.3.Dynamin, clathrin and lipid raft mediated endocytosis of F-Aβ40 and F-Aβ42

Small molecule inhibitors (specific and non-specific) were used to inhibit the dynamin dependent vesicle pinch-off, clathrin dependent endocytosis, or lipid raft-mediated uptake to assess the contribution of these processes to the internalization of F-Aβ40 and F-Aβ42 by the BBB endothelium. In these experiments, polarized hCMEC/D3 monolayers were pre-incubated with medium containing 1 % serum for at least one hour before the addition of inhibitors, to trigger endocytosis machinery (Conner and Schmid, 2003). The hCMEC/D3 cells grown on 6-well culture plates or on Transwell® filters were

pre-incubated with 80 μM Dynasore (Tocris bioscience, MO), a small molecule inhibitor of dynamin, for 30 min. Then, 3.1 μM of F-Aβ40 or F-Aβ42 was added and the monolayers were incubated for 60 min. The uptake of F-Aβ peptides was determined using flow cytometry. The polarized hCMEC/D3 monolayers were pre-incubated with 200 μM monodansylcadaverine (MDC, specific clathrin inhibitor) (Schlegel et al., 1982), 10 mM chlorpromazine (MP Biomaterials, OH) (CPZ, non-specific clathrin inhibitor) (Ogiso et al., 1981), 2.5 μM nystatin (specific lipid raft inhibitor) (Chen et al., 2011) or 5 mM methyl-β-cyclodextrin (Acros Organics, NJ) (mβCD, non- specific cholesterol chelator) (Zidovetzki and Levitan, 2007) for 30 min followed by incubation with 3.1 μM of either F-Aβ40 or F-Aβ42 for 60 min (Ivanov, 2008). All the control experiments were performed in a similar fashion without the addition of inhibitors and the intracellular fluorescence was assessed by flow cytometry.

In a separate experiment, polarized BBME cell monolayers were also pre-incubated with 10 mM mβCD for 30 min, followed by incubation with 3.1 μM of F-Aβ40 or F-Aβ42, and 20 μg/mL Alexafluor® labeled Transferrin (AF633-TRF) for 60 min. The z-series confocal micrographs were obtained after washing the filters with PBS and fixing with 4 % PFA for 1 h at 4 °C. Then Transwells® were mounted with Vectashield Antifade mounting medium with DAPI (Vector Laboratories, CA).

3.4.RESULTS

To investigate the kinetics and mechanism of Aβ40 and Aβ42 transcytosis across the BBB endothelium, we employed transcellular trafficking studies *in-vitro* in polarized human cerebral microvascular endothelial (hCMEC/D3) cells and primary bovine brain microvascular endothelial (BBME) cell monolayers.

3.4.1. Energy and temperature dependent internalization of F-Aβ40 and F-Aβ42 at the BBB endothelium (Figure 3.1 and 3.2.1)

It is known that receptor mediated endocytotic processes require energy (ATP) and are impaired at 4 °C. The uptake of F-Aβ40 and F-Aβ42 in hCMEC/D3 cells, as determined by flow cytometry **(Figure 3.1),** decreased in ATP depleted cells (red histogram) compared to the normal cells (green histogram). Also, there was a substantial decrease in the uptake of F-Aβ40 and F-Aβ42 in hCMEC/D3 cells **(Figure 3.2.1)** at 4 °C compared to that at 37 °C. Further, saturable uptake kinetics were seen at 37 °C, in comparison to the linear, but significantly lower uptake at 4 °C.

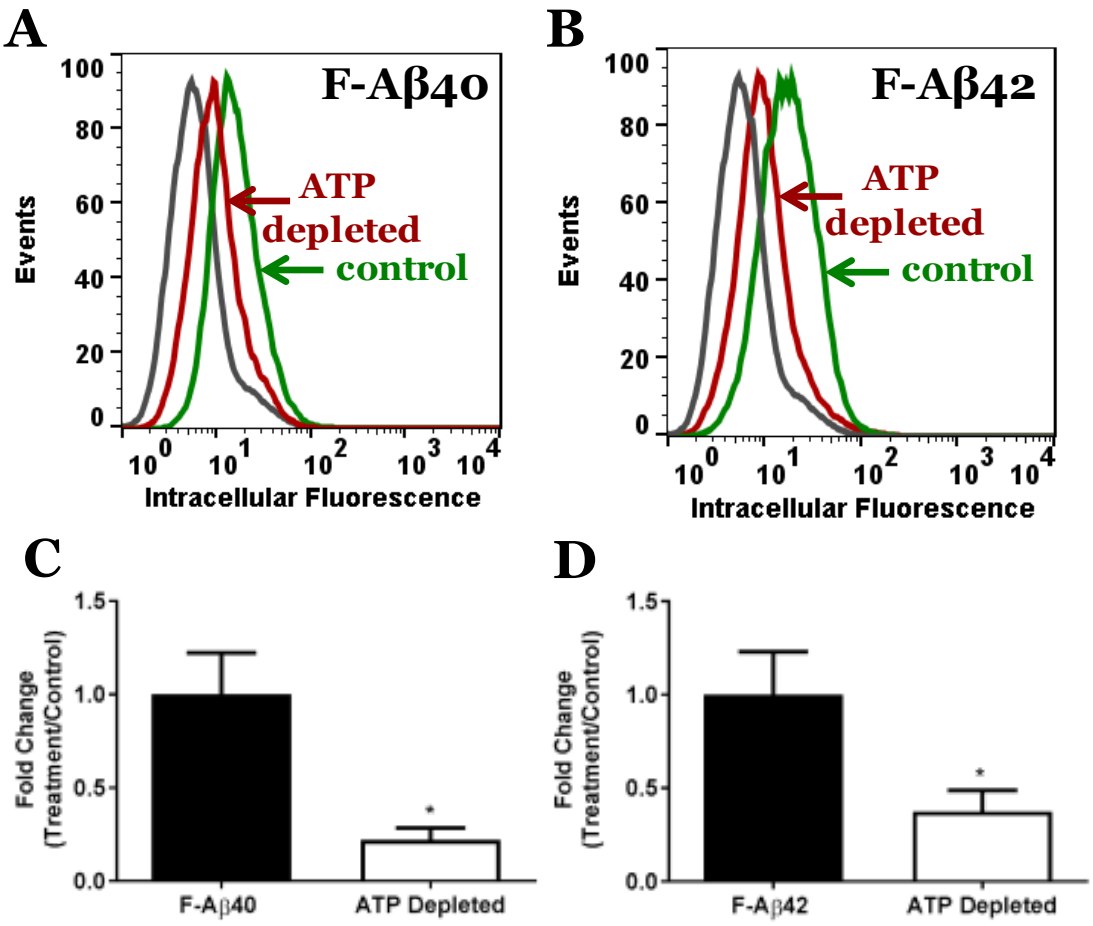

Figure 3.1. Energy dependence of F-Aβ40 and F-Aβ42 uptake in hCMEC/D3 cells as determined by flow cytometry analysis. Intracellular fluorescence histograms of hCMEC/D3 cells treated with 3.1 μM of **(A)** F-Aβ40 or **(B)** F-Aβ42 for 30 min without (green) and with (red) ATP depletion. Intracellular fluorescence of untreated control cells is shown in grey. Fold change in intracellular fluorescence of **(C)** F-Aβ40 and **(D)** F-Aβ42 expressed as mean ± S.D. Statistical significance was determined by Student's T test (*$p < 0.05$).

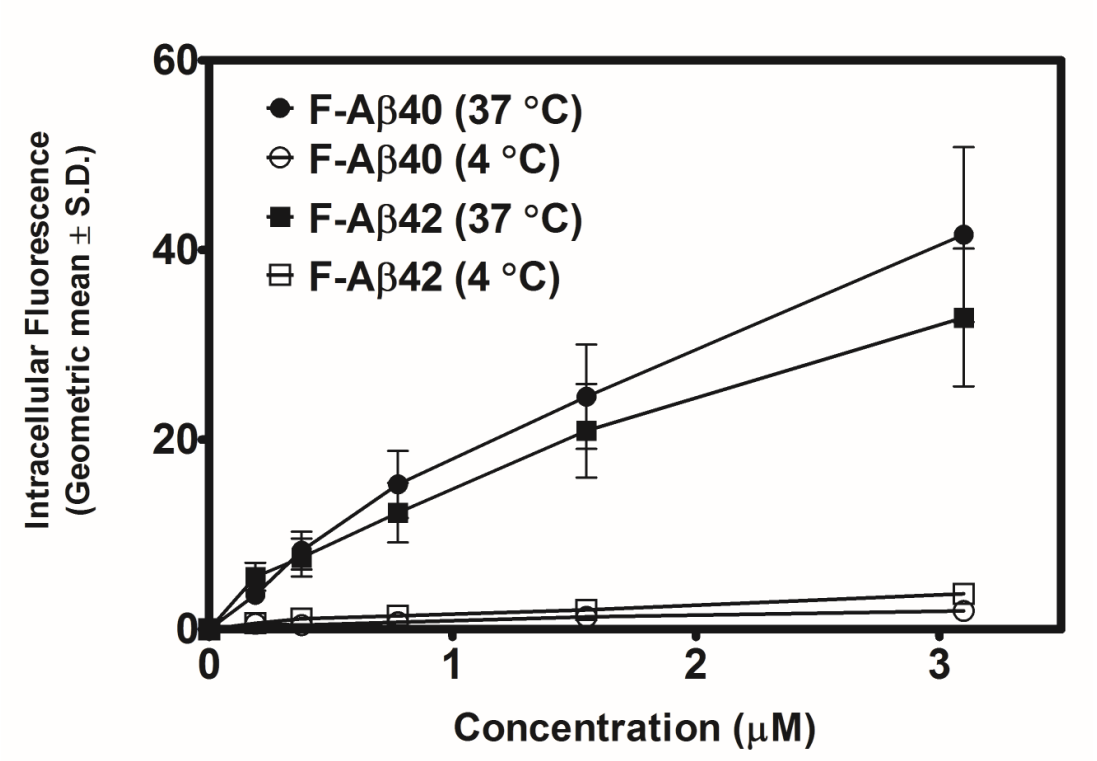

Figure 3.2.1 Total and non-specific uptake of F-Aβ40 and F-Aβ42 with increasing donor concentrations in hCMEC/D3 cells. Intracellular fluorescence of hCMEC/D3 cells incubated with various concentrations of F-Aβ40 (circle) or F-Aβ42 (square) for 30 min was assessed at either 37 ^{o}C (filled) or 4 ^{o}C (open) by flow cytometry. Extent of total uptake (37 ^{o}C) and non-specific uptake (4 °C) has been plotted as geometric mean ± S.D.

3.4.2. Saturable and polarized uptake kinetics of F-Aβ40 and F-Aβ42 in hCMEC/D3 cellular monolayers (Figure 3.2.2 and 3.3).

The specific receptor-mediated uptake of F-Aβ proteins at 37 ^{o}C was found to be saturable in hCMEC/D3 cells **(Figure 3.2.2)**. The Michaelis-Menten parameters describing F-Aβ uptake ratio showed a greater V_{max} (23.38 ± 3.5) for F-Aβ40 than for F-Aβ42 (9.28 ± 0.7) **(Table 3.1)**. No statistically significant differences in K_m values between F-Aβ40 (0.22 ± 0.14 μM) and F-Aβ42 (0.04 ± 0.04 μM) were observed. Uptake kinetics measured over time **(Figure 3.3)** indicated that luminal to abluminal (L-A) uptake of both F-Aβ40 and F-Aβ42 was greater than the abluminal-luminal (A-L) uptake. Further, in the L-A direction, F-Aβ42 uptake (1.79 ± 0.12 random units/minute or RU/min) against time was found to be higher than that of F-Aβ40 (0.55 ± 0.04 RU/min). However, in A-L direction, no significant differences in F-Aβ40 (0.11 ± 0.003 RU/min) and F-Aβ42 (0.11 ± 0.01 RU/min) uptake were observed **(Table 3.2).**

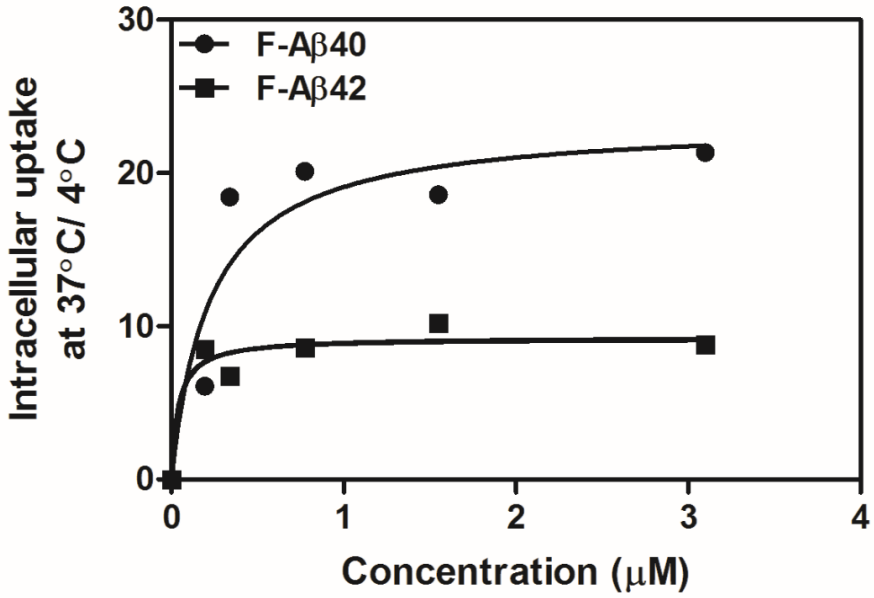

Table 3.1 Michaelis-Menten model fit

Parameter	F-Aβ40	F-Aβ42	Significance
V_{max}	23.38 ± 3.5	9.28 ± 0.7	*
K_m	0.22 ± 0.14	0.04 ± 0.04	N.S.

Figure 3.2.2. Distinct uptake kinetics of F-Aβ40 and F-Aβ42 in polarized hCMEC/D3 cell monolayers. Intracellular fluorescence in hCMEC/D3 cells incubated with various concentrations of F-Aβ40 (circle) or F-Aβ42 (square) for 30 min was assessed by flow cytometry. **(A)** Extent of specific uptake at each concentration was determined by dividing the geometric means of the intracellular fluorescence at 37 °C by that observed at 4 °C. **Table 3.1** shows the kinetic parameters predicted by fitting the observed data to Michaelis-Menten expression (Equation 2). F-Test was used to assess the statistical significance: F (DFn,DFd) = 15.56 (2,8), where DFn and DFd refer to degree of freedom of numerator and denominator, respectively.

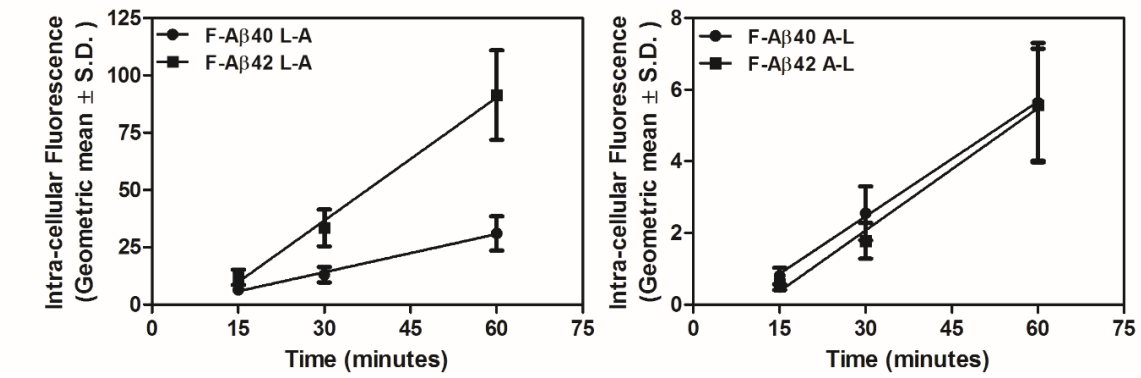

Table 3.2 Linear regression fit

Parameter	F-Aβ40 (L-A)	F-Aβ40 (A-L)	F-Aβ42 (L-A)	F-Aβ42 (A-L)
SLOPE	0.55 ± 0.04	0.11 ± 0.003	1.79 ± 0.12	0.11 ± 0.01

Figure 3.3. Differential uptake of F-Aβ40 and F-Aβ42 in hCMEC/D3 cell monolayers. Polarized hCMEC/D3 monolayer were treated with 3.1 μM of F-Aβ40 (circle) or F-Aβ42 (square) on the **(A)** luminal (L-A) or on the **(B)** abluminal (A-L) side. Cellular fluorescence due to accumulation of F-Aβ proteins in the hCMEC/D3 cells was analyzed by flow cytometry and plotted against the incubation time. Linear regression analysis was conducted (**Table 3.2)** and statistical significance was determined by F Test. L-A slopes of F-Aβ40 and F-Aβ42 were found to be different. F (DFn, DFd) = 116.9 (2,2) where DFn and DFd refer to degree of freedom of numerator and denominator, respectively.

3.4.3. Dynamin dependent uptake of F-Aβ40 and F-Aβ42 in polarized hCMEC/D3 monolayers (Figure 3.4)

To determine if Aβ endocytosis at the BBB endothelium involves dynamin, which aids in pinching off the endocytotic vesicles, the hCMEC/D3 cells were transfected with a negative dominant mutant of K44-dynamin. **(Figure 3.4.1 A-G)**. A significant decrease in green puncta of F-Aβ40 **(Figure 3.4.1 A-B)** or F-Aβ42 **(Figure 3.4.1 F-G),** and red puncta of AF633-TRF was seen in cells transfected with negative dominant mutant K44-dynamin compared to control cells. In the cells transfected with GFP-K44-dynamin **(Figure 3.4.1 C-E),** the uptake of SR101-Aβ40 (orange puncta, **Figure 3.4.1 D**) and AF633-TRF (red puncta**, Figure 3.4.1 E**) into the cytosol was inhibited. Most of the SR101-Aβ40 and AF633-TRF signals were limited to the cell circumference. However, non-transfected cells without the green fluorescence of GFP-K44-dynamin internalized SR101-Aβ40 as well as AF633-TRF. Also, in the flow cytometry studies, the uptake of F-Aβ40 and F-Aβ42 in hCMEC/D3 cells **(Figure 3.4.2)** decreased in cells pretreated with dynasore, a dynamin inhibitor (red histogram) compared to the untreated normal cells (green histogram).

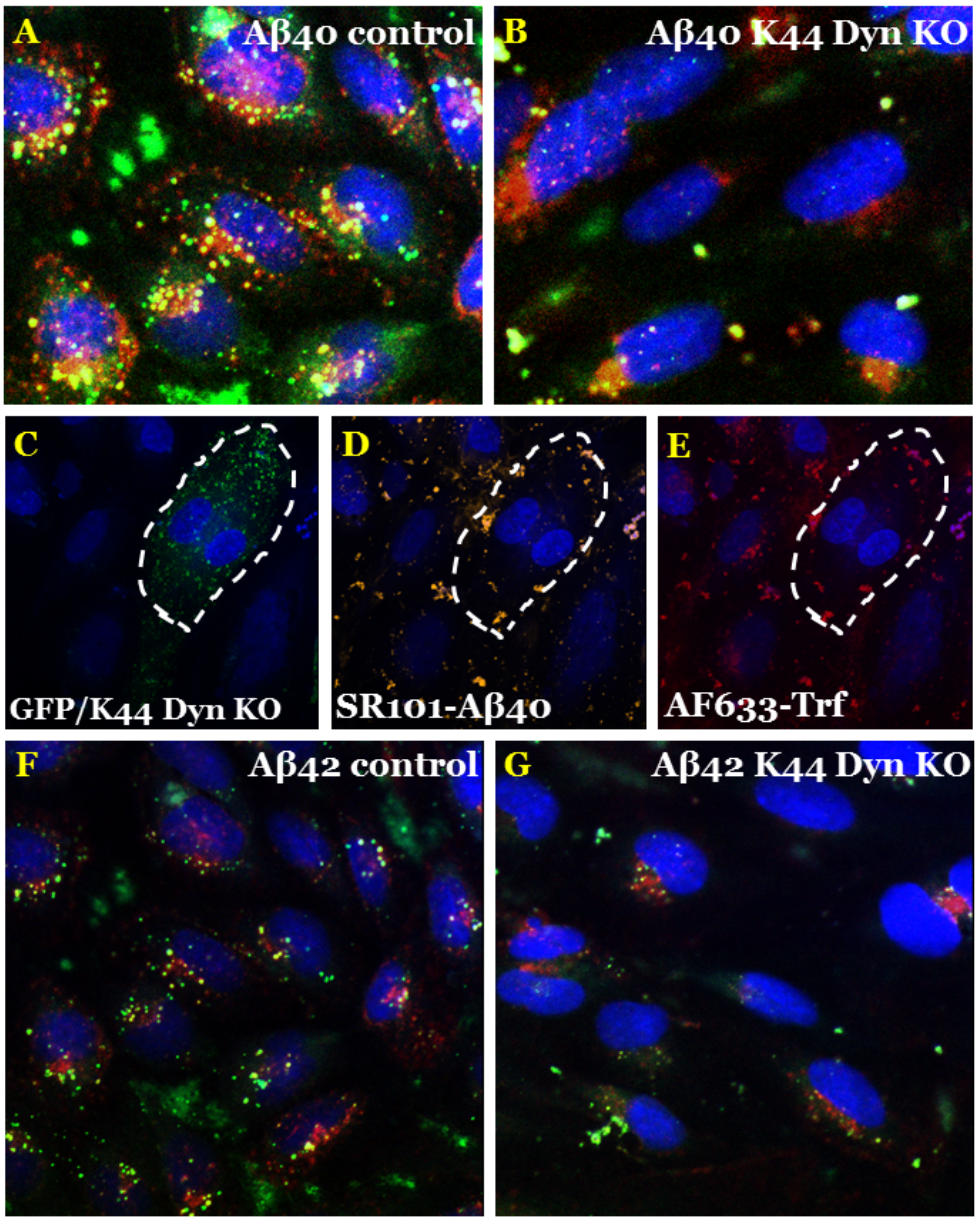

Figure 3.4.1. Dynamin dependent endocytosis of F-Aβ40 and F-Aβ42 in polarized hCMEC/D3 monolayers. A-G: Representative images of cells incubated with AF633-TRF (red), F-Aβ40 (green), F-Aβ42 (green), or SR101-Aβ40 (orange) and stained with Hoechst dye (blue) are presented. **A-B:** Decreased intracellular uptake of F-Aβ40 and AF633-TRF in **(B)** the cells transfected with K44-dynamin mutant relative to **(A)** control cells demonstrating the inability of F-Aβ40 and AF633-TRF to get into the cell without functional dynamin. Similarly, **C-E:** cells expressing **(C)** GFP/K44-Dynamin (marked by dashed white line) demonstrated a reduced uptake of **(D)** SR101-Aβ40, or **(E)** AF633-TRF. **F-G:** Uptake of F-Aβ42 and AF633-TRF was also inhibited in hCMEC/D3 cells expressing **(G)** negative dominant K44-dynamin compared to **(F)** control cells

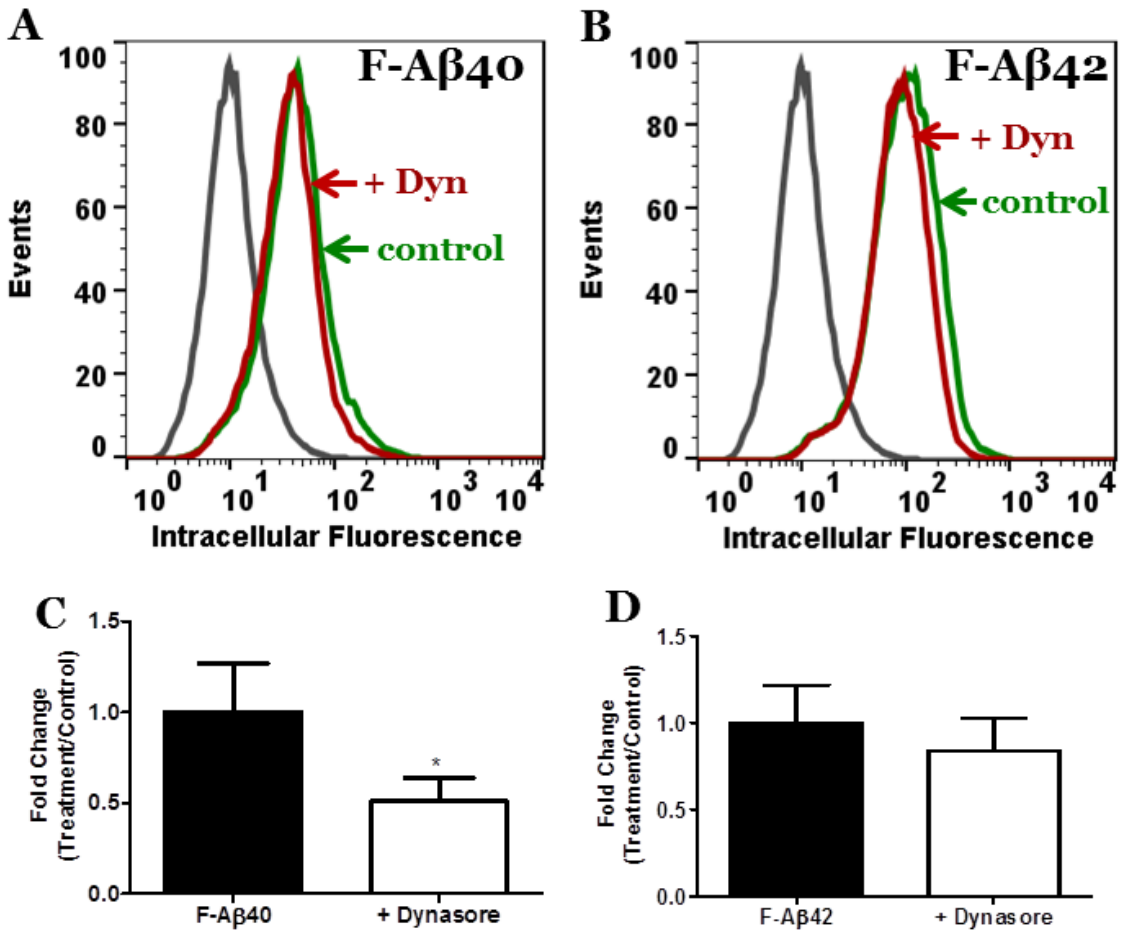

Figure 3.4.2. Effect of dynamin inhibitor on internalization of F-Aβ40 and F-Aβ42 in polarized hCMEC/D3 cells. Dynasore, a small molecule inhibitor of the vesicle pinching off protein dynamin inhibits intracellular accumulation of F-Aβ40 and F-Aβ42 as seen in flow cytometry analysis of cells incubated with 80 μM dynasore for 60 min, followed by F-Aβ incubation for 60 min. **A-B:** Intracellular fluorescence histogram of **(A)** F-Aβ40 and **(B)** F-Aβ42 pretreated with (red) and without (green) dynasore. Intracellular fluorescence of untreated control cells is shown in grey. **C-D** Fold Change of intracellular fluorescence of **(C)** F-Aβ40 and **(D)** F-Aβ42 in geometric mean ± S.D. Statistical significance was determined by Student's T test. (*$p < 0.05$).

3.4.4. F-Aβ40 endocytosis at the BBB endothelium is predominantly clathrin-mediated (Figure 3.5)

The role of clathrin-mediated endocytosis, which is a constitutive endocytotic pathway, in Aβ internalization was assessed using specific clathrin knock down studies **(Figure 3.5.1)**. In cells transfected with si-RNA clathrin, the green puncta due to F-Aβ40 uptake was significantly reduced **(Figure 3.5.1 A-B)**, whereas the prevalence of F-Aβ42 puncta did not change substantially**,** as compared to the un-transfected control cells **(Figure 3.5.1 C-D)**. AF633-TRF, which is a well-accepted ligand for the clathrin-mediated endocytosis, was used as the control **(Figure 3.5.1 A-D)**. Also, clathrin inhibitors- specific, monodancyl cadaverin (MDC) and non-specific, chlorpromazine (CPZ) **(Figure 3.5.2)** decreased the uptake of F-Aβ40 significantly whereas F-Aβ42 was only slightly affected.

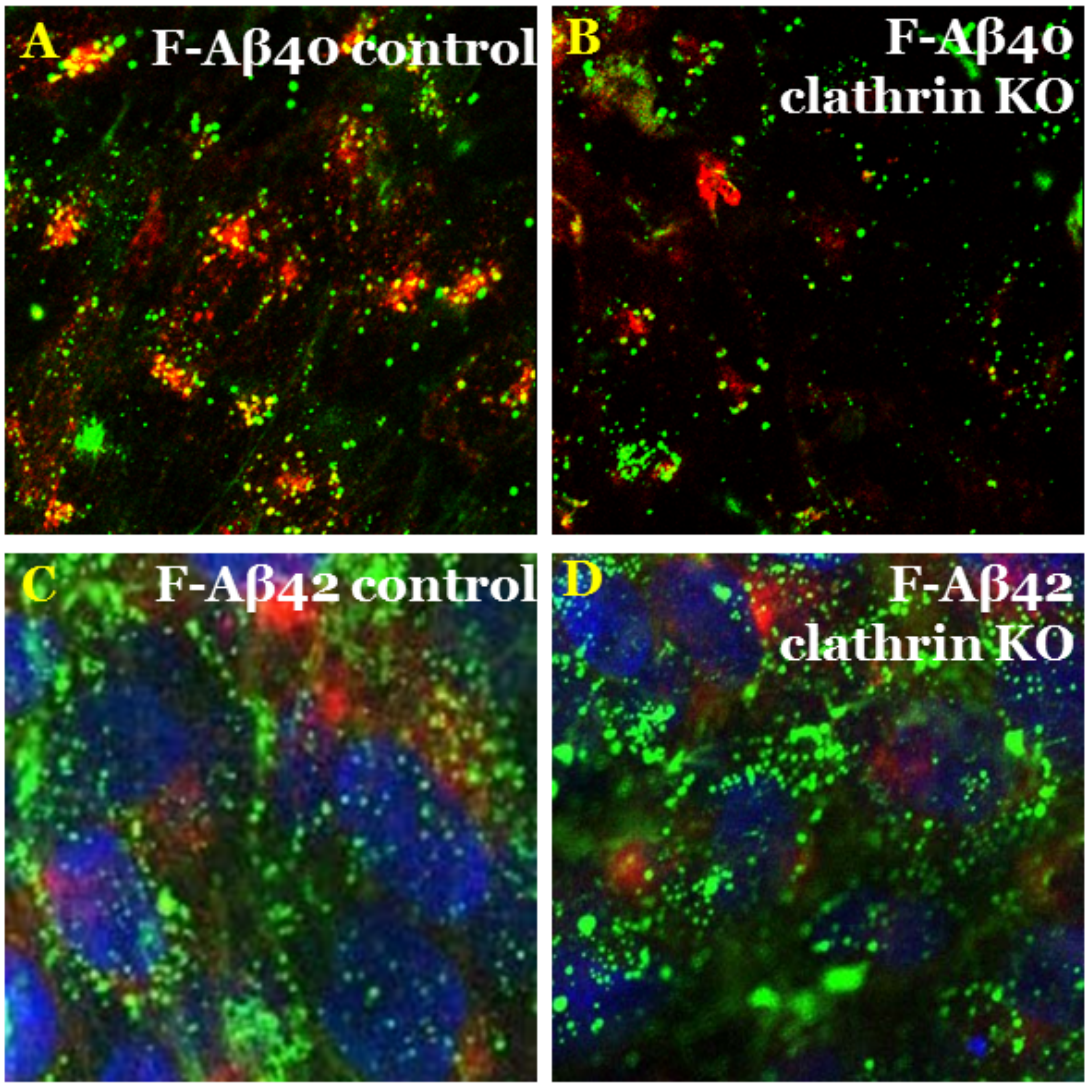

Figure 3.5.1 Clathrin mediated endocytosis of F-Aβ40, but not of F-Aβ42 in polarized hCMEC/D3 monolayers. Endocytosis of F-Aβ40 (green) and AF633-TRF (red) is reduced in **(B)** the cells knocked-out of clathrin compared to **(A)** the control cells. **C-D:** Although there is a decrease in AF633-TRF (red) uptake, no change in F-Aβ42 (green) uptake was observed in **(D)** clathrin knocked-out cells compared to **(C)** the control cells.

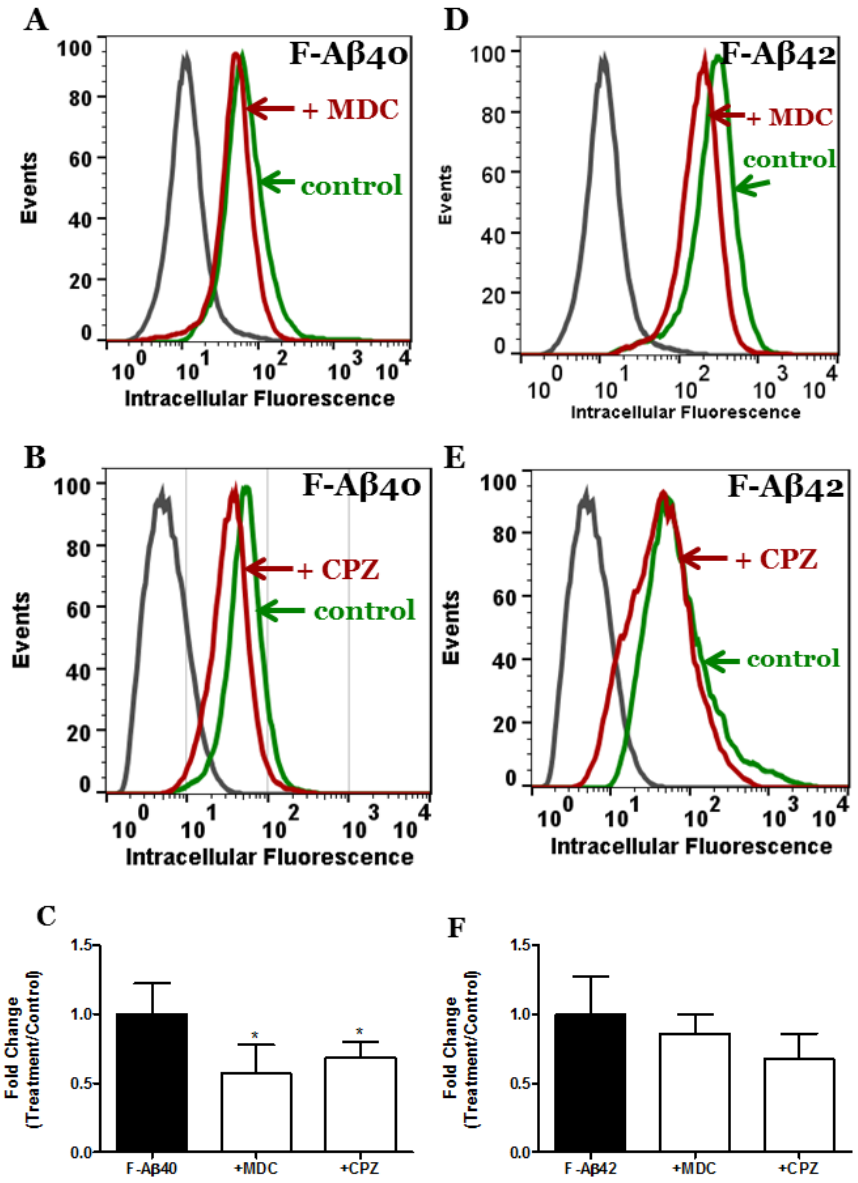

Figure 3.5.2. Endocytosis of F-Aβ40, but not of F-Aβ42, is clathrin-dependent in polarized hCMEC/D3 monolayers. A-C: Effect of clathrin inhibitors on the uptake of F-Aβ40. **A&B:** Flow cytometry histograms of hCMEC/D3 cells incubated with 3.1 µM of F-Aβ40 for 60 min pretreated with (red) and without (green) **(A)** monodancyl cadaverin (MDC), a specific inhibitor and **(B)** chlorpromazine (CPZ), a non-specific inhibitor. **(C).** Fold change in the intracellular fluorescence of F-Aβ40 with and without inhibitor treatment **D-E:** Only a slight reduction in F-Aβ42 uptake was observed after pretreatment with **(D)** MDC and **(E)** CPZ. In addition, **(F)** the fold change in the intracellular fluorescence due to Aβ42 uptake was not significantly affected by the inhibitors. Significance was determined by One-Way ANOVA followed by Dunnett's posttest. (*$p<0.05$)

3.4.5. F-Aβ42 uptake at BBB endothelium is lipid raft-mediated (Figure 3.6)

Red histogram representing the intracellular fluorescence of F-Aβ42 in hCMEC/D3 cells treated with lipid raft inhibitors, nystatin (NYS) and methyl-β-cyclodextrin (mβCD), demonstrated a left shift compared to the controls. This demonstrates a decrease in F-Aβ42 uptake compared to the control cells (green histogram) **(Figure 3.6 D-F).** However, the uptake of F-Aβ40 in hCMEC/D3 cells **(Figure 3.6 A-C)** decreased following the pre-treatment of mβCD, a non-specific cholesterol chelator (Zidovetzki and Levitan, 2007) but not following the pre-treatment of nystatin, a specific lipid-raft inhibitor (Parton and Richards, 2003).

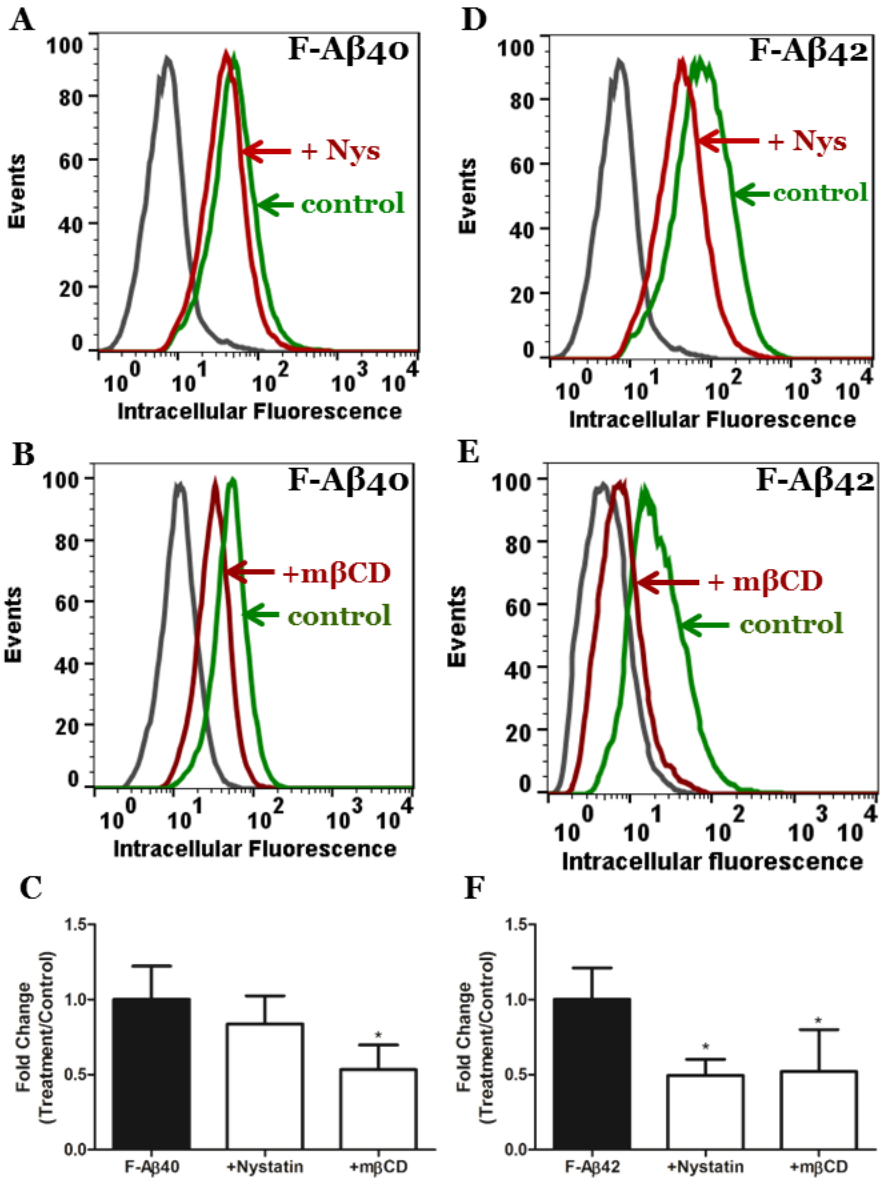

Figure 3.6. Endocytosis of F-Aβ42, but not F-Aβ40 in polarized hCMEC/D3 monolayers is mediated by lipid rafts. A-B: Flow cytometry histograms of hCMEC/D3 cells incubated with 3.1 μM of F-Aβ40 for 60 min pretreated with (red) and without (green) inhibitors. Although reduced uptake of F-Aβ40 was observed after pretreatment with the non-specific cholesterol chelator **(B)** mβCD, no change was observed after pretreatment with the specific cholesterol inhibitor **(A)** NYS. In comparison, **D-E:** Uptake of F-Aβ42 is substantially decreased after pretreatment with both **(D)** NYS and **(E)** mβCD. Untreated control cells are shown in grey. **C&F:** Fold change in the intracellular fluorescence of **(C)** F-Aβ40 and **(F)** F-Aβ42 demonstrated the lipid raft mediated uptake of F-Aβ42, but not F-Aβ40. Significance was determined by One-Way ANOVA followed by Dunnett's posttest (*$p < 0.05$).

3.4.6. F-Aβ uptake in primary bovine brain microvascular endothelial (BBME) cell monolayer (Figure 3.7)

Primary BBME cell monolayers was used to confirm the distinct uptake mechanisms of Aβ isoforms observed in polarized hCMEC/D3 cell monolayers. The ^{125}I-Aβ42 demonstrated polarized uptake in luminal to abluminal (L-A) and abluminal to luminal (A-L) directions **(Figure 3.7 A)**; L-A permeability is higher than that of A-L permeability. Confocal *z*-stack images **(Figure 3.7 B)** indicated a reduced intracellular accumulation of F-Aβ42 (green puncta) and AF633-TRF (red puncta) after **(D)** lipid raft disruption by mβCD; in comparison to **(C)** control cell monolayers. In addition, the uptake of F-Aβ40 (green puncta) was unaffected by **(B)** mβCD pre-treatment when compared to **(A)** control cells.

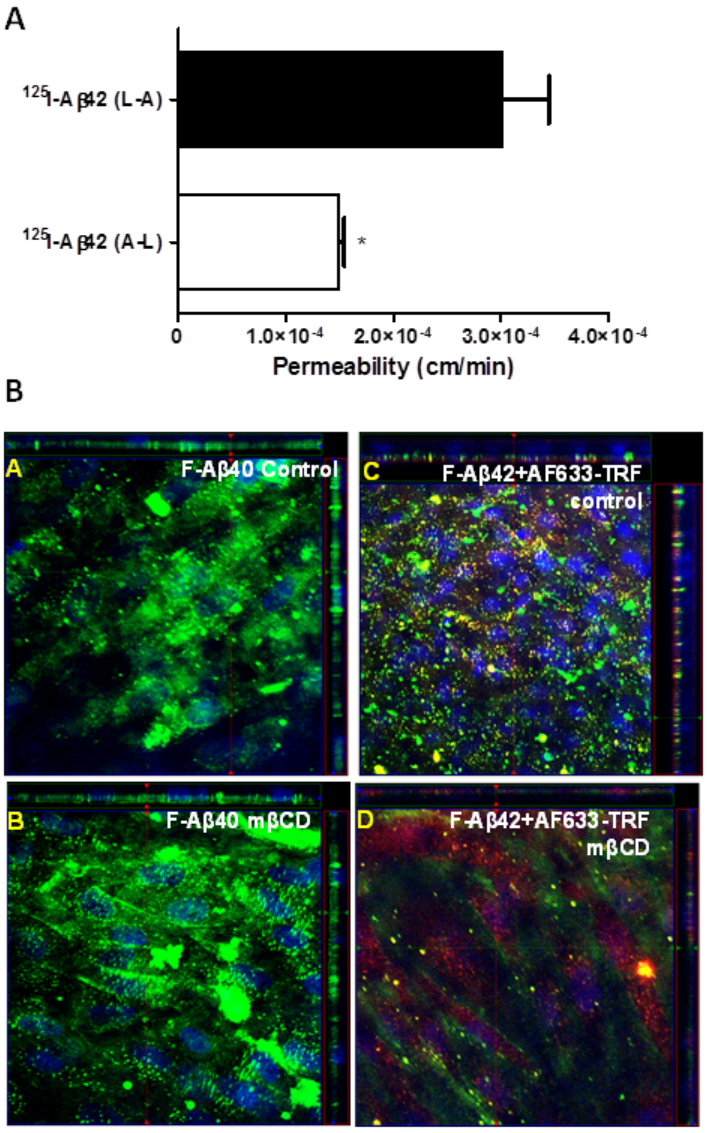

Figure 3.7 Uptake of F-Aβ42 and F-Aβ40 in bovine brain microvascular endothelial (BBME) cell monolayer treated with methyl beta cyclodextrin. A: Distinct permeability of ^{125}I-Aβ42 in the luminal to abluminal (L-A) and abluminal to luminal (A-L) direction (Mean ± SEM). Further, relative to the permeability of ^{125}I-Aβ40 that was published by our group earlier (Agyare et al., 2013); permeability of ^{125}I-Aβ42 was greater than ^{125}I-Aβ40, only in L-A direction, but not in A-L direction. *Confocal images*: Intracellular accumulation of F-Aβ42 and not F-Aβ40 is lipid raft mediated in BBME cells: **A-B** No change in the uptake of F-Aβ40 (green) was found in cells pretreated with **(B)** mβCD compared to **(A)** control cells. **C-D** Intracellular uptake of F-Aβ42 is reduced following **(D)** mβCD treatment compared to **(C)** control cells. Images shown in all three planes: *x-y* (square box), *x-z* (top horizontal panel) and *y-z* (right vertical panel).

3.5. DISCUSSION

Prolonged exposure of BBB endothelium to toxic Aβ peptides, could trigger intracellular alterations that may precipitate into BBB dysfunction in AD pathogenesis (Carrano et al., 2011; Erickson and Banks, 2013). The BBB dysfunction is typically assessed by evaluating vascular reactivity and loss in BBB integrity, which is verified by increase in the brain permeability of plasma proteins like albumin. As reviewed by Skoog et al. (Skoog, 1998), multiple studies showed an increase in the CSF/serum albumin ratio in the AD patients group with vascular defects, such as hypertension, non-insulin dependent diabetes mellitus and non-ischemic heart disease, than in control group (Blennow et al., 1990; Frölich et al., 1991; Skoog et al., 1998). Interestingly, no significant BBB dysfunction was noted in AD patients without any vascular defects (Blennow et al., 1990). While this approach may show alterations in the paracellular integrity of the BBB endothelium, but, it may not reveal the early pathophysiological changes such as the intracellular trafficking or the signaling component of the BBB endothelium; that are severely understudied.

In addition to maintaining the brain homeostasis and restricting the exposure of xenobiotics circulating in the plasma, the BBB modulates the Aβ42:Aβ40 ratios in brain and plasma (Hawkins and Davis, 2005), which were shown to be altered during AD progression such that the Aβ42:Aβ40 ratio increases in the brain parenchyma, but decreases in the plasma (Toledo et al., 2013). However, the mechanistic rationale that drives this perturbation is not known yet. Therefore, we hypothesize that the BBB endothelium may have the ability to discriminate these Aβ isoforms and traffic them independently by maintaining distinct transcytosis mechanisms and kinetics. To test this

hypothesis, we investigated the differences in the transcytosis of Aβ40 and Aβ42 at the BBB endothelium *in-vitro*. In this chapter, although we also assessed the permeability profiles encompassing the complete transcytosis process, our focus was the first step of transcytosis: uptake or endocytosis.

The receptor mediated endocytosis of Aβ at the BBB endothelium is long known. (Poduslo et al., 1999; Skoog, 1998). Multiple receptors such as RAGE and LRP have been proposed to be involved in influx and efflux of Aβ, respectively (Deane et al., 2004, 2004, 2012; Shibata et al., 2000). However, the intracellular trafficking of Aβ has so far been an unknown territory. There is evidence that LRP most likely involves lipid rafts (Yoon et al., 2007) and endocytosis of RAGE receptor could be via clathrin dependent or independent pathways (Ott et al., 2014). Understanding the intracellular trafficking at BBB endothelium is essential to comprehend the pathogenesis of several neurological ailments including AD. Further, bioinformatics analysis conducted by our collaborators has shown that the genes that code for various proteins in the intracellular cargo sorting and trafficking are down regulated in AD patient brain (Supplementary Figure 5.8). Hence, the variations in Aβ42:Aβ40 could be caused by the selective disruption of transcytotic pathways that predominantly handle Aβ40 or Aβ42. In addition, an increased expression of LRP at blood-cerebral spinal fluid barrier (BCSFB), the other barrier or portal for Aβ to clear from the brain, further asserts that receptors alone would not suffice to tackle the issue of impaired Aβ clearance (Marques et al., 2013).

In this chapter, we investigated both luminal to abluminal (L-A) and abluminal to luminal (A-L) trafficking of Aβ40 and Aβ42 and demonstrated that BBB handles the Aβ isoforms differently. We used polarized monolayers of hCMEC/D3 cells *in-vitro*, which

is a widely studied human BBB model. Although, this cell line is known to have leakier tight junctions, its human origin is of significant importance (Poller et al., 2008; Weksler, 2005). Moreover, as we employed these cells to investigate the uptake of a protein and not a small molecule, we expect this model to provide crucial information on the mechanisms of Aβ endocytosis. Earlier studies have demonstrated that the uptake of both Aβ40 and Aβ42 is energy dependent and is inhibited at the sub-physiological temperature of 4 °C, where the endocytotic mechanisms are inhibited due to the arrest of cellular physiological processes (Kandimalla et al., 2009). Our findings suggest that the uptake of Aβ proteins at the BBB endothelium is energy dependent and saturable, which are the primary characteristics of receptor-mediated uptake, and verifies the assertion that Aβ isoforms utilize receptor mediated endocytosis at the BBB endothelium. Next, we have shown that Aβ internalization is dynamin dependent. Dynamin is needed by cells to pinch the vesicles and be released into the cytosol once they are formed at the plasma membrane. We show that in the cells expressing a dominant mutant and a non-functional form of dynamin, the uptake of both Aβ40 and Aβ42 is significantly reduced, thereby, suggesting that dynamin is involved in the endocytosis of Aβ40 and Aβ42 at the BBB endothelium. Similar role of dynamin in the endocytosis of Aβ (Omtri et al., 2012) and APP (Carey et al., 2005; Ehehalt et al., 2003) has been demonstrated in neurons. Moreover, the results obtained in hCMEC/D3 model verifies the results obtained in a primary bovine endothelial cell model. Similar revelations were made from another study that demonstrated that L-A uptake of Aβ isoforms is mediated by RAGE, is inhibited at 4 °C, and is sensitive to fillipin, a cholesterol or lipid raft chelating agent (Candela et al., 2010).

Clathrin- and lipid-rafts (mediated primarily by caveolin) are the two well-studied endocytotic mechanisms that facilitate the receptor-mediated endocytosis of several macromolecules. As elegantly reviewed in (Preston et al., 2014), clathrin mediated endocytosis of transferrin (Roberts et al., 1993); or lipid rafts mediated endocytosis of insulin (Schnitzer et al., 1994) among others such as TNF-α, alpha2-macroglobulin, platelet-derived growth factor-B; would be affected if BBB endothelium becomes dysfunctional in AD. Interestingly, most of these observations have been noted in AD patients (Craft, 2007; Kovacs, 2000; Licastro et al., 2000; Namekata et al., 1997; Simpson et al., 1994; Tesseur et al., 2006).

Further, it has been shown that clathrin-mediated endocytotic processes are compromised in AD. An adaptor protein associated with clathrin coated vesicles (CCV), AP180, have been shown to be altered in superior frontal gyrus and hippocampus (Yao and Coleman, 1998). Another CCV associated protein, AP-2, has also been shown to be dysfunctional in AD (Yao et al., 2000). Moreover, there is evidence that in AD, impaired synaptic vesicular trafficking, typically involving clathrin-mediated trafficking processes is impaired way before the structural deterioration in synapses (Yao, 2004). Lipid raft machinery was also noted to be sub-optimal in AD. It was proposed that the abnormal lipid raft composition can affect the transport of substrates and modify enzymes that cleave APP (Ferrer, 2009; Rushworth and Hooper, 2010). For example, high cholesterol has been demonstrated to increase the partitioning of APP, along with BACE1 and γ-secretase components, into lipid rafts (Kosicek et al., 2010). In their excellent review Rushworth et al. (Rushworth and Hooper, 2010) describe the implication of lipid rafts in AD pathogenesis as they: (1) mediate APP processing (2) provide havens for Aβ

aggregation in the neuronal membranes; and (3) host specific neuronal receptors for toxicity (such as cellular prion protein) and signal transduction (such as glutamate receptor). Similar revelations for clathrin mediated endocytosis that is affected in the hippocampal neurons of AD brain (Granseth et al., 2006) have also been made.

Therefore, we investigated the role of both clathrin and lipid-raft endocytic mechanisms in Aβ uptake. Using specific gene knockdowns with siRNAs, we demonstrated that the endocytosis of Aβ40 and not of Aβ42 is clathrin-mediated in hCMEC/D3 monolayers. With the perturbations in clathrin-mediated endocytosis observed in AD brain, the trafficking of Aβ40 could be impaired at the BBB. On the other hand, our studies demonstrate that Aβ42 most likely uses lipid rafts-mediated uptake at the BBB endothelium. This is intriguing that the two Aβ isoforms do not utilize the canonical clathrin-mediated machinery to the same extent. Pathophysiologically, this makes sense as Aβ42, which is regarded as a pathological isoform, accesses lipid raft-mediated pathway; that is typically exploited by neurological toxins such as tetanus neurotoxin (Herreros et al., 2001) and botulinum neurotoxin (Petro et al., 2006). But Aβ40, which is considered as a physiologically relevant isoform, prefers the canonical clathrin-mediated pathway.

These distinct uptake mechanisms of Aβ40 and Aβ42 preferentially utilizing clathrin and lipid-raft mediated endocytosis processes have been hypothetically depicted in **Figure 3.8**. Aβ binds to a canonical receptor (Step 1. Binding) and gets ready to internalize (Step 2. Budding). At the same time, depending on whether it is Aβ40 or Aβ42; the respective coat protein of clathrin or caveolin (in lipid-raft) is recruited at the membrane. Once the vesicle is fully formed, it is pinched off by dynamin (Step 3.

Scission). This is followed by multiple steps involving the revelation of the targeting peptide (such as SNARE, discussed in Chapter 5), that essentially decides the fate or target of the vesicle (Steps 4-6). Briefly, it includes exposing the vesicle in cytosol (Step 4 Uncoating) so that it attaches to the cytoskeletal element (Step 5 Translocation) and finally tethers (Step 6 Tethering), docks (Step 7. Docking) to the target membrane to trigger exocytosis or fusion (Step 8 Fusion). These steps leading to exocytosis of the Aβ filled vesicles are going to be discussed in detail Chapter 5. Also, Rab proteins (family of small GTPases) assist in almost all of these cellular transcytosis steps.

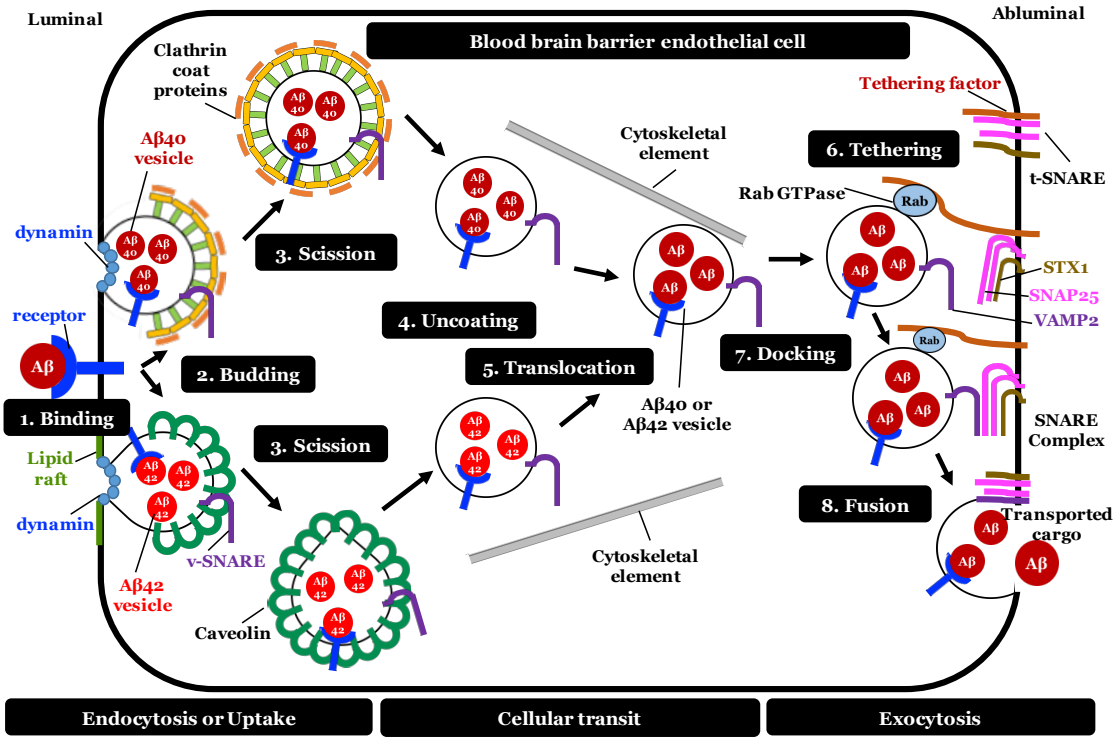

Figure 3.8 Proposed vesicular transcytosis process of Aβ at the BBB endothelium Aβ40 or Aβ42 (1) binds to the receptor at the luminal side. The Aβ40 is internalized predominantly via clathrin-mediated endocytosis. On the other hand, Aβ42 is endocytosed via lipid-raft mediated endocytosis by recruiting caveolin. The membrane around the cargo-receptor complex then (2) begins to bud, form a vesicle, and recruit coat proteins as well as targeting peptides (SNAREs). (3) Then the vesicle is cleaved from the membrane by dynamin protein by scission process (4). The free vesicle in the cytosol is then uncoated to expose the targeting peptide. (5) The uncoated vesicle is then translocated onto the other side of the cell or the acceptor organelle by microtubular cytoskeletal elements. (6) The vesicle is attached or tethered to the abluminal membrane, by a tethering factor. This process usually employs Rab GTPases. (7) The tethered vesicle then docks at the abluminal side of the membrane and the v-SNARE or VAMP-2 (targeting peptide on the vesicle) come close to the t-SNARE or SNAP-25 (targeting peptide on the target membrane) by a process called as docking. (8) Finally, VAMP-2 and SNAP-25, along with another SNARE peptide, syntaxin (STX-1), coil around each other to form the SNARE complex and bring the two membranes close to each other, and eventually fuse to release the transported cargo. As shown, this entire vesicular transport apparatus is divided into endocytosis or uptake, cellular transit and exocytosis. Steps 6-8 have been described in detail in Chapter 5.

In addition to the molecular evidence, we have also provided evidence that the kinetics of Aβ40 and Aβ42 uptake at the BBB endothelium are substantially different. The extent of L-A uptake is more than that of the A-L uptake for both Aβ isoforms, but the rate of Aβ40 uptake is greater than that of Aβ42 uptake, only in L-A direction. Although, there is no direct evidence that implicate L-A uptake in AD pathogenesis, it is interesting to note that the Aβ isoforms have different rates only in this direction. Further, the same trend was also seen in the BBME cellular monolayers, where the L-A permeability of Aβ42 was more than that in the A-L direction. In addition, on comparing with our previously published data of Aβ40 in the same cell model (Agyare et al., 2013); permeability of Aβ42 was found to be more than that of Aβ40, again, only in the L-A direction. The A-L permeability was similar. These findings further indicate that understanding the transcytosis of Aβ in the L-A direction or the plasma-to-brain direction may provide some revelations about BBB dysfunction that eventually leads to AD pathology.

In summary, this is the first evidence that demonstrated the independent uptake of Aβ isoforms at the BBB. Earlier studies have claimed that Aβ40 and Aβ42 are internalized at the BBB via common transport system (Martel et al., 1996). However, our data suggests that although both Aβ40 and Aβ42 isoforms use receptor-mediated endocytosis, the endocytotic machineries they engage vary. The Aβ40 primarily uses clathrin, whereas Aβ42 uses lipid raft machinery to transcytose the BBB endothelium from the L-A side. Based on the extent to which these pathways are disrupted in AD, the dynamic equilibrium between plasma and brain Aβ42 and Aβ40 levels could be

differentially impacted, and this may be reflected as changes in Aβ42:Aβ40 ratios; as observed in AD patients.

CHAPTER FOUR

4. ASSESSMENT OF AMYLOID BETA UPTAKE KINETICS AT THE BLOOD BRAIN BARRIER ENDOTHELIUM USING QUANTITATIVE MODELING

4.1. SUMMARY

Elucidation of amyloid beta (Aβ) interactions with the BBB endothelium is expected to provide clues to understand the role of BBB in maintaining the dynamic equilibrium between plasma and brain Aβ levels, and the trafficking perturbations leading to their accumulation as plaques in the brain in Alzheimer's disease (AD). Traditional tissue uptake measurements for the brain may not offer detailed information on the binding and uptake of the Aβ at the BBB endothelium. However, dynamic brain imaging of ^{125}I-Aβ tracer injected into the plasma by dynamic single photon emission computed tomography (SPECT-CT) enables quantitative estimation of initial binding as well as total uptake of Aβ into the BBB and subsequently into the brain parenchyma. In this work, brain (and BBB tissue) uptake observations from SPECT-CT and plasma from traditional PK measurements were used to employ pharmacokinetic modeling and graphical model plot approaches (Patlak and Logan plot) as tools to dissect the differential kinetics of Aβ isoforms at the BBB endothelium. Using these two independent approaches of (1) PK model with designated number of compartments, and (2) graphical model assuming no fixed number of compartments; we demonstrate that the rate of uptake of Aβ42 was more than that of Aβ40 at the BBB endothelium as well as into the brain parenchyma. However, the extent of

uptake of Aβ40 into the BBB endothelium was more than that of Aβ42 that distributes relatively quickly into the brain parenchyma.

4.2. INTRODUCTION

In Chapter Three, Aβ isoforms were shown to utilize distinct uptake mechanisms at the BBB endothelium. Aβ40 is primarily clathrin mediated, whereas Aβ42 employs lipid rafts to get into the endothelial cell. In this chapter, we elucidated differential kinetics of Aβ40 and Aβ42 uptake at the BBB endothelium. To accomplish such a task *in-vivo* via conventional methods could be fraught with artifacts associated with the quantification of protein of interest in the brain tissue. Therefore, we employed imaging techniques and quantitative modeling approaches to investigate the interactions of Aβ radiotracers with the BBB endothelium.

Quantitative analysis of the initial uptake of Aβ in the brain is expected to delineate the differential interactions of Aβ isoforms with the BBB endothelium. Quantifying the radioactivity associated with brain as imaged by dynamic single photon emission computed tomography-computed tomography (SPECT-CT) provides an opportunity to capture the initial interactions of Aβ proteins with the BBB, which could be missed in steady state brain uptake measurements. Kinetic information of Aβ in the plasma pool is determined by measuring the radioactivity in plasma samples collected over time by gamma counter. In addition, to elucidate the trends in both plasma and brain (or BBB) pools *simultaneously* and predict the blood-to-brain transfer constants; two approaches: (1) pharmacokinetic compartment modeling; and (2) Patlak and Logan graphical-plot methods were employed.

In the first approach, a three-compartment model was constructed using PhoenixWinNonlin® 6.4. The model equations were fitted to brain (SPECT-CT) and plasma (Gamma counter) observations *simultaneously,* and parameters were estimated.

In the second approach, theoretical models: (1) Patlak plot; and (2) Logan plot; were employed and the linear slopes, referred to as influx clearance (K_i) in Patlak plot and distribution volume (V_T) in Logan plot, were estimated. These commonly employed graphical methods to describe radiotracer kinetics allowed us to linearize the brain and plasma observations without making any assumptions about the number of compartments. The Patlak and Logan plots describe the kinetics of an *irreversible* or a *reversible* tracer, respectively. As explained in subsequent sections, initial interactions of Aβ with the BBB endothelium are *reversible* and then become *irreversible* as the probe enters the brain parenchyma.

4.3. MATERIALS AND METHODS

4.3.1. DATA COLLECTION

4.3.1.1. Aβ proteins synthesis, radioiodination and plasma pharmacokinetics

The Aβ40 and Aβ42 were synthesized as described earlier (Kandimalla et al., 2005) and monomers were prepared according to the procedure described by Klein (Klein et al., 2004). The Aβ proteins were radioiodinated and the plasma pharmacokinetic studies were conducted on 24-week old C57B6/SJL (WT) as described in the earlier chapters.

4.3.1.2. Brain uptake studies using dynamic Single Photon Emission Computed Tomography- Computed Tomography (SPECT-CT)

A 500 μCi dose of ^{125}I-Aβ40 and ^{125}I-Aβ42 was administered to 24-week-old WT mice. Brain uptake of ^{125}I-Aβ was determined by dynamic planar imaging (Gamma Medica Ideas Pre-Clinical Imaging, Northridge, CA) using the low energy and high resolution parallel-hole collimator with 12.5 cm FOV; 13:36 min acquisition time; 64 projections (10 sec per projection); and reported resolution of 1 to 2 μm. The CT acquisition was a continuous circular orbit with a 50 μm slice thickness; 256 images at 80 kVp with a 0.28 mA current; and a reported resolution of 43 μm. Dynamic SPECT-CT images were processed and analyzed using Biomedical Image Quantification and Kinetic Modeling Software version 2.85 (PMOD Technologies, Switzerland).

4.3.2. DATA ANALYSIS

4.3.2.1. Mathematical model for circulating Aβ-BBB interactions

To evaluate the uptake of Aβ40 and Aβ42 at the BBB endothelium and subsequently into the brain, a quantitative mathematical model with three compartments was constructed. Compartment 1: Plasma or Central compartment; Compartment 2: Tissue compartment and Compartment 3: Blood brain barrier and brain compartment. The model (shown in **Figure 4.1**) was based on the following assumptions:

1. Uniform mixing in all the three compartments.
2. Tissue compartment comprises of all the peripheral tissues and organs except the brain and BBB endothelium.
3. Compartment 3 is a combination of BBB endothelium and brain. However, assuming that Aβ protein takes more than five minutes to enter the brain via the BBB endothelium, the brain radioactivity obtained from dynamic SPECT-CT imaging in the first five minutes was assumed to be associated with the BBB endothelium. This assumption is reasonable as (1) Aβ, a protein, primarily relies on transcytosis to get into the brain. Further, transcellular pathways or transcytosis processes usually require energy; and mostly, are relatively slower than passive diffusion (Alberts et al., 2002). Also, (2) initial linearity of Logan plot (**Figure 4.7) (**validated until 5 minutes) is lost at later times indicating that Aβ is in the reversible compartment (BBB endothelium) initially, beyond which it most likely enters the irreversible compartment (brain). Based on this assumption, to elucidate the initial kinetics, the third compartment could be assumed as the BBB endothelium, thus, simplifying the model presented in **Figure 4.1 B**.

4. Elimination is strictly from the central compartment. In other words, the elimination from BBB and the tissue compartment is negligible when compared to the elimination from the central compartment.

A.

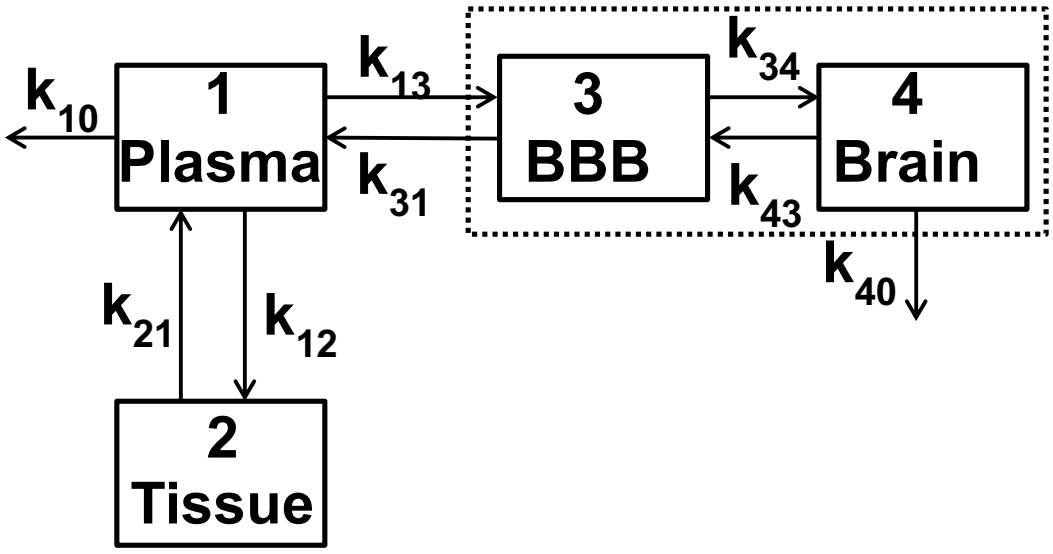

B.

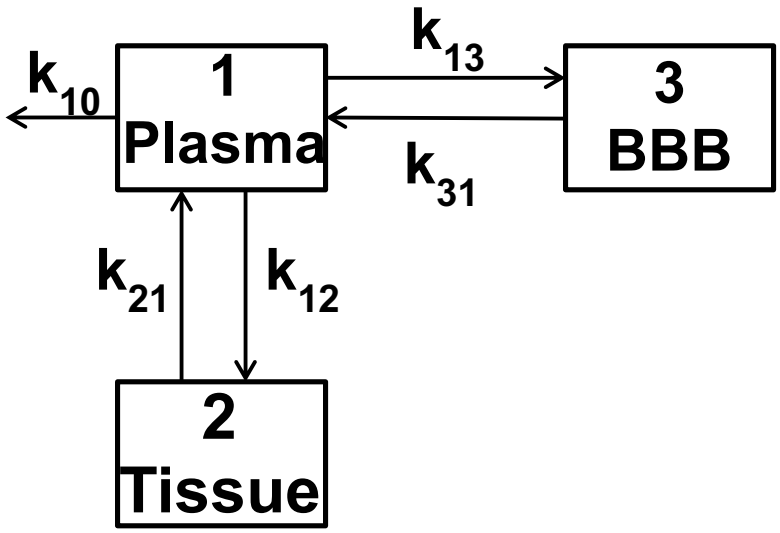

Figure 4.1 Pharmacokinetic models describing amyloid beta interactions with brain at the BBB interface. (A) Model comprising of plasma, tissue, BBB and brain compartments along with their corresponding rate constants. The k_{40} is the elimination rate constant from the brain compartment, which describes the clearance processes other than the BBB clearance. As our assay was unable to resolve BBB and brain compartments separately, they are combined as one compartment (dashed box), thus reducing the model to a simpler model **(B)**. The inherent assumption made in the data interpretation was that the first five minute kinetics describes the interactions of Aβ proteins with solely the BBB endothelium.

4.3.2.1.1. Model description.

Compartment 1: plasma and highly perfused tissues or central compartment; compartment 2: other peripheral organs and tissues; compartment 3: BBB endothelium; and compartment 4: brain. The rate constants describe: transfer from plasma to peripheral tissues (k_{12}) and vice versa (k_{21}); transfer between plasma and BBB endothelium (k_{13}), and in the reverse direction (k_{31}); and k_{34} and k_{43}, are BBB endothelium-brain and brain-BBB endothelium transfer rate constants, respectively. The k_{10} denotes the elimination rate constant from the central compartment, whereas the k_{40} describes Aβ elimination directly from the brain, which includes enzymatic degradation by proteases, phagocytosis by microglia and astrocytes, and/or perivascular clearance. It is assumed that the short time exposure (< 5 min) to the BBB endothelium is insufficient to attain detectable levels in the brain compartment. Hence, this model has been reduced to a simpler model depicted in **Figure 4.1 B** and compiled on PhoenixWinNonlin® 6.4. Finally, the model was run as a population using a naïve pooled method with an additive error model. Although, no additional information about the between subject variabillity (BSV) was obtained using this method, the degree of freedom allowed by the model, greater confidence in the predicted parameters. Such a compromise on BSV has been reported earlier to obtain accurate predictions for small sample sizes (Mahmood, 2012). Also, this approach allowed us to individually define doses administered to animals. The initial estimates for the fixed effect parameters (listed below) were provided for both Aβ40 and Aβ42; either based on the *in-vitro* uptake studies (k_{13} and k_{31}), or the pharmacokinetic parameters (k_{12}, k_{21}, k_{10}, V) predicted by curve-fitting the *in-vivo*

plasma data. Lastly, the model was allowed to converge based on the equations described below and the defined parameters were predicted.

The ^{125}I-Aβ was administered to the plasma compartment via intravenous (femoral) bolus injection. The initial conditions in various compartments were:

$$C_{plasma} = \frac{Dose}{V} \quad (2)$$

$$C_{tissue} = C_{BBB} = 0 \quad (3)$$

where, *Dose* refers to the total dose administered in mass or radioactivity μCi units, V stands for apparent volume of distribution in milliliters (mL), C_{plasma}, C_{tissue} *and* C_{BBB} stand for concentration in plasma, tissue and BBB, respectively. After equilibration, there is dynamic transport of Aβ between the compartments as defined by the model. Thus, rate of change of Aβ concentration in the particular compartment becomes:

$$\frac{dC_{plasma}}{dt} = -(k_{10} + k_{13} + k_{12}).C_{plasma} + k_{21}.C_{tissue} + k_{31}.C_{BBB} \quad (4)$$

$$\frac{dC_{tissue}}{dt} = k_{12}.C_{plasma} - k_{21}.C_{tissue} \quad (5)$$

$$\frac{dC_{BBB}}{dt} = k_{13}.C_{plasma} - k_{31}.C_{BBB} \quad (6)$$

Where, $\frac{dC_{plasma}}{dt}$, $\frac{dC_{tissue}}{dt}$, $\frac{dC_{BBB}}{dt}$ depicts the rate of change of Aβ tracer concentration in plasma, tissue and BBB compartment, respectively.

Various kinetic parameters were predicted by simultaneously fitting the model to plasma radioactivity (obtained from gamma counter and simulated to dose match

SPECT-CT) and brain tissue radioactivity (obtained from SPECT-CT imaging after removing the counts in the cerebral vasculature). To obtain the vascular contribution or counts in the cerebral vasculature, simulated plasma concentrations (SPECT-CT dose matched) were multiplied with average vascular volume obtained from 10 animals. Finally, the model fit was assessed by various goodness-of-fit criteria. (**Appendix)**.

4.3.2.2. Patlak and Logan Plots: Theoretical graphical methods to evaluate circulating Aβ transport into the brain via the BBB endothelium

Graphical plot approaches such as Patlak and Logan take a rather simplistic approach to commonly employed linear models, such as the one described above. The idea is to linearize and convert the model equations into one equation evaluated at time points corresponding to the scanning times to provide fewer parameters- mostly a slope and an intercept. Specifically, these approaches describe a way to linearize the blood-to-brain tissue distribution so that the slope of the line, influx clearance or K_i in Patlak plot (Patlak et al., 1983), and distribution volume or V_T in Logan plot (Logan et al., 1990), can be compared between Aβ isoforms. Mostly, blood-to-brain transfer is described by the following three parameters: (1) extraction fraction; (2) washout (efflux) parameter; and (3) K_i or influx clearance. It has been demonstrated that for solutes that cross the BBB slowly, K_i is the only parameter that can be determined accurately. (Patlak et al., 1983; Patlak and Blasberg, 1985). Logan plot (Logan, 2003; Logan et al., 1990) also describes the same mechanism (entry into the tissue), but the ligand is expected to follow reversible kinetics for the duration of the experiment.

4.3.2.2.1. Theory and assumptions of graphical model plots

4.3.2.2.1.1. General blood-to-brain exchange model and Patlak plot

The **Figure 4.2**, describes the general, blood-to-brain exchange model. No assumption has been made about the time course of arterial concentrations or the particular arrangement and the number of compartments involved. However, it describes a set of compartments, probably in series, between the plasma and brain parenchyma. This final transfer is assumed to be at the BBB, which is unidirectional or irreversible, and the flux dominates the blood-to-brain distribution of the protein during the experiment. This assumption essentially means that for the time course of the experiment, there is greater influx than efflux of the substance into the brain. Although, it may not be entirely true physiologically, during the experiment, when there is a greater influx, the assumption is deemed to be valid. Moreover, this approach eliminates the need for a vascular marker or an intravascular distribution correction.

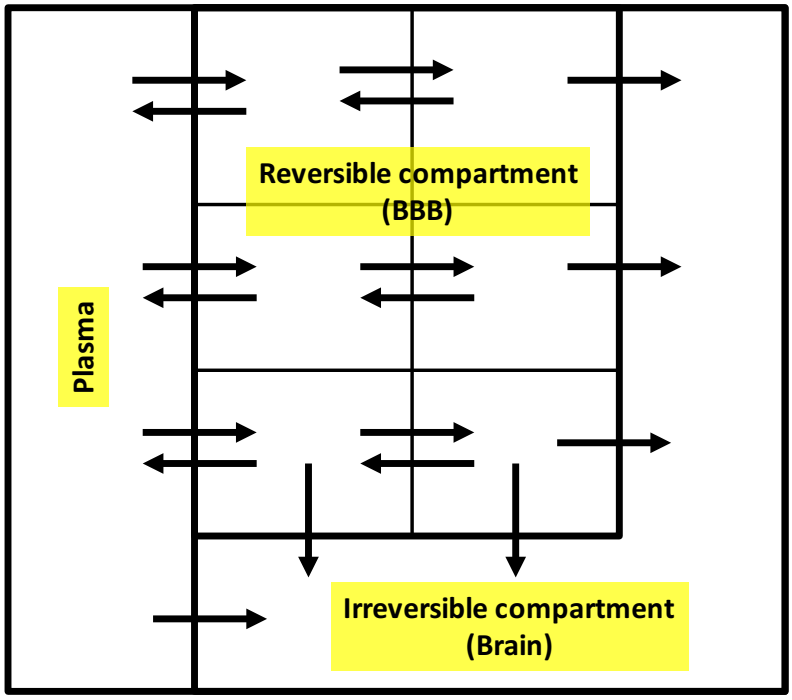

Figure 4.2 Blood- brain exchange model for theoretical graphical plot approaches. Reversible region of *n* compartments freely exchanges with plasma. Solute can enter the irreversible (brain) region but cannot leave. Patlak Plot describes the entry into the irreversible compartment (brain). Logan plot is used to describe the entry into the reversible compartment (BBB endothelium) Adapted from (Patlak et al., 1983).

In this work, the theoretical model approach is used to assess: (1) brain uptake (obtained from dynamic SPECT-CT imaging), and (2) plasma pharmacokinetics (obtained after administered intravenous bolus injections of ^{125}I-Aβ). The following assumptions of the theoretical model have been considered:

1. Plasma is the only source of the radiolabeled Aβ (^{125}I-Aβ).
2. The concentration of ^{125}I-Aβ in the plasma varies with time.
3. The reversible compartment is the BBB endothelium, where a rapid exchange of ^{125}I-Aβ between plasma and its receptors at the BBB is expected. However, once

^{125}I-Aβ enters the endothelial cell and subsequently the brain parenchyma, it is deemed irreversible.

4. Brain parenchymal region is the irreversible compartment; once ^{125}I-Aβ enters the irreversible compartment, it does not come back into the plasma or BBB intact during the course of the experiment..
5. The transfer within all these compartments obeys first order kinetics.
6. There are no significant structural alterations or metabolism within the physiological compartments during the course of the experiment. If at all there is metabolism, the metabolites carrying ^{125}I label predominantly gets trapped within the brain or the irreversible tissue only.
7. There is no pre-existent radiolabeled ^{125}I-Aβ in the brain or BBB. And if there is, it follows the same tracer kinetics as the freshly injected tracer.

The Patlak plot is generated by plotting A_m/C_p vs. $\int_0^t C_p d\tau / C_p$. Slope becomes linear after time t > t_P^*. The t_P^* refers to the time after which the Patlak slope becomes linear, which is indicative of the time to attain pseudo equilibrium between the plasma and reversible (BBB) compartments. In our studies, as described below, this t_P^* is assumed to ≤ 5 minutes. The parameter of interest is the slope or K_i, also called as influx clearance or Patlak constant. The Patlak equation is represented as:

$$A_{m_{t>t*}} = K_i \int_0^t C_p d\tau + (V_0 + V_p) C_p \quad (7)$$

where,

$A_m = total\ amount\ of\ ^{125}I\text{-}A\beta$ *in the brain tissue, until time t*

$C_p = plasma\ concentration\ at\ time\ t$

$$\int_0^t C_p d\tau = plasma\ AUC\ until\ time\ t$$

$$K_i = influx\ clearance$$

$$V_0 + V_p = intercept = total\ distribution\ volume\ (V_D)$$

The V_D is also called as, rapidly reversible volume (vascular volume + BBB complex + any other extravascular compartment in parallel with the BBB and rapidly exchanges with plasma), It should be noted that this distribution volume or rapidly reversible volume, theoretically defines the same distribution volume or V_T, which is estimated by the slope of Logan plot. However, in theory, this V_0, represents the 'lower limit' of the rapidly reversible volume (vascular compartment, BBB). In fact, V_0 or the ordinate intercept obtained by extrapolating the linear portion of the Patlak slope is equal to or less than the apparent steady state distribution volume of Aβ in all the reversible and exchangeable compartments, including blood space of the tissue. Therefore, the absolute value of V_0 may be lower than that of V_T, as is seen in our findings as well. However, this means that in these graphical method approaches, it is possible to predict the volume of distribution of vascular space without using a vascular marker. Another advantage is that there is no restriction on the number of compartments; hence, it is a compartment independent approach

It was further elaborated in the earlier publications that expounded the theory of Patlak plots that this approach is not valid if the (1) biological state of the analyte is changed during the experiment, and (2) the animal model used is not reproducible from one subject to another. Also, non-specific binding is expected to influence the slope but not the intercept of the graphical plot.

Moreover, adhering to the model, the following conditions were ensured while calculating the slope parameter:

1. Unidirectionality: The assumption of unidirectional transfer is satisfied by estimating the slope from the linear portion of the Patlak plot.
2. Insignificant efflux: In the Patlak plot, if a concave trend is seen at $t > t_P^*$, then a significant back flux is suspected. However, Patlak made amendments to this notion by affirming that as long as the tracer, ^{125}I-Aβ in this case, is 'nearly' irreversibly bound, and the net influx is positive for an appreciable duration of time, the Patlak plot could still describe the uptake kinetics into the irreversible compartment (brain)

Although, we did not see concavity indicating significant back flux in our Patlak plots, our compartmental model has shown that there could be some reversibility of ^{125}I-Aβ interactions with the BBB, at least during the early phase. Therefore, we employed Patlak plots to determine the uptake rate constant into the irreversible compartment (brain parenchyma) after the distribution equilibrium has been reached and the Logan plots to capture the reversible interactions of ^{125}I-Aβ proteins with its receptors at the BBB endothelium. Accordingly, the initial kinetics (0-5 min) were considered as reversible (described the Logan Plot) and the 5-40 min data is assumed to describe irreversible uptake into the brain compartment (described by the Patlak Plot). This transition where Aβ moves from reversible to irreversible compartment (BBB-brain) was quite evident in our results from longer time SPECT-CT measurements as the plot loses its linearity. In other words, Patlak and Logan plots describe different stages of the process; interactions of Aβ proteins with receptors at the BBB endothelium is assumed to be reversible, whereas the uptake of Aβ into brain was assumed to be irreversible. Hence, the slope of

the Logan plot provides an estimate of the distribution volume (V_T) of Aβ proteins into the BBB endothelium. On the other hand, the slope of the Patlak plot provides an estimate of uptake (influx clearance, K_i) into the brain parenchyma via the BBB endothelium.

4.3.2.2.1.2.Logan plot theory

Logan extended the theoretical foundation laid by Gjedde and Patlak to the reversible binding systems. Unlike the Patlak plot, the Logan plot does not assume irreversible trapping and assumes that the radiotracers injected have a rapid dissociation constant and a rapid efflux from tissue. Like with the Patlak plot, no particular model structure is assumed with the Logan plot. The Logan equation is depicted below:

$$\frac{\int_0^t ROI(t)dt}{ROI(t)} = V_T . \frac{\int_0^t C_p dt}{ROI(t)} + \text{b} \quad (8)$$

and the Logan plot is generated by plotting

$$\frac{\int_0^t ROI(t)dt}{ROI(t)} \; vs. \; \frac{\int_0^t C_p dt}{ROI(t)} \quad (9)$$

where,

$ROI(t)$ = *amount of* ^{125}*I-Aβ associated with the brain as measured by PET/SPECT in the region of interest or ROI until time t*

$\int_0^t ROI\ (t)dt$ = *Brain AUC until time t*

C_p = *the concentration of tracer in the plasma until time t*

$\int_0^t C_p dt$ = *plasma AUC until time t*

V_T = *Slope of the linear equation, referred to as the distribution volume*

b = Intercept of the linear equation

The slope and intercept can be further elaborated mechanistically as per the model. This is discussed in the application section. **(4.3.2.2.2.1.)**

It should be noted that, in Patlak plot (equation 7), normalizing term is the plasma concentration (C_p) in the denominator, whereas in Logan Plot, (equation 8), it is the brain (BBB tissue) amount or ROI(t). This also means that 'linearity' in the two plots hold different meanings. The linearity (constant slope) in the Logan plot is reached when the equilibrium (or pseudo equilibrium) between the plasma and BBB endothelium is attained (t_L^* or Lag time), and remains linear until the ligand is associated with BBB endothelium displaying reversible kinetics. When this linearity is lost, the reversibility assumption is no longer valid, and the ligand is assumed to enter the irreversible compartment or brain. The linear slope in the Patlak plot, reached at time t_P^*, refers to the equilibrium (or pseudo equilibrium) between the plasma and reversible compartment or BBB endothelium. However, depending upon several factors, including the ligand, measurement times and interval, it may be difficult to identify t_P^* and t_L^* individually. Also, these times indicate the exposure time of the tissue that may not be the same as the measurement times, that is the time at which the measurement is taken.

4.3.2.2.2. Application strategy for Logan and Patlak plots

Dynamic SPECT-CT data from brain was assumed to follow reversible kinetics at the surface of the BBB, initially and then reach the irreversible compartment, brain parenchyma. Therefore, first five minutes (0-5 minutes) SPECT-CT data was used to construct the Logan plot and 5-40 minutes data was used to construct the Patlak plot. Plasma observations were simulated for individual animals and doses from the PK

profiles obtained earlier. The slope and intercept for both Logan and Patlak plots were obtained and assessed.

4.3.2.2.2.1. Logan plot application

Like previously described (Logan, 2003; Logan et al., 1990; Meyer and Ichise, 2001), we assume two separate functional compartments (**Figure 4.3**), ^{125}I-Aβ is injected into the plasma compartment (concentration C_p) and enters the BBB endothelium compartment via reversible interactions with the receptors at the luminal surface (amount C_1).

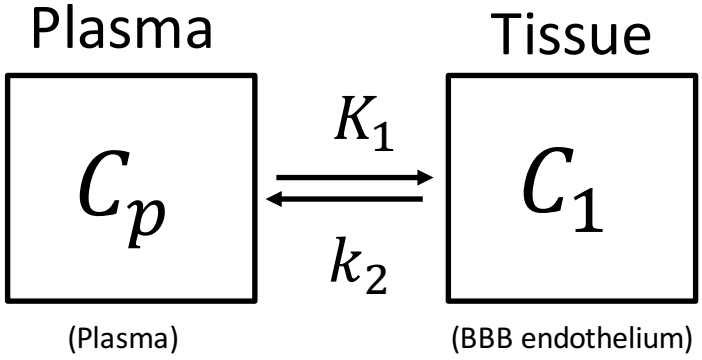

Figure 4.3. Logan model describing the reversible receptor-binding kinetics of Aβ at BBB endothelium. Logan Plot analysis of two compartment model system describing the blood to BBB distribution of ^{125}I-Aβ injected into the plasma compartment (C_p) and enters the BBB endothelium (C_1) (via receptors following reversible kinetics as per the transfer rate constants mentioned.

Further, the ^{125}I-Aβ transfer between the compartments is described as follows:

K_1 = clearance (volume / time), representing ^{125} I-Aβ entry into the tissue or BBB endothelium.

k_2 = *rate constant describing the efflux (time^{-1}) of ^{125} I-Aβ from the tissue or BBB endothelium.*

λ = *partition coefficient between the plasma and tissue or BBB endothelium compartment. It is the ratio of ^{125} I-Aβ in the tissue compartment to the plasma compartment at equilibrium, which is the ratio of K_1/ k_2. Units in volume.*

The use of radiolabeled tracers, ^{125} I-Aβ, may help elucidating the kinetics without saturating the receptors. The linear slope and intercept from Logan Plot is then described as:

$$Slope\ or\ V_T\ = \lambda + V_p \tag{10}$$

$$Intercept = \frac{-1}{k_2(1+\frac{V_p}{\lambda})} \tag{11}$$

where, V_p refers to the plasma volume in ROI (BBB endothelium).

The Logan slope refers to the total distribution volume V_T, which is the sum of partition coefficient and plasma volume. On the other hand, the x-intercept has units of time. Further, it should be noted that, K_1/ k_2.in Logan plot and k_{13}/ k_{31} in the mathematical model refer to the same process, but they are not the same; K_1/ k_2.is the Logan slope, which has units of volume (V_T), whereas k_{13}/ k_{31} has no units.

4.3.2.2.2.1. Patlak Plot application

As described in one application of Patlak plot, **Figure 4.4** (Logan, 2003; Logan et al., 1990; Meyer and Ichise, 2001), which is relevant for Aβ kinetics, we assume two tissue compartments- BBB endothelium (reversible compartment, C_1) and brain

(irreversible compartment, C_2) and the plasma compartment (C_p). The ^{125}I-Aβ was injected into the plasma compartment.

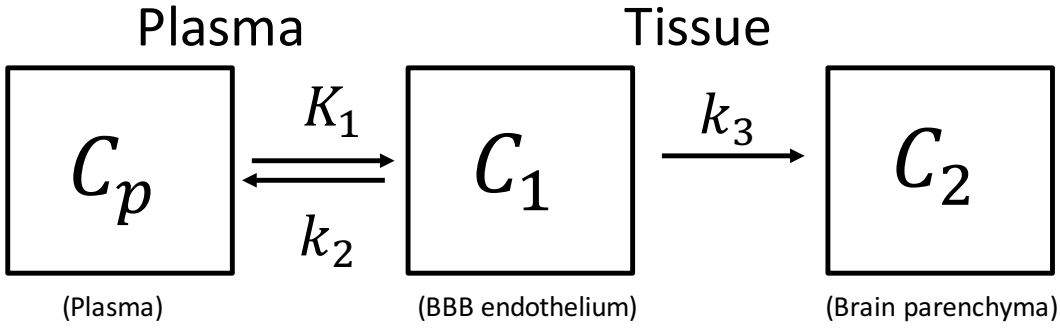

Figure 4.4. Model for the application of Patlak plot describing irreversible uptake kinetics of ^{125}I-Aβ into the brain tissue via the BBB endothelium. Patlak plot analysis of a three compartment model describing ^{125}I-Aβ distribution from blood (plasma) to brain tissue (via the BBB endothelium). The ^{125}I-Aβ is injected into the plasma compartment (C_p), enters the tissue compartment, which comprises of brain (C_2) and BBB endothelium(C_1), as per the transfer rate constants outlined.

The slope is thus described as:

$$Slope\ or\ K_i = \frac{K_1 k_3}{k_2 + k_3} = \frac{K_1 \lambda k_3}{K_1 + \lambda k_3} \quad (10)$$

Where, $K_1, k_2\ and\ k_3$ are respective clearance, and transfer rate constants and $\lambda = \frac{K_1}{k_2}$. However, Patlak plot can provide an estimate of slope or K_i, which is a function of λ. Direct estimation of λ is obtained as the slope in Logan plot (V_T). Further $K_1$is a function of blood flow. Although λ is not a function of blood flow, K_i still depends upon blood flow and capillary permeability. Therefore, an increase or change in K_i could be due to a change in binding or just the blood flow. While, K_i by itself is unable to provide information about the receptor dynamics or ligand binding (λ), the Logan slope (V_T)

could provide the magnitude of ligand binding and interaction with receptors at the BBB interface. Hence, the distribution volumes (V_T) obtained as the slopes of Logan plot were employed to assess differential interactions of ^{125}I-Aβ40 and ^{125}I-Aβ42 with the receptors at the BBB interface. On the other hand, their influx clearances (K_i) into brain, which were estimated by determining the slopes of Patlak plots, were also compared.

4.4. RESULTS

4.4.1. Mathematical model predicts a greater affinity of Aβ40 than Aβ42 at the BBB endothelium (Figure 4.5)

The quantitative model described in **Figure 4.1** was simultaneously fitted to the plasma and dynamic-SPECT brain data of ^{125}I-Aβ obtained in WT mice. The model equations adequately fitted the observed data points for brain and plasma profiles of ^{125}I-Aβ40 and ^{125}I-Aβ42 **(Figure 4.5)**. Comparison of the parameter estimates **(Table 4.1)** revealed statistically significant differences of plasma-tissue parameter estimates (k_{12}, k_{21} and k_{10}) between in ^{125}I-Aβ40 and ^{125}I-Aβ42. Volume of distribution or V was predicted to be 3.1-fold greater for ^{125}I-Aβ42 (16.47 ± 1.28 mL) than for ^{125}I-Aβ40 (5.15 ± 0.37 mL). The plasma PK profiles of ^{125}I-Aβ40 and ^{125}I-Aβ42 were also shown to be statistically significant. Also, parameter estimates describing the early plasma-brain interactions (k_{13} and k_{31}) between ^{125}I-Aβ40 and ^{125}I-Aβ42 were found to be significantly different. As ^{125}I-Aβ peptides are associated with the BBB endothelium for the first five minutes, the model predicts a lower value estimate of 'on' k_{13} rate constant, 'off' k_{31} rate constant and correspondingly, dissociation constant or ratio of k_{31} to $k_{13,}$ (i.e. k_{31}/k_{13} or k_d) for ^{125}I-Aβ40 (k_{13} = 0.004 ± 0.0006 min^{-1}, k_{31} = 0.43 ± 0.05 min^{-1} and k_{31}/k_{13} = 107.5) than ^{125}I-Aβ42 (k_{13} = 0.009 ± 0.001min^{-1}, k_{31} = 3.2 ± 0.35 min^{-1} and k_{31}/k_{13} = 355.5). Finally, the plasma-to-brain clearance (CL_{13}), estimated as the product of k_{13} and V, for ^{125}I-Aβ42 (0.148 mL/min) was 7.4-fold greater than that of ^{125}I-Aβ40 (0.02 mL/min).

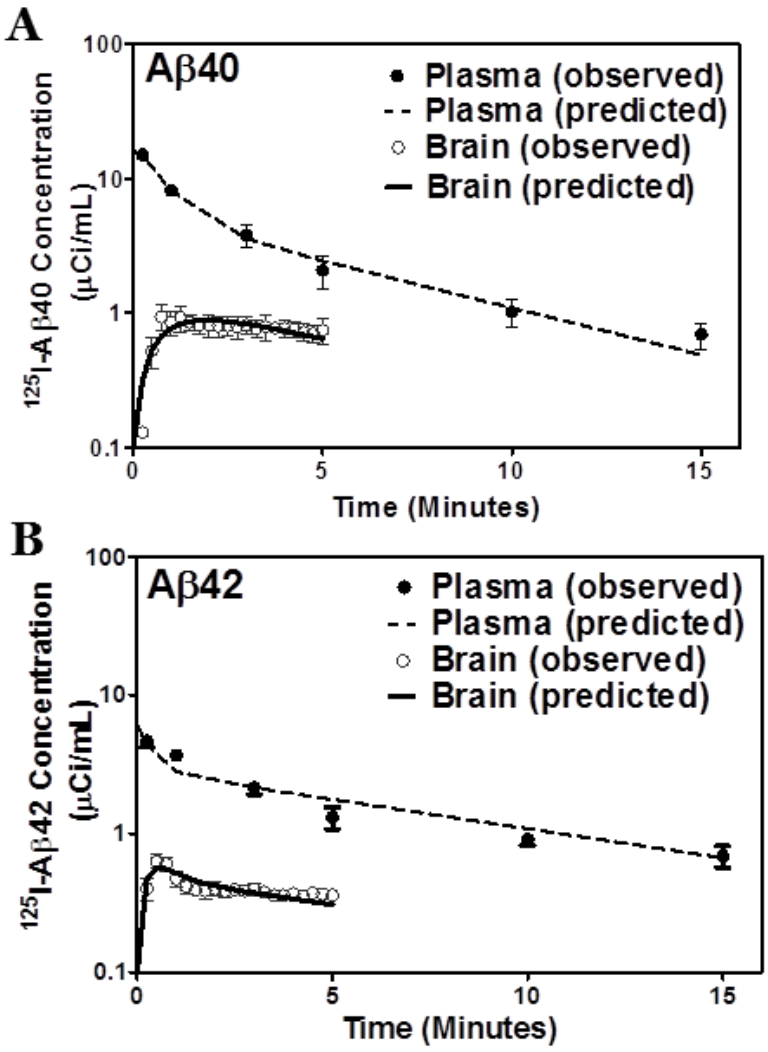

Table 4.1 Quantitative PK model predictions

Parameter	^{125}I-Aβ40	^{125}I-Aβ42	Significance
k_{12} (min^{-1})	0.59 ± 0.08	1.32 ± 0.38	*
k_{21} (min^{-1})	0.50 ± 0.02	1.37 ± 0.14	***
k_{10} (min^{-1})	0.44 ± 0.05	0.19 ± 0.019	**
k_{13} (min^{-1})	0.004 ± 0.0006	0.009 ± 0.001	***
k_{31} (min^{-1})	0.43 ± 0.05	3.2 ± 0.35	***
k_d or k_{31}/k_{13}	107.5	355.5	
V (mL)	5.15 ± 0.37	16.47 ± 1.28	***

Significance determined by Student's t-test (*p < 0.05, **p<0.01, ***p<0.0001)

Figure 4.5 Plasma and brain pharmacokinetics of ^{125}I-Aβ40 and ^{125}I-Aβ42 in 24-week-old WT mice. Pharmacokinetic profile of (**A**) ^{125}I-Aβ40 and (**B**) ^{125}I-Aβ42 in plasma (open circles- observed values and dashed lines: predicted data) and brain (dark circles- observed values and solid lines: predicted data)**.** Compartmental pharmacokinetic model depicted in **Figure 4.1** was simultaneously fitted to plasma and brain data using PhoenixWinNonlin® 6.4.

Table 4.1 The pharmacokinetic parameters predicted by the model for ^{125}I-Aβ40 and ^{125}I-Aβ42 were presented as estimated value ± standard error. The statistical significance of the difference between ^{125}I-Aβ40 and ^{125}I-Aβ42 for each parameter was assessed by Student's t-test (*$p < 0.05$, **$p<0.01$, ***$p<0.001$).

4.4.2. Logan plots predict a greater slope parameter for Aβ42 than Aβ40 at the BBB endothelium (**Figure 4.6 and 4.7**)

The slope describing the distribution volume (V_T) of ^{125}I-Aβ42 (55.78 ± 1.25 μL) is 1.4-fold greater than that of ^{25}I-Aβ40 (39.73 ± 0.07 μL) **(Figure 4.6).** The lag time (x-intercept) of Aβ40 (26.1 min) is more than that of Aβ42 (9.15 min). Further, it is evident from the plot that the slope deviates from linearity at later times, which suggests that the assumption of reversible kinetics is no longer valid **(Figure 4.7)**.

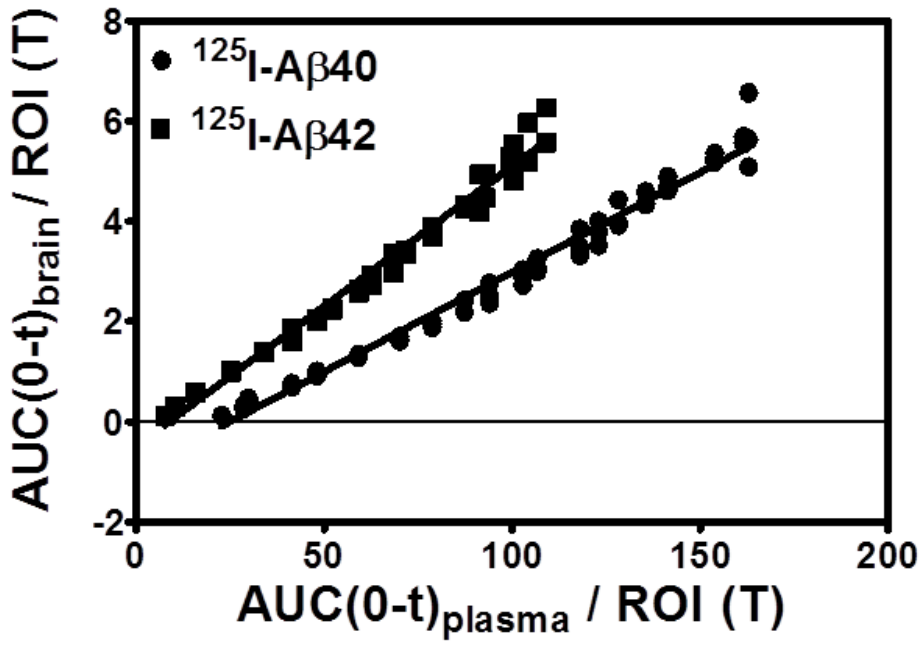

Table 4.2 Logan plot model fit

Parameter	^{125}I-Aβ40	^{125}I-Aβ42	Significance
Slope (μL)	39.73 ± 0.07	55.78 ± 1.25	***

Significance determined by Student's t-test (***p < 0.0001)

Figure 4.6 Logan plot describing the distribution volume of ^{125}I-Aβ into the brain (BBB) from plasma in 24-week WT mice. Logan plots of ^{125}I-Aβ40 (circle) and ^{125}I-Aβ42 (square). Estimates of distribution volume for ^{125}I-Aβ40 and ^{125}I-Aβ42 were obtained from the slopes (estimate ± standard error). Statistical significance was assessed by Student's t-test (*p<0.05)

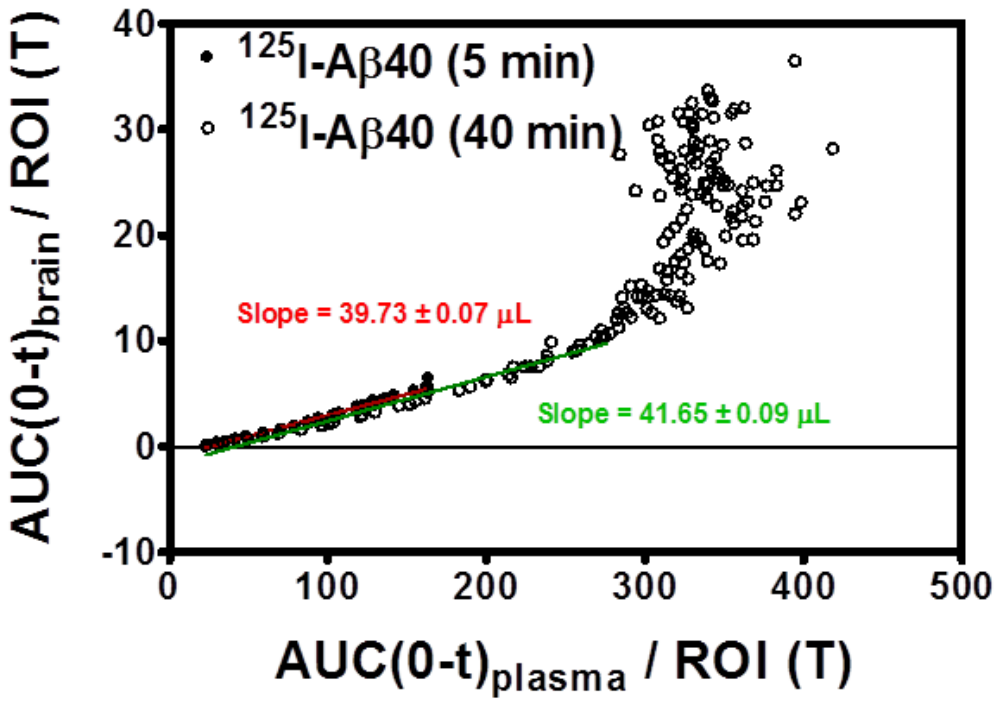

Figure 4.7 Logan plot describing the distribution volume of ^{125}I-Aβ into the brain (BBB) from plasma in 24-week WT mice. (A) Logan plots of ^{125}I-Aβ40 from measurements obtained until 5 minutes (filled circle) and separately, till 40 minutes (open circles). Slope parameter estimates (red: 5 minutes and green: 40 minutes) demonstrate the loss in linearity beyond 5 minutes such that Logan plot assumption is no longer valid. (estimate ± standard error).

4.4.3. Patlak plot predicts greater plasma-brain influx rate constant for Aβ42 than for Aβ40 (Figure 4.8)

The Patlak plot estimated a 1.8-fold greater influx clearance (K_i or slope) into the brain for Aβ42 (3.3 ± 0.07 X 10^{-5} mL/min) than for Aβ40 (1.75 ± 0.03 X 10^{-5} mL/min) (***$p<0.0001$). Also, y-intercept, which is an estimate of the distribution volume of reversible compartment, was 5.3-fold larger for Aβ42 (29.92 ± 5.24 X 10^{-5} mL) than for Aβ40 (5.59 ± 3.4 X 10^{-5} mL). (**$p<0.001$)

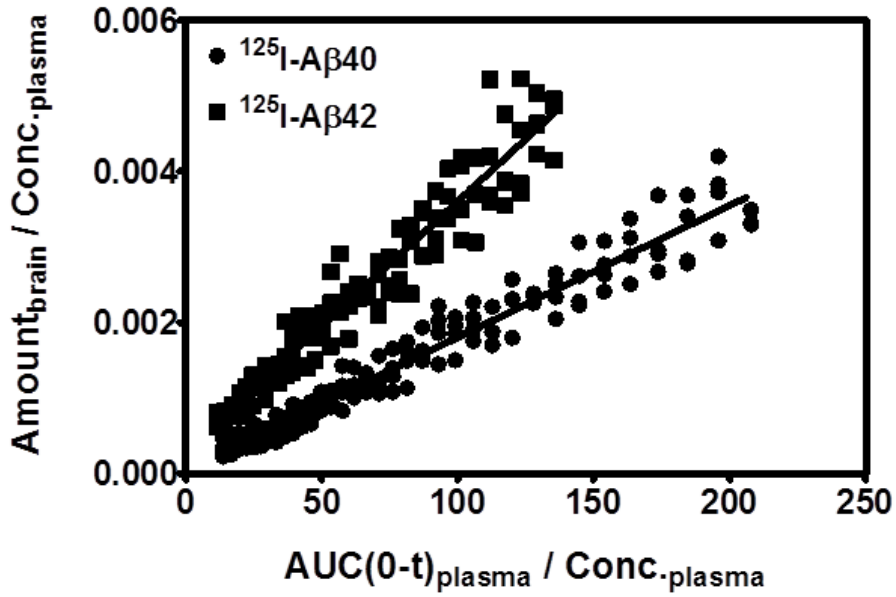

Table 4.3 Patlak plot model fit

Parameter	^{125}I-Aβ40	^{125}I-Aβ42	Significance
K_i (X 10^{-5} mL/min)	1.75 ± 0.03	3.30 ± 0.07	***
V_0 (X 10^{-5} mL)	5.59 ± 3.4	29.92 ± 5.24	**

Significance determined by Student's t-test (***p < 0.0001, **p< 0.01)

Figure 4.8 Patlak plot describing the Aβ influx clearance into brain via the BBB in 24-week WT mice. Solid circles represent ^{125}I-Aβ40, whereas solid squares represent ^{125}I-Aβ42. Slope parameter or Influx clearance (K_i) is presented as estimate ± standard error. Difference in the parameter estimates between ^{125}I-Aβ40 and ^{125}I-Aβ42 is statistically significant. Student's t-test (**p<0.01 and ***p<0.0001).

4.5. DISCUSSION

Imbalance in plasma and brain Aβ levels could be due to perturbations in Aβ trafficking at the BBB endothelium in AD brain (Erickson and Banks, 2013; Marques et al., 2013). These trafficking disturbances could be due to incompetency of the molecular players involved in Aβ transcytosis at the BBB, which are reflected in aberrant Aβ trafficking kinetics at the BBB, and the disposition of Aβ proteins in plasma and brain compartments. Owing to the differential trafficking mechanisms shared by Aβ40 and Aβ42 at the BBB, the BBB trafficking perturbations could disproportionately affect Aβ40 and Aβ42, differentially alter their kinetics in plasma and brain compartments, and bring changes in Aβ42:Aβ40 ratios in AD progression.

Bi-exponential disposition of Aβ proteins in plasma have been previously described (Ghiso et al., 2004; Kandimalla et al., 2005; Qosa et al., 2014). In addition, a biphasic decline in brain Aβ levels has been documented in APP,PS1 animals (Yuede et al., 2016) and humans (Cirrito et al., 2003). However, no direct comparison between the kinetics of the two main Aβ isoforms, Aβ40 and Aβ42, has been made. This information will be critical to comprehend the physiological processes behind Aβ42:Aβ40 ratio that increases in brain and decreases in plasma during AD progression. Therefore, it is imperative to elucidate the distribution kinetics of these two isoforms separately.

Impaired clearance and not overproduction was claimed to be primarily responsible for Aβ accumulation in the brain (Mawuenyega et al., 2010). The clearances of Aβ40 and Aβ42 in AD patients compared to non-demented individuals of similar age were found to be respectively 0.72- and 0.69- fold lower (Mawuenyega et al., 2010). However, to our understanding, no investigations on the plasma-to-brain influx kinetics of Aβ40 and

Aβ42 have been conducted so far. As the transport of Aβ isoforms at the BBB endothelium is bidirectional and interdependent (Eisele et al., 2014; Hamaguchi et al., 2012), it is critical to investigate the contributions of both these processes to brain amyloid burden and AD progression.

The objective of the work presented in this chapter was to compare the kinetics of Aβ40 and Aβ42 uptake at the BBB endothelium, and subsequently into the brain parenchyma. The plasma-to-brain uptake kinetics was expected to resolve the association between plasma Aβ levels (luminal exposure) and AD progression. Owing to the lower concentrations compared to the brain, plasma Aβ may not directly enhance the brain amyloid burden. However, chronic exposure of BBB to luminal Aβ could disrupt the critical signaling/trafficking pathways at the BBB, and diminish the ability of the BBB to efflux brain Aβ proteins. We believe that Aβ40 and Aβ42 differentially affect the BBB function; hence, their kinetics at the BBB, which could affect their luminal and abluminal prevalence, should be carefully elucidated.

Furthermore, conventional methodologies of measuring radiolabeled Aβ post intravenous or intracerebral injections using steady state measurements (Shibata et al., 2000) or microdialysis (Cirrito et al., 2003) would not be able to dissect the immediate changes at BBB endothelium. Hence, dynamic SPECT-CT imaging techniques were employed to resolve differential interactions of Aβ proteins with the BBB endothelium and their subsequent transcytosis into the brain. However, SPECT-CT brain imaging does not distinguish the uptake of ^{125}I-Aβ peptides into the BBB endothelium versus the brain parenchyma. Therefore, initial interactions of ^{125}I-Aβ peptides with the BBB endothelium were elucidated by investigating kinetic changes in the brain-associated radioactivity

during the first five minutes following intravenous administration. The Logan plots for 0-5 minutes assumes that up to 5 minutes, Aβ interactions with the BBB endothelium are still reversible. This assumption is reasonable as Aβ peptides have low permeability at the BBB. Moreover, the linearity of the Logan plot is lost at later time points, which is likely due to the entry of the tracer into the irreversible compartment, mostly the brain parenchyma. Hence, we employed Patlak plots to predict influx clearance into the irreversible compartment, beyond 5 minutes.

Further, to eliminate the radioactivity dose differences between the PK experiments and SPECT-CT imaging, plasma observations were individually simulated for the corresponding SPECT-CT dose. This enabled us to curve-fit plasma and brain observations *simultaneously* to predict and compare ^{125}I-Aβ40 and ^{125}I-Aβ42 kinetics in plasma and brain compartments. Also, to eliminate the contribution of radioactivity in the circulation to the total brain activity, the radioactivity counts in the plasma were subtracted from the total brain SPECT-CT counts. This enabled us to fit the precise brain 'tissue' (parenchyma) observations in the model. As explained earlier, graphical model approaches, Patlak and Logan plot did not need any such adjustment. Finally, although two different instruments (gamma counter and SPECT-CT) were used to measure radioactivity in plasma and brain respectively, no conversion factor was employed. This was justified as the instrument conversion factor, a constant scaling factor, is expected to have equal contribution to both ^{125}I-Aβ40 and ^{125}I-Aβ42 kinetics, and hence would not alter relative differences in kinetic parameters of the peptides.

The proposed PK model predicted significant differences in the kinetics of ^{125}I-Aβ40 and ^{125}I-Aβ42 in plasma and brain compartments. The differences in predicted

transfer rate constants between the plasma and tissue (peripheral tissue and brain) verified the possibility of different plasma PK profiles of ^{125}I-Aβ40 and ^{125}I-Aβ42 presented in Chapter Two. The greater k_{13} for ^{125}I-Aβ42 than for ^{125}I-Aβ40 indicated the possibility that the rate of influx of ^{125}I-Aβ42 is more than that of ^{125}I-Aβ40. Also, CL_{13} (influx clearance, that was assessed as a product of k_{13} and V), was greater for ^{125}I-Aβ42 than ^{125}I-Aβ40. This is also confirmed by the higher Patlak influx rate (K_i) for ^{125}I-Aβ42 than for ^{125}I-Aβ40. While the Patlak plot describes the net clearance into the BBB endothelium and beyond, into the brain parenchyma, no distinctions could be drawn between influx and efflux rate constants from the Patlak plot. The PK model predicted higher k_{31} for ^{125}I-Aβ42 than for ^{125}I-Aβ40. Also, the ratio of k_{31} to k_{13} (k_{31}/k_{13}), more commonly designated as the dissociation constant or k_d, was greater for ^{125}I-Aβ42 than ^{125}I-Aβ40. These results indicate that the affinity of ^{125}I-Aβ40 to the receptors at the BBB endothelium could be higher than that of ^{125}I-Aβ42. This result is not surprising as Aβ40 was demonstrated to have greater affinity for the putative Aβ receptors, LRP1 and possibly for RAGE (Deane et al., 2009, 2004, 2012), than Aβ42. However, the luminal uptake of F-Aβ42 was significantly greater than that of F-Aβ40.These model predictions are also confirmed by the studies conducted in hCMEC/D3 cell monolayers *in-vitro* (Chapter Three, Figure 3.3). It is important to note that the greater endothelial uptake of ^{125}I-Aβ40 over ^{125}I-Aβ42, does not translate into higher rates of transcytosis. We postulate that the following factors may contribute towards this finding: (1) *affinity*: macromolecules with only optimal affinities could be transcytosed and translate to higher permeability across the cellular barriers. (Thomas, 2000). That is, macromolecules with considerably high affinity to the endothelium may get bound or stuck onto the

endothelium and do not enter the parenchyma altogether, or experience a significant delay in their internalization. Therefore, it is possible that the higher affinity of Aβ40 may indeed reduce its ability to trancytose across the BBB. (2) *ineffective exocytosis:* Our earlier publication had demonstrated that a vasculotropic mutant form of Aβ40, Dutch-Aβ40, accumulates more in the cerebral vasculature than Aβ40 by inhibiting its own exocytosis (Agyare et al., 2013). Therefore it is possible that Aβ40, which is more vasculotropic than Aβ42 accumulates in the BBB endothelium by inhibiting its own exocytosis, and demonstrate lower translocation into the brain parenchyma.

The slope of the Logan plot, which represents distribution volume (V_T), was greater for Aβ42 than for Aβ40. This may indicate the greater receptor occupancy of Aβ42 on the BBB endothelium compared to that of Aβ40. These results, support the PK model predictions of greater affinity, but lower extent of uptake of Aβ40 than Aβ42 at the BBB endothelium. Further, this is also supported by t_L^*, (x-intercept) values from Logan plot, where, Aβ42, equilibrates faster (shorter lag time) and begins to distribute quickly, whereas Aβ40, with its greater affinity, takes longer (longer lag time) to equilibrate. Higher distribution volume for Aβ42 compared to Aβ40 has also been predicted by the Patlak Plot. As can be deduced from the Equation 7, y-intercept of the Patlak plot refers to the distribution volume within the reversible compartments, including the BBB endothelial surface.

The Patlak plot predicts greater slope, which represents greater influx clearance (or transcytosis) into the irreversible compartment (brain), for Aβ42 than for Aβ40. This is in line with the Logan plot trends as well. The Logan slope (V_T) and Patlak slope (K_i), represent two distinct parameters. Greater V_T of Aβ42 than Aβ40 suggests more

distribution into the BBB endothelium and beyond, whereas, greater Ki of Aβ42 than Aβ40 suggests greater rate of transcytosis (clearance) into the brain of Aβ42 compared to Aβ40. Moreover, CL_{13}, plasma-to-BBB influx clearance calculated using the predictions from the PK model, was higher for Aβ42 than Aβ40. These observations indicate the clearance of Aβ42 into the BBB endothelium, as well as into the brain parenchyma, is greater than that of Aβ40. These observations contradict the earlier findings of BBB permeability measurements in 24-week old WT animals presented in Chapter Two, Figure 2.3 that demonstrated that permeability surface area product or PS value of Aβ42 is 0.78-fold lower than that of Aβ40. The PS values measured in those studies estimated the steady state brain permeability 15 minutes after ^{125}I-Aβ injection in plasma, followed by harvesting the total brain tissue and measuring the radioactivity counts in gamma counter. Therefore, it may be possible that these PS values primarily measure endothelial cell accumulation and not the brain parenchyma. In such a case, PS value of Aβ40 could be more than that of Aβ42, due to its greater tendency to accumulate at the endothelium, as observed in this Chapter by multiple approaches.

In summary, the quantitative models predict that Aβ40 has greater affinity (lower k_d) to the BBB endothelium than Aβ42. However, Aβ42 exhibits higher permeability across the BBB endothelium based on the higher slope value in Patlak Plot. This is also supported by the larger volume of distribution of Aβ42 than Aβ40 predicted by Logan plot. On the other hand, Aβ40 tends to stay into the BBB endothelium longer. These model predictions help us to infer that Aβ40 may accumulate in the BBB endothelium and is unable to transcytose as efficiently as Aβ42. This prolonged stay, probably, enables it to interfere with the intra-endothelial trafficking apparatus; and subsequently,

result in disrupted trafficking or the impaired Aβ clearance at the BBB endothelium, which is observed during AD progression. One such interference with the SNARE exocytosis assembly, which could possibly explain the lower transcytosis and greater BBB accumulation of Aβ40 than Aβ42, will be elaborated in the subsequent chapter (Chapter Five).

CHAPTER FIVE

5. AMYLOID BETA INTERFERES WITH SNARE MEDIATED VESICULAR FUSION PROCESSES

5.1. SUMMARY

SNARE (Soluble NSF Attachment protein Receptor, where NSF stands for N-ethyl–maleimide-sensitive fusion protein) mediated vesicular fusion processes have been implicated in Alzheimer's disease (AD). However, the causal association between SNARE dysfunction and AD pathogenesis has not been clearly elucidated. Amyloid beta (Aβ) proteins accumulate as amyloid plaques in the brain, which is most likely due to impaired clearance of Aβ peptides. Earlier studies have claimed that vesicular exocytosis perturbations could be responsible for the impaired exocytosis of Aβ proteins at the BBB, which is one of the primary portals that clear Aβ from brain. Further, synaptic function has also been known to be disrupted in AD, which eventually triggers cognitive disabilities. In this chapter, using sophisticated microscopic techniques of fluorescence resonance energy transfer (FRET) followed by fluorescence lifetime imaging microscopy (FLIM), we demonstrate that Aβ directly interferes with the interactions between two SNARE proteins: vesicle associated membrane protein (VAMP-2) and synaptosomal associated protein of 25 kDa (SNAP-25). Moreover, we also provide preliminary evidence that VAMP-2 is also involved in Aβ exocytosis. Hence, our findings suggest that Aβ may interfere with its own exocytosis as well as the exocytosis of several

biomolecules, including transferrin and insulin at the BBB endothelium, in addition to causing synaptic dysfunction in neurons.

5.2. INTRODUCTION

Synaptic vesicle recycling- the process of neurotransmitter exocytosis from small round vesicles into the synaptic cleft and retrieval of the components involved in the process- is one of the best controlled processes in cell biology (Rizzoli, 2014). Therefore, interference at any step of this process could lead to deleterious pathophysiological consequences. Similarly, vesicular transcytosis involving the intracellular delivery of cargo molecules from the donor organelle or cell to the specific receiver compartment- is a highly monitored event, critical for cell survival. Although the precise mechanisms involved in intracellular trafficking are still an enigma to biologists, all vesicular transport processes can be described by these four steps: (1) budding or formation of the vesicle from the plasma membrane; (2) movement of vesicles towards the acceptor compartment by diffusion or propelled by microtubular motors along the cytoskeletal tracks; (3) tethering, or attachment of the vesicle to the acceptor plasma membrane; and lastly (4) fusion or exocytosis.

The exocytosis, an integral step in transcytosis as well as in synaptic fusion, shares similar cellular organization involving SNARE exocytosis assembly that brings the vesicular membrane closer to the plasma membrane, and facilitate their fusion to release the vesicular cargo to the extracellular space (Cai et al., 2007). This process is accomplished by two sister SNARE assembly proteins- the vesicular SNARE (v-SNARE) and the target SNARE (t-SNARE). The v-SNARE is located on the vesicular membrane, and the t-SNARE is located on the plasma membrane or on the membrane of a target organelle. During exocytosis, the v- and t-SNAREs interact and facilitate the fusion of both membranes by utilizing the energy that is released during the formation of

a four-helix bundle of corresponding SNARE proteins, right before exocytosis. The formation of this bundle leads to a tight connection at the fusion site. After the exocytosis is accomplished, the helical SNARE complex is uncoiled, and the dissociated SNAREs are recycled. The energy required for this complex operation is supplied by the ATPase activity of NSF. Strategic subcellular localization that imparts specificity to membrane fusion events and the ability to form stable complex to facilitate membrane fusion, make SNAREs, the fundamental fusion factors (Duman and Forte, 2003).

For vesicular docking and fusion events with the plasma membrane, a vesicle protein such as, synaptobrevin or vesicle-associated membrane protein (VAMP-2), and two plasma membrane proteins- syntaxin and synaptosomal associated protein of 25 kDa (SNAP-25)- come close together and are tightly assembled into a complex. Then, SNAP and NSF are involved in the disassembly process, which involves the recovery of VAMP-2 with the vesicular membrane and retaining of syntaxin as well as SNAP-25 on the plasma membrane. These will then be available for fusion with newly docked vesicles (Chen et al., 2001; Degtyar et al., 2013). Although SNARE proteins have been demonstrated to carry out the fusion process themselves, the sudden fusion events after an action potential requires calcium, that binds to C2 domain of synaptotagmin, which eventually interacts with SNARE proteins to accelerate the fusion process (Tucker et al., 2004). Though, the precise events in this membrane fusion process are not fully known, it is believed that the N terminals of VAMP-2, syntaxin and SNAP-25, come together to form a tight coiled helical SNARE complex, whereas the C terminals are embedded in their respective membranes (Degtyar et al., 2013) **(Figure 5.1)**.

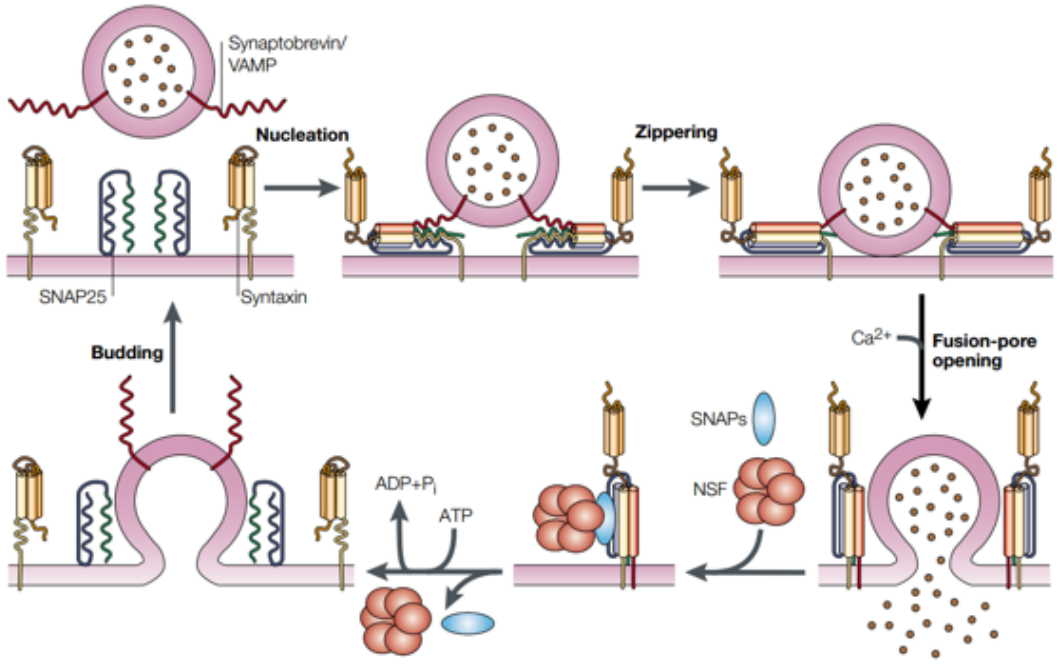

Figure 5.1 Synaptic vesicular exocytosis process by SNAREs assembly and disassembly. Synaptobrevin (VAMP-2) interacts with SNAP-25 and Syntaxin to zip the two membranes together by forming a SNARE complex to trigger exocytosis or fusion. After fusion, N-ethylmaleimide-sensitive fusion protein (NSF) and soluble NSF-attachment proteins (SNAPs) disassemble the core complexes that remain on the same membrane to recycle them for another round of fusion. Reused after permission.(Rizo and Südhof, 2002)

We hypothesize that disruptions in SNARE machinery at the BBB endothelium affect Aβ transcytosis, and consequently Aβ clearance at the BBB in AD brain. Moreover, synaptic neurotransmission has been known to be disrupted in AD. However, the precise mechanistic understanding of these disrupted processes has not been elucidated. In addition, several links between SNAREs and AD pathology have been proposed in the literature. Recently, the formation of SNARE complexes was shown to be substantially reduced in postmortem brains of AD patients (Sharma et al., 2012). Also, aberration in SNARE complex formation could lead to cognitive defects (Corradini et al., 2009; Honer et al., 2002), that might be triggered by misfolded proteins (Choi et al.,

2015, 2013). It was also shown that a reduction in presynaptic SNARE protein interactions, between SNAP-25 and syntaxin, were directly associated with AD pathology (Honer et al., 2012) as well as in the Lewy-Body Variant of AD (Mukaetova-Ladinska et al., 2009). Moreover, the expression of snyaptobrevin (VAMP-2) is significantly decreased in all AD brain regions (Sze et al., 2000). The VAMP-2 interacts with calmodulin and regulates calcium dependent exocytosis (Quetglas et al., 2002). It is further known that calcium signaling is affected in AD. However, the role of SNARE machinery in Aβ transcytosis at the BBB and the mechanistic link between impaired SNARE assemblies and amyloid accumulation in AD brain in not clearly established.

The amyloidogenic and toxic Aβ42 was shown to affect neurotransmitter release by disrupting the interaction between synaptophysin and VAMP-2 (Russell et al., 2012). Synaptophysin (p 38) is another SNARE protein that directly binds to (Calakos and Scheller, 1994) and assists in targeting (Pennuto et al., 2003) of VAMP-2. Their interaction is known to be upregrulated during neuronal development, and Aβ has been shown to interfere with it (Russell et al., 2012). Moreover, Aβ, along with α-synuclein, the protein that accumulates in Parkinson's brain, have been demonstrated to block SNARE dependent vesicular fusion (Choi et al., 2015). Furthermore, it was shown that Aβ is capable of directly binding to Syntaxin1a and impairing SNARE mediated exocytosis (Yang et al., 2015). While, interference with any of these processes may affect the exocytosis of vesicular contents, the experimental evidence is lacking.

In this work, we provide direct evidence that Aβ inhibits the functional interactions between VAMP-2 and SNAP-25 at neuronal membranes using sophisticated microscopy tools of fluorescent resonance imaging microscopy (FRET), followed by fluorescent

lifetime imaging microscopy (FLIM). Moreover, we also demonstrate that Aβ may use this machinery to exocytose itself from the cell; and consequently inhibits its own exocytosis. Finally, we also provide preliminary evidence that this mechanism is common to vesicular exocytosis in neurons as well as the transcytosis at the BBB. This commonality provides mechanistic link between the impaired clearance of Aβ, due to perturbation of vesicular transcytosis at BBB endothelium, and synaptic dysfunction in AD.

5.2.1. Theory of Fluorescence resonance energy transfer (FRET) fluorescence lifetime imaging microscopy (FLIM)

Foster Resonance Energy Transfer, is a process by which a fluorophore (donor) in its excited state transfers some of its energy to a neighboring molecule (acceptor) by non-radiative dipole-dipole interaction (Berney and Danuser, 2003; Förster, 2012; Piston and Kremers, 2007). If the acceptor is also a fluorophore, the process is also referred to as Fluorescence Resonance Energy Transfer (FRET). During the steady state *intensity based* FRET microscopy, two different approaches could be used to capture the energy transfer: (1) Emission measurement: Donor is excited and the decrease in donor emission or the increase in acceptor emission is measured. (2) Acceptor photobleaching: Donor is excited and its emission is captured before and after the photobleaching of the acceptor. To better understand the theoretical concept of FRET-FLIM measurements; the simplified version of the Jablonski diagram has been reviewed below.

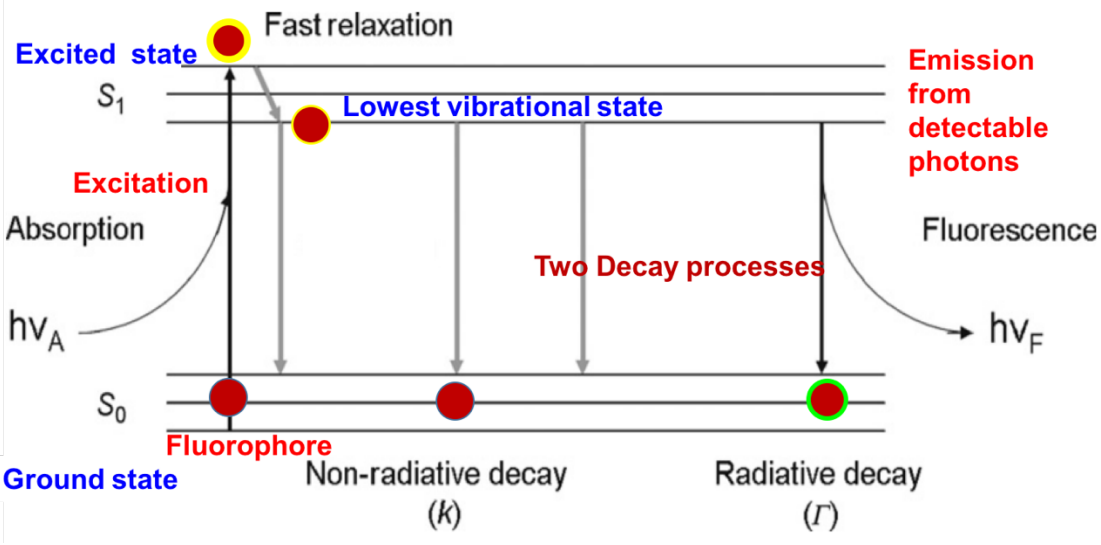

Figure 5.2 Simplified version of Jablonski diagram illustrating the concept of fluorescence and the two decay processes for the decaying fluorophore from the lowest vibrational state of the excited state. Modified from Chang et al., 2007.

The S_0 represents the ground state and S_1 represents the first excited state. Horizontal lines depict the different vibrational states of the fluorophore (Becker, 2010; Becker et al., 2006; Chang et al., 2007). After exposure to the designated wavelength light, the fluorophore is excited and then rapidly relaxes to the lowest vibrational state within the excited state. From that point, the fluorophore could return to the ground state via one of the two decay processes: non radiative decay (k) or radiative decay (Γ). Radiative decay is responsible for the fluorescence emission, which is dependent on the electronic properties of the isolated fluorophore. On the other hand, non-radiative decay is expected to be dependent on the local dynamic environment of the fluorophore, such as, its interactions with other fluorophores or quenchers in the FRET system. Hence, either of the two processes- radiative decay (or changes in fluorescence intensity) or non-radiative decay (or changes in fluorescence lifetime) are capable of depopulating or

decreasing the number of fluorophores in the lowest vibrational excited state (Lakowicz, 2006).

This situation can be described mathematically by the following equation:

$$\frac{dN(t)}{dt} = -(\Gamma + k)N(t) \qquad (1$$

where,

$\frac{dN(t)}{dt}$ = decay rate of the fluorescence emission intensity

Γ = non-radiative decay rate

k = radiative decay rate

$N(t)$ = total decaying population of the fluorphores

The decay rate of the fluorescence emission intensity is proportional to the total decaying population of the fluorophores and is attributed to both decay processes. It can be re-written in its exponential form:

$$N(t) = N_o e^{-(\Gamma+k)t} = N_o e^{-t/\tau} \qquad (2)$$

$$\tau = \frac{1}{\Gamma+k} \qquad (3)$$

where,

N_o = initial number of fluorescent molecules in first excited state

τ = fluorescence lifetime, where τ is the inverse of the sum of two decay rates.

The τ is refered to as the fluorescence lifetime, and is defined as the average time a molecule spends in the excited state prior to returning to the ground state. This lifetime

(τ) is determined in the FLIM studies. Expectedly, FRET leads to a change in the fluorescence emission of the donor by changing the radiative decay rate. This brings changes in the lifetime of the donor, which are captured in fluorescent lifetime imaging microscopy or FLIM.

In the microscopy field, fluorescence property can be assessed by either of the two ways described in equation 2: (i) steady state fluorescence microscopy (SSFM) also called as intensity based measurements, which measures $N(t)$; and (ii) fluorescence lifetime imaging microscopy that measures the lifetime property τ. Interestingly, these two analytical measurements differ in their sensitivities and the information provided. Intensity based measurements, that are more commonly employed, measure the total intensity of the fluorophore. It provides information about the cell morphology, intracellular content, but is sensitive to a variety of things such as the source intensity, detector gain settings, optical loss sample, variation in sample fluorophore concentration, photobleaching, microscope focusing, and spectral overlap. On the other hand, FLIM measures the lifetime property of the fluorophore. This essentially tells how rapidly the fluorophore decays, which is an intrinsic property of the fluorophore, and unlike intensity, does not change with the amount of fluorophore. The FLIM provides spatially resolved images of fluorophore lifetimes that are actually sensitive to the local environment of the fluorophore, and is totally independent of all the factors described earlier that influence the intensity.

In FRET, there is a pair of fluorophores, the donor (cyan fluorescent protein or CFP) and the acceptor (yellow fluorescent protein or YFP). The emission of the donor overlaps with the excitation of the acceptor. As a result, there is transfer of energy from

the donor to the acceptor. Before FRET, the two fluorophores are separate; on exciting CFP, only CFP will emit. However, when the CFP-YFP are close to each other and CFP is excited, some energy gets transferred from CFP to YFP, thereby exciting YFP. Consequently, YFP can also emit now. However, this is a very sensitive phenomenon that can happen only if all the three FRET conditions are met: (1) spectral overlap- emission of donor overlaps with the excitation of acceptor; (2) distance between donor and acceptor is less than 10 nm- this property is exploited in several FRET experiments to image interacting organelles in live cells; and (3) orientation of the two fluorophores should be optimal to facilitate the transfer (Broussard et al., 2013).

5.3. MATERIALS AND METHODS

5.3.1. Vectors, cell culture and transfections

The plasmid mCer-4aa-VAMP2 (Addgene plasmid #53233) and its corresponding FRET partner mCit-4aa-SNAP25B (Addgene plasmid # 53235) were obtained as a gift from Robert Zucker (Department of Molecular and Cellular Biology, University of California at Berkeley). Neuroblastoma 2a (N2A) cells were cultured in Dulbecco's modified Eagle's medium supplemented with 10 % fetal bovine serum (FBS) and 1 % penicillin-streptomycin, and maintained at 37 °C in 5 % (v/v) CO_2 and 95% (v/v) air. The hCMEC/D3 cells were cultured in supplemented EBM-3 medium, as described earlier in Chapter 3. Either cells were grown on coverslip-bottom culture dishes (MatTek Corporation, MA). After 3 days, cells were transfected overnight with mCer-4aa-VAMP2 or Cer-VAMP2 (donor only), mCit-4aa-SNAP25B or Cit-SNAP25 (acceptor only), or both (mCer-4aa-VAMP2:mCit-4aa-SNAP25B in the ratio of 1:1) using Effectene transfection reagent (Qiagen) as per the manufacturer's protocol. The total DNA amount used was 1 μg and was kept the same for all dishes. Following day, the culture medium was replaced and the cells were allowed to recover from the transfection. While the hCMEC/D3 cells were imaged directly, the N2A cells were differentiated by incubating them with differentiating medium (DMEM supplemented with 1 % FBS and 0.2 mM retinoic acid), 24 hours before the experiment. The differentiation was confirmed by visual examination of cells and formation of dendrites and neurites.

Fifteen minutes before the experiment, the cells were replaced with Krebs-Ringer bicarbonate buffer (115 mM NaCl, 5 mM KCl, 24 mM $NaHCO_3$, 2.5 mM $CaCl_2$, 1 mM $MgCl_2$, 10 mM HEPES pH 7.4 and 0.1% BSA). All FRET-FLIM imaging experiments

were conducted at normal (unstimulated exocytosis) and high potassium (stimulated exocytosis) conditions. After image acquisition under normal potassium levels, the KCl concentration was raised to 55 mM by spiking the medium with 100 μL of concentrated KCl solution. Cells were imaged immediately following the high potassium stimulation. The FM dye (FM® 4-64, Invitrogen) was used to track the exocytosis.

5.3.2. Confocal laser scanning microscopy and image analysis

All FRET and FLIM experiments were performed at the University of Minnesota imaging center (Minneapolis, MN). The constructs mCer-4aa-VAMP2 and mCit-4aa-SNAP25B served as FRET donor and acceptor, respectively. The donor lifetime of mCer-4aa-VAMP2 was measured in FLIM studies. FRET intensity experiments were performed on transfected live cells an Olympus FluoView FV1000 IX2 Inverted Confocal microscope with FLIM detector, and the image acquisition settings are described below. Data acquisition was performed using a 512 X 512-pixel image size, using a PLAPON 60X O NA1:42 objective lens. Separate fluorescence emission channels were collected simultaneously in three different sequential phases at 2.5X zoom.

Table 5.1 Image acquisition settings in FRET intensity experiments

Sequential phases	Simultaneous channels	PMT Voltage	Excitation	Emission	Instrument settings
Phase 1	Channel 1 (CFP/YFP/FRET, exciting CerVAMP2 and capturing CerVAMP2)	600V	405 nm	475 nm	BF position (460 nm) and BF range (40 nm)
	Channel 2 (CFP/YFP/FRET, exciting CerVAMP2 and capturing FRET or CitSNAP25)	360 V	405 nm	0 nm, mirror	BF position (515 nm) and BF range (100 nm)
Phase 2	Channel 3 (FM 4-64, exciting FM Dye and capturing FM Dye)	660 V	488 nm	0 nm, mirror	BF position (610 nm), and BF range (100 nm).
Phase 3	Channel 4 (ECFP, exciting	600 V	405 nm	475 nm	BF position

	CerVAMP2 and capturing CerVAMP2)				(460 nm) and BF range (40 nm)
	Channel 5 (EYFP, exciting CitSNAP25 and capturing CitSNAP25)	360 V	515 nm	0 nm, mirror	BF position (530 nm) and BF range (100 nm).

Spectrum separation was kept 'on' throughout the image acquisition. Acquired images were viewed and were processed using FIJI ImageJ 1.50i software (Wayne Rasband, National Institutes of Health, USA).

5.3.2.1. Intensity image processing

The confocal intensity images were obtained in all different channels as described above and were processed individually to account for the following: (1) the bleed over from the Channel 1 (Cerulean) into Channel 2 (FRET channel); (2) original donor intensity in Channel 1 (Cerulean), that will indirectly impact the intensity in Channel 2 (FRET channel). The functional FRET interactions between the Cer-VAMP2 and Cit-SNAP25 are expected to happen at the site of exocytosis on the plasma membrane, Hence, using the band and mask tool, the region of interest (ROI) was defined to measure the intensity of just the membrane, and not the complete cell. This was done as follows.

Step I: Estimation of channel bleed-over using Cer-VAMP2 only. In the cells transfected with Cer-VAMP2, intensity in Channel 1 (I_1) and FRET Channel or Channel 2 (I_2) were measured. Since, there was no acceptor or Cit-SNAP25 in this system, the intensity in the FRET channel (Channel 2) was considered as the bleed over. Quantitatively, the bleed over factor is defined as,

$$Bleed\ over\ factor = I_2/I_1 \quad (4)$$

where, I_2 = intensity of Channel 2 (FRET channel) in donor only (Cer-VAMP2) system.

I_1= intensity of Channel 1 (Cerulean channel) in donor only (Cer-VAMP2) system.

Step 2: FRET channel intensity correction using dual transfection or Cer-VAMP2 and Cit-SNAP25 or FRET systems. In the dual transfection systems, Corrected FRET after removing the bleed over is calculated as follows. Intensity in Channel 1 (I_3) and FRET Channel or Channel 2 (I_4) is measured. Corrected FRET is then calculated as,

$$Corrected\ FRET = I_4 - \left(\frac{I_2}{I_1} * I_3\right) \qquad (5)$$

where, I_4 = intensity of Channel 2 (FRET channel) in double transfected FRET control system

I_3 = intensity of Channel 1 (Cerulean channel) in double transfected FRET control system.

Thus, corrected FRET image was constructed by the software and its intensity I_5 was measured.

Step 3: Calculate the effective transfer ratio (ETR) in treated and untreated FRET systems. As the magnitude of FRET is inherently dependent on the original intensity in Channel 1 (Cerulean channel), the ETR was calculated as,

$$ETR = \frac{I_5}{I_3} \qquad (6)$$

The final ETR image was software-constructed and color-coded as shown. Finally, the intensity I_6 of the constructed ETR image was measured and plotted as mean intensity.

Schematically, these steps are explained by the following pictographic:

Steps to calculate effective FRET transfer

1. Estimate cerulean channel bleed over in FRET channel using Cer-VAMP2 only (negative control) system

N2A cells transected with Cerulean-VAMP2
Excite: Cerulean
Capture:

Channel 1:
Cerulean intensity

$$Channel_1\ Intensity = I_1$$

Channel 2:
FRET or citrine intensity

$$Channel_2\ Intensity = I_2$$

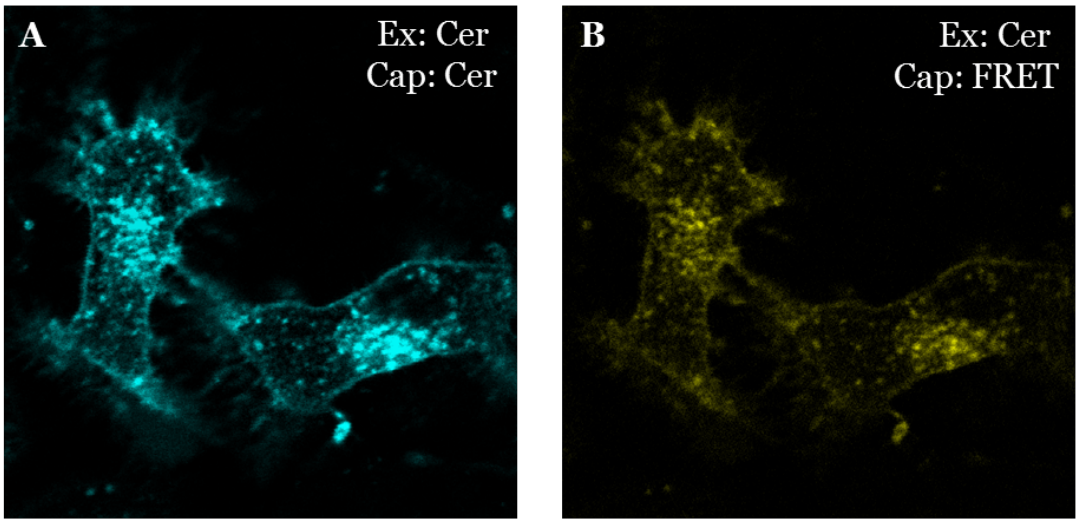

$$Bleed\ over\ factor = \frac{I_2}{I_1}$$

N2A cells transfected with Cerulean-VAMP2 (donor only or negative control) is used to calculate the bleed over. Cerulean is excited and subsequently intensity is captured in two channels: (1) Cerulean channel or channel 1 (I_1) and (2) FRET or citrine channel or channel 2 (I_2). As citrine is not excited directly, the captured intensity is FRET due to the energy transfer from cerulean (donor). Moreover, as there is no citrine or acceptor in the system, there is no FRET, and what is captured in channel 2 is nothing but bleed over from channel 1. Finally, bleed over factor is calculated as per the equation. The average bleed over factor used in calculation is an average from three different studies.

2. Estimate corrected FRET using dual transfected (Cerulean-VAMP2 and Citrine-SNAP25) or FRET systems

N2A cells transected with Cerulean-VAMP2 and Citrine-SNAP25
Excite: Cerulean
Capture:

Channel 1:
Cerulean intensity

$$Channel_1\ Intensity = I_3$$

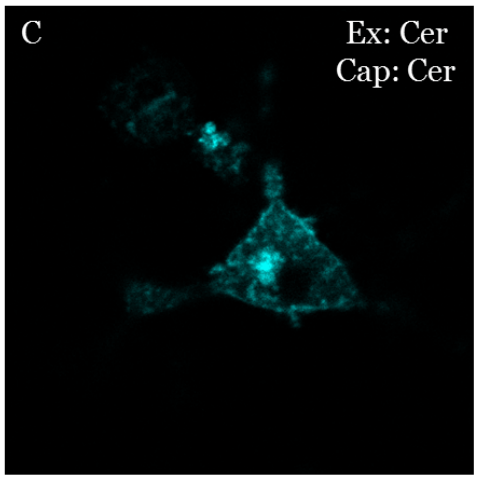

Channel 2:
FRET or citrine intensity

$$Channel_2\ Intensity = I_4$$

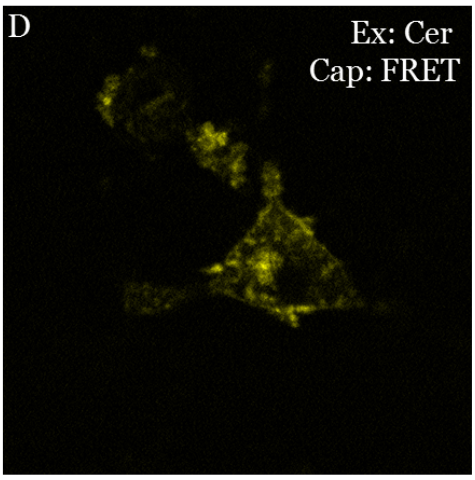

$$Corrected\ FRET = I_4 - (\frac{I_2}{I_1} * I_3)$$

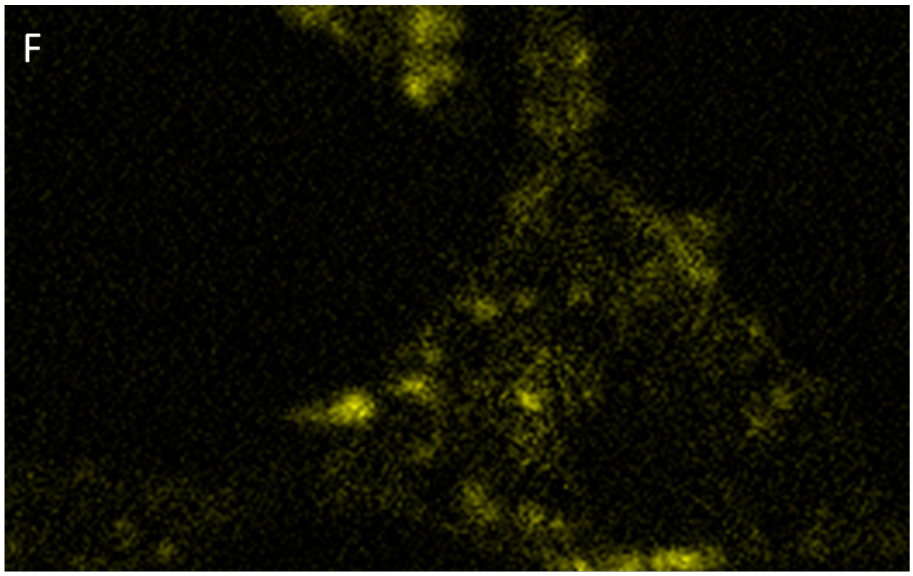

$$\boldsymbol{Corrected\ FRET\ Intensity = I_5}$$

FRET correction is done for all dual transfected N2A cells (Cer-VAMP2 and Cit-SNAP25 systems). As an example, we discuss the FRET only or positive control system. Cerulean is excited and subsequently intensity is captured in two channels: (1) Cerulean channel or channel 1 (I_3) and (2) FRET or citrine channel or channel 2 (I_4). As citrine is not excited directly, the captured intensity is FRET due to the energy transfer from cerulean (donor), and the bleed over. This cerulean channel bleed over is removed using the factor calculated in step 1, as per the equation. Finally, the corrected FRET intensity image (F) is constructed by the software (after removing the bleed over). This corrected intensity is denoted as I_5.

3. Construct and estimate effective FRET transfer ratio image from corrected FRET image

Image analysis:
Normalizing corrected FRET to donor intensity

Corrected FRET image (F) / Cerulean channel image (C)

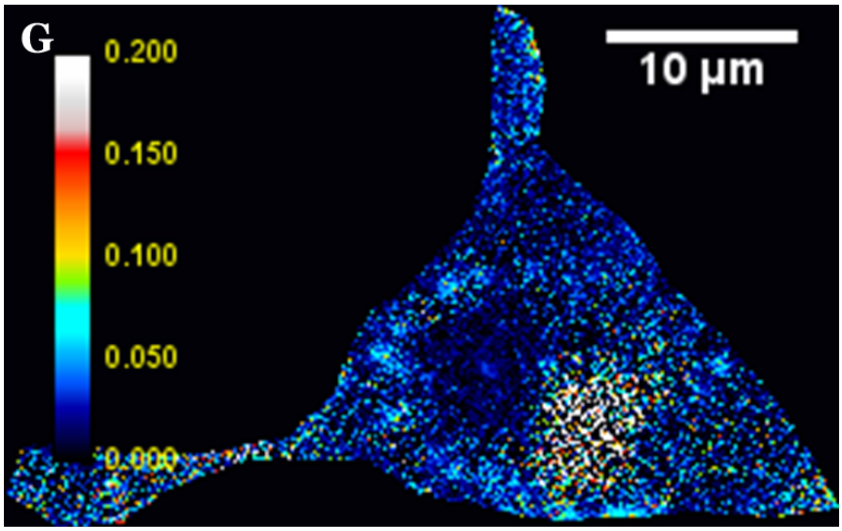

$$Effective\ FRET\ Transfer\ Ratio\ (I_6) = \frac{I_5}{I_3}$$

In continuation from Step 2, effective FRET transfer is estimated for all corrected-FRET images. Here, we continue with the FRET only or positive control system as an example. As the FRET transfer is also dependent on the original intensity of the amount of donor in the system, the corrected FRET determined is normalized to the donor intensity. As it is a ratio, this parameter is called as the Effective FRET Transfer Ratio I_6 as per the equation described above. This is the effective FRET transfer independent of donor intensity. The image is color coded from max FRET transfer (0.200) to least FRET transfer (0.000). However, this should be interpreted carefully as it could be deceptive in regions with no-low donor intensiies. Finally. the intensity of this image at the membrane is measured and reported using the mask tool in Fiji.

5.3.3. TCSPC-FLIM acquisition and analysis

Time-correlated single-photon counting (TCSPC) measurements were made under 800-820 nm two photon excitation (TPE), which efficiently excited cerulean, without any detectable direct excitation or emission from citrine. We used a time domain system that pulsed lasers at 405 nm with a Hybrid GaAsP cathode detector with emission filter setups of 480/30nm band pass for CFP emission.

Off-line FLIM data analysis was performed using SPCImage software (Becker & Hickl). The fluorescence was assumed to be a multiexponential (monoexponential decay for Cer-VAMP2 only systems and biexponential for dual transfected FRET systems). In addition, binning and threshold was kept constant at 3 and 5 respectively. The ROI was adjusted to limit the analysis of the functional interactions occurring at the membrane from the intensity window and subsequent color-coded spatial lifetime image (distribution of life time in space) and frequency histogram was obtained after calculating the decay matrix. The mean lifetime in the ROI at the membrane, τ_m was estimated from the software (± SD). Also, as vesicle fusion reactions do not happen at all places on the membrane, n=30 distinct fusion processes (pixels) on the membrane were compared in a total of five independent cells (n=5) (image acquisitions) and precise $\tau_m$at that pixel was measured. The fusion processes were selected using the FM dye exocytosis as the reference. Finally, the median lifetimes of control (Cer-VAMP2 and FRET) and treatments were compared in the scatter plot. Every point of interest was selected from the intensity (and not lifetime) window to avoid bias. Further, mean photon counts of 10^2-10^3 and χ^2 values less than 2.5 was maintained as a selection criteria for every fusion process (point of interest). Model was confirmed to fit the data well by checking for the

random distribution of weighted residuals around zero. Finally, the FRET efficiency is calculated as:

$$E = 1 - \frac{\tau_{m_{FRET}}}{\tau_{m_{donor}}} \quad (7)$$

Where, E = FRET efficiency, $\tau_{m_{FRET}}$ = mean lifetime of Cer-VAMP2 in a FRET system (N2A cells transfected with Cer-VAMP2 and Cit-SNAP25), and $\tau_{m_{donor}}$ = mean lifetime of Cer-VAMP2 in a donor only system (N2A cells transfected with Cer-VAMP2 only).

5.3.4. Fixed cell microscopy and cellular imaging

Normal (untransfected) or transfected N2A cells or primary cultured neurons were grown on cover slip bottom dishes and were treated with 3.1 μM of F-Aβ40, F-Aβ42 or F-Dutch Aβ40 for 60 min followed by 20 μg/mL of AF633-TRF for 30 min. In TeNT experiments, the cells were pretreated with TeNT for 60 min followed by F-Aβ treatment. Cells were then washed with PBS and nuclei were stained with Hoechst Dye (0.5 μg/mL in PBS) for 5 min. Lastly, the dishes were fixed in 4 % para-formaldehyde (PFA) at 4 °C for 60 min, mounted with ProLong® gold antifade reagent (Life technologies, OR) and dried overnight before imaging by laser confocal microscopy.

5.3.5. Permeability across the BBB endothelium

Polarized hCMEC/D3 cellular monolayer was incubated with ^{125}I-Aβ40 or ^{125}I-Aβ42 in tracer amounts on either luminal or on the abluminal side. Multiple samples were taken from the contralateral chamber (receiver compartment containing the blank medium) till 90 min to assess radioactivity transcytosed across the BBB endothelium.

Flux of ^{125}I-Aβ across the BBB endothelium was calculated as the slope of cumulative amount of ^{125}I-Aβ accumulating in the receiver chamber versus time. The apparent permeability coefficients were calculated by normalizing the flux with the initial concentration of ^{125}I-Aβ protein added to the donor chamber and the surface area of the Transwell® filter used. This permeability coefficient, expressed as cm/min was compared in L-A and A-L directions. In the TeNT treatments, the monolayers were pretreated with TeNT for 60 min prior to adding ^{125}I-Aβ.

5.4. RESULTS

5.4.1. Aβ decreases the effective FRET transfer between Cer-VAMP2 and Cit-SNAP25 in differentiated N2A cells (Figure 5.3)

Representative images from the confocal microscopy demonstrate decrease in functional FRET interactions between Cer-VAMP2 and Cit-SNAP25 in N2A cells pretreated with Aβ40 **(Figure 5.3.1-3.2 C),** Aβ42 **(Figure 5.3.1-3.2 D)** for 24 h, and TeNT **(Figure 5.3.1-3.2 E)** for 1 h in comparison to the FRET control system **(Figure 5.3.1-3.2 B)**. The measured FRET intensity (yellow) in control cells after bleed-over correction **(Figure 5.3.1 B)** is greater than that of the negative control- Cer-VAMP2 only system **(Figure 5.3.1 A),** and when cells are pretreated with Aβ40 **(Figure 5.3.1 C),** Aβ42 **(Figure 5.3.1 D)** and TeNT **(Figure 5.3.1 E).** This is more evident in the software constructed effective transfer ratio images, where the membranes in dual transfected cells pretreated with Aβ40 **(Figure 5.3.2 C),** Aβ42 **(Figure 5.3.2 D)** and TeNT **(Figure 5.3.1 E)** are mostly blue, which represents low effective FRET or ETR, and closer to the donor Cer-VAMP2 system **(Figure 5.3.2 A),** than that of dual transfected control cells **(Figure 5.3.2 B)**. Further, this decrease is demonstrated semi-quantitatively **(Figure 5.3.3)** by comparing the mean values of the membrane intensity or effective FRET transfer in images from Figure 5.3.2.

Further, the cerulean and the uncorrected FRET channel are presented in **Supplementary figure S-5.1** without LUT adjustment**.** Moreover, the red fluorescence intensity due to FM dye exocytosis **(Supplementary figure S-5.2)** confirms the presence of active exocytosis within these cells. Also, images from Phase 3: independent cerulean and citrine channel, validate the transfection of Cer-VAMP2 and Cit-SNAP25

(Supplementary figure S-5.2) in all the treated system; confirm that decrease in FRET is not due to poor transfection but due to the interference with the FRET interaction. The same trend is also seen when exocytosis is stimulated at high potassium condition **(Supplementary figure S-5.3)**

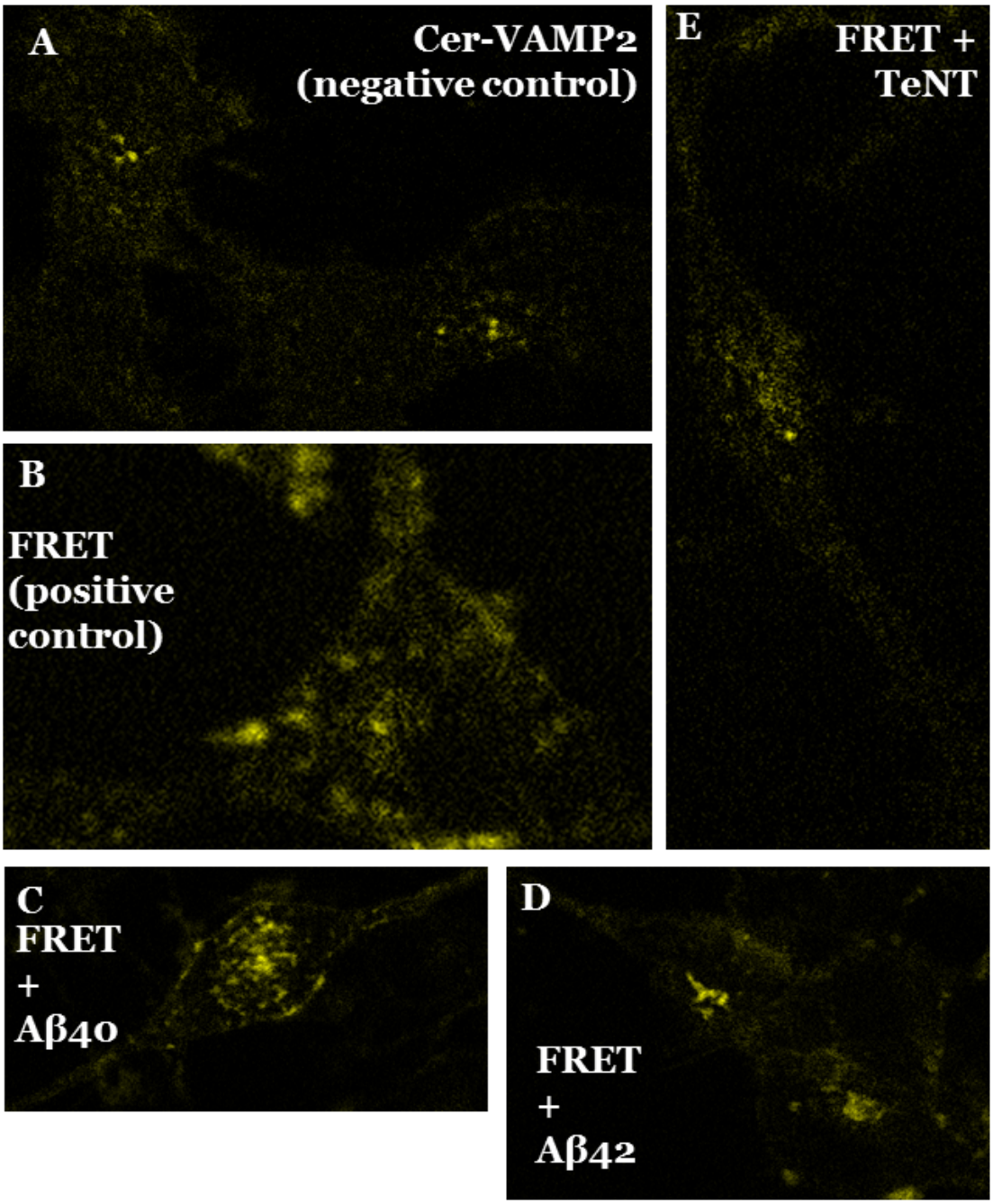

Figure 5.3.1 Representative corrected intensity images capturing FRET in transfected N2A cells A-E Images obtained by exciting cerulean and capturing citrine (FRET) in cells transfected with either **(A)** Cer-VAMP2 only or **(B-E)** Cer-VAMP2 and Cit-SNAP25. Demonstrated FRET intensity is corrected for cerulean channel bleed over by software. **A-B** Considerable FRET is seen at the membrane in **(B)** dual transfected cells or FRET (positive control), in comparison to **(A)** negative control cerulean-only transfected cell. **C-E** FRET intensity images in dual transfected cells pretreated with **(C)** Aβ40; **(D)** Aβ42; and **(E)** TeNT.

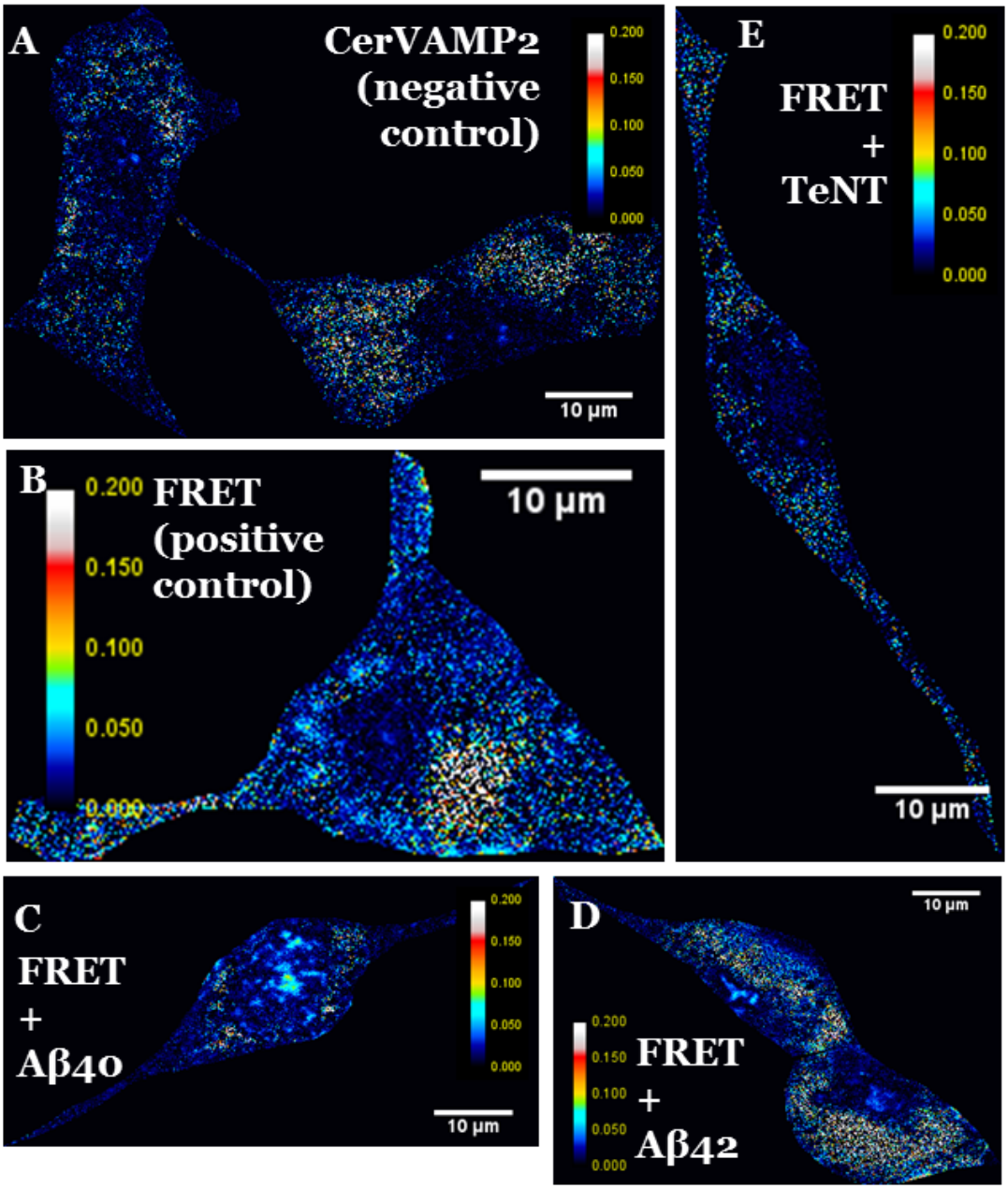

Figure 5.3.2 Representative effective FRET transfer ratio images in transfected N2A cells A-E Software constructed images of corrected FRET (Fig 5.3.1) normalized to the donor intensity (Cerulean channel, Supplementary S-5.1) in cells transfected with either **(A)** Cer-VAMP2 only or **(B-E)** Cer-VAMP2 and Cit-SNAP25. Images demonstrate the effective FRET transfer per donor intensity; color coded from dark blue (least FRET transfer per donor intensity) to white (maximum FRET transfer per donor intensity). **A-B** At the plasma membrane, considerable effective FRET transfer per donor intensity is seen in **(B)** dual transfected cells [FRET (positive control)], in comparison to **(A)** negative control (cerulean-only transfected cell). **C-E** Effective FRET transfer ratio images in dual transfected cells pretreated with **(C)** Aβ40; **(D)** Aβ42; and **(E)** TeNT.

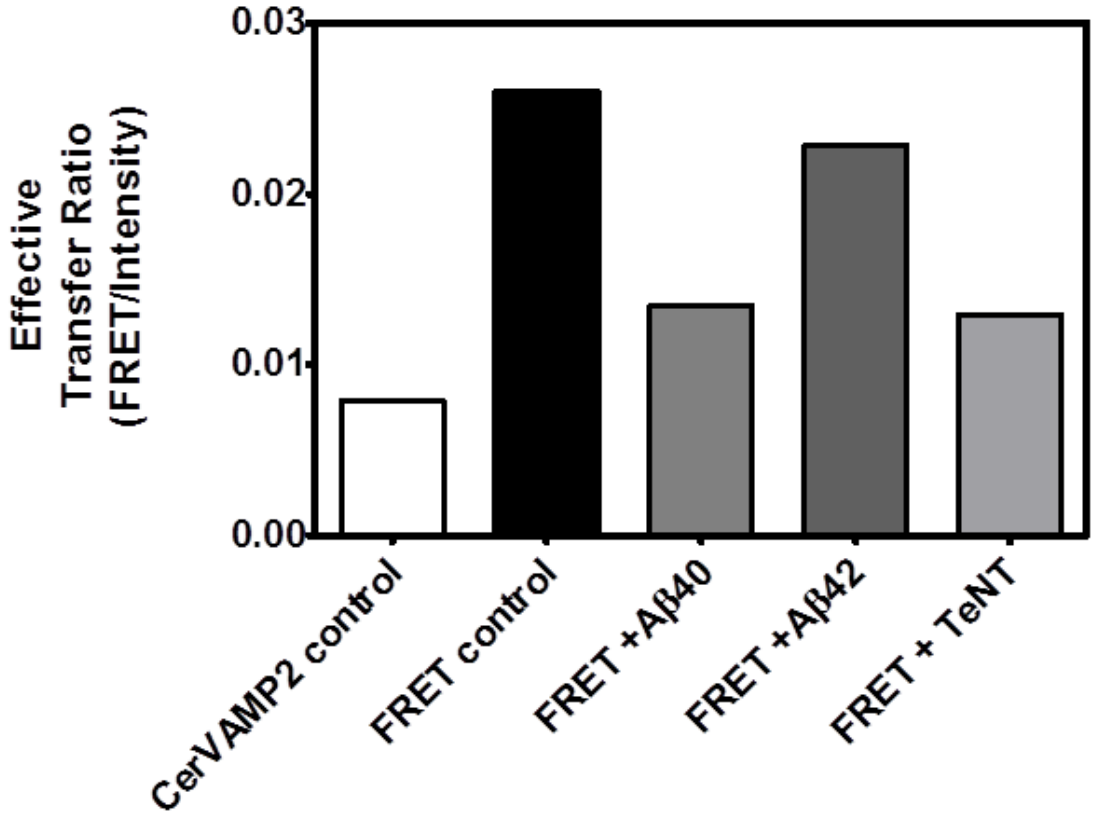

Figure 5.3.3 Quantitative plot of effective FRET transfer ratios of membrane intensities represented in Figure 5.3.2 Data demonstrates effective FRET transfer ratio or corrected FRET normalized to the donor (cerulean channel) intensity measured only at membrane using mask tool in Fiji software. Bars represent mean effective transfer ratio (ETR) intensity at the membrane.

5.4.2. Aβ isoforms increase donor lifetime and decrease functional FRET efficiency between Cer-VAMP2 and Cit-SNAP25 in differentiated N2A cells (Figure 5.4)

Spatial lifetime images and spectral frequency histograms demonstrate an increase in donor lifetime and a decrease in the FRET efficiency between Cer-VAMP2 and Cit-SNAP25 in N2A cells pretreated with Aβ40 **(Figure 5.4.1 C),** Aβ42 **(Figure 5.4.1 D)** for 24 h, or with TeNT **(Figure 5.4.1 E)** for 1 h, compared to the FRET controls **(Figure 5.4.1 B).** Lifetime increased with rightwards shift into blue range in cells treated with Aβ40, as observed in spatial image and frequency histogram **(Figure 5.4.1 C)**. Similar effects were also observed with treatments with Aβ42 **(Figure 5.4.1 D),** and TeNT **(Figure 5.4.1 E)**. The goodness of multi-exponential model fit is verified by the random distribution of residuals **(Supplementary figure S.5.4)**. Significant increase in the τ_m of FRET system (~2000 ps), pretreated with Aβ40 (~2600 ps), Aβ42 (~2600 ps) and TeNT (~2400 ps) showed the decrease in the corresponding FRET and the FRET efficiency from ~ 20% to 2-10%. This is demonstrated in the cumulative table of software projected τ_m values, and their ranges **(Table 5.2, Figure 5.4)**, as well as τ_m lifetime and FRET efficiency measurements from the actual 30 vesicular fusion events **(Figure 5.4.2).** As can be seen, the increase in τ_m lifetime and the decrease in FRET efficiency is irrespective of mono-exponential **(Figure 5.4.2)** or bi-exponential model fit **(Supplementary figure 5.4.6)** The same trend is also seen when exocytosis is stimulated by exposing N2A cells to high potassium condition **(Supplementary figure S-5.5).**

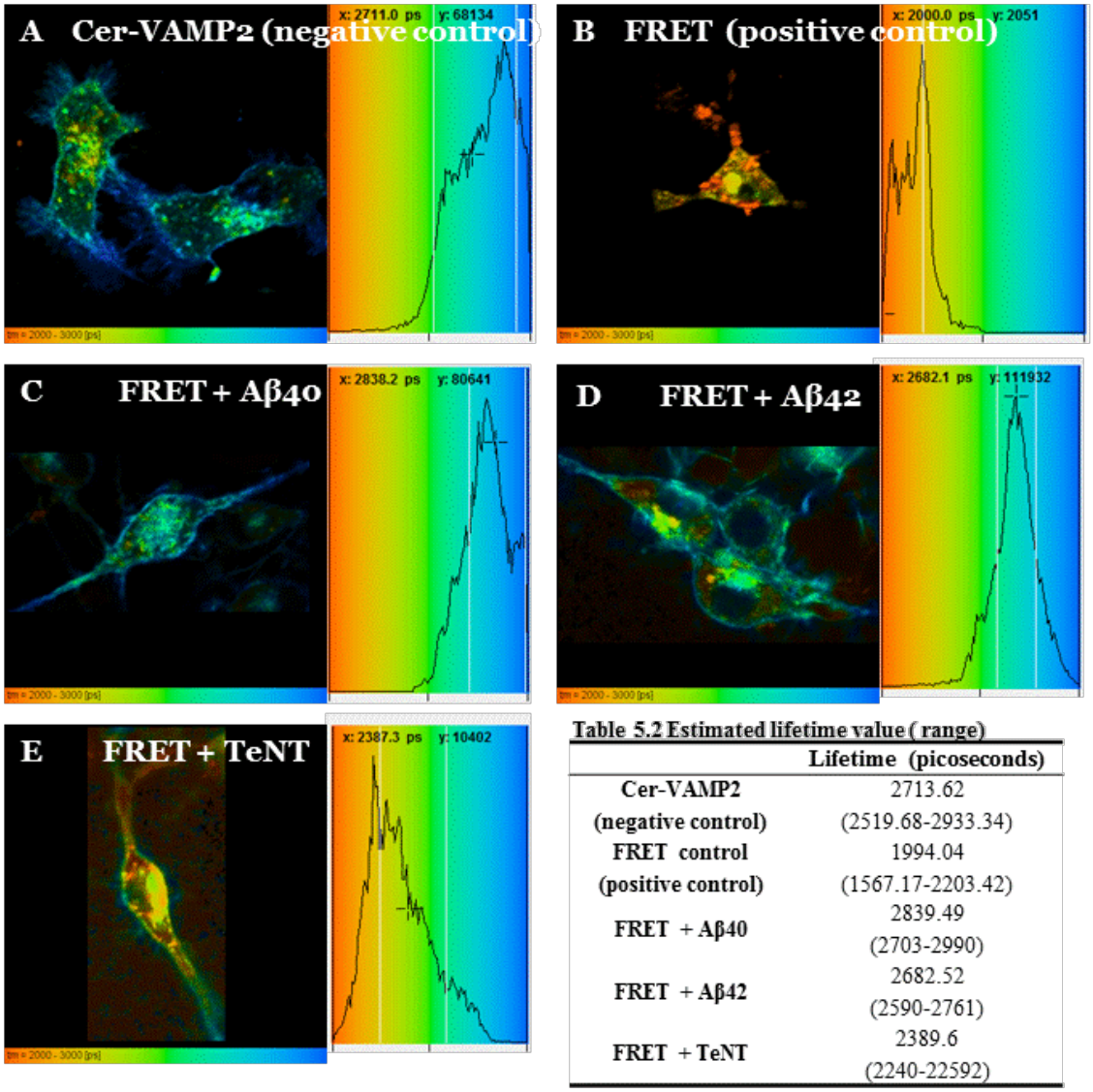

Table 5.2 Estimated lifetime value (range)

	Lifetime (picoseconds)
Cer-VAMP2 (negative control)	2713.62 (2519.68-2933.34)
FRET control (positive control)	1994.04 (1567.17-2203.42)
FRET + Aβ40	2839.49 (2703-2990)
FRET + Aβ42	2682.52 (2590-2761)
FRET + TeNT	2389.6 (2240-22592)

Figure 5.4.1 Spatial lifetime images of donor (cerulean) lifetime and corresponding frequency histograms in transfected N2A cells. A-E Spatial lifetime images and frequency histograms obtained by measuring lifetime of cerulean (donor) by Time Correlated Single Photon Counting (TSCPC) in cells transfected with either **(A)** Cer-VAMP2 only or **(B-E)** Cer-VAMP2 and Cit-SNAP25. Histogram represents lifetime frequency at the plasma membrane. **A-B** Lifetime decreases from the blue range in **(A)** negative control cerulean-only transfected cell to yellow range in **(B)** dual transfected cells or FRET (positive control).**C-E** In the presence of **(C)** Aβ40; **(D)** Aβ42; and **(E)** TeNT; donor lifetime increases back from yellow to blue range . Color code represents lifetime from 2000 (red) to 2700 (blue) picoseconds. **Table 5-2** shows changes in donor (cerulean) lifetime as estimated by B&H software for the membrane ROI in picoseconds (range)

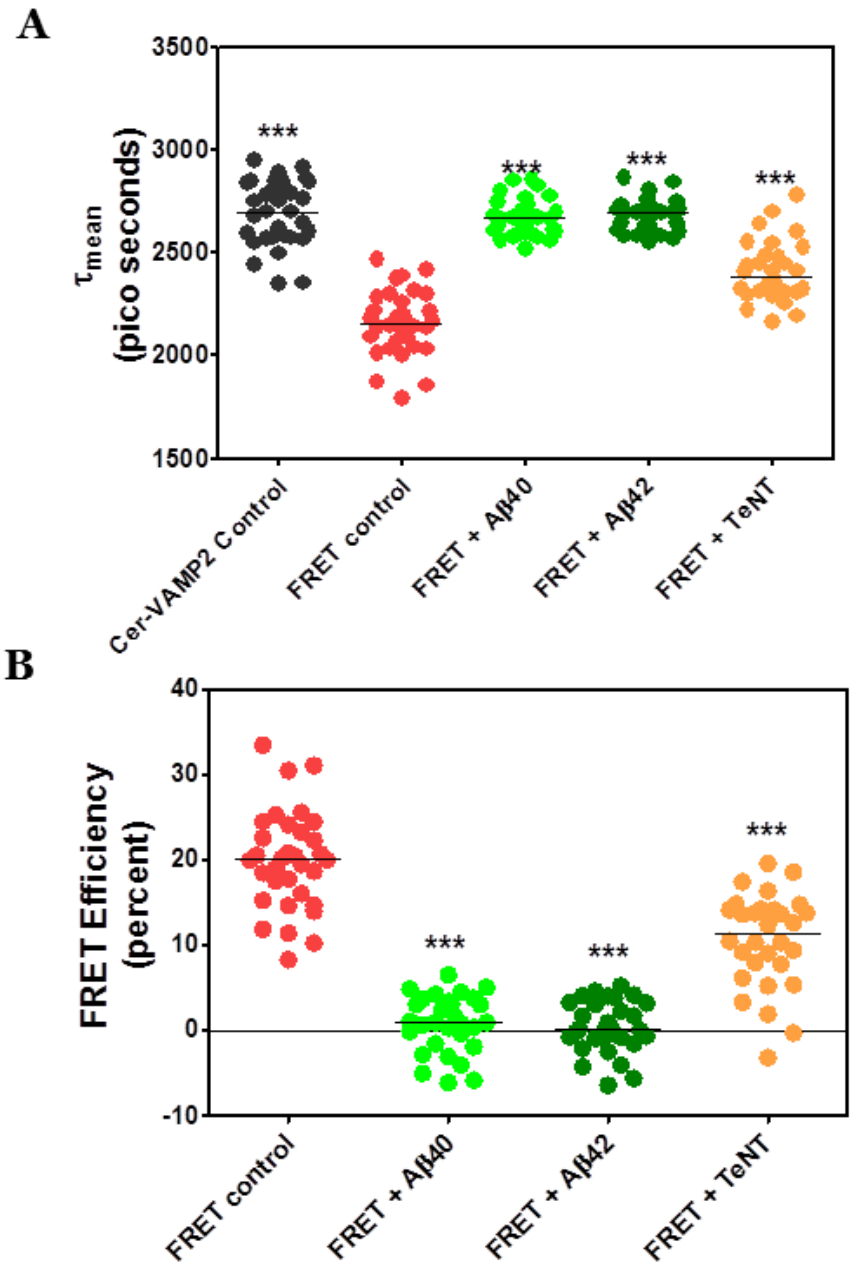

Figure 5.4.2 Lifetime measurements and corresponding FRET efficiency of functional vesicular fusion events in N2A cells. Changes in **(A)** τ_{mean} or mean lifetime of donor (cerulean) and **(B)** FRET efficiency in cells transfected with cer-VAMP2 only (Cer-VAMP2 control) or both Cer-VAMP2 and Cit-SNAP25 (FRET) that are pretreated with Aβ40, Aβ42 or TeNT. Over 30-40 functional vesicular fusion processes at the plasma membrane are estimated using FM dye image as the reference. Data represented as scatter dot plot of individual measurements as well as the median. Significance determined using One-Way ANOVA followed by Dunnett's Post Test (*** $p<0.001$).

5.4.3. Aβ isoforms increase donor lifetime and decrease FRET between Cer-VAMP2 and Cit-SNAP25 in polarized hCMEC/D3 cells (Figure 5.5)

Similar to N2A cells, spatial lifetime images and spectral frequency histograms demonstrate an increase in donor lifetime and a decrease in the FRET efficiency between Cer-VAMP2 and Cit-SNAP25 in hCMEC/D3 cells pretreated with Aβ40 **(Figure 5.5.1 C),** Aβ42 **(Figure 5.5.1 D)** for 24 h, or with TeNT **(Figure 5.5.1 E)** for 1 h, compared to the FRET controls **(Figure 5.5.1 B).** Lifetime increased with rightwards shift into blue range in cells treated with Aβ40, as observed in spatial image and frequency histogram **(Figure 5.5.1 C)**. Similar effects were also observed with treatments with Aβ42 **(Figure 5.5.1 D),** and TeNT **(Figure 5.5.1 E)**. The goodness of multi-exponential model fit is verified by the random distribution of residuals **(Supplementary figure S-5.6)**. This increase in lifetime and corresponding decrease in FRET is demonstrated in the cumulative table of software projected τ_m values, and its range **(Table 5-3, Figure 5.5)**.

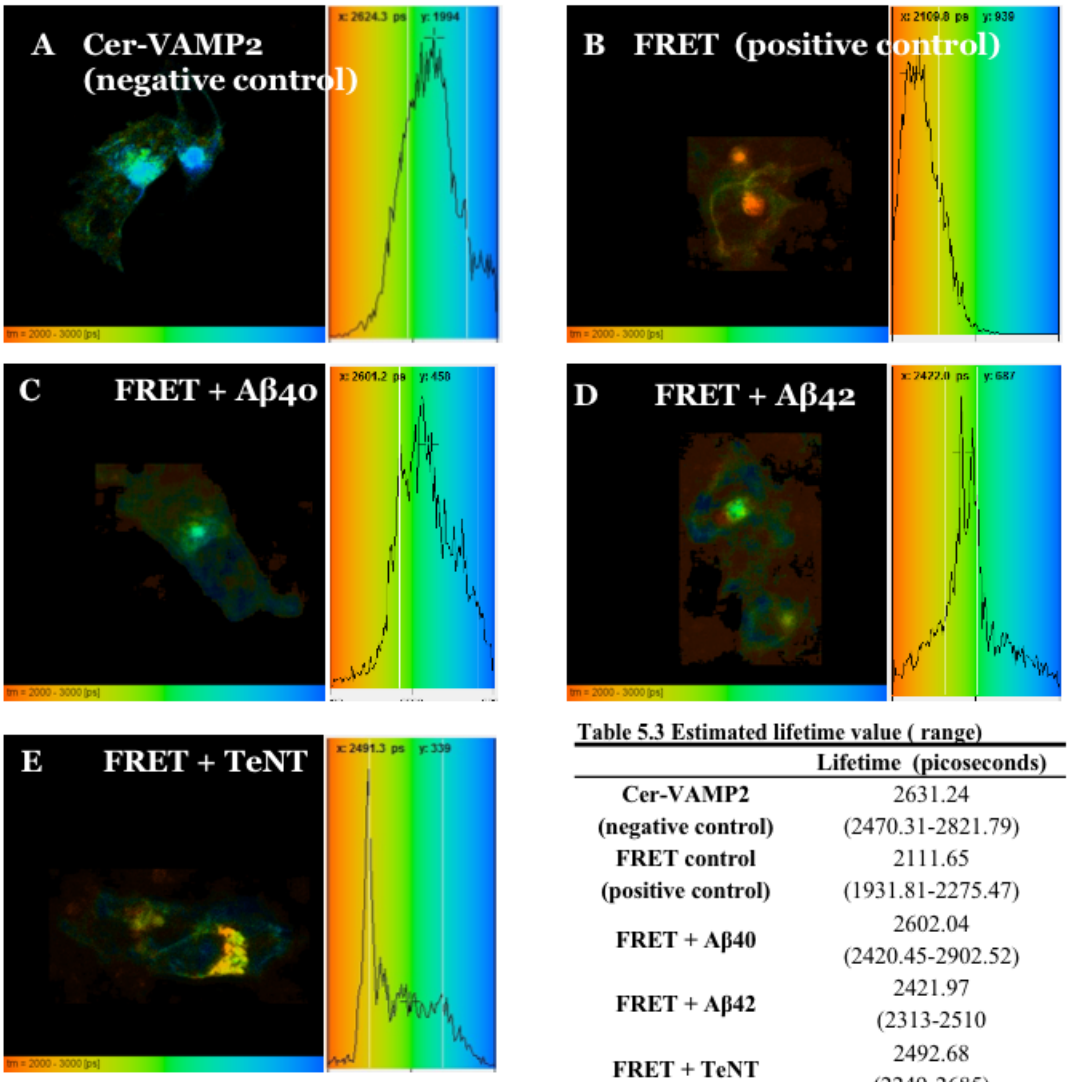

Table 5.3 Estimated lifetime value (range)

	Lifetime (picoseconds)
Cer-VAMP2 (negative control)	2631.24 (2470.31-2821.79)
FRET control (positive control)	2111.65 (1931.81-2275.47)
FRET + Aβ40	2602.04 (2420.45-2902.52)
FRET + Aβ42	2421.97 (2313-2510
FRET + TeNT	2492.68 (2249-2685)

Figure 5.5 Spatial lifetime images of donor (cerulean) lifetime and corresponding frequency histograms in transfected hCMEC/D3 Cells. A-E Spatial lifetime images and frequency histograms obtained by measuring lifetime of cerulean (donor) by TCSPC in cells transfected with either **(A)** Cer-VAMP2 only or **(B-E)** Cer-VAMP2 and cit-SNAP25. Histogram represents lifetime frequency at the plasma membrane surface. **A-B** Lifetime decreases from the blue (low donor life time) in **(A)** negative control cerulean-only transfected cell to yellow (higher donor life time) in **(B)** dual transfected cells or FRET (positive control). **C-E** In the presence of **(C)** Aβ40; **(D)** Aβ42; and **(E)** TeNT; donor lifetime increases from yellow to blue range. Color code represents lifetime from 2000 (red) to 2700 (blue) picoseconds. **Table 5.3.** shows changes in donor (cerulean) lifetime as estimated by B&H software for the membrane ROI.

5.4.4. Aβ isoforms directly inhibit endogenous VAMP2 in differentiated N2A Cells (Figure 5.6)

Western-blots demonstrated a time dependent decrease of VAMP2 in differentiated N2A cells after treatment with Aβ40, Aβ42 and mutant DutchAβ40. Quantitative estimation with the loading control (GAPDH) demonstrated a 50 % decrease in VAMP2 expression by 24 h.

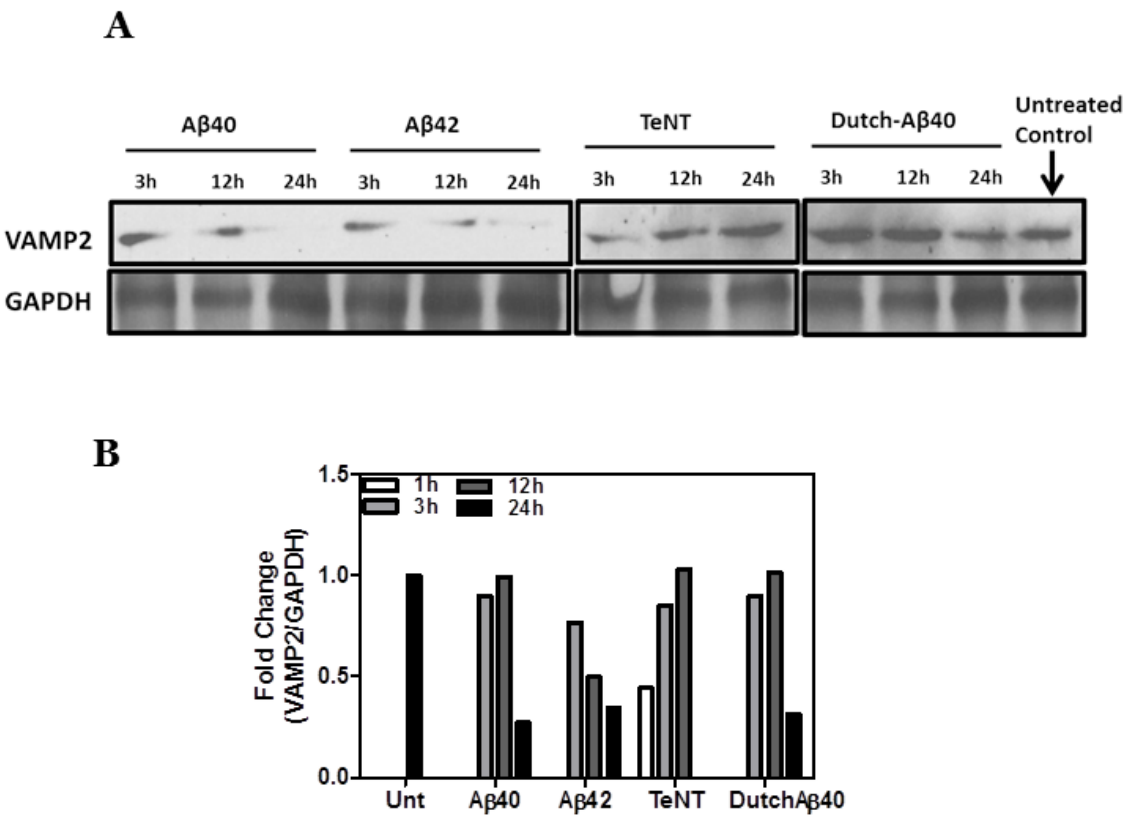

Figure 5.6 Western blots of endogenous VAMP-2 expression in treated N2A cells. A-B. Aβ isoforms (Aβ40 and Aβ42) and mutant Dutch-Aβ40 cleave endogenous VAMP-2 in a time dependent manner. TeNT is used as a control to cleave VAMP-2 at shorter time points. The quantification of **(A)** VAMP-2 band intensity and endogenous loading control GAPDH is represented as **(B)** fold changes in various treatments.

5.4.5. Aβ isoforms colocalize with VAMP2 in differentiated N2A Cells (Figure 5.7)

Representative images of fixed N2A cells that were transfected with Cer-VAMP2 and treated with F-Aβ (green) demonstrated colocalizion of Cer-VAMP2 (red) with F-Aβ40 **(Figure 5.7 (a))** and F-Aβ42 **(Figure 5.7 (b))**. Moreover, this colocalization increases, which appears as more yellow puncta, when the cells are pretreated with TeNT, in case of F-Aβ40 **(Figure 5.7 (c))** as well as F-Aβ42 **(Fig 5.7 (d)).**

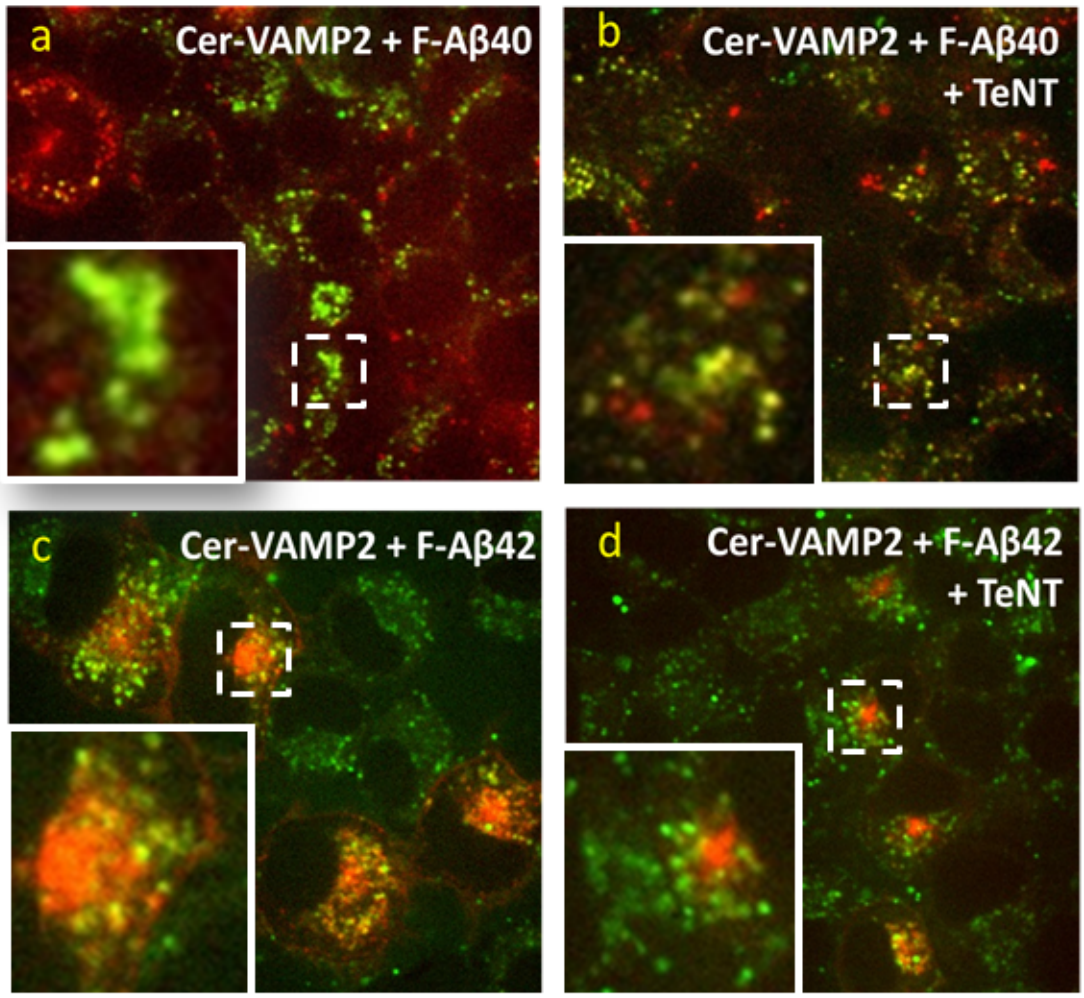

Figure 5.7 Colocalization of Cer-VAMP2 and Aβ isoforms in N2A cells. A-B. Increase in the co-localization (denoted by the yellow color**)** of F-Aβ40 (green), with Cer-VAMP2 (red) when cells are pretreated with **(B)** tetanus toxin (TeNT) in comparison to **(A)** control cells. **C-D.** Increase in the co-localization of F-Aβ42 (green), with Cer-VAMP2 (red) when cells are pretreated with **(D)** tetanus toxin (TeNT) in comparison to **(C)** control. The box area is zoomed in the inset.

5.4.6. TeNT pretreatment increases the accumulation of Aβ proteins in primary neurons (Figure 5.8).

Representative images of primary neurons pretreated with TeNT followed by F-Aβ (green) and AF633-TRF (red). The accumulation of F-Aβ40 and AF633-TRF increased after pretreatment with TeNT **(Figure 5.8 (b))** in comparison to the control **(Figure 5.8 (a)).** Also, the uptake of F-DutchAβ40, a vasculotropic mutant form of Aβ40, and AF633-TRF increased after pretreatment with TeNT **(Figure 5.8 (d))** in comparison to the control **(Figure 5.8 (c)).**

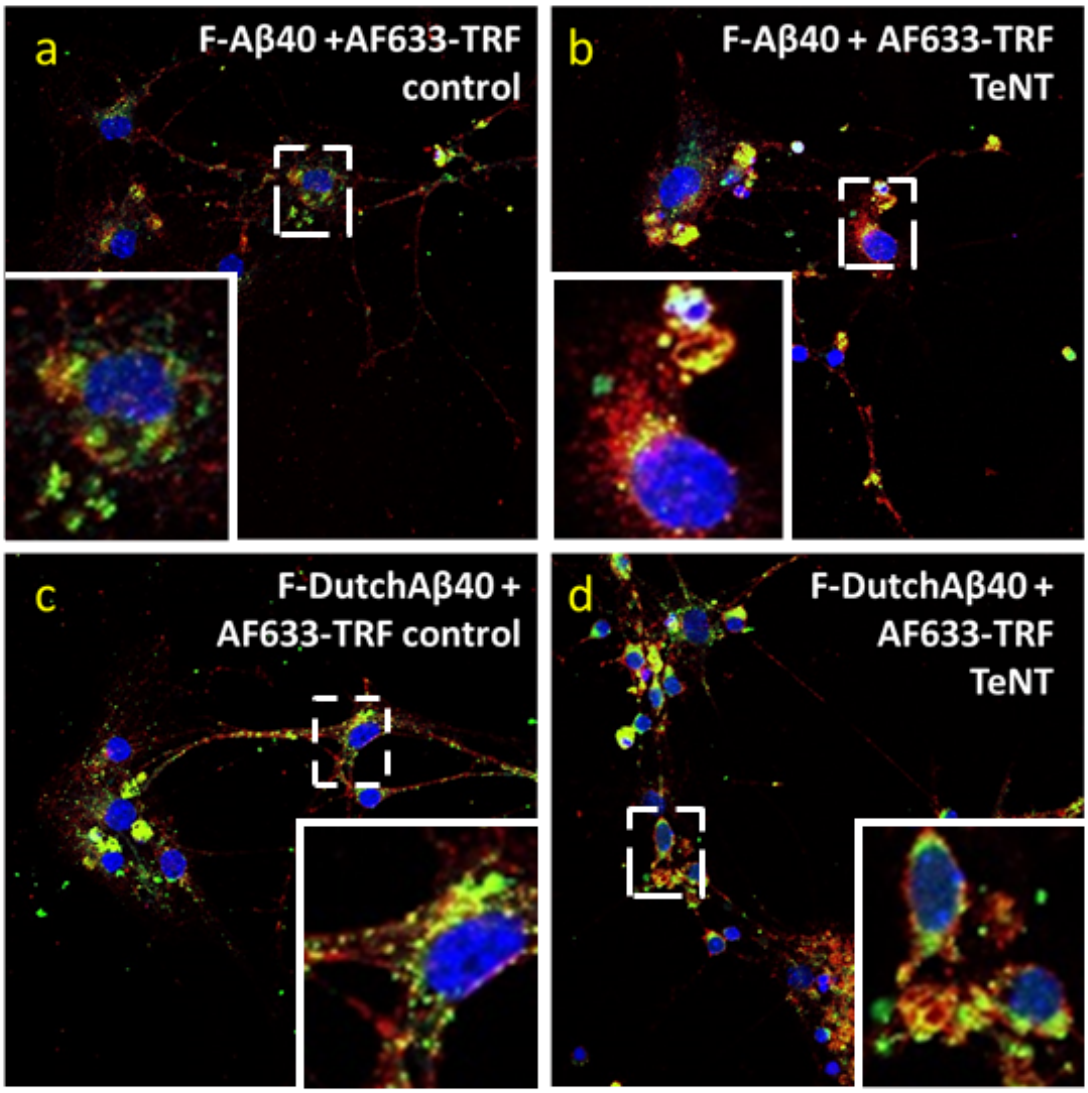

Figure 5.8 Representative images of primary neuronal cultures treated with Aβ proteins following VAMP-2 disruption by TeNT. A-B. Accumulation of F-Aβ40 (green) and AF633-TRF (red) increases when cells are pretreated with **(B)** TeNT in comparison to **(A)** control cells. **C-D** Accumulation of a mutant form, F-DutchAβ40 (green), and AF633-TRF (red) increases when cells are pretreated with **(D)** TeNT in comparison to **(C)** control cells The box area is zoomed in the inlet.

5.4.7. TeNT pretreatment reduces the luminal to abluminal (L-A) permeability of Aβ proteins across BBB endothelium (Figure 5.9)

The permeability of ^{125}I-Aβ across the polarized monolayer of hCMEC/D3 cells grown on Transwell® filters, decreased significantly if the cells were pretreated with TeNT in the luminal to abluminal (L-A direction). No change was seen in the abluminal to luminal (A-L) direction.

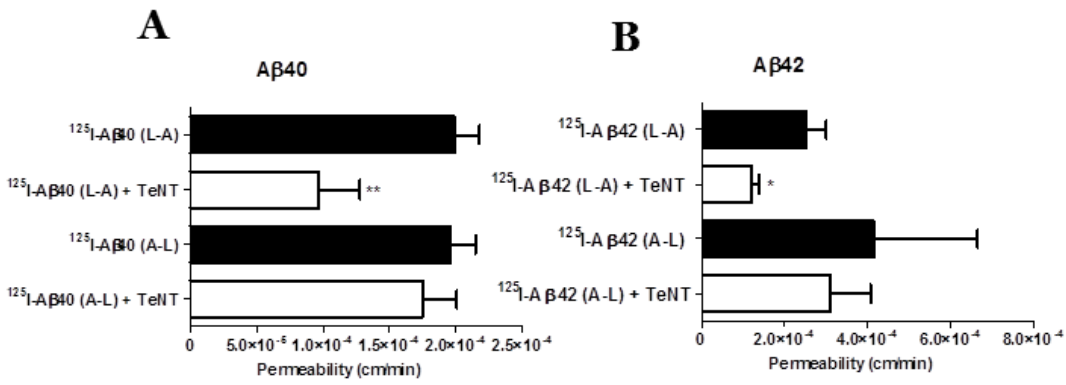

Figure 5.9 Permeability of Aβ isoforms across the polarized hCMEC/D3 cell monolayers after inhibiting VAMP-2 by TeNT. The hCMEC/D3 cells grown on Transwell® filter were treated with ^{125}I-Aβ proteins on either luminal or abluminal side. Permeability is measured as described in either luminal to abluminal (L-A) or abluminal to luminal (A-L) direction. **A-B** Impairing VAMP-2 by TeNT decreases the permeability of **(A)** Aβ40 and **(B)** Aβ42 only from L-A direction. Significance is determined by Student's t-test (*$p<0.05$)

5.5. DISCUSSION

Cognitive decline in AD patients has been linked to the synaptic dysfunction in hippocampus and cortex (Huang and Mucke, 2012; Sheng et al., 2012), two brain regions that are known to be affected in AD. Bioinformatics analysis from our lab that compared gene expression of 161 AD patient brains with age matched non-demented individuals demonstrated downregulation of SNARE assembly and VAMP-2. (Supplementary figure S-5.8). The clinical manifestations of these deficits are temporarily alleviated by acetylcholine esterase inhibitors. However, this indirect way of stimulating the neuronal synapses is just a symptomatic relief, and does not intervene with the disease progression.

Involvement of toxic Aβ proteins in AD pathogenesis has been reasonably well established. Previous publications from our lab have shown that Aβ protein is transported in 'vesicles' across the BBB endothelium, and the vesicular transcytosis is most likely disrupted in AD (Agyare et al., 2013). Obviously, this constitutive vesicular transcytotic process, which includes endocytosis, cellular transit and exocytosis is not unique for Aβ, but could also affect the trafficking of other biomolecules.

It has been shown that that the molecular mediators in SNARE exocytosis overlap between neurons and epithelial cells (Coco et al., 1999; Hong, 2005; Proux-Gillardeaux et al., 2005; Steegmaier et al., 2000), the same could be true between neurons and BBB endothelial cells. . For example, VAMP-2 is involved in L-A transport and VAMP-7 and VAMP-8 are involved in A-L transport (Fields et al., 2007; Proux-Gillardeaux et al., 2005). Although, in epithelial cells, VAMP-2 was shown to interact with SNAP-23 instead of SNAP-25, the two are supposed to be quite similar in structure and function(Low et al., 1998; Russell J. Diefenbach et al., 2002)

Based on these evidences that suggest direct or indirect links between SNARE assembly and AD pathology, two questions have been addressed in the study outlined in this chapter. (1) what is the effect of Aβ on the fusion between VAMP-2 and SNAP-25 in neurons? (2) does Aβ employ similar apparatus (VAMP-2 and SNAP-25) to exocytose from neurons and BBB endothelial cells?

To address the first question, established FRET-pair constructs of Cer-VAMP2 and Cit-SNAP25 have been employed. The effect of Aβ isoforms on the FRET between Cer-VAMP2 and Cit-SNAP25 was investigated using: (1) simple *intensity* based confocal microscopy, and (2) fluorescence *lifetime* based microscopy (FLIM). These two sequential measurements on the same sample provided a powerful tool to not only detect the changes in FRET interactions qualitatively, but also quantitatively. Further, several controls such as: multichannel-simultaneous followed by multiphase-sequential measurements; bleed over correction in intensity measurements and binning; threshold correction; multicomponent analysis and model-fit validation in lifetime measurements were employed to avoid artifacts. Moreover, the studies were conducted in both hCMEC/D3 cells (BBB model), and in differentiated mouse neuroblastoma (N2A) cells that have been used earlier to study SNARE interactions. (Medine et al., 2007).

The FRET-FLIM studies outlined in this chapter have clearly indicated that Aβ could directly interfere with the fusion of VAMP-2 and SNAP-25. We demonstrated FRET interaction between Cer-VAMP2 and Cit-SNAP25, using both intensity and lifetime approaches, decreased in the presence of Aβ40 and Aβ40. The N2A cells, a neuronal cell line, was expected to demonstrate exocytosis process more profoundly than hCMEC/D3 cells, a BBB endothelium model, simply because of their developmental

biology and functioning at synapses. Therefore, the relatively lower intensities in hCMEC/D3 cells in comparison to N2A cells was not surprising. Further, as changes in lifetime are sensitive to the environment and not affected by the intensity of the fluorophore, only spectral lifetime measurements were employed in hCMEC/D3 cells to avoid artifact due to weaker intensity signals. Due to its established ability to cleave VAMP-2 (Chen et al., 2008), tetanus neurotoxin (TeNT) was used as a positive control in our experiments. Further, to make sure that only functional fusion events were considered for analysis, only the FRET on the plasma membrane was evaluated, and the FM® 4-64 dye was used to specifically locate these exocytosis events. The same trend was seen with the exocytosis stimulated with high potassium. (Supplementary section, Figure S-5.5). Apart from the functional FRET interactions at the membrane, we also observed the substantial presence of orphan SNARE complexes (FRET interactions) in the cytosol, which were also reported by several other investigators (Degtyar et al., 2013; Gaffield and Betz, 2006). Although we did not employ syntaxin-1 (the third SNARE peptide in the helical complex) in our measurements as our goal was to investigate the final fusion step between VAMP-2 and SNAP-25, the syntaxin-1a normally expressed in the cell was assumed to participate in the formation of the SNARE complex. Our study could not resolve if change in the FRET intensity was due to Aβ binding to syntaxin (Yang et al., 2015), SNAP-25 (Honer et al., 2012), VAMP-2 (Choi et al., 2015) or synaptophysin (Russell et al., 2012). But, our data certainly shows that the final event of exocytosis where the SNARE complex formed among VAMP-2, SNAP-25 and the constitutive syntaxin is inhibited. This finding explains the lower number of functional SNARE complexes as observed in the AD brain (Sharma et al., 2012).

Next, to address the second question, we used fixed-cell confocal microscopy, western blot experiments and BBB permeability studies. Tetanus neurotoxin (TeNT) that cleaves VAMP-2 was employed as a positive control. The colocalization studies in N2A cells clearly demonstrated that Aβ isoforms colocalize with VAMP-2 and therefore are capable of perturbing VAMP-2 function. This might also suggest that Aβ utilizes VAMP-2 for its own exocytosis. Therefore, when VAMP-2 is made unavailable, by cleaving with TeNT, the Aβ colocalization with VAMP-2 increases. Further, as VAMP-2 was externally transfected in these experiments, rather than the substantial differences in the expression of VAMP-2, changes in its function was observed. To confirm this trend, we used a different model, primary neurons as well. As expected, a significant increase in the accumulation of Aβ40 and Dutch-Aβ40 (cerebrovascular mutant of Aβ40) was seen after TeNT treatment was used to inhibit VAMP-2 function. Further, our western blot study clearly demonstrated that Aβ was capable of cleaving VAMP-2 in a time dependent manner. This difference was not very apparent in the cells that overexpress VAMP-2.

Finally, the permeability studies conducted using polarized hCMEC/D3 cell monolayer grown on Transwell® filters clearly demonstrated a decrease in Aβ permeability upon TeNT exposure; but only in the luminal to abluminal (L-A) direction. VAMP-2 has been known to be involved in just L-A transport, whereas VAMP-7 and VAMP-8 are involved in A-L transport. (Chen et al., 2001; Fields et al., 2007; Proux-Gillardeaux et al., 2005; Steegmaier et al., 2000). Moreover, TeNT specifically cleaves VAMP-2. It could be suggested from these results that, L-A transport of Aβ is most likely disrupted due to VAMP-2 perturbations in AD. This idea was further supported by a separate pharmacokinetic simulation model as well. Moreover, VAMP-2 and SNAP-25

have been recently shown to be involved in not just exocytosis but also clathrin dependent endocytosis (Zhang et al., 2013)- a process- that Aβ40 uses to get internalized by the BBB endothelium. Since, permeability quantifies the entire transcytosis process involving endocytosis, cellular transit, and exocytosis, our study would not be able to dissect the perturbations caused to VAMP-2 mediated exocytosis or endocytosis that decrease Aβ permeability. However, as in N2A cells, we saw an *increase* and not a decrease in Aβ accumulation; most likely it is the exocytosis of Aβ, that is mediated by VAMP-2.In neurons, VAMP-2 is essential for fast exocytosis of neurotransmitters release and rapid endocytosis (Deák et al., 2004). This idea that AD is a disease of vesicular transport system is not new (Suzuki, 2006), but instead of just impaired trafficking of APP (Groemer et al., 2011), that will indirectly affect the production of Aβ, there might be issues with the transcytosis of Aβ itself.

In summary, our work demonstrates that Aβ interferes with the vesicular fusion step between two SNARE proteins,VAMP-2 and SNAP-25, in neurons, and most likely at the BBB endothelium. Further, Aβ uses this apparatus for vesicular exocytosis in neurons and transcytosis at the BBB endothelium. This finding provides a mechanistic understanding towards impaired Aβ clearance, which involves transcytosis at the BBB endothelium, and disrupted synaptic transmission in AD. Furthermore, impairment in these processes may also explain the dysregulated trafficking of other biomolecules such as insulin and transferrin in an AD brain.

CHAPTER SIX

6. CONCLUDING REMARKS AND FUTURE DIRECTIONS

6.1. Concluding remarks

Unlike diseases where the therapeutic challenge is to make the drug available in right concentrations to the right location, AD field is still struggling with deciphering the basic pathogenesis of the disease, to be able to identify drug targets to eventually design effective therapies. Sporadic AD, which accounts for more than 90 % of AD cases, is believed primarily to be a disease of impaired clearance, where the BBB is one of the main portals of Aβ clearance from the brain. Further, the BBB endothelium is believed to maintain the dynamic equilibrium of plasma and brain Aβ levels, and also alter Aβ42:Aβ40 ratios in brain and plasma.

We have demonstrated that Aβ40 is internalized by clathrin-mediated endocytosis, whereas the endocytosis of Aβ42 is via lipid rafts. These differential uptake and trafficking mechanisms could allow the BBB endothelium to independently modulate Aβ42:Aβ40 ratios in the brain and plasma. Further, we delved into the under-investigated area of BBB dysfunction in the perspective of vesicular transcytosis that may impair the ability of BBB to handle Aβ proteins, or for that matter the trafficking of several other proteins. We elucidated the manner in which Aβ could impact these processes, and monitored the vesicular trafficking apparatus (involved with endocytosis, cellular transit and exocytosis) potentially harnessed by Aβ isoforms, and likely by other biomolecules.

We have shown that Aβ interferes with the SNARE exocytosis assembly, and may impact the trafficking of insulin and transferrin that use SNAREs for BBB transcytosis, if any of these steps in the vesicular transport machinery are dysfunctional. Moreover, it could also affect Aβ clearance from the AD brain.

The step-wise approach of the research strategy as well as the summary of results have been presented in **Figure 6.1**

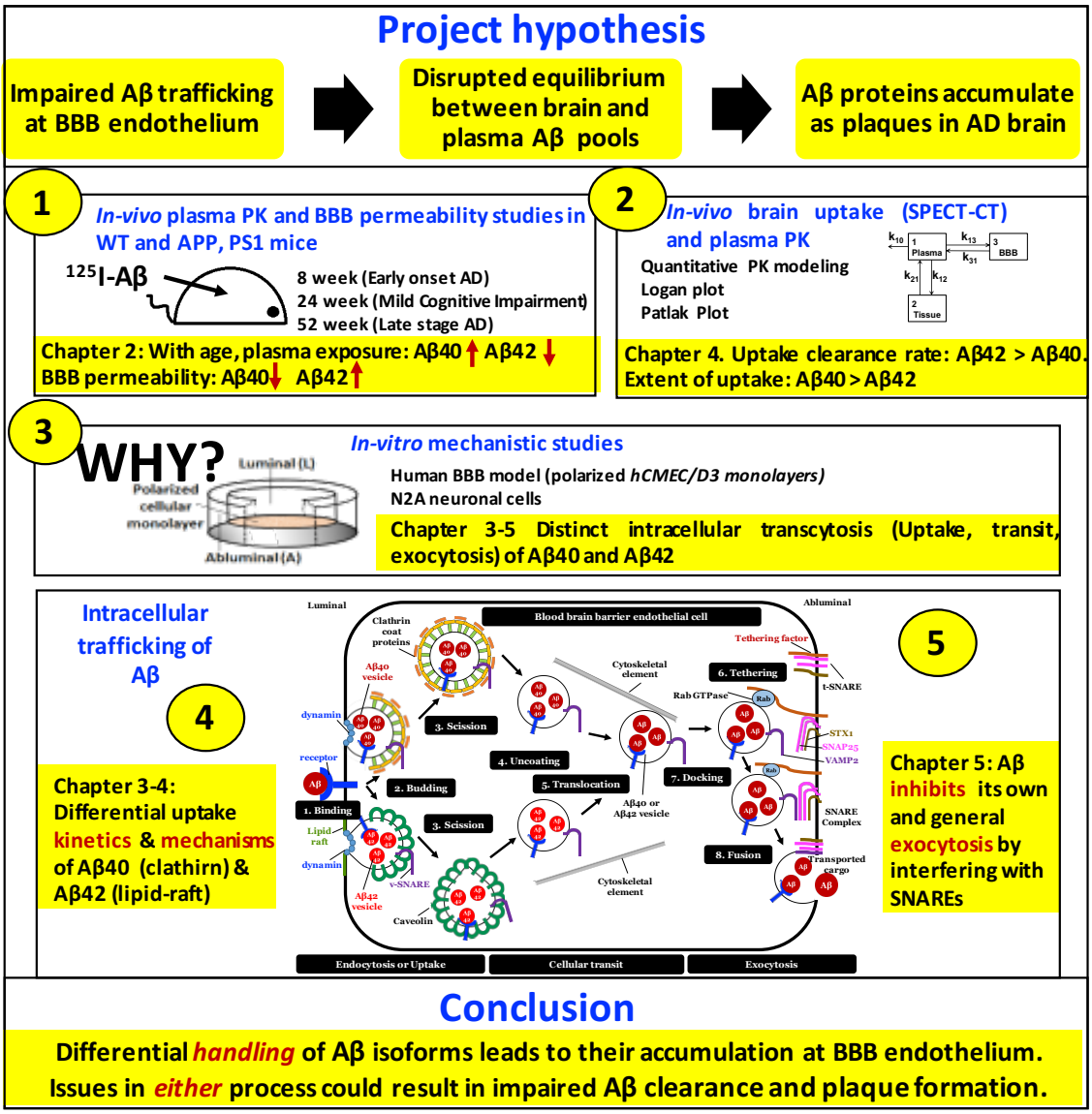

Figure 6.1 Thesis project research strategy and conclusions.

6.2. Results summary

This thesis work demonstrated an *age* dependent plasma PK of Aβ40 and Aβ42 in early (8-week), mild (24-week), and late stage (52-week) WT and APP,PS1 mice. The BBB permeability studies demonstrated a decrease in Aβ40, and an increase in Aβ42 permeability, with age **(Chapter 2)**. This suggested disproportionate luminal exposure of BBB endothelium to Aβ40 and Aβ42. Further dissecting the initial uptake kinetics by quantitative modeling of plasma pharmacokinetic and brain SPECT-CT imaging data predicted higher dissociation constant (K_d or k_{31}/k_{13}) for Aβ42 than Aβ40. Patlak and Logan plots predicted a higher input clearance into the brain for Aβ42 compared to Aβ40. **(Chapter 3-4).**

We then conducted *in-vitro* trafficking studies using polarized hCMEC/D3 cell monolayers to elucidate BBB permeability at the cellular level. By evaluating stepwise endothelial Aβ trafficking (endocytosis or uptake, transit, and exocytosis), we quantified the polarized uptake of Aβ isoforms with differential *kinetic* profiles over time and concentration. Also, studies with small molecule inhibitors and genetic knockdowns of endocytotic processes showed *distinct* uptake mechanisms of Aβ isoforms at the BBB endothelium. The uptake of Aβ40 is via clathrin-mediated endocytosis, whereas the uptake of Aβ42 is via lipid-raft mediated endocytosis. **(Chapter 3-4).**

Moreover, we have shown that Aβ utilizes vesicle-associated-membrane-protein (VAMP-2) to exocytose on the abluminal side of the endothelial cell. Fluorescent-resonance-energy-transfer (FRET) fluorescent-lifetime-imaging microscopy (FLIM), revealed that Aβ could inhibit the fusion of two sister SNAREs (VAMP-2 and SNAP-25) and impact endothelial exocytosis. By doing so, Aβ may not only inhibit its own

exocytosis, but may affect the transcytosis of other biomolecules (insulin, transferrin) that use SNARE machinery for exocytosis. Therefore, Aβ peptides could perturb brain homeostasis and neuronal synaptic transmission that rely upon SNARE exocytosis **(Chapter 5)**.

To our understanding, we are *first* to demonstrate that the transcytosis of Aβ40 and Aβ42 are handled differently by the BBB endothelium. This novel assertion provides a mechanistic vantage point to describe Aβ clearance, perturbed Aβ42:Aβ40 ratios, and dysregulated transport of endogenous proteins at the BBB observed in AD patients.

We have also shown that Aβ40 accumulates in the BBB endothelium more than Aβ42. The longer stay in BBB endothelium implies that Aβ40 will have more time to affect the vesicular transport machinery at the BBB endothelium. Further, this increased exposure of BBB endothelium to the toxic Aβ proteins could profoundly contribute to BBB dysfunction that impair Aβ clearance at the BBB endothelium.

6.3. Future directions

Despite progress made in this thesis work in understanding cellular apparatus involved with Aβ clearance at the BBB, there are still several unanswered questions that need to be further explored. Firstly, our studies demonstrated differential trafficking of Aβ40 and Aβ42 at the BBB endothelium, only in the luminal to abluminal (L-A) direction. It is equally important to explore how Aβ proteins perturb VAMP-7 and VAMP-8, which mediate luminal exocytosis. Next, we specifically explored just the two extremes of transcytosis- endocytosis uptake and exocytosis. It would be interesting to see how the cellular transit apparatus (Rabs and microtubular cytoskeleton) involved in

this orchestrated event is affected by Aβ peptides. Although our findings suggest that accumulation of toxic Aβ would trigger BBB dysfunction, before making it leaky and dysfunction, a direct evidence substantiating this hypothesis would be helpful.

BIBLIOGRAPHY

Aguzzi, A., Rajendran, L., 2009. The Transcellular Spread of Cytosolic Amyloids, Prions, and Prionoids. Neuron 64, 783–790. doi:10.1016/j.neuron.2009.12.016

Agyare, E.K., Leonard, S.R., Curran, G.L., Yu, C.C., Lowe, V.J., Paravastu, A.K., Poduslo, J.F., Kandimalla, K.K., 2013. Traffic jam at the blood-brain barrier promotes greater accumulation of Alzheimer's disease amyloid-beta proteins in the cerebral vasculature. Mol. Pharm. 10, 1557–1565. doi:10.1021/mp300352c

Akaaboune, M., Allinquant, B., Farza, H., Roy, K., Magoul, R., Fiszman, M., Festoff, B.W., Hantaï, D., 2000. Developmental Regulation of Amyloid Precursor Protein at the Neuromuscular Junction in Mouse Skeletal Muscle. Mol. Cell. Neurosci. 15, 355–367. doi:10.1006/mcne.2000.0834

Alafuzoff, I., Adolfsson, R., Bucht, G., Winblad, B., 1983. Albumin and immunoglobulin in plasma and cerebrospinal fluid, and blood-cerebrospinal fluid barrier function in patients with dementia of Alzheimer type and multi-infarct dementia. J. Neurol. Sci. 60, 465–72.

Alberts, B., Johnson, A., Lewis, J., Raff, M., Roberts, K., Walter, P., 2002. Molecular Biology of the Cell. Garland Science.

Ascolani, A., Balestrieri, E., Minutolo, A., Mosti, S., Spalletta, G., Bramanti, P., Mastino, A., Caltagirone, C., Macchi, B., 2012. Dysregulated NF-κB Pathway in Peripheral Mononuclear Cells of Alzheimer's Disease Patients. Curr. Alzheimer Res. 9, 128–137. doi:10.2174/156720512799015091

Baranello, R.J., Bharani, K.L., Padmaraju, V., Chopra, N., Lahiri, D.K., Greig, N.H., Pappolla, M.A., Sambamurti, K., 2015. Amyloid-beta protein clearance and degradation (ABCD) pathways and their role in Alzheimer's disease. Curr. Alzheimer Res. 12, 32–46.

Becker, W., 2010. The bh TCSPC Handbook. Scanning 1–566.

Becker, W., Bergmann, a., Haustein, E., Petrasek, Z., Schwille, P., Biskup, C., Kelbauskas, L., Benndorf, K., Klöcker, N., Anhut, T., Riemann, I., König, K., 2006. Fluorescence lifetime images and correlation spectra obtained by multidimensional time-correlated single photon counting. Microsc. Res. Tech. 69, 186–195. doi:10.1002/jemt.20251

Bell, R.D., Sagare, A.P., Friedman, A.E., Bedi, G.S., Holtzman, D.M., Deane, R., Zlokovic, B. V, 2007. Transport pathways for clearance of human Alzheimer's amyloid beta-peptide and apolipoproteins E and J in the mouse central nervous system. J. Cereb. Blood Flow Metab. 27, 909–918. doi:10.1038/sj.jcbfm.9600419

Benilova, I., Karran, E., De Strooper, B., 2012. The toxic Aβ oligomer and Alzheimer's disease: an emperor in need of clothes. Nat. Neurosci. 15, 349–57. doi:10.1038/nn.3028

Berney, C., Danuser, G., 2003. FRET or No FRET: A Quantitative Comparison. Biophys. J. 84, 3992–4010. doi:10.1016/S0006-3495(03)75126-1

Blasko, I., Kemmler, G., Jungwirth, S., Wichart, I., Krampla, W., Weissgram, S., Jellinger, K., Tragl, K.H., Fischer, P., 2010. Plasma amyloid beta-42 independently predicts both late-onset depression and Alzheimer disease. Am J Geriatr. Psychiatry 18. doi:10.1097/JGP.0b013e3181df48be

Blennow, K., de Leon, M.J., Zetterberg, H., 2006. Alzheimer's disease. Lancet 368, 387–403. doi:10.1016/S0140-6736(06)69113-7

Blennow, K., Wallin, A., Fredman, P., Karlsson, I., Gottfries, C.G., Svennerholm, L., 1990. Blood-brain barrier disturbance in patients with Alzheimer's disease is related to vascular factors. Acta Neurol. Scand. 81, 323–6.

Bowman, G.L., Quinn, J.F., 2008. Alzheimer's disease and the Blood-Brain Barrier: Past, Present and Future. Aging health 4, 47–55. doi:10.2217/1745509X.4.1.47

Broussard, J.A., Rappaz, B., Webb, D.J., Brown, C.M., 2013. Fluorescence resonance energy transfer microscopy as demonstrated by measuring the activation of the serine/threonine kinase Akt. Nat. Protoc. 8, 265–281. doi:10.1038/nprot.2012.147

Caglayan, S., Takagi-Niidome, S., Liao, F., Carlo, A.-S., Schmidt, V., Burgert, T., Kitago, Y., Füchtbauer, E.-M., Füchtbauer, A., Holtzman, D.M., Takagi, J., Willnow, T.E., 2014. Lysosomal sorting of amyloid-β by the SORLA receptor is impaired by a familial Alzheimer's disease mutation. Sci. Transl. Med. 6, 223ra20. doi:10.1126/scitranslmed.3007747

Cai, H., Reinisch, K., Ferro-Novick, S., 2007. Coats, Tethers, Rabs, and SNAREs Work Together to Mediate the Intracellular Destination of a Transport Vesicle. Dev. Cell 12, 671–682. doi:10.1016/j.devcel.2007.04.005

Calakos, N., Scheller, R.H., 1994. Vesicle-associated membrane protein and synaptophysin are associated on the synaptic vesicle. J. Biol. Chem. 269, 24534–7.

Candela, P., Gosselet, F., Saint-Pol, J., Sevin, E., Boucau, M.C., Boulanger, E., Cecchelli, R., Fenart, L., 2010. Apical-to-basolateral transport of amyloid-β peptides through blood-brain barrier cells is mediated by the receptor for advanced glycation end-products and is restricted by p-glycoprotein. J. Alzheimer's Dis. 22, 849–859. doi:10.3233/JAD-2010-100462

Cao, H., Chen, J., Awoniyi, M., Henley, J.R., McNiven, M.A., 2007. Dynamin 2 mediates fluid-phase micropinocytosis in epithelial cells. J. Cell Sci. 120, 4167–77. doi:10.1242/jcs.010686

Carpentier, M., Robitaille, Y., DesGroseillers, L., Boileau, G., Marcinkiewicz, M., 2002. Declining Expression of Neprilysin in Alzheimer Disease Vasculature: Possible Involvement in Cerebral Amyloid Angiopathy. J. Neuropathol. Exp. Neurol. 61, 849–856. doi:10.1093/jnen/61.10.849

Carrano, A., Hoozemans, J.J.M., van der Vies, S.M., Rozemuller, A.J.M., van Horssen, J., de Vries, H.E., 2011. Amyloid Beta induces oxidative stress-mediated blood-brain barrier changes in capillary amyloid angiopathy. Antioxid. Redox Signal. 15, 1167–1178. doi:10.1089/ars.2011.3895

Casey, C.A., Lee, S.M.L., Aziz-Seible, R., McVicker, B.L., 2008. Impaired receptor-mediated endocytosis: its role in alcohol-induced apoptosis. J. Gastroenterol. Hepatol. 23 Suppl 1, S46-9. doi:10.1111/j.1440-1746.2007.05275.x

Castellani, R., Lee, H., Siedlak, S., 2009. Reexamining Alzheimer's disease: evidence for a protective role for amyloid-β protein precursor and amyloid-β. J. Alzheimer's Dis. 18, 447–452. doi:10.3233/JAD-2009-1151.Reexamining

Chang, C.-W., Sud, D., Mycek, M.-A., 2007. Fluorescence lifetime imaging microscopy. Methods Cell Biol. 81, 495–524. doi:10.1016/S0091-679X(06)81024-1

Chen, X., Hui, L., Soliman, M.L., Geiger, J.D., 2014. Altered Cholesterol Intracellular Trafficking and the Development of Pathological Hallmarks of Sporadic AD. J.

Park. Dis. Alzheimer's Dis. 1.
Chen, Y.A., Scheller, R.H., Medical, H.H., 2001. SNARE-MEDIATED MEMBRANE FUSION 2, 98–106.
Choi, B.-K., Choi, M.-G., Kim, J.-Y., Yang, Y., Lai, Y., Kweon, D.-H., Lee, N.K., Shin, Y.-K., 2013. Large -synuclein oligomers inhibit neuronal SNARE-mediated vesicle docking. Proc. Natl. Acad. Sci. 110, 4087–4092. doi:10.1073/pnas.1218424110
Choi, B.-K., Kim, J.-Y., Cha, M.-Y., Mook-Jung, I., Shin, Y.-K., Lee, N.K., 2015. β-Amyloid and α-Synuclein Cooperate To Block SNARE-Dependent Vesicle Fusion. Biochemistry 54, 1831–1840. doi:10.1021/acs.biochem.5b00087
Cirrito, J.R., May, P.C., O'Dell, M.A., Taylor, J.W., Parsadanian, M., Cramer, K., Cramer, J.W., Audia, J.E., Nissen, J.S., Bales, K.R., Paul, S.M., DeMattos, R.B., Holtzman, D.M., 2003. In Vivo Assessment of Brain Interstitial Fluid with Microdialysis reveals Plaque-Associated Changes in Amyloid-β Metabolism and Half-Life. Neuroscience 23, 8844–8853.
Corradini, I., Verderio, C., Sala, M., Wilson, M.C., Matteoli, M., 2009. SNAP-25 in Neuropsychiatric Disorders. Ann. N. Y. Acad. Sci. 1152, 93–99. doi:10.1111/j.1749-6632.2008.03995.x
Coulson, E.., Paliga, K., Beyreuther, K., Masters, C.., 2000. What the evolution of the amyloid protein precursor supergene family tells us about its function. Neurochem. Int. 36, 175–184. doi:10.1016/S0197-0186(99)00125-4
Deák, F., Schoch, S., Liu, X., Südhof, T.C., Kavalali, E.T., 2004. Synaptobrevin is essential for fast synaptic-vesicle endocytosis. Nat. Cell Biol. 6, 1102–1108. doi:10.1038/ncb1185
de la Monte, S.M., Wands, J.R., 2008. Alzheimer's disease is type 3 diabetes-evidence reviewed. J. Diabetes Sci. Technol. 2, 1101–13.
Deane, R., Bell, R.D., Sagare, A., Zlokovic, B. V, 2009. Clearance of amyloid-beta peptide across the blood-brain barrier: implication for therapies in Alzheimer's disease. CNS Neurol. Disord. Drug Targets 8, 16–30. doi:10.2174/187152709787601867
Deane, R., Wu, Z., Sagare, A., Davis, J., Du Yan, S., Hamm, K., Xu, F., Parisi, M., LaRue, B., Hu, H.W., Spijkers, P., Guo, H., Song, X., Lenting, P.J., Van Nostrand, W.E., Zlokovic, B. V., 2004. LRP/amyloid beta-peptide interaction mediates differential brain efflux of Abeta isoforms. Neuron 43, 333–44. doi:10.1016/j.neuron.2004.07.017
Deane, R., Wu, Z., Zlokovic, B. V., 2004. RAGE (Yin) versus LRP (Yang) balance regulates Alzheimer amyloid beta-peptide clearance through transport across the blood-brain barrier. Stroke 35, 2628–2631. doi:10.1161/01.STR.0000143452.85382.d1
Deane, R., Zheng, W., Zlokovic, B. V., 2004d. Brain capillary endothelium and choroid plexus epithelium regulate transport of transferrin-bound and free iron into the rat brain. J. Neurochem. 88, 813–820. doi:10.1046/j.1471-4159.2003.02221.x
Deane, R.J.R.J., Singh, I., Sagare, A.P., Bell, R.D., Ross, N.T., LaRue, B., Love, R., Perry, S., Paquette, N., Deane, R.J.R.J., Thiyagarajan, M., Zarcone, T., Fritz, G., Friedman, A.E., Miller, B.L., Zlokovic, B. V, 2012. A multimodal RAGE-specific inhibitor reduces amyloid beta-mediated brain disorder in a mouse model of Alzheimer disease. J Clin Invest 122, 1377–1392. doi:10.1172/JCI58642DS1

De Reuck, J.L., 2012. The significance of small cerebral bleeds in neurodegenerative dementia syndromes. Aging Dis. 3, 307–12.

Degtyar, V., Hafez, I.M., Bray, C., Zucker, R.S., 2013. Dance of the SNAREs: assembly and rearrangements detected with FRET at neuronal synapses. J. Neurosci. 33, 5507–23. doi:10.1523/JNEUROSCI.2337-12.2013

DeMattos, R., Bales, K., Cummins, D., 2001. Peripheral anti-Aβ antibody alters CNS and plasma Aβ clearance and decreases brain Aβ burden in a mouse model of Alzheimer's disease. Proc.

Duman, J.G., Forte, J.G., 2003. What is the role of SNARE proteins in membrane fusion? Am. J. Physiol. Cell Physiol. 285, C237–C249. doi:10.1152/ajpcell.00091.2003

Eisele, Y.S., Fritschi, S.K., Hamaguchi, T., Obermüller, U., Füger, P., Skodras, A., Schäfer, C., Odenthal, J., Heikenwalder, M., Staufenbiel, M., Jucker, M., 2014. Multiple Factors Contribute to the Peripheral Induction of Cerebral β-Amyloidosis. J. Neurosci. 34, 10264–73. doi:10.1523/JNEUROSCI.1608-14.2014

Eisenberg, D., Jucker, M., 2012. The amyloid state of proteins in human diseases. Cell 148, 1188–1203. doi:10.1016/j.cell.2012.02.022

Erickson, M. a, Banks, W. a, 2013. Blood-brain barrier dysfunction as a cause and consequence of Alzheimer's disease. J. Cereb. Blood Flow Metab. 33, 1500–13. doi:10.1038/jcbfm.2013.135

Ertekin-Taner, N., Younkin, L.H., Yager, D.M., Parfitt, F., Baker, M.C., Asthana, S., Hutton, M.L., Younkin, S.G., Graff-Radford, N.R., 2008. Plasma amyloid protein is elevated in late-onset Alzheimer disease families. Neurology 70, 596–606. doi:10.1212/01.wnl.0000278386.00035.21

Fagan, A.M., Mintun, M.A., Mach, R.H., Lee, S.Y., Dence, C.S., Shah, A.R., LaRossa, G.N., Spinner, M.L., Klunk, W.E., Mathis, C.A., DeKosky, S.T., Morris, J.C., Holtzman, D.M., 2006. Inverse relation between in vivo amyloid imaging load and cerebrospinal fluid Abeta;42 in humans. Ann. Neurol. 59, 512–519. doi:10.1002/ana.20730

Fang, F., Lue, L.-F., Yan, S., Xu, H., Luddy, J.S., Chen, D., Walker, D.G., Stern, D.M., Yan, S., Schmidt, A.M., Chen, J.X., Yan, S.S., 2010. RAGE-dependent signaling in microglia contributes to neuroinflammation, Abeta accumulation, and impaired learning/memory in a mouse model of Alzheimer's disease. FASEB J. 24, 1043–1055. doi:10.1096/fj.09-139634

Farris, W., Mansourian, S., Chang, Y., Lindsley, L., Eckman, E.A., Frosch, M.P., Eckman, C.B., Tanzi, R.E., Selkoe, D.J., Guenette, S., 2003. Insulin-degrading enzyme regulates the levels of insulin, amyloid beta-protein, and the beta-amyloid precursor protein intracellular domain in vivo. Proc. Natl. Acad. Sci. U. S. A. 100, 4162–7. doi:10.1073/pnas.0230450100

Ferrer, I., 2009. Altered mitochondria, energy metabolism, voltage-dependent anion channel, and lipid rafts converge to exhaust neurons in Alzheimer's disease. J. Bioenerg. Biomembr.

Fields, I.C., Shteyn, E., Pypaert, M., Proux-Gillardeaux, V., Kang, R.S., Galli, T., Fölsch, H., 2007. v-SNARE cellubrevin is required for basolateral sorting of AP-1B-dependent cargo in polarized epithelial cells. J. Cell Biol. 177, 477–488. doi:10.1083/jcb.200610047

Figurski, M.J., Waligorska, T., Toledo, J., Vanderstichele, H., Korecka, M., Lee, V.M.,

Trojanowski, J.Q., Shaw, L.M., 2012. Improved protocol for measurement of plasma beta-amyloid in longitudinal evaluation of Alzheimer's Disease Neuroimaging Initiative study patients. Alzheimers Dement 8. doi:10.1016/j.jalz.2012.01.001

Förster, T., 2012. Energy migration and fluorescence. J. Biomed. Opt.

Fraldi, A., Annunziata, F., Lombardi, A., Kaiser, H.-J., Medina, D.L., Spampanato, C., Fedele, A.O., Polishchuk, R., Sorrentino, N.C., Simons, K., Ballabio, A., 2010. Lysosomal fusion and SNARE function are impaired by cholesterol accumulation in lysosomal storage disorders. EMBO J. 29, 3607–20. doi:10.1038/emboj.2010.237

Fukumoto, H., Tennis, M., Locascio, J.J., Hyman, B.T., Growdon, J.H., Irizarry, M.C., 2003. Age but not diagnosis is the main predictor of plasma amyloid beta-protein levels. Arch Neurol 60. doi:10.1001/archneur.60.7.958

Gaffield, M. a, Betz, W.J., 2006. Imaging synaptic vesicle exocytosis and endocytosis with FM dyes. Nat. Protoc. 1, 2916–2921. doi:10.1038/nprot.2006.476

Ghiso, J., Calero, M., Matsubara, E., Governale, S., Chuba, J., Beavis, R., Wisniewski, T., Frangione, B., 1997. Alzheimer's soluble amyloid ?? is a normal component of human urine. FEBS Lett. 408, 105–108. doi:10.1016/S0014-5793(97)00400-6

Ghiso, J., Shayo, M., Calero, M., Ng, D., Tomidokoro, Y., Gandy, S., Rostagno, A., Frangione, B., 2004. Systemic catabolism of Alzheimer's A??40 and A??42. J. Biol. Chem. 279, 45897–45908. doi:10.1074/jbc.M407668200

Giedraitis, V., Sundelöf, J., Irizarry, M.C., Gårevik, N., Hyman, B.T., Wahlund, L.O., Ingelsson, M., Lannfelt, L., 2007. The normal equilibrium between CSF and plasma amyloid beta levels is disrupted in Alzheimer's disease. Neurosci. Lett. 427, 127–131. doi:10.1016/j.neulet.2007.09.023

Giuffrida, M.L., Caraci, F., Pignataro, B., Cataldo, S., De Bona, P., Bruno, V., Molinaro, G., Pappalardo, G., Messina, A., Palmigiano, A., Garozzo, D., Nicoletti, F., Rizzarelli, E., Copani, A., 2009. Beta-amyloid monomers are neuroprotective. J. Neurosci. 29, 10582–7. doi:10.1523/JNEUROSCI.1736-09.2009

Graff-Radford, N.R., Crook, J.E., Lucas, J., Boeve, B.F., Knopman, D.S., Ivnik, R.J., Smith, G.E., Younkin, L.H., Petersen, R.C., Younkin, S.G., 2007. Association of low plasma Abeta42/Abeta40 ratios with increased imminent risk for mild cognitive impairment and Alzheimer disease. Arch Neurol 64. doi:10.1001/archneur.64.3.354

Granseth, B., Odermatt, B., Royle, S.J., Lagnado, L., 2006. Clathrin-Mediated Endocytosis Is the Dominant Mechanism of Vesicle Retrieval at Hippocampal Synapses. Neuron 51, 773–786. doi:10.1016/j.neuron.2006.08.029

Haass, C., Schlossmacher, M.G., Hung, A.Y., Vigo-Pelfrey, C., Mellon, A., Ostaszewski, B.L., Lieberburg, I., Koo, E.H., Schenk, D., Teplow, D.B., 1992. Amyloid beta-peptide is produced by cultured cells during normal metabolism. Nature 359, 322–5. doi:10.1038/359322a0

Hamaguchi, T., Eisele, Y.S., Varvel, N.H., Lamb, B.T., Walker, L.C., Jucker, M., 2012. The presence of amyloid beta seeds, and not age per se, is critical to the initiation of amyloid beta deposition in the brain. Acta Neuropathol. 123, 31–37. doi:10.1007/s00401-011-0912-1

Hansson, O., Stomrud, E., Vanmechelen, E., Ostling, S., Gustafson, D.R., Zetterberg, H., Blennow, K., Skoog, I., 2012. Evaluation of plasma Abeta as predictor of Alzheimer's disease in older individuals without dementia: a population-based

study. J Alzheimers Dis 28.
Harik, S.I., 2011. Changes in the glucose transporter of brain capillaries. http://dx.doi.org/10.1139/y92-252.
Hartmann, T., Bieger, S.C., Brühl, B., Tienari, P.J., Ida, N., Allsop, D., Roberts, G.W., Masters, C.L., Dotti, C.G., Unsicker, K., Beyreuther, K., 1997. Distinct sites of intracellular production for Alzheimer's disease A beta40/42 amyloid peptides. Nat. Med. 3, 1016–1020. doi:10.1038/nm0997-1016
Hawkins, B.T., Davis, T.P., 2005. The Blood-Brain Barrier / Neurovascular Unit in Health and Disease. Pharmacol. Rev. 57, 173–185. doi:10.1124/pr.57.2.4.173
Hebert, L.E., Beckett, L.A., Scherr, P.A., Evans, D.A., 2013. Annual incidence of Alzheimer disease in the United States projected to the years 2000 through 2050. Alzheimer Dis. Assoc. Disord. 15, 169–73.
Honer, W.G., Barr, a M., Sawada, K., Thornton, a E., Morris, M.C., Leurgans, S.E., Schneider, J. a, Bennett, D. a, 2012. Cognitive reserve, presynaptic proteins and dementia in the elderly. Transl. Psychiatry 2, e114. doi:10.1038/tp.2012.38
Honer, W.G., Falkai, P., Bayer, T. a, Xie, J., Hu, L., Li, H.-Y., Arango, V., Mann, J.J., Dwork, A.J., Trimble, W.S., 2002. Abnormalities of SNARE mechanism proteins in anterior frontal cortex in severe mental illness. Cereb. Cortex 12, 349–356. doi:10.1093/cercor/12.4.349
Horwood, N., Davies, D.C., 1994. Immunolabelling of hippocampal microvessel glucose transporter protein is reduced in Alzheimer's disease. Virchows Arch. 425, 69–72. doi:10.1007/BF00193951
Huang, Y., Mucke, L., 2012. Alzheimer mechanisms and therapeutic strategies. Cell 148, 1204–1222. doi:10.1016/j.cell.2012.02.040
Huizing, M., Anikster, Y., Gahl, W.A., 2001. Hermansky-Pudlak syndrome and Chediak-Higashi syndrome: disorders of vesicle formation and trafficking. Thromb. Haemost. 86, 233–45.
Iliff, J.J., Wang, M., Liao, Y., Plogg, B. a., Peng, W., Gundersen, G. a., Benveniste, H., Vates, G.E., Deane, R., Goldman, S. a., Nagelhus, E. a., Nedergaard, M., 2012. A Paravascular Pathway Facilitates CSF Flow Through the Brain Parenchyma and the Clearance of Interstitial Solutes, Including Amyloid . Sci. Transl. Med. 4, 147ra111-147ra111. doi:10.1126/scitranslmed.3003748
Jack, C.R., Knopman, D.S., Jagust, W.J., Shaw, L.M., Aisen, P.S., Weiner, M.W., Petersen, R.C., Trojanowski, J.Q., 2010. Hypothetical model of dynamic biomarkers of the Alzheimer's pathological cascade. Lancet. Neurol. 9, 119–28. doi:10.1016/S1474-4422(09)70299-6
Jaeger, L.B., Dohgu, S., Hwang, M.C., Farr, S.A., Murphy, M.P., Fleegal-DeMotta, M.A., Lynch, J.L., Robinson, S.M., Niehoff, M.L., Johnson, S.N., Kumar, V.B., Banks, W.A., 2009a. Testing the neurovascular hypothesis of Alzheimer's disease: LRP-1 antisense reduces blood-brain barrier clearance, increases brain levels of amyloid-beta protein, and impairs cognition. J. Alzheimers. Dis. 17, 553–70. doi:10.3233/JAD-2009-1074
Jaeger, L.B., Dohgu, S., Hwang, M.C., Farr, S.A., Murphy, M.P., Fleegal-DeMotta, M.A., Lynch, J.L., Robinson, S.M., Niehoff, M.L., Johnson, S.N., Kumar, V.B., Banks, W.A., 2009b. Testing the neurovascular hypothesis of Alzheimer's disease: LRP-1 antisense reduces blood-brain barrier clearance, increases brain levels of

amyloid-beta protein, and impairs cognition. J. Alzheimers. Dis. 17, 553–70. doi:10.3233/JAD-2009-1074

Jaffe, A.B., Toran-Allerand, C.D., Greengard, P., Gandy, S.E., 1994. Estrogen regulates metabolism of Alzheimer amyloid beta precursor protein. J. Biol. Chem. 269, 13065–8.

Jentsch, T.J., Maritzen, T., Zdebik, A.A., 2005. Chloride channel diseases resulting from impaired transepithelial transport or vesicular function. J. Clin. Invest. 115, 2039–46. doi:10.1172/JCI25470

Joo, Y., Ha, S., Hong, B.-H., Kim, J. a, Chang, K.-A., Liew, H., Kim, S., Sun, W., Kim, J.-H., Chong, Y.H., Suh, Y.-H., Kim, H.-S., 2010. Amyloid precursor protein binding protein-1 modulates cell cycle progression in fetal neural stem cells. PLoS One 5, e14203. doi:10.1371/journal.pone.0014203

Jung, S.S., Nalbantoglu, J., Cashman, N.R., 1996. Alzheimer's beta-amyloid precursor protein is expressed on the surface of immediately ex vivo brain cells: a flow cytometric study. J. Neurosci. Res. 46, 336–48. doi:10.1002/(SICI)1097-4547(19961101)46:3<336::AID-JNR7>3.0.CO;2-L

Kalaria, R.N., Harik, S.I., 1989. Abnormalities of the glucose transporter at the blood-brain barrier and in brain in Alzheimer's disease. Prog. Clin. Biol. Res. 317, 415–21.

Kamenetz, F., Tomita, T., Hsieh, H., Seabrook, G., Borchelt, D., Iwatsubo, T., Sisodia, S., Malinow, R., 2003. APP Processing and Synaptic Function. Neuron 37, 925–937. doi:10.1016/S0896-6273(03)00124-7

Kandimalla, K.K., Curran, G.L., Holasek, S.S., Gilles, E.J., Wengenack, T.M., Poduslo, J.F., 2005. Pharmacokinetic analysis of the blood-brain barrier transport of 125I-amyloid beta protein 40 in wild-type and Alzheimer's disease transgenic mice (APP,PS1) and its implications for amyloid plaque formation. J. Pharmacol. Exp. Ther. 313, 1370–1378. doi:10.1124/jpet.104.081901.gested

Karran, E., Mercken, M., Strooper, B. De, 2011. The amyloid cascade hypothesis for Alzheimer's disease: an appraisal for the development of therapeutics. Nat. Rev. Drug Discov. 10, 698–712. doi:10.1038/nrd3505

Kawarabayashi, T., Younkin, L.H., Saido, T.C., Shoji, M., Ashe, K.H., Younkin, S.G., 2001. Age-dependent changes in brain, CSF, and plasma amyloid (beta) protein in the Tg2576 transgenic mouse model of Alzheimer's disease. J. Neurosci. 21, 372–381.

Kerridge, C., Belyaev, N.D., Nalivaeva, N.N., Turner, A.J., 2014. The Aβ-clearance protein transthyretin, like neprilysin, is epigenetically regulated by the amyloid precursor protein intracellular domain. J. Neurochem. doi:10.1111/jnc.12680

Kim, S., Sato, Y., Mohan, P.S., Peterhoff, C., Pensalfini, A., Rigoglioso, A., Jiang, Y., Nixon, R.A., 2015. Evidence that the rab5 effector APPL1 mediates APP-βCTF-induced dysfunction of endosomes in Down syndrome and Alzheimer's disease. Mol. Psychiatry. doi:10.1038/mp.2015.97

Kimura, N., Okabayashi, S., Ono, F., 2012. Dynein dysfunction disrupts intracellular vesicle trafficking bidirectionally and perturbs synaptic vesicle docking via endocytic disturbances: A potential mechanism underlying age-dependent impairment of cognitive function. Am. J. Pathol. 180, 550–561. doi:10.1016/j.ajpath.2011.10.037

Kirazov, E., Kirazov, L., Bigl, V., Schliebs, R., 2001. Ontogenetic changes in protein

level of amyloid precursor protein (APP) in growth cones and synaptosomes from rat brain and prenatal expression pattern of APP mRNA isoforms in developing rat embryo. Int. J. Dev. Neurosci. 19, 287–296. doi:10.1016/S0736-5748(01)00012-0

Klein, W.., Stine, W.., Teplow, D.., 2004. Small assemblies of unmodified amyloid β-protein are the proximate neurotoxin in Alzheimer's disease. Neurobiol. Aging 25, 569–580. doi:10.1016/j.neurobiolaging.2004.02.010

Kugaevskaya, E. V., 2012. Angiotensin converting enzyme and Alzheimer's disease. Biochem. Suppl. Ser. B Biomed. Chem. 6, 11–22. doi:10.1134/S199075081201009X

LaFerla, F.M., Green, K.N., Oddo, S., 2007. Intracellular amyloid-beta in Alzheimer's disease. Nat. Rev. Neurosci. 8, 499–509. doi:10.1038/nrn2168

Lai, A.Y., McLaurin, J., 2012. Clearance of amyloid-β peptides by microglia and macrophages: the issue of what, when and where. Future Neurol. 7, 165–176. doi:10.2217/fnl.12.6

Lakowicz, J.R., 2006. Introduction to Fluorescence, in: Principles of Fluorescence Spectroscopy. Springer US, Boston, MA, pp. 1–26. doi:10.1007/978-0-387-46312-4_1

Lee, S., Sato, Y., Nixon, R.A., 2011. Primary lysosomal dysfunction causes cargo-specific deficits of axonal transport leading to Alzheimer-like neuritic dystrophy. Autophagy 7, 1562–3.

Logan, J., 2003. A review of graphical methods for tracer studies and strategies to reduce bias. Nucl. Med. Biol. 30, 833–844. doi:10.1016/S0969-8051(03)00114-8

Logan, J., Fowler, J.S., Volkow, N.D., Wolf, A.P., Dewey, S.L., Schlyer, D.J., MacGregor, R.R., Hitzemann, R., Bendriem, B., Gatley, S.J., 1990. Graphical analysis of reversible radioligand binding from time-activity measurements applied to [N-11C-methyl]-(-)-cocaine PET studies in human subjects. J. Cereb. Blood Flow Metab. 10, 740–7. doi:10.1038/jcbfm.1990.127

Lorenzl, S., Albers, D.S., Relkin, N., Ngyuen, T., Hilgenberg, S.L., Chirichigno, J., Cudkowicz, M.E., Beal, M.F., 2003. Increased plasma levels of matrix metalloproteinase-9 in patients with Alzheimer's disease. Neurochem. Int. 43, 191–6.

Lui, J.K., Laws, S.M., Li, Q.-X.X., Villemagne, V.L., Ames, D., Brown, B., Bush, A.I., De Ruyck, K., Dromey, J., Ellis, K.A., Faux, N.G., Foster, J., Fowler, C., Gupta, V., Hudson, P., Laughton, K., Masters, C.L., Pertile, K., Rembach, A., Rimajova, M., Rodrigues, M., Rowe, C.C., Rumble, R., Szoeke, C., Taddei, K., Taddei, T., Trounson, B., Ward, V., Martins, R.N., AIBL Research Group, 2010. Plasma amyloid-beta as a biomarker in Alzheimer's disease: the AIBL study of aging. J Alzheimers Dis 20, 1233–42. doi:10.3233/JAD-2010-090249

Mackic, J.B., Stins, M., McComb, J.G., Calero, M., Ghiso, J., Kim, K.S., Yan, S. Du, Stern, D., Schmidt, A.M., Frangione, B., Zlokovic, B. V., 1998. Human blood-brain barrier receptors for Alzheimer's amyloid-β 1-40. Asymmetrical binding, endocytosis, and transcytosis at the apical side of brain microvascular endothelial cell monolayer. J. Clin. Invest. 102, 734–743. doi:10.1172/JCI2029

Mahmood, I., 2012. Naive Pooled–Data Approach for Pharmacokinetic Studies in Pediatrics With a Very Small Sample Size. Am. J. Ther. 21, 1. doi:10.1097/MJT.0b013e31824ddee3

Marchi, N., Cavaglia, M., Fazio, V., Bhudia, S., Hallene, K., Janigro, D., 2004. Peripheral markers of blood-brain barrier damage. Clin. Chim. Acta 342, 1–12. doi:10.1016/j.cccn.2003.12.008

Marques, F., Sousa, J.C., Sousa, N., Palha, J.A., 2013. Blood – brain-barriers in aging and in Alzheimer ' s disease 1–9.

Marr, R.A., Rockenstein, E., Mukherjee, A., Kindy, M.S., Hersh, L.B., Gage, F.H., Verma, I.M., Masliah, E., 2003. Neprilysin gene transfer reduces human amyloid pathology in transgenic mice. J. Neurosci. 23, 1992–6.

Martel, C., Mackic, J., McComb, J., Ghiso, J., 1996. Blood-brain barrier uptake of the 40 and 42 amino acid sequences of circulating Alzheimer's amyloid β in guinea pigs. Neuroscience.

Maruyama, M., Higuchi, M., Takaki, Y., Matsuba, Y., Tanji, H., Nemoto, M., Tomita, N., Matsui, T., Iwata, N., Mizukami, H., Muramatsu, S., Ozawa, K., Saido, T.C., Arai, H., Sasaki, H., 2005. Cerebrospinal fluid neprilysin is reduced in prodromal Alzheimer's disease. Ann. Neurol. 57, 832–42. doi:10.1002/ana.20494

Matsuoka, Y., Andrews, H.F., Becker, A.G., Gray, A.J., Mehta, P.D., Sano, M.C., Dalton, A.J., Aisen, P.S.,. The relationship of plasma Abeta levels to dementia in aging individuals with Down syndrome. Alzheimer Dis. Assoc. Disord. 23, 315–8. doi:10.1097/WAD.0b013e3181aba61e

Mawuenyega, K.G., Sigurdson, W., Ovod, V., Munsell, L., Kasten, T., Morris, J.C., Yarasheski, K.E., Bateman, R.J., 2010a. Decreased clearance of CNS beta-amyloid in Alzheimer's disease. Science (80-.). 330, 1774. doi:10.1126/science.1197623

Mawuenyega, K.G., Sigurdson, W., Ovod, V., Munsell, L., Kasten, T., Morris, J.C., Yarasheski, K.E., Bateman, R.J., 2010b. Decreased Clearance of CNS -Amyloid in Alzheimer's Disease. Science (80-.). 330, 1774–1774. doi:10.1126/science.1197623

Mayeux, R., Honig, L.S., Tang, M.X., Manly, J., Stern, Y., Schupf, N., Mehta, P.D., 2003. Plasma Aβ40 and Aβ42 and Alzheimer's disease: relation to age, mortality, and risk. Neurology 61. doi:10.1212/01.WNL.0000091890.32140.8F

Mayeux, R., Tang, M.X., Jacobs, D.M., Manly, J., Bell, K., Merchant, C., Small, S.A., Stern, Y., Wisniewski, H.M., Mehta, P.D., 1999. Plasma amyloid beta-peptide 1-42 and incipient Alzheimer's disease. Ann Neurol 46. doi:3.0.CO;2-A

McGowan, E., Pickford, F., Kim, J., Onstead, L., Eriksen, J., Yu, C., Skipper, L., Murphy, M.P., Beard, J., Das, P., Jansen, K., DeLucia, M., Lin, W.-L., Dolios, G., Wang, R., Eckman, C.B., Dickson, D.W., Hutton, M., Hardy, J., Golde, T., 2005. Aβ42 Is Essential for Parenchymal and Vascular Amyloid Deposition in Mice. Neuron 47, 191–199. doi:10.1016/j.neuron.2005.06.030

Medine, C.N., Rickman, C., Chamberlain, L.H., Duncan, R.R., 2007. Munc18-1 prevents the formation of ectopic SNARE complexes in living cells. J. Cell Sci. 120, 4407–4415. doi:10.1242/jcs.020230

Mehta, P.D., Pirttilä, T., Mehta, S.P., Sersen, E. a, Aisen, P.S., Wisniewski, H.M., 2000. Plasma and cerebrospinal fluid levels of amyloid beta proteins 1-40 and 1-42 in Alzheimer disease. Arch. Neurol. 57, 100–105. doi:10.1001/archneur.57.1.100

Meyer, J.H., Ichise, M., 2001. Modeling of Receptor Ligand Data in PET and SPECT Imaging : A Review of 11, 30–39.

Miklossy, J., Qing, H., Radenovic, A., Kis, A., Vileno, B., Làszló, F., Miller, L., Martins, R.N., Waeber, G., Mooser, V., Bosman, F., Khalili, K., Darbinian, N., McGeer, P.L.,

2010. Beta amyloid and hyperphosphorylated tau deposits in the pancreas in type 2 diabetes. Neurobiol. Aging 31, 1503–15. doi:10.1016/j.neurobiolaging.2008.08.019

Mooradian, A.D., 1997. Central nervous system complications of diabetes mellitus — a perspective from the blood–brain barrier. Brain Res. Rev. 23, 210–218. doi:10.1016/S0165-0173(97)00003-9

Mukaetova-Ladinska, E.B., Xuereb, J.H., Garcia-Sierra, F., Hurt, J., Gertz, H.-J., Hills, R., Brayne, C., Huppert, F. a, Paykel, E.S., McGee, M. a, Jakes, R., Honer, W.G., Harrington, C.R., Wischik, C.M., 2009. Lewy body variant of Alzheimer's disease: selective neocortical loss of t-SNARE proteins and loss of MAP2 and alpha-synuclein in medial temporal lobe. ScientificWorldJournal. 9, 1463–1475. doi:10.1100/tsw.2009.151

Nalivaeva, N.N., Turner, A.J., 2013. The amyloid precursor protein: A biochemical enigma in brain development, function and disease. FEBS Lett. 587, 2046–2054. doi:10.1016/j.febslet.2013.05.010

National Institute on Aging, N. institute of H., 2015. Alzheimer's disease: Unraveling the Mystery.

Nedergaard, M., 2013. Garbage truck of the brain. Science 340, 1529–30. doi:10.1126/science.1240514

Niederwolfsgruber, E., Schmitt, T.L., Blasko, I., Trieb, K., Steger, M.M., Maczek, C., Hager, J., Bobak, K., Steiner, E., Grubeck-Loebenstein, B., 1998. The production of the Alzheimer amyloid precursor protein (APP) in extraneuronal tissue does not increase in old age. J Gerontol A Biol Sci Med Sci 53, B186-90.

Octave, J.-N., Pierrot, N., Ferao Santos, S., Nalivaeva, N.N., Turner, A.J., 2013. From synaptic spines to nuclear signaling: nuclear and synaptic actions of the amyloid precursor protein. J. Neurochem. 126, 183–90. doi:10.1111/jnc.12239

Okereke, O.I., Xia, W., Selkoe, D.J., Grodstein, F., 2009. Ten-year change in plasma amyloid beta levels and late-life cognitive decline. Arch Neurol 66. doi:10.1001/archneurol.2009.207

Omtri, R.S., Davidson, M.W., Arumugam, B., Poduslo, J.F., Kandimalla, K.K., 2012. Differences in the Cellular Uptake and Intracellular Itineraries of Amyloid Beta Proteins 40 and 42: Rami fi cations for the Alzheimer' s Drug Discovery.

Owen, J.B., Sultana, R., Aluise, C.D., Erickson, M.A., Price, T.O., Bu, G., Banks, W.A., Butterfield, D.A., 2010. Oxidative modification to LDL receptor-related protein 1 in hippocampus from subjects with Alzheimer disease: implications for Aβ accumulation in AD brain. Free Radic. Biol. Med. 49, 1798–803. doi:10.1016/j.freeradbiomed.2010.09.013

Pacheco-Quinto, J., 2013. Endothelin-converting enzymes and related metalloproteases in Alzheimer's disease. … Alzheimer's Dis.

Parihar, M.S., Brewer, G.J., 2010. Amyloid-β as a modulator of synaptic plasticity. J. Alzheimers. Dis. 22, 741–63. doi:10.3233/JAD-2010-101020

Pascale, C.L., Miller, M.C., Chiu, C., Boylan, M., Caralopoulos, I.N., Gonzalez, L., Johanson, C.E., Silverberg, G.D., 2011. Amyloid-beta transporter expression at the blood-CSF barrier is age-dependent. Fluids Barriers CNS 8, 21. doi:10.1186/2045-8118-8-21

Patlak, C.S., Blasberg, R.G., 1985. Graphical Evaluation of Blood-to-Brain Transfer Constants from Multiple-T ime Uptake Data. Generalizations 584–590.

Patlak, C.S., Blasberg, R.G., Fenstermacher, J.D., 1983. Graphical evaluation of blood-to-brain transfer constants from multiple-time uptake data. J. Cereb. Blood Flow Metab. 3, 1–7. doi:10.1038/jcbfm.1985.87

Pearson, H. a, Peers, C., 2006. Physiological roles for amyloid beta peptides. J. Physiol. 575, 5–10. doi:10.1113/jphysiol.2006.111203

Pennuto, M., Bonanomi, D., Benfenati, F., Valtorta, F., 2003. Synaptophysin I controls the targeting of VAMP2/synaptobrevin II to synaptic vesicles. Mol. Biol. Cell 14, 4909–19. doi:10.1091/mbc.E03-06-0380

Phiel, C., Wilson, C., Lee, V., Klein, P., 2003. GSK-3α regulates production of Alzheimer's disease amyloid-β peptides. Nature.

Piston, D.W., Kremers, G.-J., 2007. Fluorescent protein FRET: the good, the bad and the ugly. Trends Biochem. Sci. 32, 407–414. doi:10.1016/j.tibs.2007.08.003

Plant, L.D., Boyle, J.P., Smith, I.F., Peers, C., Pearson, H. a, 2003. The production of amyloid beta peptide is a critical requirement for the viability of central neurons. J. Neurosci. 23, 5531–5535. doi:23/13/5531 [pii]

Plant, L.D., Webster, N.J., Boyle, J.P., Ramsden, M., Freir, D.B., Peers, C., Pearson, H.A., 2006. Amyloid beta peptide as a physiological modulator of neuronal "A"-type K+ current. Neurobiol. Aging 27, 1673–83. doi:10.1016/j.neurobiolaging.2005.09.038

Poduslo, J.F., Curran, G.L., Haggard, J.J., Biere, a L., Selkoe, D.J., 1997. Permeability and residual plasma volume of human, Dutch variant, and rat amyloid beta-protein 1-40 at the blood-brain barrier. Neurobiol. Dis. 4, 27–34. doi:10.1006/nbdi.1997.0132

Poduslo, J.F., Curran, G.L., Sanyal, B., Selkoe, D.J., 1999. Receptor-mediated transport of human amyloid beta-protein 1-40 and 1-42 at the blood-brain barrier. Neurobiol. Dis. 6, 190–9. doi:10.1006/nbdi.1999.0238

Poller, B., Gutmann, H., Krähenbühl, S., Weksler, B., Romero, I., Couraud, P.O., Tuffin, G., Drewe, J., Huwyler, J., 2008. The human brain endothelial cell line hCMEC/D3 as a human blood-brain barrier model for drug transport studies. J. Neurochem. 107, 1358–1368. doi:10.1111/j.1471-4159.2008.05730.x

Proux-Gillardeaux, V., Rudge, R., Galli, T., 2005. The tetanus neurotoxin-sensitive and insensitive routes to and from the plasma membrane: Fast and slow pathways? Traffic 6, 366–373. doi:10.1111/j.1600-0854.2005.00288.x

Qian, Z.M., Wang, Q., 1998. Expression of iron transport proteins and excessive iron accumulation in the brain in neurodegenerative disorders. Brain Res. Rev. 27, 257–267. doi:10.1016/S0165-0173(98)00012-5

Qosa, H., Abuasal, B.S., Romero, I. a., Weksler, B., Couraud, P.O., Keller, J.N., Kaddoumi, A., 2014. Differences in amyloid-β clearance across mouse and human blood-brain barrier models: Kinetic analysis and mechanistic modeling. Neuropharmacology 79, 668–678. doi:10.1016/j.neuropharm.2014.01.023

Quetglas, S., Iborra, C., Sasakawa, N., De Haro, L., Kumakura, K., Sato, K., Leveque, C., Seagar, M., 2002. Calmodulin and lipid binding to synaptobrevin regulates calcium-dependent exocytosis. EMBO J. 21, 3970–3979. doi:10.1093/emboj/cdf404

Rice, H.C., Townsend, M., Bai, J., Suth, S., Cavanaugh, W., Selkoe, D.J., Young-Pearse, T.L., 2012. Pancortins interact with amyloid precursor protein and modulate cortical cell migration. Development 139, 3986–96. doi:10.1242/dev.082909

Rizo, J., Südhof, T.C., 2002. Snares and Munc18 in synaptic vesicle fusion. Nat. Rev. Neurosci. 3, 641–653. doi:10.1038/nrn898

Rizzoli, S.O., 2014. Synaptic vesicle recycling: steps and principles. EMBO J. 33, 788–822. doi:10.1002/embj.201386357

Rogaeva, E., Meng, Y., Lee, J.H., Gu, Y., Kawarai, T., Zou, F., Katayama, T., Baldwin, C.T., Cheng, R., Hasegawa, H., Chen, F., Shibata, N., Lunetta, K.L., Pardossi-Piquard, R., Bohm, C., Wakutani, Y., Cupples, L.A., Cuenco, K.T., Green, R.C., Pinessi, L., Rainero, I., Sorbi, S., Bruni, A., Duara, R., Friedland, R.P., Inzelberg, R., Hampe, W., Bujo, H., Song, Y.-Q., Andersen, O.M., Willnow, T.E., Graff-Radford, N., Petersen, R.C., Dickson, D., Der, S.D., Fraser, P.E., Schmitt-Ulms, G., Younkin, S., Mayeux, R., Farrer, L.A., St George-Hyslop, P., 2007. The neuronal sortilin-related receptor SORL1 is genetically associated with Alzheimer disease. Nat. Genet. 39, 168–77. doi:10.1038/ng1943

Rushworth, J., Hooper, N., 2010. Lipid rafts: linking Alzheimer's amyloid-β production, aggregation, and toxicity at neuronal membranes. Int. J. Alzheimers. Dis.

Russell, C.L., Semerdjieva, S., Empson, R.M., Austen, B.M., Beesley, P.W., Alifragis, P., 2012. Amyloid-β acts as a regulator of neurotransmitter release disrupting the interaction between synaptophysin and VAMP2. PLoS One 7. doi:10.1371/journal.pone.0043201

Sagare, A., Deane, R., Bell, R.D., Johnson, B., Hamm, K., Pendu, R., Marky, A., Lenting, P.J., Wu, Z., Zarcone, T., Goate, A., Mayo, K., Perlmutter, D., Coma, M., Zhong, Z., Zlokovic, B. V, 2007. Clearance of amyloid-beta by circulating lipoprotein receptors. Nat. Med. 13, 1029–1031. doi:10.1038/nm1635

Sagare, A.P., Bell, R.D., Zlokovic, B. V, 2013. Neurovascular Defects and Faulty Amyloid- ᴺᴸ Vascular Clearance in Alzheimer ' s Disease 33. doi:10.3233/JAD-2012-129037

Saido, T., Leissring, M. a, 2012. Proteolytic degradation of amyloid beta-protein. Cold Spring Harb Perspect Med 2, a006379. doi:10.1101/cshperspect.a006379

Schupf, N., Patel, B., Silverman, W., Zigman, W.B., Zhong, N., Tycko, B., Mehta, P.D., Mayeux, R., 2001. Elevated plasma amyloid β-peptide 1–42 and onset of dementia in adults with Down syndrome. Neurosci. Lett. 301, 199–203. doi:10.1016/S0304-3940(01)01657-3

Schupf, N., Tang, M.X., Fukuyama, H., Manly, J., Andrews, H., Mehta, P., Ravetch, J., Mayeux, R., 2008. Peripheral Aβ subspecies as risk biomarkers of Alzheimer's disease. Proc Natl Acad Sci USA 105. doi:10.1073/pnas.0805902105

Selkoe, D.J., 1991. The Molecular of Alzheimer ' s Pathology Disease Review. Neuron 6, 487–498. doi:10.1016/0896-6273(91)90052-2

Selkoe, D.J., Podlisny, M.B., 2002. Deciphering the genetic basis of Alzheimer's disease. Annu. Rev. Genomics Hum. Genet. 3, 67–99. doi:10.1146/annurev.genom.3.022502.103022

Selkoe, D.J., Schenk, D., 2003. Alzheimer's disease: molecular understanding predicts amyloid-based therapeutics. Annu. Rev. Pharmacol. Toxicol. 43, 545–584. doi:10.1146/annurev.pharmtox.43.100901.140248

Sharma, M., Burré, J., Südhof, T., 2012. Proteasome inhibition alleviates SNARE-dependent neurodegeneration. Sci. Transl. Med.

Sheng, M., Sabatini, B.L., Südhof, T.C., 2012. Synapses and Alzheimer's disease. Cold

Spring Harb. Perspect. Biol. 4. doi:10.1101/cshperspect.a005777
Shi, D.Y., Bierhaus, A., Nawroth, P.P., Stern, D.M., 2009. RAGE and Alzheimer's disease: A progression factor for amyloid-beta- induced cellular perturbation? J. Alzheimer's Dis. 16, 833–843. doi:10.3233/JAD-2009-1030
Shibata, M., Yamada, S., Ram Kumar, S., Calero, M., Bading, J., Frangione, B., Holtzman, D.M., Miller, C. a., Strickland, D.K., Ghiso, J., Zlokovic, B. V., 2000. Clearance of Alzheimer's amyloid-β1-40 peptide from brain by LDL receptor-related protein-1 at the blood-brain barrier. J. Clin. Invest. 106, 1489–1499. doi:10.1172/JCI10498
Shoji, M., Hirai, S., Furiya, Y., Endoh, R., Mori, H., 1997. Amyloid b protein 42 (43) in cerebrospinal fluid of patients with Alzheimer ' s disease 148, 41–45.
Simić, G., Kostović, I., Winblad, B., Bogdanović, N., 1997. Volume and number of neurons of the human hippocampal formation in normal aging and Alzheimer's disease. J. Comp. Neurol. 379, 482–94.
Skoog, I., 1998. Status of risk factors for vascular dementia. Neuroepidemiology 17, 2–9.
Slemmon, J.R., Hughes, C.M., Campbell, G.A., Flood, D.G., 1994. Increased levels of hemoglobin-derived and other peptides in Alzheimer's disease cerebellum. J. Neurosci. 14, 2225–35.
Smith, D.E., Johanson, C.E., Keep, R.F., 2004. Peptide and peptide analog transport systems at the blood-CSF barrier. Adv. Drug Deliv. Rev. doi:10.1016/j.addr.2004.07.008
Soba, P., Eggert, S., Wagner, K., Zentgraf, H., Siehl, K., Kreger, S., Löwer, A., Langer, A., Merdes, G., Paro, R., Masters, C.L., Müller, U., Kins, S., Beyreuther, K., 2005. Homo- and heterodimerization of APP family members promotes intercellular adhesion. EMBO J. 24, 3624–34. doi:10.1038/sj.emboj.7600824
Steegmaier, M., Lee, K.C., Prekeris, R., Scheller, R.H., 2000. SNARE protein trafficking in polarized MDCK cells. Traffic 1, 553–560. doi:tra010705 [pii]
Stelzmann, R. a., Schnitzlein, H.N., Murtagh, F.R., 1995. An English I ' ranslation of Alzheimer ' s 1907 Paper , " ijber eine eigenartige Erlranliung der Hirnrinde ." Clin. Anat. 8, 429–431. doi:10.1068/p5028
Sultana, R., Perluigi, M., Allan Butterfield, D., 2013. Lipid peroxidation triggers neurodegeneration: a redox proteomics view into the Alzheimer disease brain. Free Radic. Biol. Med. 62, 157–69. doi:10.1016/j.freeradbiomed.2012.09.027
Sundelöf, J., Giedraitis, V., Irizarry, M.C., Sundström, J., Ingelsson, E., Rönnemaa, E., Arnlöv, J., Gunnarsson, M.D., Hyman, B.T., Basun, H., Ingelsson, M., Lannfelt, L., Kilander, L., 2008. Plasma beta amyloid and the risk of Alzheimer disease and dementia in elderly men: a prospective, population-based cohort study. Arch Neurol 65. doi:10.1001/archneurol.2007.57
Sutcliffe, J.G., Hedlund, P.B., Thomas, E. a., Bloom, F.E., Hilbush, B.S., 2011. Peripheral reduction of β-amyloid is sufficient to reduce brain β amyloid: Implications for Alzheimer's disease. J. Neurosci. Res. 89, 808–814. doi:10.1002/jnr.22603
Suzuki, T., 2006. Trafficking of Alzheimer's Disease-Related Membrane Proteins and Its Participation in Disease Pathogenesis. J. Biochem. 139, 949–955. doi:10.1093/jb/mvj121
Sze, C.I., Bi, H., Kleinschmidt-Demasters, B.K., Filley, C.M., Martin, L.J., 2000.

Selective regional loss of exocytotic presynaptic vesicle proteins in Alzheimer's disease brains. J. Neurol. Sci. 175, 81–90. doi:10.1016/S0022-510X(00)00285-9

Takuma, K., Fang, F., Zhang, W., Yan, S., Fukuzaki, E., Du, H., Sosunov, A., McKhann, G., Funatsu, Y., Nakamichi, N., Nagai, T., Mizoguchi, H., Ibi, D., Hori, O., Ogawa, S., Stern, D.M., Yamada, K., Yan, S.S., 2009. RAGE-mediated signaling contributes to intraneuronal transport of amyloid-beta and neuronal dysfunction. Proc. Natl. Acad. Sci. U. S. A. 106, 20021–20026. doi:10.1073/pnas.0905686106

Tanzi, R.E., 2012. The genetics of Alzheimer disease. Cold Spring Harb. Perspect. Med. 2. doi:10.1101/cshperspect.a006296

Tayler, H., 2013. Endothelin-converting enzymes, Afl and oxidative stress in Alzheimer's disease.

Thomas, G.D., 2000. Effect of Dose, Molecular Size, and Binding Affinity on Uptake of Antibodies, in: Drug Targeting. Humana Press, New Jersey, pp. 115–132. doi:10.1385/1-59259-075-6:115

Toledo, J.B., Shaw, L.M., Trojanowski, J.Q., 2013. Plasma amyloid beta measurements - a desired but elusive Alzheimer's disease biomarker. Alzheimers. Res. Ther. 5, 8. doi:10.1186/alzrt162

Toledo, J.B., Vanderstichele, H., Figurski, M., Aisen, P.S., Petersen, R.C., Weiner, M.W., Jack, C.R., Jagust, W., Decarli, C., Toga, A.W., Toledo, E., Xie, S.X., Lee, V.M., Trojanowski, J.Q., Shaw, L.M., 2011. Factors affecting Abeta plasma levels and their utility as biomarkers in ADNI. Acta Neuropathol 122. doi:10.1007/s00401-011-0861-8

Tucker, W.C., Weber, T., Chapman, E.R., 2004. Reconstitution of Ca2+-regulated membrane fusion by synaptotagmin and SNAREs. Science 304, 435–8. doi:10.1126/science.1097196

Uemura, E., Greenlee, H.W., 2001. Amyloid beta-peptide inhibits neuronal glucose uptake by preventing exocytosis. Exp. Neurol. 170, 270–276. doi:10.1006/exnr.2001.7719

van Oijen, M., Hofman, A., Soares, H.D., Koudstaal, P.J., Breteler, M.M., 2006. Plasma Abeta(1-40) and Abeta(1-42) and the risk of dementia: a prospective case-cohort study. Lancet Neurol 5. doi:10.1016/S1474-4422(06)70501-4

Vignini, A., Giulietti, A., Nanetti, L., Raffaelli, F., Giusti, L., Mazzanti, L., Provinciali, L., n.d. Alzheimer's Disease and Diabetes: New Insights and Unifying Therapies. doi:23363296

Wada, H., 1998. Blood-brain barrier permeability of the demented elderly as studied by cerebrospinal fluid-serum albumin ratio. Intern. Med. 37, 509–13.

Wang, J., Dickson, D.W., Trojanowski, J.Q., Lee, V.M., 1999. The levels of soluble versus insoluble brain Abeta distinguish Alzheimer's disease from normal and pathologic aging. Exp. Neurol. 158, 328–337. doi:10.1006/exnr.1999.7085

Wang, J., Dickson, D.W., Trojanowski, J.Q., Lee, V.M.-Y., 1999. The Levels of Soluble versus Insoluble Brain Aβ Distinguish Alzheimer's Disease from Normal and Pathologic Aging. Exp. Neurol. 158, 328–337. doi:10.1006/exnr.1999.7085

Watkin, L.B., Jessen, B., Wiszniewski, W., Vece, T.J., Jan, M., Sha, Y., Thamsen, M., Santos-Cortez, R.L.P., Lee, K., Gambin, T., Forbes, L.R., Law, C.S., Stray-Pedersen, A., Cheng, M.H., Mace, E.M., Anderson, M.S., Liu, D., Tang, L.F., Nicholas, S.K., Nahmod, K., Makedonas, G., Canter, D.L., Kwok, P.-Y., Hicks, J.,

Jones, K.D., Penney, S., Jhangiani, S.N., Rosenblum, M.D., Dell, S.D., Waterfield, M.R., Papa, F.R., Muzny, D.M., Zaitlen, N., Leal, S.M., Gonzaga-Jauregui, C., Boerwinkle, E., Eissa, N.T., Gibbs, R.A., Lupski, J.R., Orange, J.S., Shum, A.K., 2015. COPA mutations impair ER-Golgi transport and cause hereditary autoimmune-mediated lung disease and arthritis. Nat. Genet. 47, 654–660. doi:10.1038/ng.3279

Weksler, B.B., 2005. Blood-brain barrier-specific properties of a human adult brain endothelial cell line. FASEB J. 26, 1–26. doi:10.1096/fj.04-3458fje

Weller, R., Subash, M., Preston, S., Mazanti, I., Carare, R., 2008. Perivascular Drainage of Amyloid-b Peptides from the Brain and Its Failure in Cerebral Amyloid Angiopathy and Alzheimer's Disease. Brain Pathol.

Yaffe, K., Weston, a., Graff-Radford, N.R., Satterfield, S., Simonsick, E.M., Younkin, S.G., Younkin, L.H., Kuller, L., Ayonayon, H.N., Ding, J., Harris, T.B., 2011. Association of Plasma -Amyloid Level and Cognitive Reserve With Subsequent Cognitive Decline. JAMA J. Am. Med. Assoc. 305, 261–266. doi:10.1001/jama.2010.1995

Yang, Y., Kim, J., Kim, H.Y., Ryoo, N., Lee, S., Kim, Y., Rhim, H., Shin, Y.-K., 2015a. Amyloid-β Oligomers May Impair SNARE-Mediated Exocytosis by Direct Binding to Syntaxin 1a. Cell Rep. 12, 1244–1251. doi:10.1016/j.celrep.2015.07.044

Yang, Y., Kim, J., Kim, H.Y., Ryoo, N., Lee, S., Kim, Y., Rhim, H., Shin, Y.-K., 2015b. Amyloid-β Oligomers May Impair SNARE-Mediated Exocytosis by Direct Binding to Syntaxin 1a, Cell Reports. doi:10.1016/j.celrep.2015.07.044

Yao, P., 2004. Synaptic frailty and clathrin-mediated synaptic vesicle trafficking in Alzheimer's disease. Trends Neurosci.

Yao, P., Weimer, J., O'Herron, T., Coleman, P., 2000. Clathrin assembly protein AP-2 is detected in both neurons and glia, and its reduction is prominent in layer II of frontal cortex in Alzheimer's disease. Neurobiol. Aging.

Yao, P.J., Coleman, P.D., 1998. Reduced O-glycosylated clathrin assembly protein AP180: implication for synaptic vesicle recycling dysfunction in Alzheimer's disease. Neurosci. Lett. 252, 33–36. doi:10.1016/S0304-3940(98)00547-3

Yoon, I.-S., Chen, E., Busse, T., Repetto, E., Lakshmana, M.K., Koo, E.H., Kang, D.E., 2007. Low-density lipoprotein receptor-related protein promotes amyloid precursor protein trafficking to lipid rafts in the endocytic pathway. FASEB J. 21, 2742–52. doi:10.1096/fj.07-8114com

Yoshiyama, Y., Asahina, M., Hattori, T., 2000. Selective distribution of matrix metalloproteinase-3 (MMP-3) in Alzheimer's disease brain. Acta Neuropathol.

Yuede, C.M., Lee, H., Restivo, J.L., Davis, T.A., Hettinger, J.C., Wallace, C.E., Young, K.L., Hayne, M.R., Bu, G., Li, C., Cirrito, J.R., 2016. Rapid in vivo measurement of β-amyloid reveals biphasic clearance kinetics in an Alzheimer's mouse model. J. Exp. Med. 213, 677–685. doi:10.1084/jem.20151428

Zhang, S., Murphy, T.H., 2007. Imaging the impact of cortical microcirculation on synaptic structure and sensory-evoked hemodynamic responses in vivo. PLoS Biol. 5, 1152–1167. doi:10.1371/journal.pbio.0050119

Zhang, Z., Wang, D., Sun, T., Xu, J., Chiang, H.-C., Shin, W., Wu, L.-G., 2013. The SNARE proteins SNAP25 and synaptobrevin are involved in endocytosis at hippocampal synapses. J. Neurosci. 33, 9169–75. doi:10.1523/JNEUROSCI.0301-

13.2013
Zlokovic, B. V, 2010. Neurodegeneration and the neurovascular unit. Nat. Med. 16, 1370–1371. doi:10.1038/nm1210-1370

CHAPTER TWO

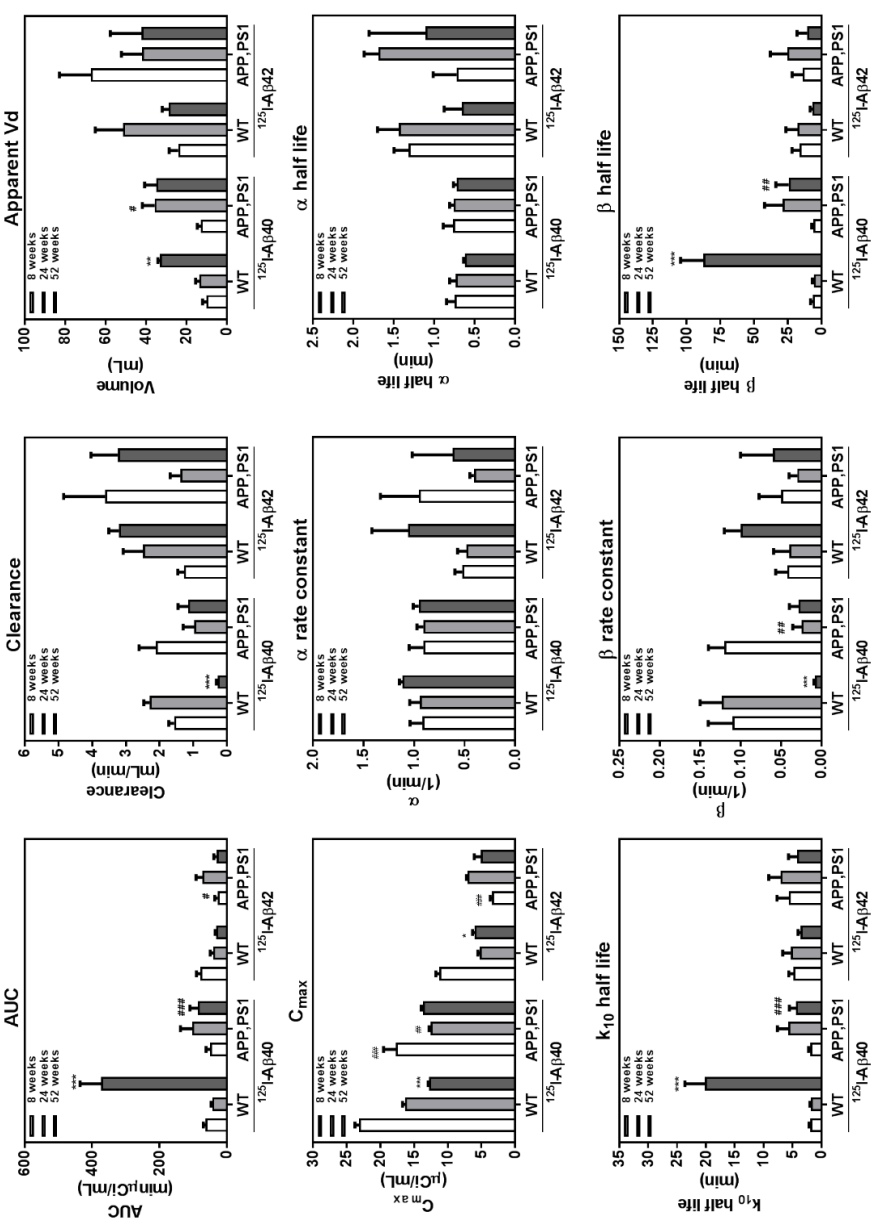

Figure S-2.1Predicted pharmacokinetic parameters of ^{125}I-Aβ40 and ^{125}I-Aβ42 in WT and APP,PS1 mice at 8, 24, 52 weeks. Two compartment model was fit to the plasma data obtained after intravenous bolus injections of 100μCi of ^{125}I-Aβ40 and ^{125}I-Aβ42 and the parameters. Data are mean ± S.D. (n = 3-6) Significance Age (** $p < 0.01$ and *** $p < 0.001$) and WT versus APP,PS1 (### $p< 0.001$) by Two-Way ANOVA followed by Bonferroni post-hoc tests.

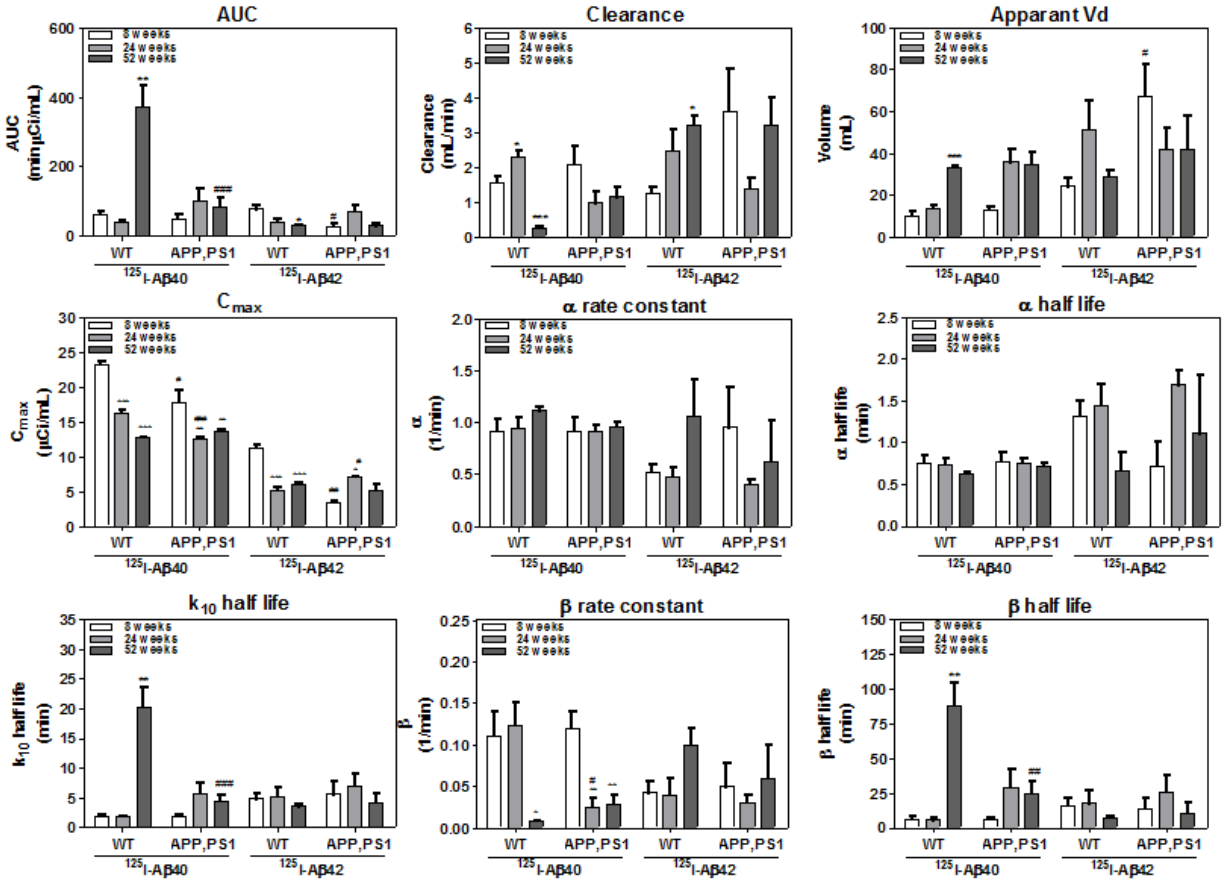

Figure S-2.2Predicted pharmacokinetic parameters of ^{125}I-Aβ40 and ^{125}I-Aβ42 in WT and APP,PS1 mice at 8, 24, 52 weeks. Two compartment model was fit to the plasma data obtained after intravenous bolus injections of 100μCi of ^{125}I-Aβ40 and ^{125}I-Aβ42 and the parameters. Data are mean ± S.D. (n = 3-6) Significance Age (** $p < 0.01$ and *** $p < 0.001$) and WT versus APP,PS1 (### $p< 0.001$) by One-Way ANOVA followed by Bonferroni post-hoc tests.

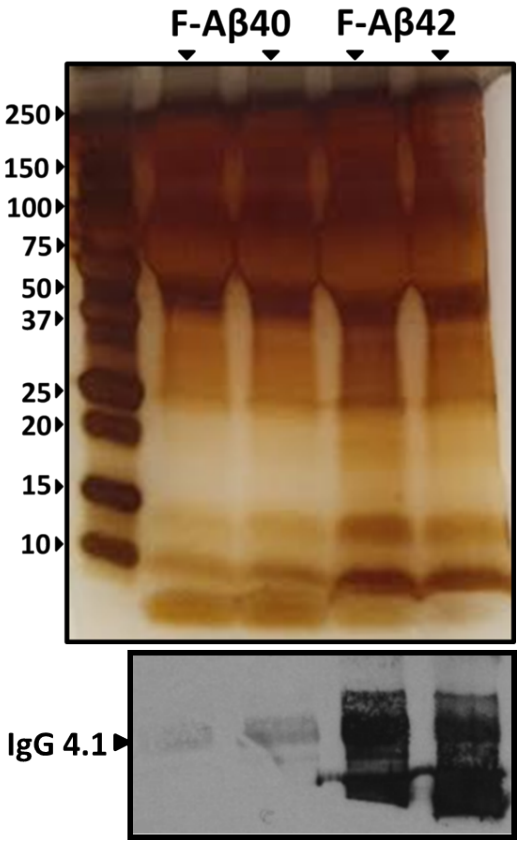

Figure S-3.1. Representative blots characterizing oligomeric species of F-Aβ peptide solutions used in the experiments by SDS-PAGE. Silver stain (top panel) and western-blot (bottom panel) analysis of freshly prepared F-Aβ peptide solutions used in experiments. Column L-R: protein ladder and corresponding molecular weight (in kDa), F-Aβ40 (in duplicate) and F-Aβ42 (in duplicate). IgG 4.1 primarily probes Aβ fibrils. Molecular weights of monomeric Aβ40 and Aβ42 are 4329.86 Da and 4514.05 Da, respectively.

CHAPTER FOUR

Pharmacokinetic model and output from Phoenix WinNonlin® 6.4

Aβ40:

Model:

```
Date: Jun 14, 2016 9:49:39 PM Local
/******************************** Begin Mappings *************************/
Main : 3 Comp_edited.Data.Dat_plasma_brain_indi_5 min
Sort :
ID : Mouse_ID
A1 :
A1 Rate :
Time : Time
CObs : Cp
CObs_A3 : Cb

Dosing : (Internal)

Parameters : <None>

Parameters.Mapping : <None>

Random Effects : <None>

/******************************** End Mappings  *************************/



Phoenix Build 6.4.0.768
test(){
deriv(A1 = - (A1 * Ke)- (A1 * K12- A2 * K21)- (A1 * K13- A3 * K31))
urinecpt(A0 = (A1 * Ke))
deriv(A2 = (A1 * K12- A2 * K21))
deriv(A3 = (A1 * K13- A3 * K31))
C = A1 / V
dosepoint(A1, idosevar = A1Dose, infdosevar = A1InfDose, infratevar = A1InfRate)
error(CEps = 0.1)
observe(CObs = C + CEps)
error(CEps_A3 = 0.001)
observe(CObs_A3 = A3 + CEps_A3)
stparm(V = tvV)
stparm(Ke = tvKe)
stparm(K12 = tvK12)
stparm(K21 = tvK21)
stparm(K13 = tvK13)
stparm(K31 = tvK31)
fixef(tvV = c(, 4.33, ))
fixef(tvKe = c(, 0.1, ))
```

fixef(tvK12 = c(, 0.54,))
fixef(tvK21 = c(, 0.435,))
fixef(tvK13 = c(, 0.011,))
fixef(tvK31 = c(, 0.7,))
}
---
id("Mouse_ID")
time("Time")
obs(CObs<-"Cp")
obs(CObs_A3<-"Cb")
table(file="table01.csv",V,Ke,K12,K21,K13,K31,CMultStdev)
---
id("Mouse_ID")
time("Time")
dose(A1<-"A1", "A1 Rate")

Run Options
Method: Naive pooled
N Iter:1000
Input sorted by subject+time
Enabling automatic log transform (if applicable)
ODE solver method: matrix exponent
Method of computing standard errors: Central Diff
Sandwich standard errors
Confidence Level %95
Use FOCE Hessian
Simple run was performed

Table 01

Mouse_ID	time	V	Ke	K12	K21	K13	K31
1	0	4.76519	0.45655	0.914431	0.701386	0.000862	0.754815
2	0	4.76519	0.45655	0.914431	0.701386	0.000862	0.754815
3	0	4.76519	0.45655	0.914431	0.701386	0.000862	0.754815
4	0	4.76519	0.45655	0.914431	0.701386	0.000862	0.754815
5	0	4.76519	0.45655	0.914431	0.701386	0.000862	0.754815
6	0	4.76519	0.45655	0.914431	0.701386	0.000862	0.754815

Doses:

Mouse_ID	time	dosepoint	amt	rate	ss	path	strip

1	0.001	A1	100	0	0	1
2	0.001	A1	100	0	0	1
3	0.001	A1	100	0	0	1
4	0.001	A1	376.2	0	0	1
5	0.001	A1	324.5	0	0	1
6	0.001	A1	333.3	0	0	1

Initial estimates:

Scenario	parameter	init	low	high
	tvV	4.33		
	tvKe	0.1		
	tvK12	0.54		
	tvK21	0.435		
	tvK13	0.011		
	tvK31	0.7		

Theta:

Parameter	Estimate	Units	Stderr	CV%	2.5% CI	97.5% CI	
tvV	4.76519		0.643817	13.51083	3.481142	6.049238	347.3
tvKe	0.45655		0.058376	12.78641	0.340122	0.572978	13.654
tvK12	0.914431		0.461368	50.45406	-0.00573	1.834597	163.36
tvK21	0.701386		0.13315	18.98388	0.435827	0.966945	183.58
tvK13	0.000862		0.000176	20.44714	0.000511	0.001214	2.61E-05
tvK31	0.754815		0.109188	14.46552	0.537047	0.972583	24.311
stdev0	0.696574		0.232349	33.35595	0.23317	1.159978	
stdev1	0.016264		0.002463	15.14473	0.011351	0.021176	

Overall:

RetCode	LogLik	-2LL	AIC	BIC	nParm	nObs	nSub	EpsShrinkage	Condition
1	143	-285.92	-269.9	-251	8	78	6	0	24095.33

Plots:
q-q IWRES:

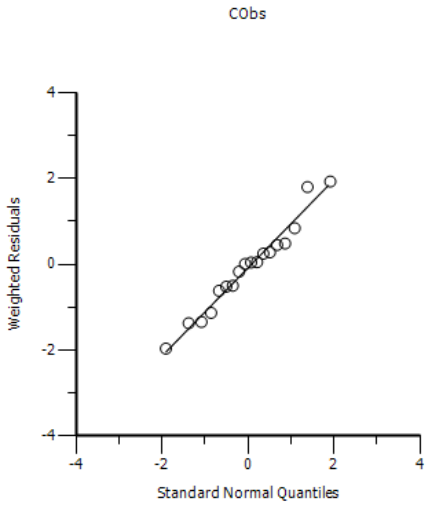

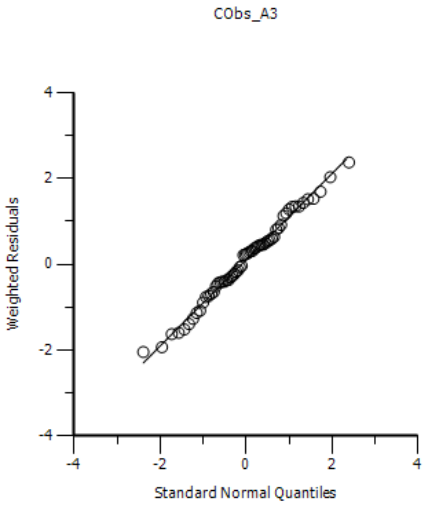

WRES vs Predicted

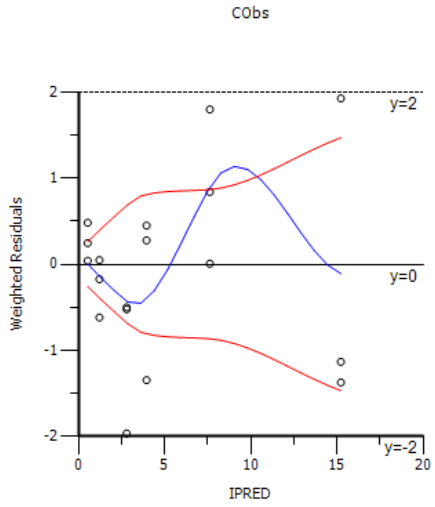

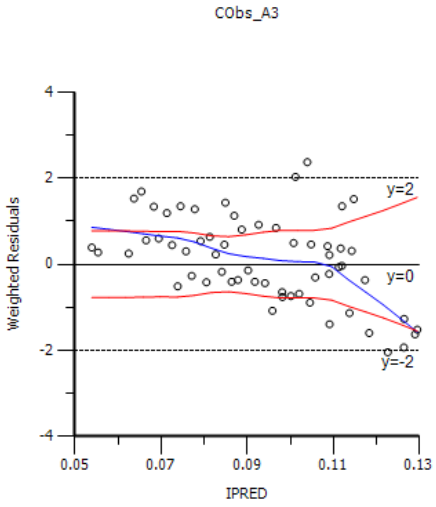

DV versus Predicted

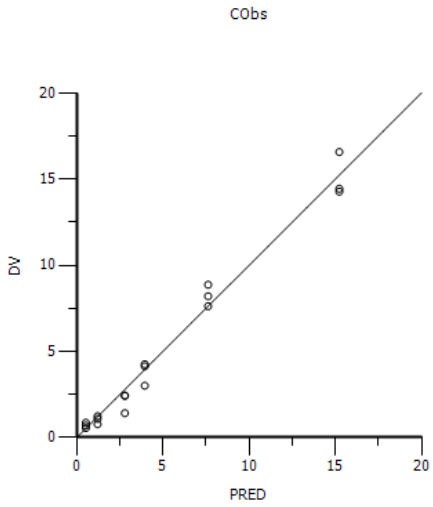
CObs
DV
PRED
0
5
10
15
20

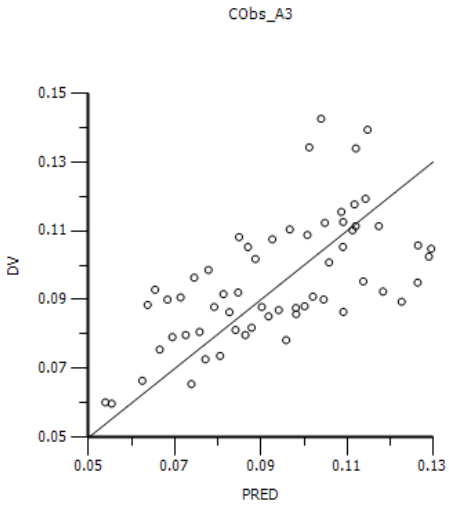
CObs_A3
DV
PRED
0.05
0.07
0.09
0.11
0.13
0.15

Aβ42:

Model:

Date: Jun 14, 2016 11:04:30 PM Local

/********** Begin Mappings **********/

Main : 3 Comp_edited.Data.Dat_plasma_brain_indi

Sort :

ID : Mouse_ID

A1 :

A1 Rate :

Time : Time

CObs : Cp

CObs_A3 : Cb

Dosing : (Internal)

Parameters : <None>

Parameters.Mapping : <None>

Random Effects : <None>

/********** End Mappings **********/

Phoenix Build 6.4.0.768

```
test(){
deriv(A1 = - (A1 * Ke)- (A1 * K12- A2 * K21)- (A1 * K13- A3 * K31))
urinecpt(A0 = (A1 * Ke))
deriv(A2 = (A1 * K12- A2 * K21))
deriv(A3 = (A1 * K13- A3 * K31))
C = A1 / V
dosepoint(A1, idosevar = A1Dose, infdosevar = A1InfDose, infratevar = A1InfRate)

error(CEps = 0.001)
observe(CObs = C + CEps * sqrt(1 + (C)^2 * (CMultStdev1/sigma())^2))
error(CEps_A3 = 0.1)
observe(CObs_A3 = A3 + CEps_A3 )
stparm(V = tvV)
stparm(Ke = tvKe)
stparm(K12 = tvK12)
stparm(K21 = tvK21)
stparm(K13 = tvK13)
stparm(K31 = tvK31)
stparm(CMultStdev1 = tvCMultStdev1)
```

```
fixef(tvV = c(0, 5, ))
fixef(tvKe = c(0, 0.2, ))
fixef(tvK12 = c(0, 1.2, ))
fixef(tvK21 = c(0, 1.2, ))
fixef(tvK13 = c(0, 0.03, ))
fixef(tvK31 = c(0, 3.5,))
fixef(tvCMultStdev1 = c(0,0.01,))

}


-----------------------------------
id("Mouse_ID")
time("Time")
obs(CObs<-"Cp")
obs(CObs_A3<-"Cb")

-----------------------------------
id("Mouse_ID")
time("Time")
dose(A1<-"A1", "A1 Rate")
-----------------------------------
Run Options
Method: Naive pooled
N Iter:1000
Input sorted by subject+time
Enabling automatic log transform (if applicable)
ODE solver method: matrix exponent
Method of computing standard errors: Central Diff
Sandwich standard errors
Confidence Level %95
Use FOCE Hessian
Simple run was performed

Table 01

table(file="table01.csv",V,Ke,K12,K21,K13,K31,CMultStdev)

Mouse_ID    time    V       Ke      K12     K21     K13     K31
1       0       16.0484         0.201757        1.32859         1.26285         0.001274
        3.47595
2       0       16.0484         0.201757        1.32859         1.26285         0.001274
        3.47595
```

3	0	16.0484	0.201757	1.32859	1.26285	0.001274
	3.47595					
4	0	16.0484	0.201757	1.32859	1.26285	0.001274
	3.47595					
5	0	16.0484	0.201757	1.32859	1.26285	0.001274
	3.47595					

Doses:

Scenario	Mouse_ID	time	dosepoint	amt	rate	ss	path	strip
	1	0.001	A1	100	0	0	1	
	2	0.001	A1	100	0	0	1	
	3	0.001	A1	100	0	0	1	
	4	0.001	A1	337.3	0	0	1	
	5	0.001	A1	320.7	0	0	1	

Initial estimates:

Scenario	parameter	init	low	high
	tvV	5	0	
	tvKe	0.2	0	
	tvK12	1.2	0	
	tvK21	1.2	0	
	tvK13	0.03	0	
	tvK31	3.5	0	
	tvCMultStdev1	0.01	0	

1.

Theta:

Parameter	Estimate	Units	Stderr	CV%	2.5% CI	97.5% CI	Var. Inf. factor
tvV	16.0484		1.464582	9.12603	13.10522	18.99158	1169700
tvKe	0.201757		0.018123	8.982408	0.165338	0.238176	193.98
tvK12	1.32859		0.388652	29.25293	0.547567	2.109613	40021
tvK21	1.26285		0.12131	9.606012	1.01907	1.50663	2874.5
tvK13	0.001274		0.000105	8.281049	0.001062	0.001486	0.000718
tvK31	3.47595		0.4968	14.29249	2.477596	4.474304	68222
tvCMultStdev1	0.209586		0.042548	20.30079	0.124084	0.295088	0
stdev0	0.001001		0.000605	60.4498	-0.00022	0.002217	
stdev1	0.004395		0.00037	8.408294	0.003652	0.005138	

Overall:

LogLik	-2LL	AIC	BIC	nParm	nObs	nSub	EpsShrinkage	Condition
152.3629	-304.726	-286.726	-268.182	9	58	5	0	7.05E+09

Plots:

q-q IWRES:

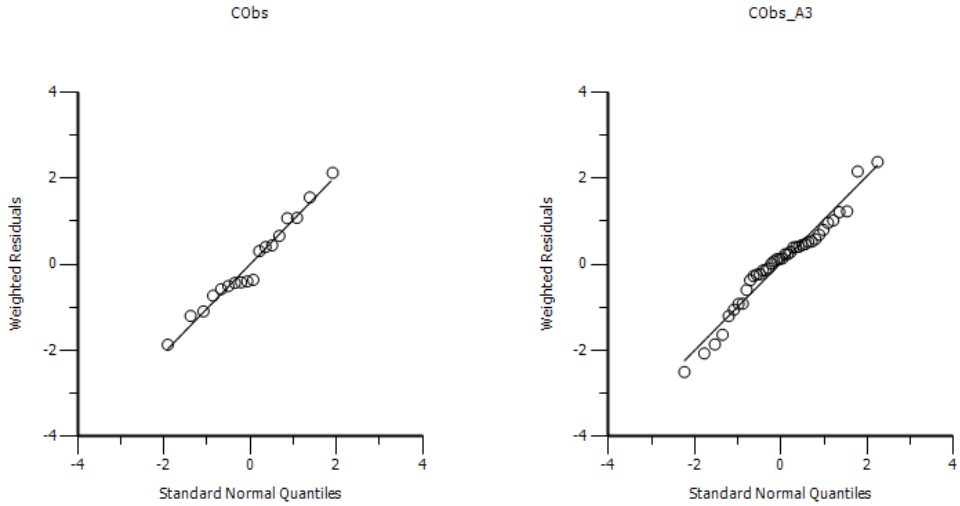

WRES vs Predicted

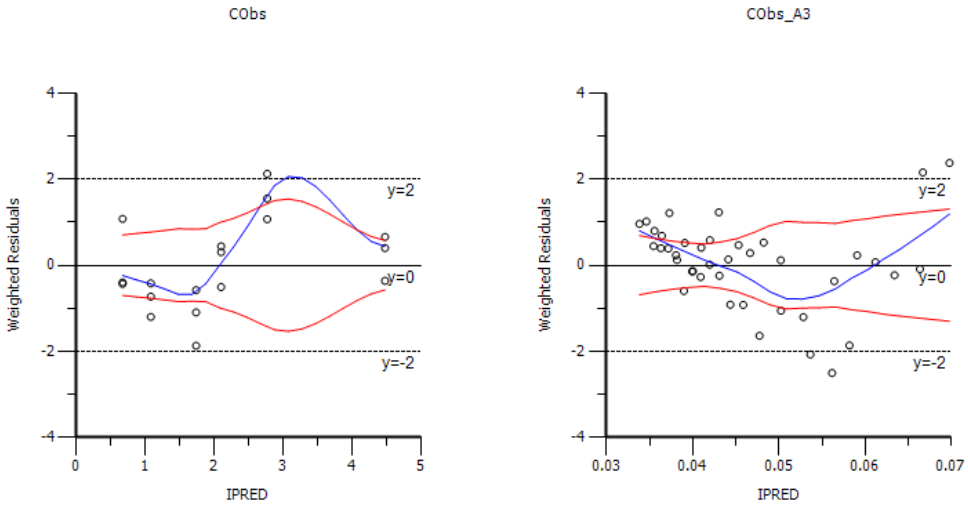

DV versus Predicted

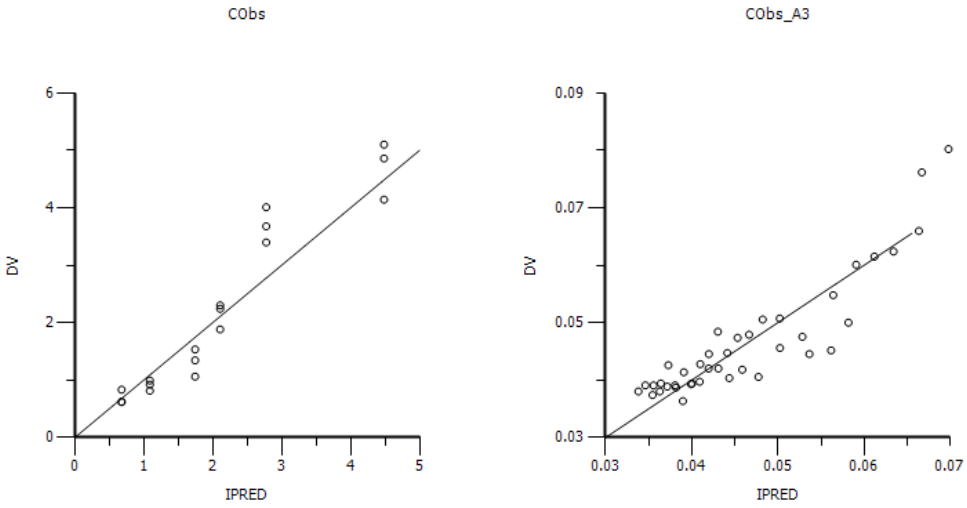
CObs
DV
IPRED
0
2
4
6
0
1
2
3
4
5
CObs_A3
DV
IPRED
0.03
0.05
0.07
0.09
0.03
0.04
0.05
0.06
0.07

CH APTER 5

Intensity images

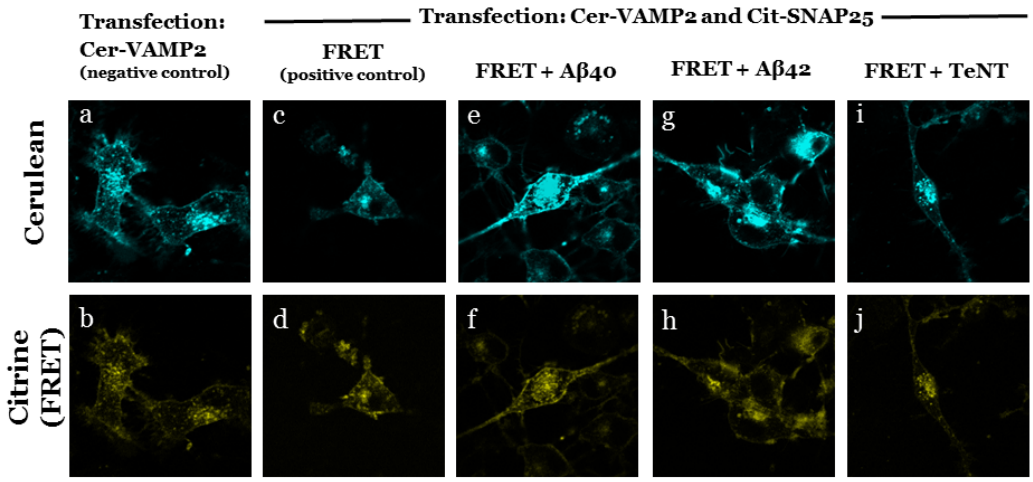

Figure S-5.1. Representative intensity images in cerulean and FRET channel in transfected N2A cells. Images are obtained by exciting cerulean (donor) and capturing cerulean (top panel) and citrine or FRET (bottom panel) that gets excited due to FRET. The FRET channel is a combination of FRET and bleed over from cerulean channel. Cells are either transfected by **(a-b)** donor Cer-VAMP2 only (negative control); or **(c-j)** both- donor Cer-VAMP2 and acceptor Cit-SNAP25; and are subsequently pretreated with **(e-f)** Aβ40; **(g-h)** Aβ42 or **(i-j)** TeNT. **(c-d)** FRET only system serves as the positive control. FRET intensities (bottom panel) are subsequently corrected for cerulean channel bleed over (using negative control intensities) and normalized to donor intensities to obtain effective FRET transfer ratios.

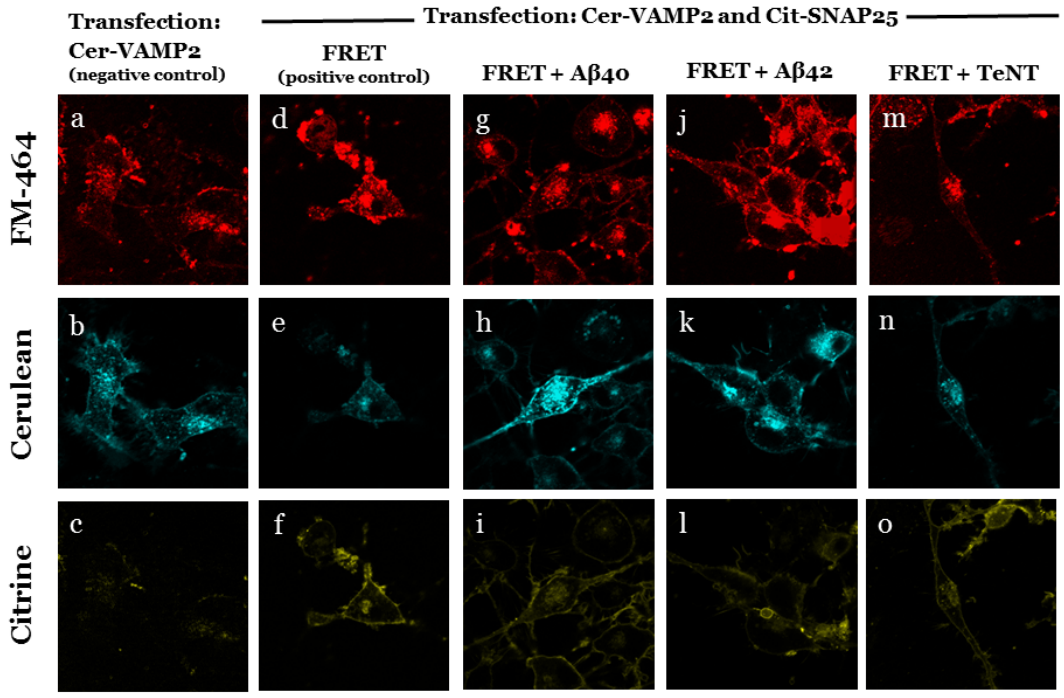

Figure S-5.2. Representative intensity images in FM-464, cerulean and citrine channel in transfected N2A cells. Images are obtained by exciting and capturing FM-464 dye (top panel), cerulean (middle panel) and and citrine (bottom panel). Individual excitation and capture of donor (cerulean) and acceptor (citrine) demonstrates efficient mono or dual transfection. Red punctan of FM 4-64 demonstrate active exocytosis at membrane and enables specific vesicle fusion process analysis. Cells are either transfected by **(a-c)** donor Cer-VAMP2 only (negative control); or **(d-o)** both- donor Cer-VAMP2 and acceptor Cit-SNAP25; and are subsequently pretreated with **(g-i)** Aβ40; **(j-l)** Aβ42 or **(m-o)** TeNT. **(d-f)** FRET only system serves as the positive control.

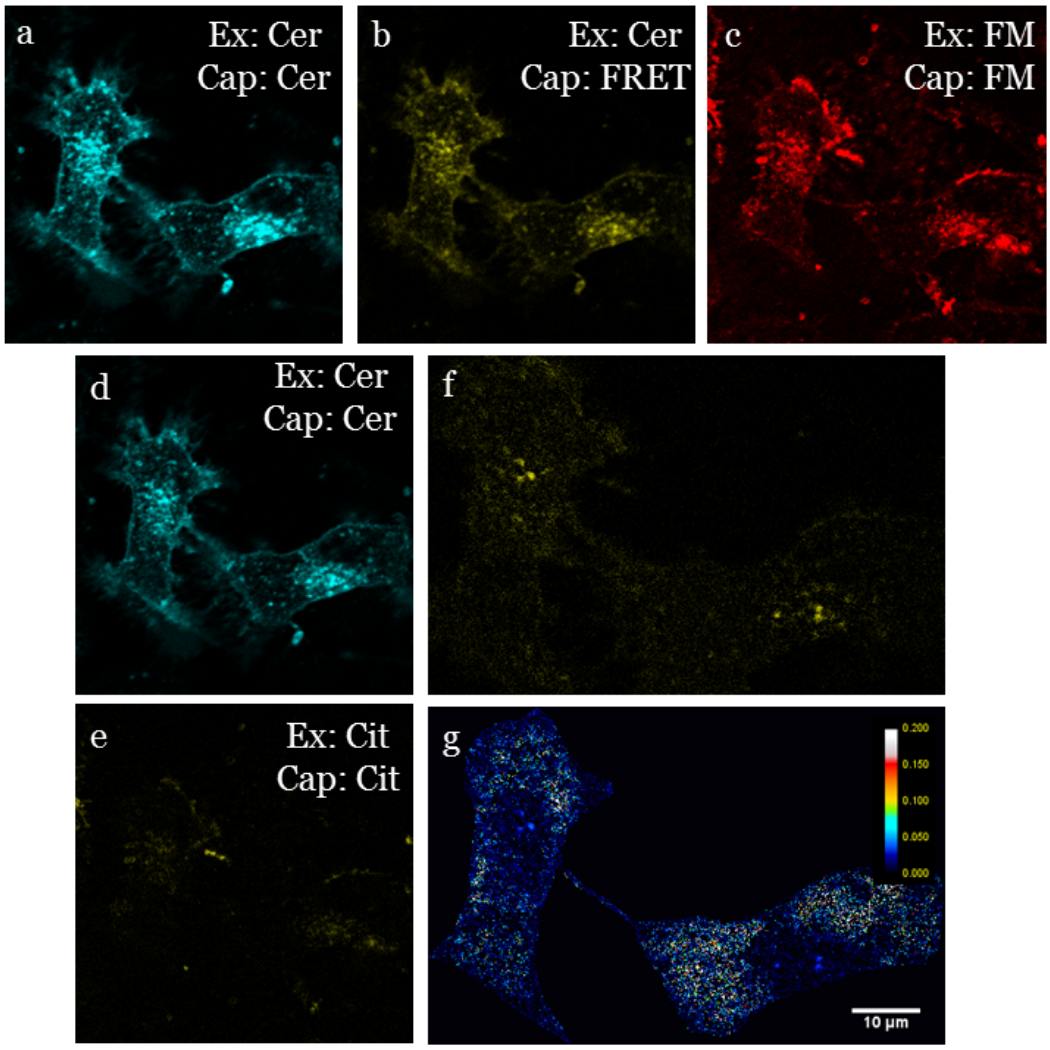

Figure S-5.3.1. Representative intensity images of N2A transfected with cerulean-VAMP2 only (donor control). Images are taken in five channels split into three phases: Phase 1**(a)** excite and capture cerulean; **(b)** excite cerulean and capture citrine (FRET); Phase 2: **(c)** excite and capture FM-464; Phase 3: **(d)** excite and capture cerulean; **(e)** excite and capture citrine; **(f)** Software constructed FRET image after bleed over correction from (b); **(g)** Software constructed effective transfer ratio (ETR) image after bleed over and donor intensity correction.

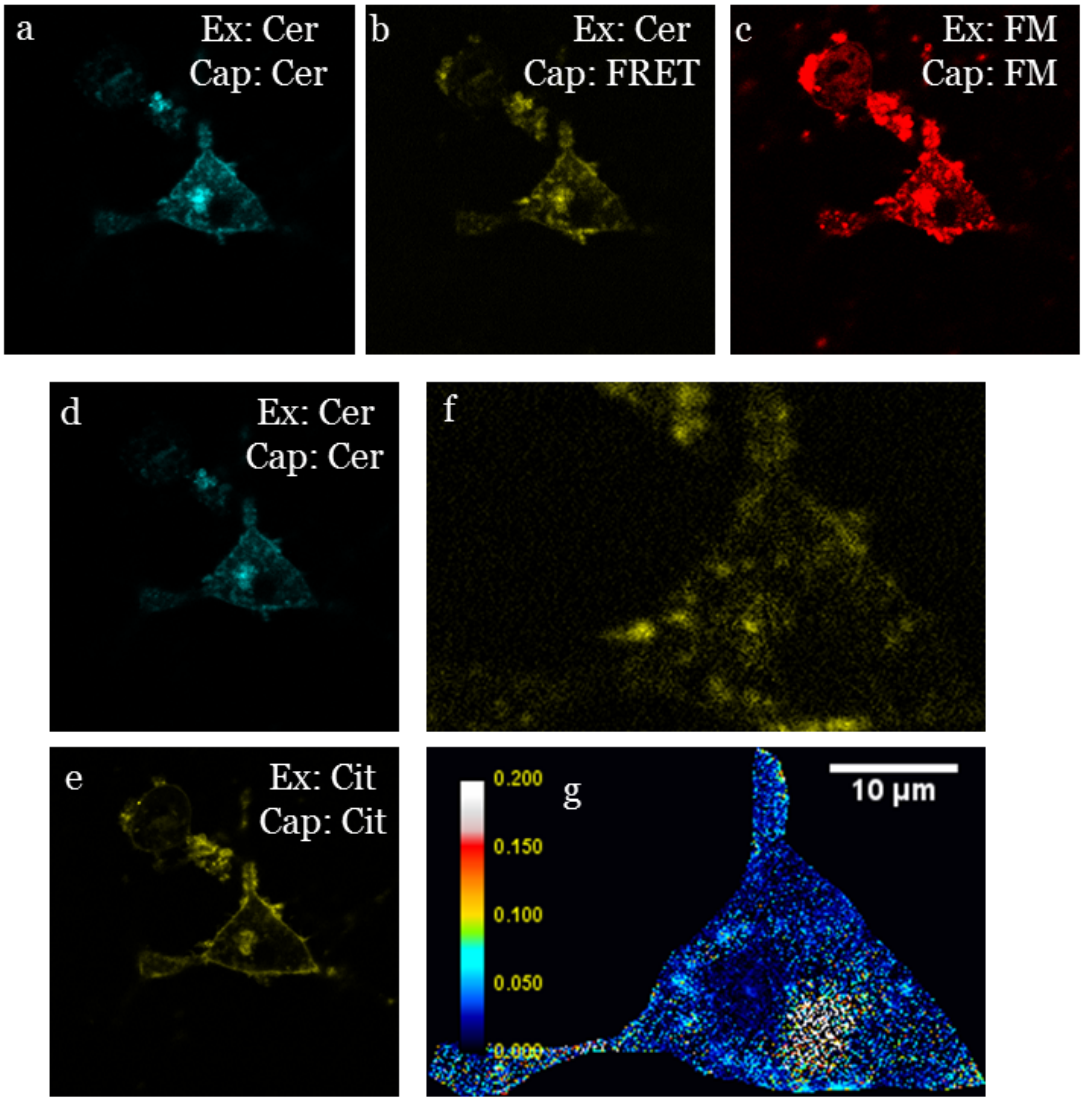

Figure S-5.3.2. Representative intensity images of N2A transfected with cerulean-VAMP2 and citrine-SNAP25 (FRET control). Images are taken in five channels split into three phases: Phase 1**(a)** excite and capture cerulean; **(b)** excite cerulean and capture citrine (FRET); Phase 2: **(c)** excite and capture FM-464; Phase 3: **(d)** excite and capture cerulean; **(e)** excite and capture citrine; **(f)** Software constructed FRET image after bleed over correction from (b); **(g)** Software constructed effective transfer ratio (ETR) image after bleed over and donor intensity correction.

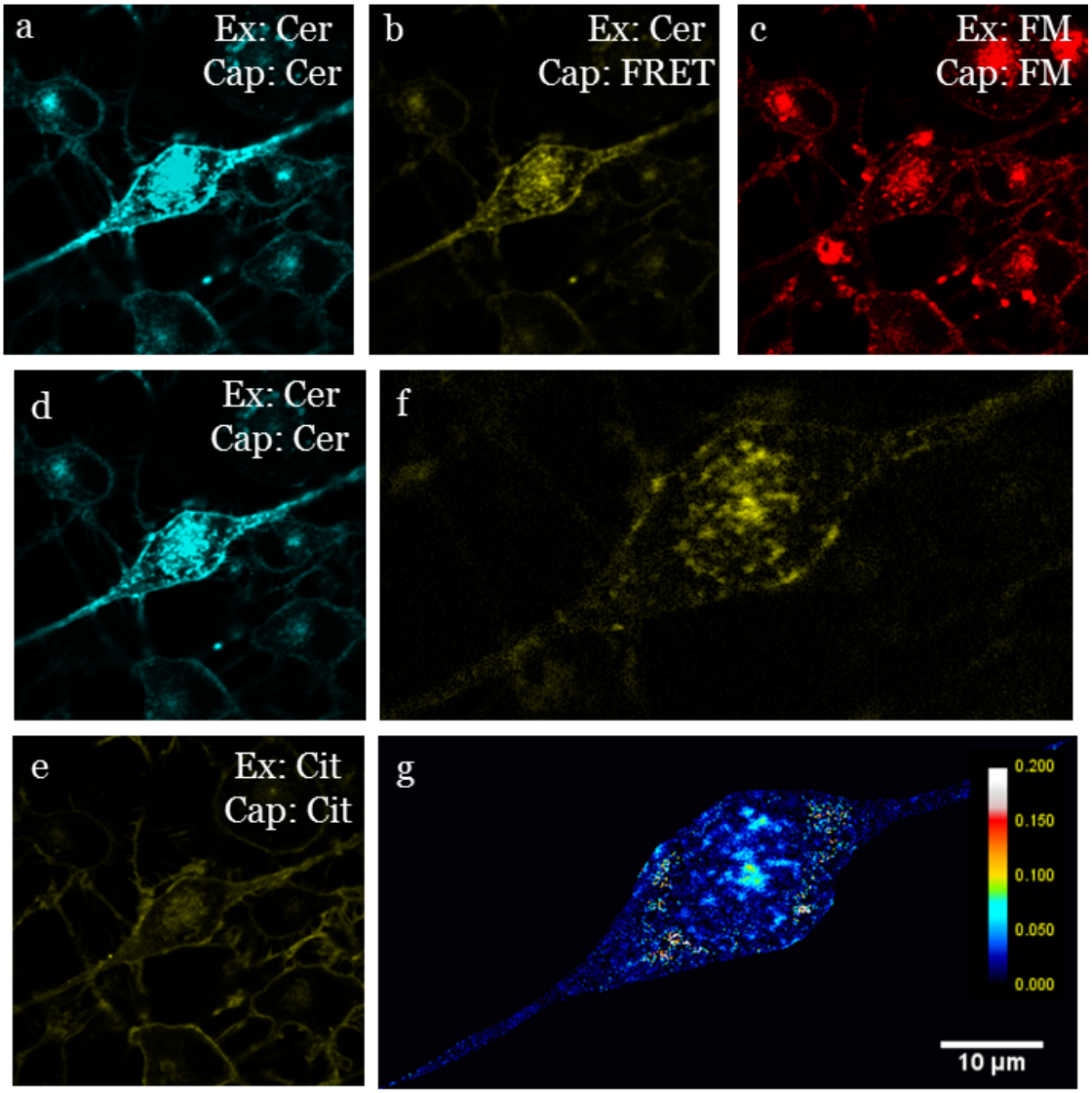

Figure S-5.3.3. Representative intensity images of N2A transfected with cerulean-VAMP2 and citrine-SNAP25 pretreated with Aβ40. Images are taken in five channels split into three phases: Phase 1**(a)** excite and capture cerulean; **(b)** excite cerulean and capture citrine (FRET); Phase 2: **(c)** excite and capture FM-464; Phase 3: **(d)** excite and capture cerulean; **(e)** excite and capture citrine; **(f)** Software constructed FRET image after bleed over correction from (b); **(g)** Software constructed effective transfer ratio (ETR) image after bleed over and donor intensity correction.

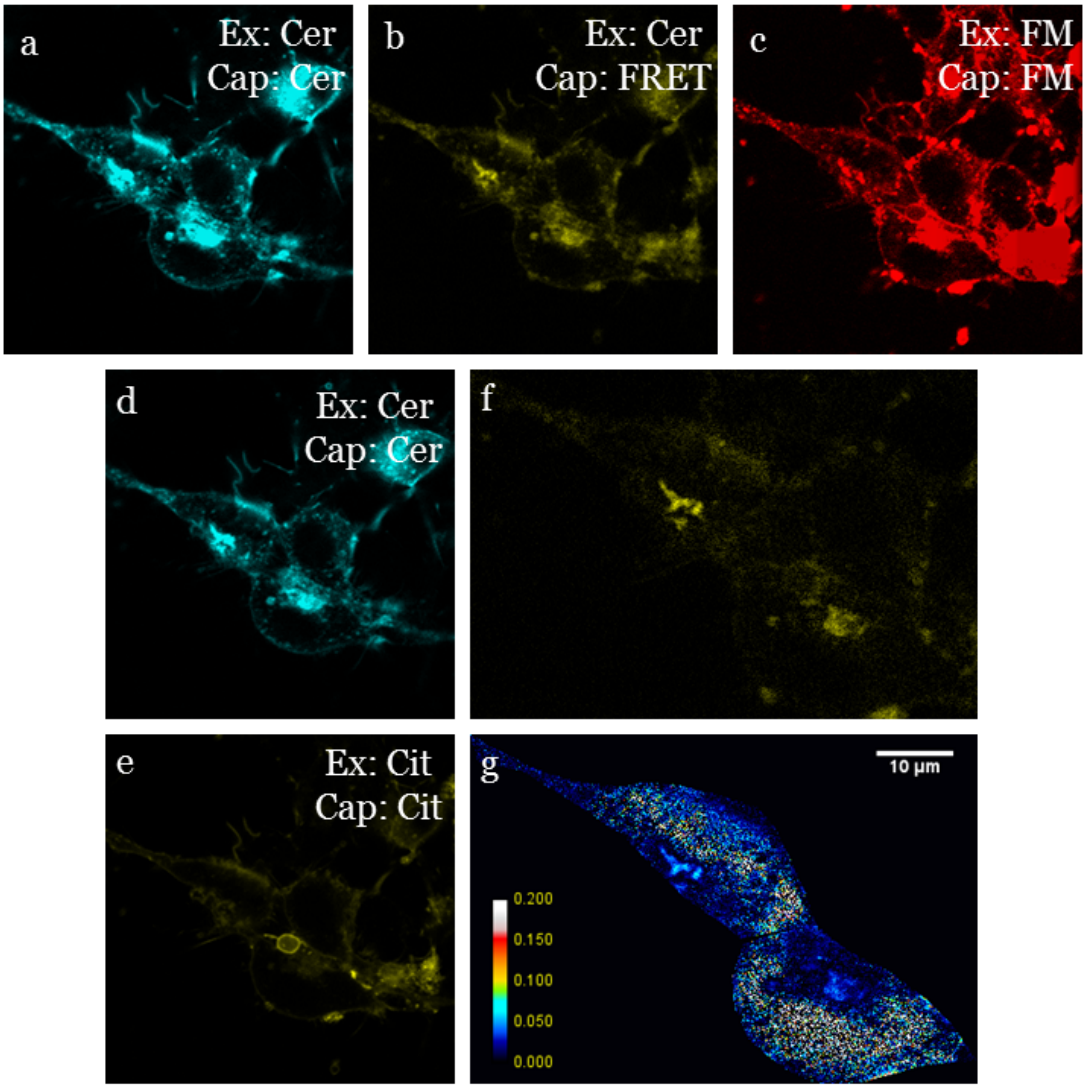

Figure S-5.3.4. Representative intensity images of N2A transfected with cerulean-VAMP2 and citrine-SNAP25 pretreated with Aβ42. Images are taken in five channels split into three phases: Phase 1**(a)** excite and capture cerulean; **(b)** excite cerulean and capture citrine (FRET); Phase 2: **(c)** excite and capture FM-464; Phase 3: **(d)** excite and capture cerulean; **(e)** excite and capture citrine; **(f)** Software constructed FRET image after bleed over correction from (b); **(g)** Software constructed effective transfer ratio (ETR) image after bleed over and donor intensity correction.

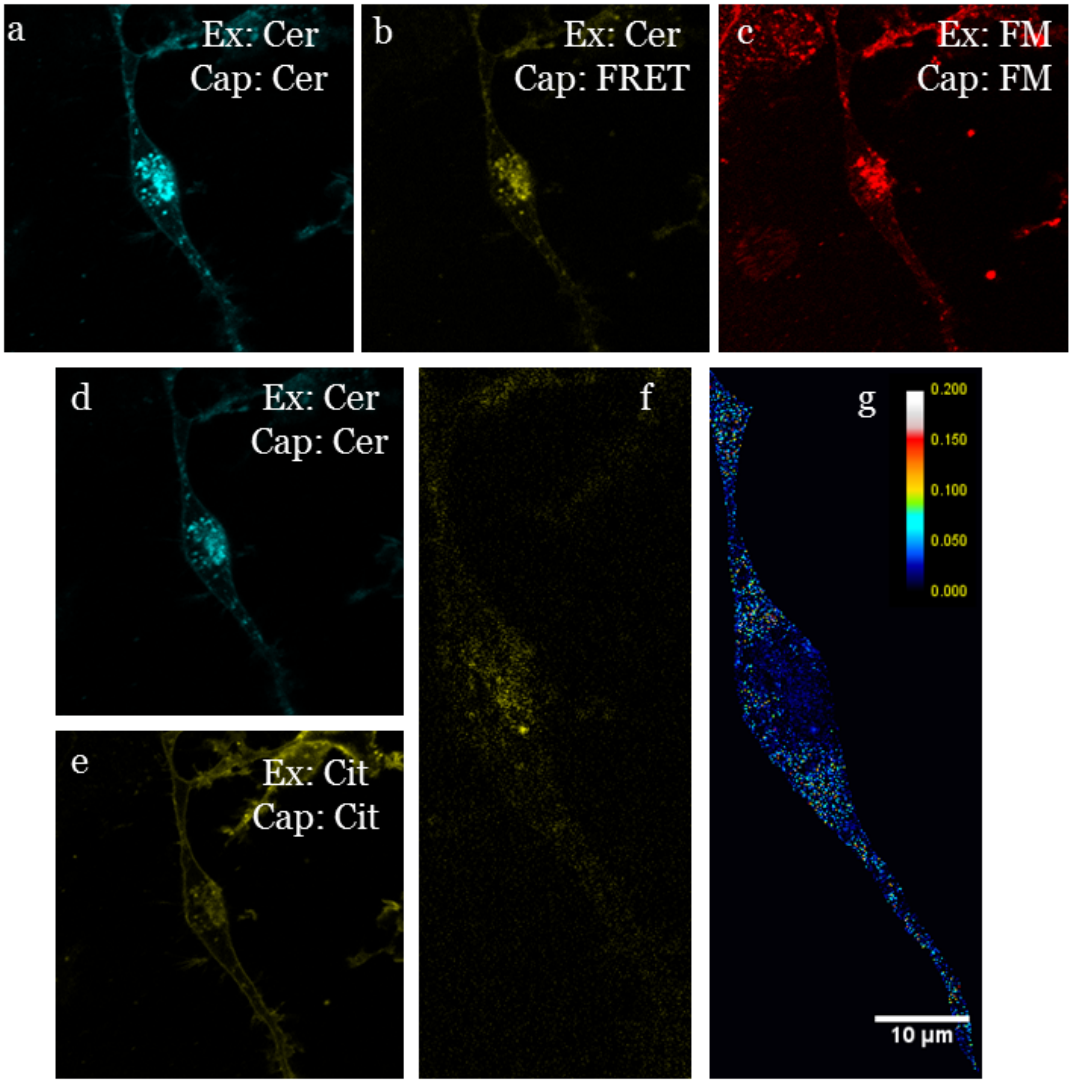

Figure S-5.3.5. Representative intensity images of N2A transfected with cerulean-VAMP2 and citrine-SNAP25 pretreated with TeNT. Images are taken in five channels split into three phases: Phase 1**(a)** excite and capture cerulean; **(b)** excite cerulean and capture citrine (FRET); Phase 2: **(c)** excite and capture FM-464; Phase 3: **(d)** excite and capture cerulean; **(e)** excite and capture citrine; **(f)** Software constructed FRET image after bleed over correction from (b); **(g)** Software constructed effective transfer ratio (ETR) image after bleed over and donor intensity correction.

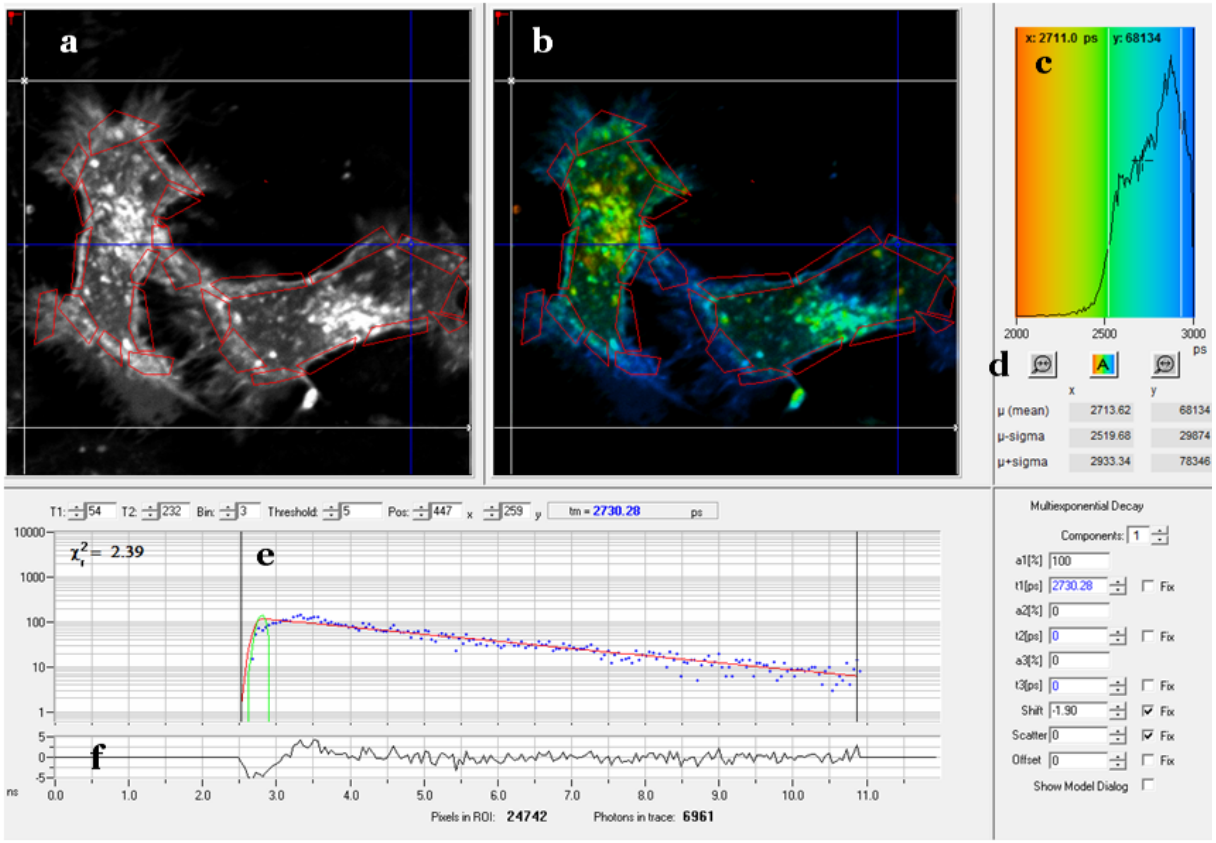

Figure S-5.4.1. Fluorescence lifetime image of N2A cells transfected with cerulean-VAMP2 (donor only) negative control system. Screen shot image of SPCImage software demonstrate **(a)** intensity image **(b)** spatially resolved lifetime image, followed by **(c)** frequency histogram of the lifetime in that ROI; color coded for the range 2000 (red) to 3000 (blue) picoseconds and quantified for **(d)** mean average lifetime and corresponding range. The decaying photons have been fit to **(e)** mono-exponential decay, that fits well, as checked by **(f)** random distribution of weighted residuals and chi square value < 2.5. The red regions in (a)intensity and (b) lifetime windows represent the region of interest (ROI) that have been used to depict the (c) frequency histogram. The mean lifetime at that point (vesicular fusion process) can be assessed by moving the cursor and obtaining the reading.

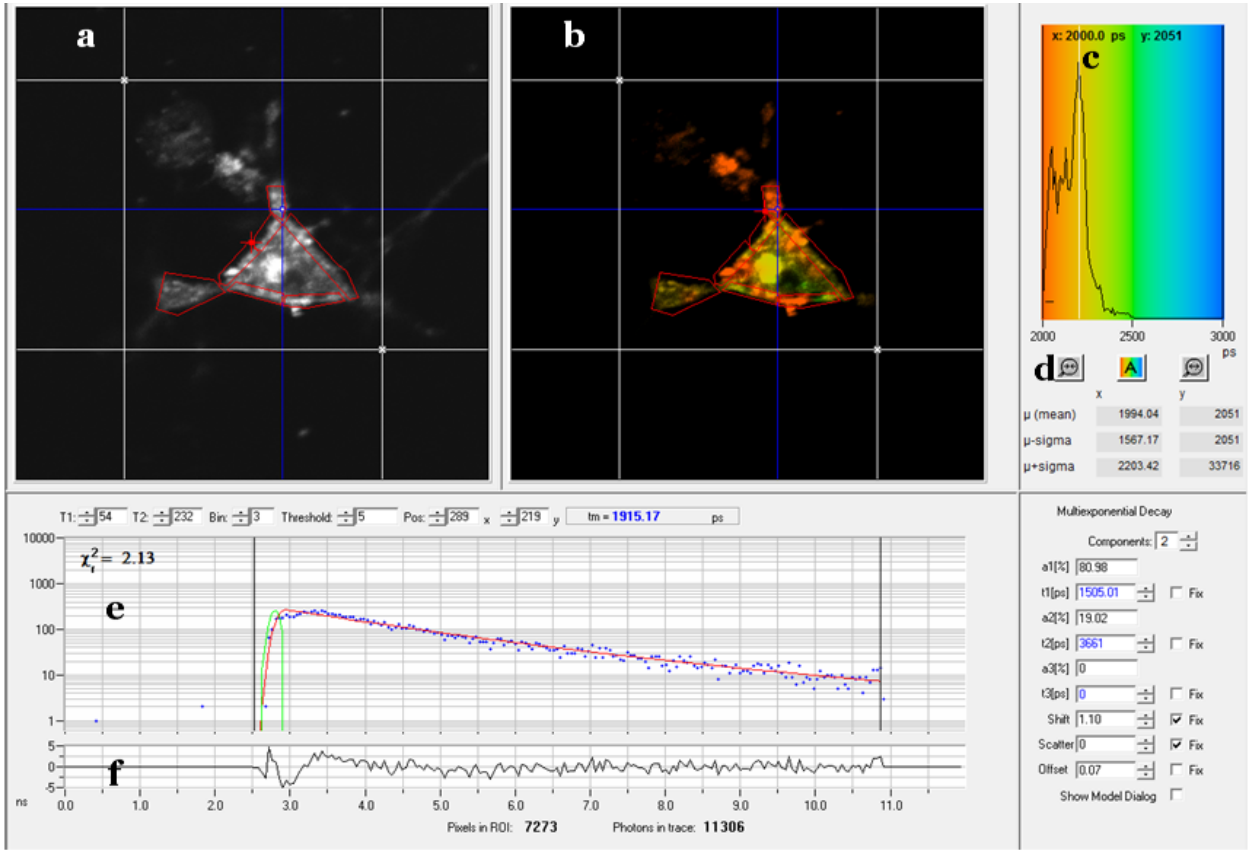

Figure S-5.4.2. Fluorescence lifetime image of N2A cells transfected with cerulean-VAMP-2 and citrine-SNAP25 (FRET or positive control system). Screen shot image of SPCImage software demonstrate **(a)** intensity image **(b)** spatially resolved lifetime image, followed by **(c)** frequency histogram of the lifetime in that ROI; color coded for the range 2000 (red) to 3000 (blue) picoseconds and quantified for **(d)** mean average lifetime and corresponding range. The decaying photons have been fit to **(e)** mono-exponential decay, that fits well, as checked by **(f)** random distribution of weighted residuals and chi square value < 2.5. The red regions in (a)intensity and (b) lifetime windows represent the region of interest (ROI) that have been used to depict the (c) frequency histogram. The mean lifetime at that point (vesicular fusion process) can be assessed by moving the cursor and obtaining the reading.

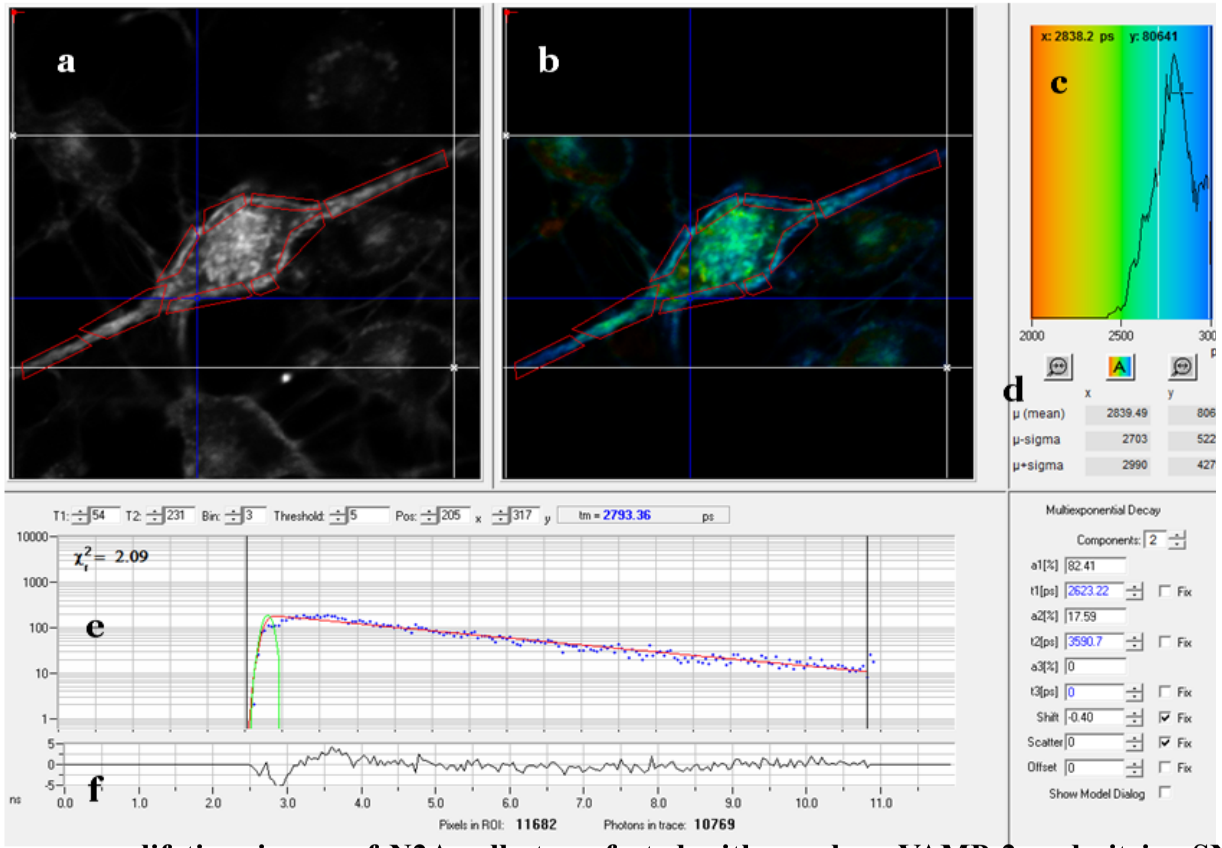

Figure S-5.4.3. Fluorescence lifetime image of N2A cells transfected with cerulean-VAMP-2 and citrine-SNAP25; that has been pretreated with Aβ40. Screen shot image of SPCImage software demonstrate **(a)** intensity image **(b)** spatially resolved lifetime image, followed by **(c)** frequency histogram of the lifetime in that ROI; color coded for the range 2000 (red) to 3000 (blue) picoseconds and quantified for **(d)** mean average lifetime and corresponding range. The decaying photons have been fit to **(e)** mono-exponential decay, that fits well, as checked by **(f)** random distribution of weighted residuals and chi square value < 2.5. The red regions in (a)intensity and (b) lifetime windows represent the region of interest (ROI) that have been used to depict the (c) frequency histogram. The mean lifetime at that point (vesicular fusion process) can be assessed by moving the cursor and obtaining the reading.

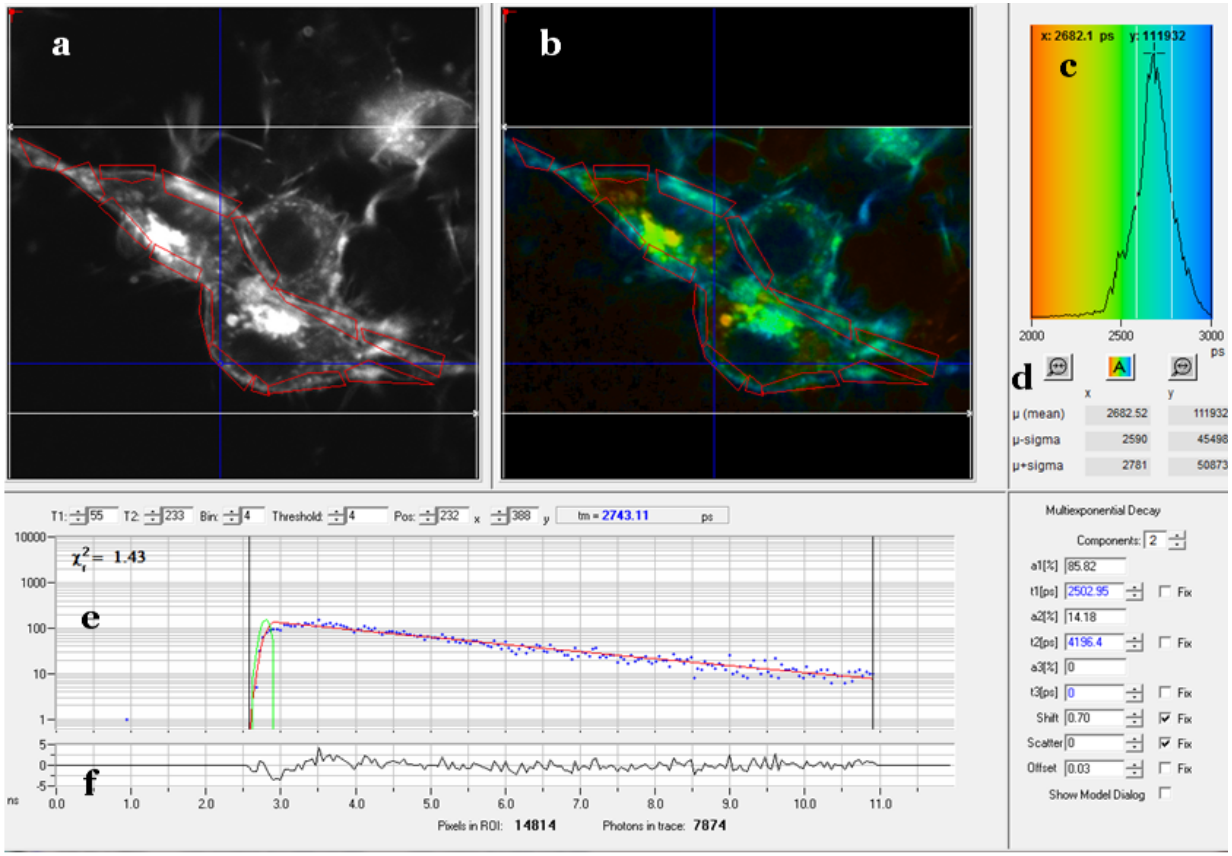

ure S-5.4.4. Fluorescence lifetime image of N2A cells transfected with cerulean-VAMP-2 and citrine-SNAP25; that has been pretreated with Aβ42. Screen shot image of SPCImage software demonstrate **(a)** intensity image **(b)** spatially resolved lifetime image, followed by **(c)** frequency histogram of the lifetime in that ROI; color coded for the range 2000 (red) to 3000 (blue) picoseconds and quantified for **(d)** mean average lifetime and corresponding range. The decaying photons have been fit to **(e)** mono-exponential decay, that fits well, as checked by **(f)** random distribution of weighted residuals and chi square value < 2.5. The red regions in (a)intensity and (b) lifetime windows represent the region of interest (ROI) that have been used to depict the (c) frequency histogram. The mean lifetime at that point (vesicular fusion process) can be assessed by moving the cursor and obtaining the reading.

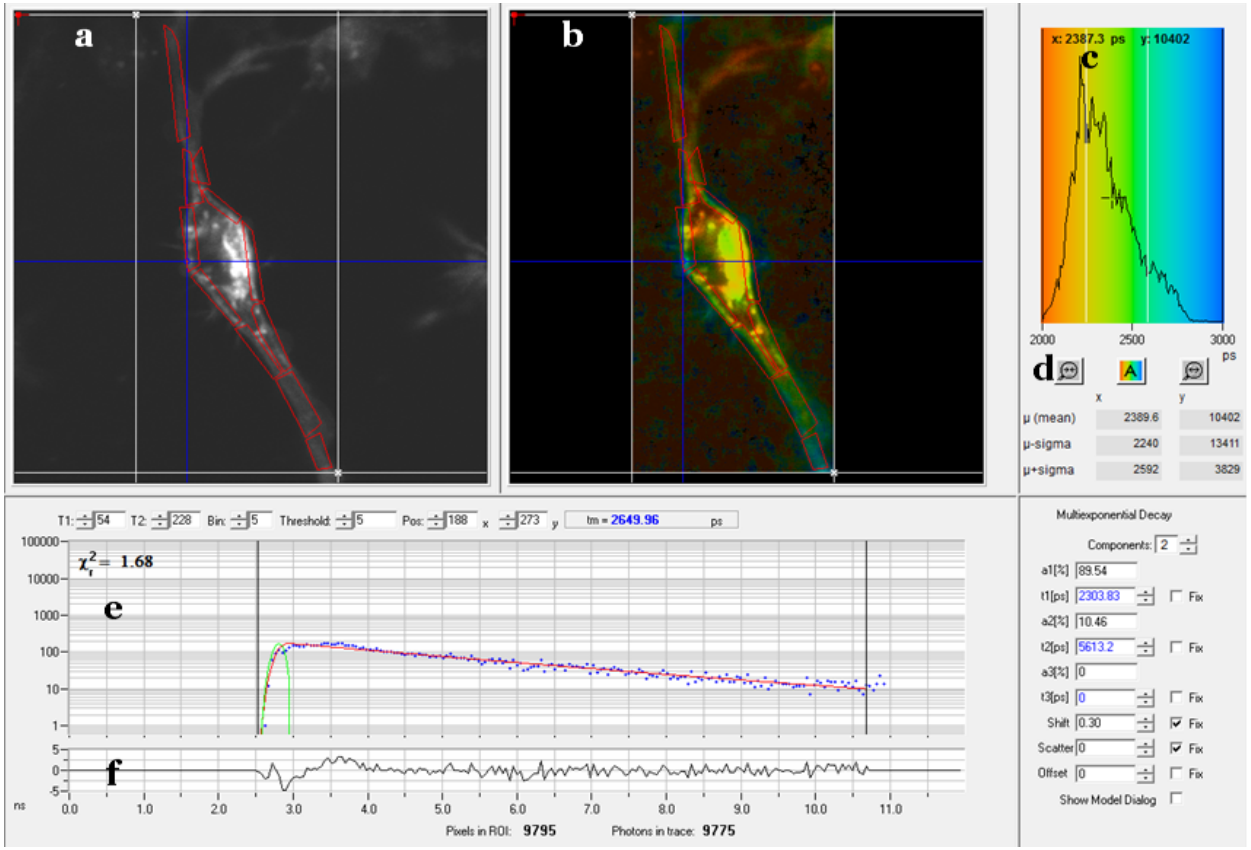

Figure S-5-4.5. Fluorescence lifetime image of N2A cells transfected with cerulean-VAMP-2 and citrine-SNAP25; that has been pretreated with TeNT. Screen shot image of SPCImage software demonstrate **(a)** intensity image **(b)** spatially resolved lifetime image, followed by **(c)** frequency histogram of the lifetime in that ROI; color coded for the range 2000 (red) to 3000 (blue) picoseconds and quantified for **(d)** mean average lifetime and corresponding range. The decaying photons have been fit to **(e)** mono-exponential decay, that fits well, as checked by **(f)** random distribution of weighted residuals and chi square value < 2.5. The red regions in (a)intensity and (b) lifetime windows represent the region of interest (ROI) that have been used to depict the (c) frequency histogram. The mean lifetime at that point (vesicular fusion process) can be assessed by moving the cursor and obtaining the reading.

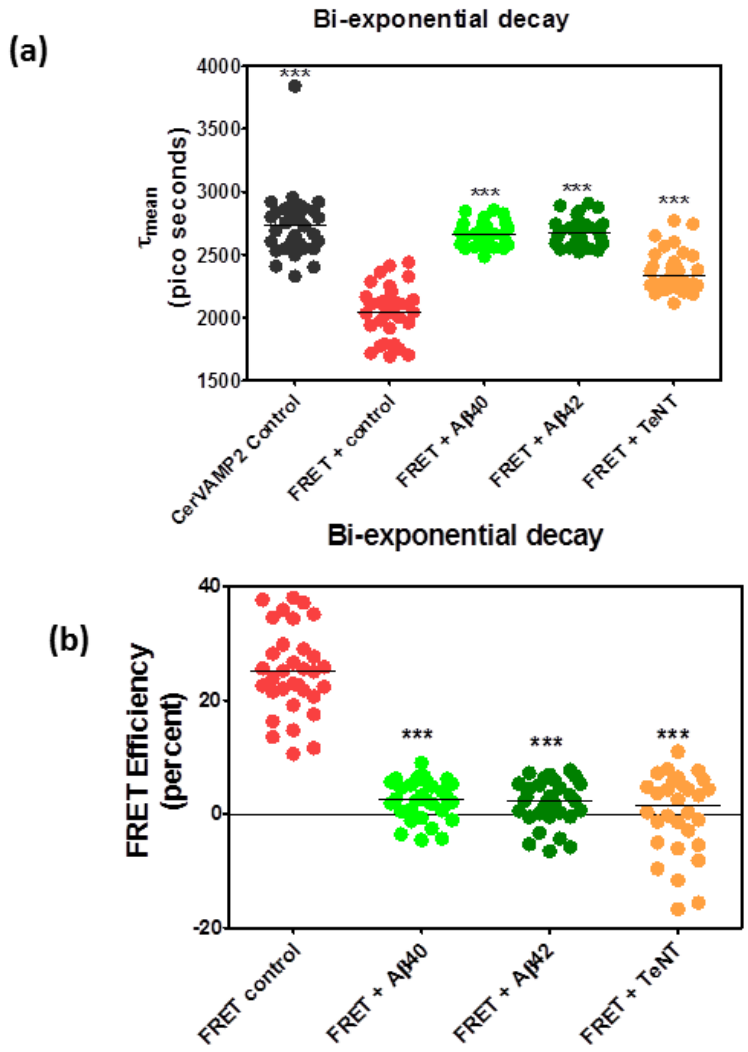

Figure S-5.4.6. Lifetime measurements and corresponding FRET efficiency of functional vesicular fusion processes in transfected N2A cells. A-B Changes in **(A)** τ_{mean} or mean lifetime of donor (cerulean) and **(B)** FRET efficiency in cells transfected with cer-VAMP2 only (Cer-VAMP2 control) or both cer-VAMP2 and Cit-SNAP25 (FRET) that are pretreated with Aβ40, Aβ42 or TeNT. 30-40 functional vesicular fusion processes at membrane are estimated using FM dye channel image. Data represented as scatter dot plot of individual lifetime measurement from bi-exponential decay plot and corresponding median. Significance determined using one-way ANOVA test. (*** $p<0.001$)

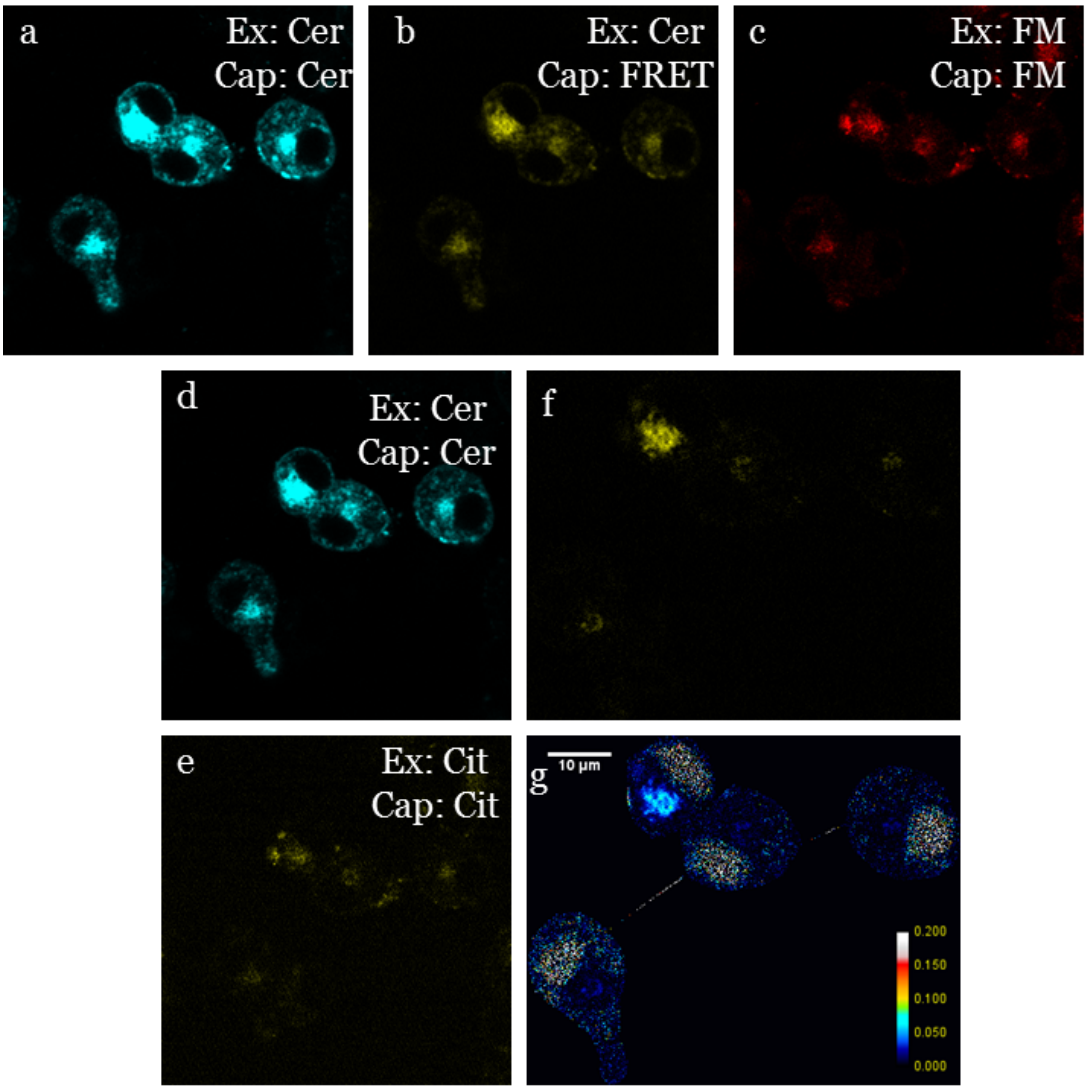

Figure S-5.5.1. Representative intensity images of N2A transfected with cerulean-VAMP2 only (donor control) at high potassium. Images are taken in five channels split into three phases: Phase 1**(a)** excite and capture cerulean; **(b)** excite cerulean and capture citrine (FRET); Phase 2: **(c)** excite and capture FM-464; Phase 3: **(d)** excite and capture cerulean; **(e)** excite and capture citrine; **(f)** Software constructed FRET image after bleed over correction from (b); **(g)** Software constructed effective transfer ratio (ETR) image after bleed over and donor intensity correction.

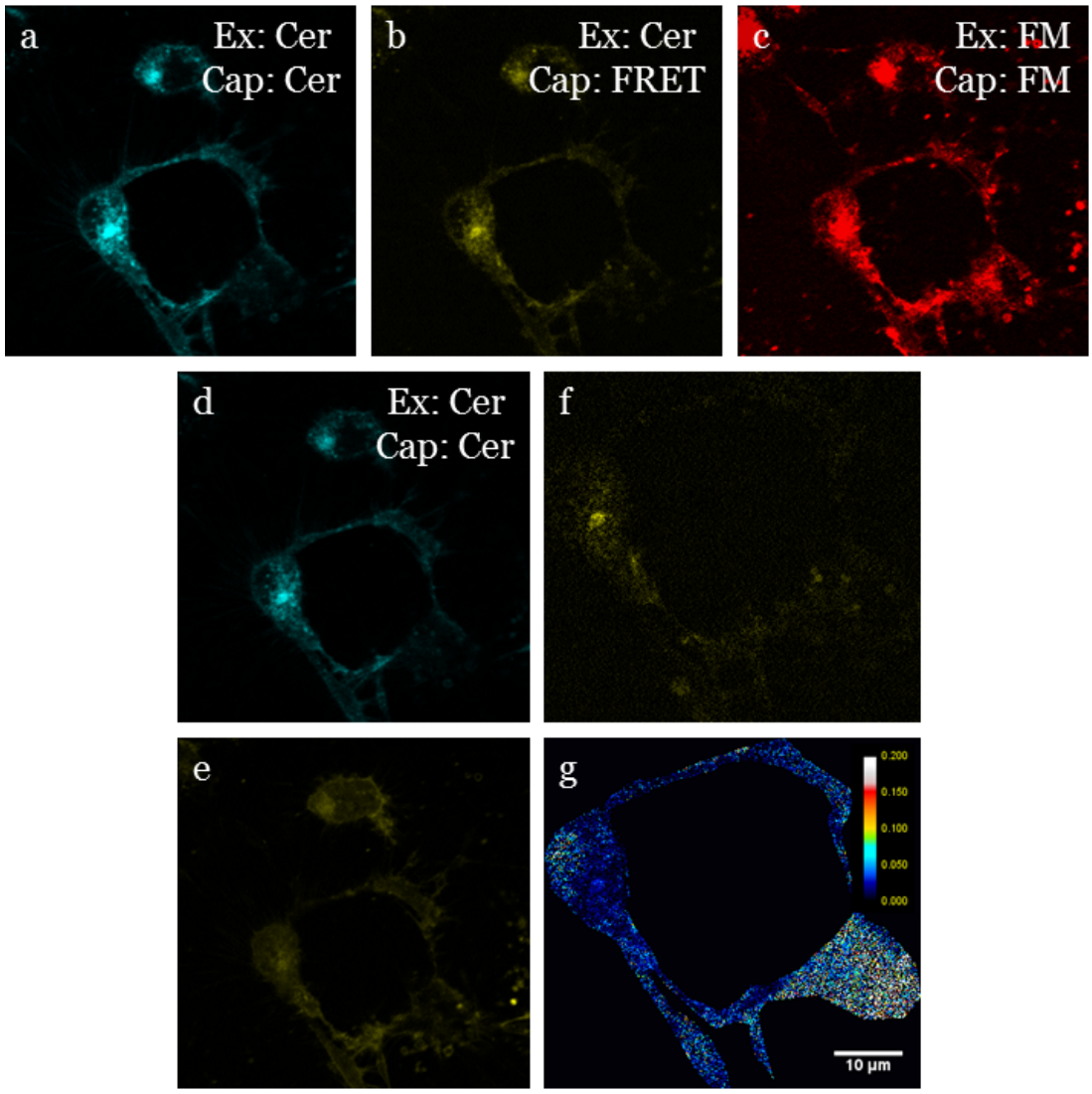

Figure S-5.5.2. Representative intensity images of N2A transfected with cerulean-VAMP2 and citrine-SNAP25 (FRET control) at high potassium. Images are taken in five channels split into three phases: Phase 1**(a)** excite and capture cerulean; **(b)** excite cerulean and capture citrine (FRET); Phase 2: **(c)** excite and capture FM-464; Phase 3: **(d)** excite and capture cerulean; **(e)** excite and capture citrine; **(f)** Software constructed FRET image after bleed over correction from (b); **(g)** Software constructed effective transfer ratio (ETR) image after bleed over and donor intensity correction.

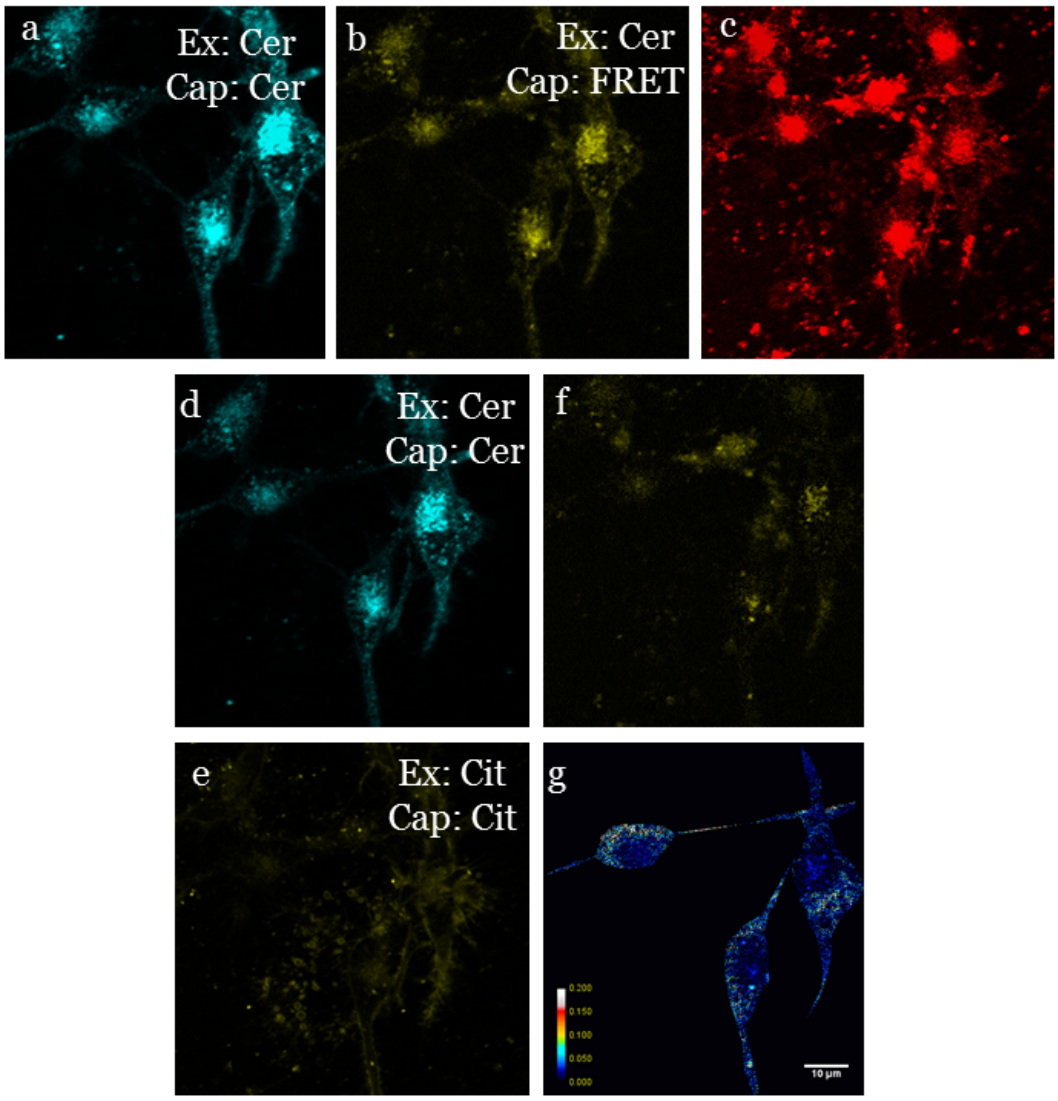

Figure S-5.5.3. Representative intensity images of N2A transfected with cerulean-VAMP2 and citrine-SNAP25 pretreated with Aβ40 at high potassium. Images are taken in five channels split into three phases: Phase 1**(a)** excite and capture cerulean; **(b)** excite cerulean and capture citrine (FRET); Phase 2: **(c)** excite and capture FM-464; Phase 3: **(d)** excite and capture cerulean; **(e)** excite and capture citrine; **(f)** Software constructed FRET image after bleed over correction from (b); **(g)** Software constructed effective transfer ratio (ETR) image after bleed over and donor intensity correction.

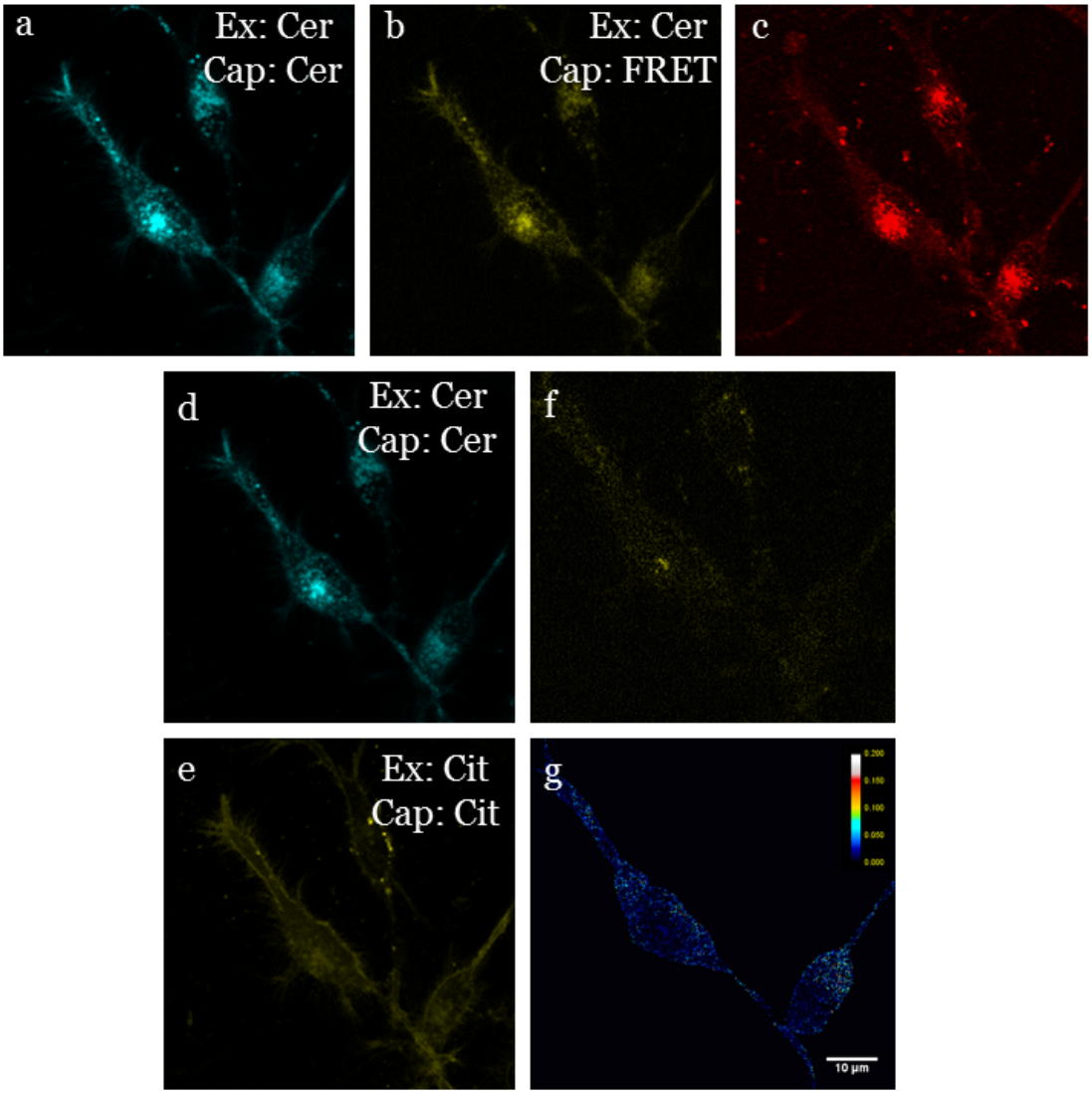

Figure S-5.5.4. Representative intensity images of N2A transfected with cerulean-VAMP2 and citrine-SNAP25 pretreated with Aβ42 at high potassium. Images are taken in five channels split into three phases: Phase 1**(a)** excite and capture cerulean; **(b)** excite cerulean and capture citrine (FRET); Phase 2: **(c)** excite and capture FM-464; Phase 3: **(d)** excite and capture cerulean; **(e)** excite and capture citrine; **(f)** Software constructed FRET image after bleed over correction from (b); **(g)** Software constructed effective transfer ratio (ETR) image after bleed over and donor intensity correction.

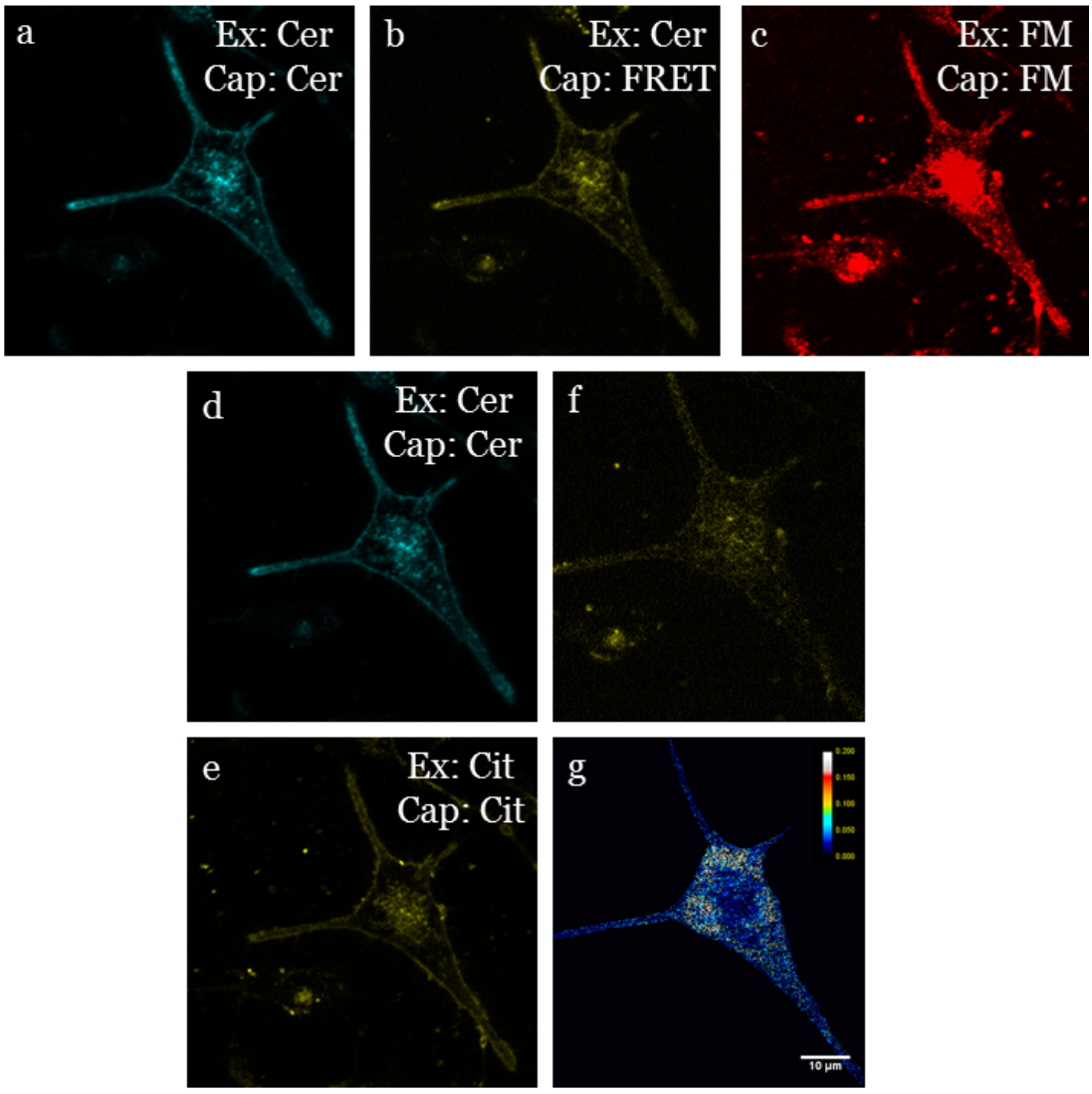

Figure S-5.5.5. Representative intensity images of N2A transfected with cerulean-VAMP2 and citrine-SNAP25 pretreated with TeNT at high potassium. Images are taken in five channels split into three phases: Phase 1**(a)** excite and capture cerulean; **(b)** excite cerulean and capture citrine (FRET); Phase 2: **(c)** excite and capture FM-464; Phase 3: **(d)** excite and capture cerulean; **(e)** excite and capture citrine; **(f)** Software constructed FRET image after bleed over correction from (b); **(g)** Software constructed effective transfer ratio (ETR) image after bleed over and donor intensity correction.

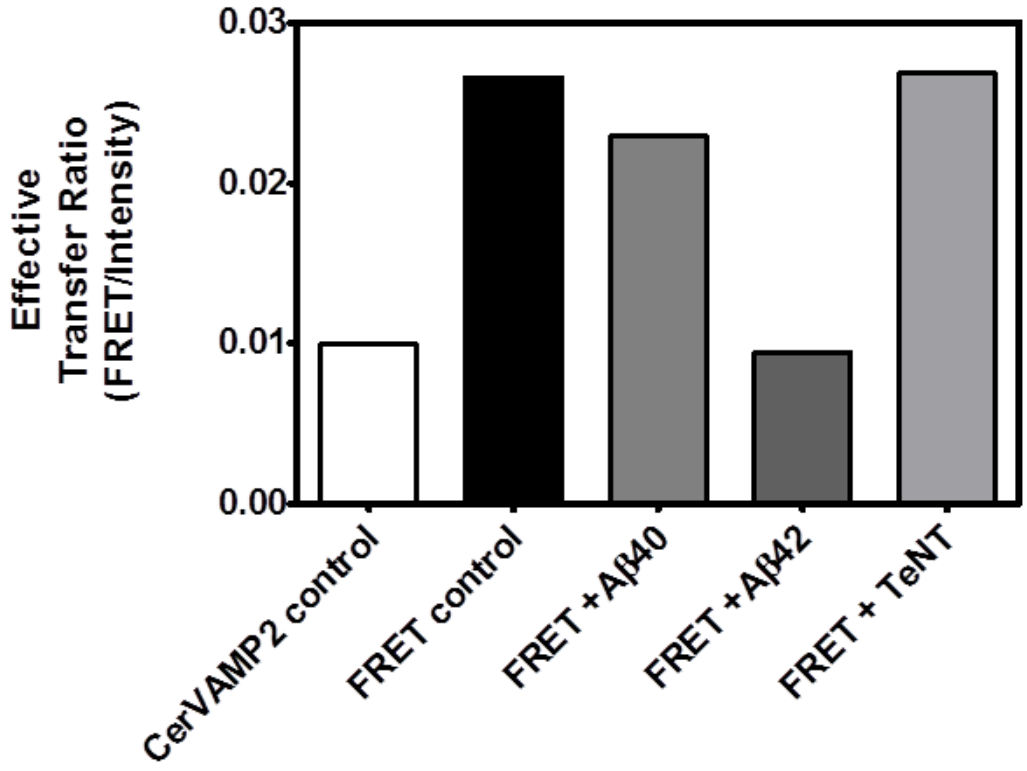

Figure S-5.5.6. Semi quantitative plot of effective FRET transfer ratios of membrane intensities represented in Figures S-5.5. Data demonstrates effective FRET transfer ratio or corrected FRET normalized to the donor (cerulean channel) intensity measured only at membrane using mask tool in Fiji software. Bars represent mean ETR intensity at the membrane.

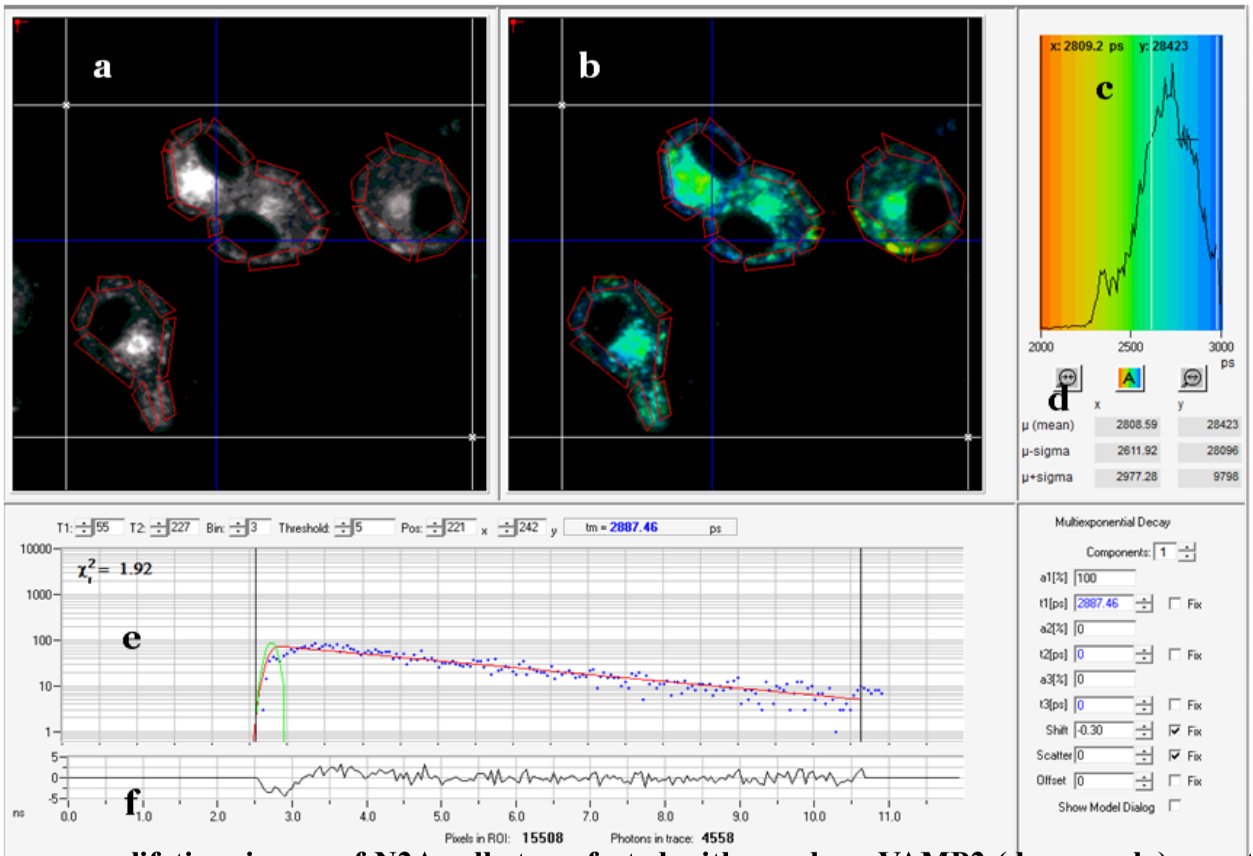

Figure S-5-6.1. Fluorescence lifetime image of N2A cells transfected with cerulean-VAMP2 (donor only) negative control system at high potassium. Screen shot image of SPCImage software demonstrate **(a)** intensity image **(b)** spatially resolved lifetime image, followed by **(c)** frequency histogram of the lifetime in that ROI; color coded for the range 2000 (red) to 3000 (blue) picoseconds and quantified for **(d)** mean average lifetime and corresponding range. The decaying photons have been fit to **(e)** mono-exponential decay, that fits well, as checked by **(f)** random distribution of weighted residuals and chi square value < 2.5. The red regions in (a)intensity and (b) lifetime windows represent the region of interest (ROI) that have been used to depict the (c) frequency histogram. The mean lifetime at that point (vesicular fusion process) can be assessed by moving the cursor and obtaining the reading.

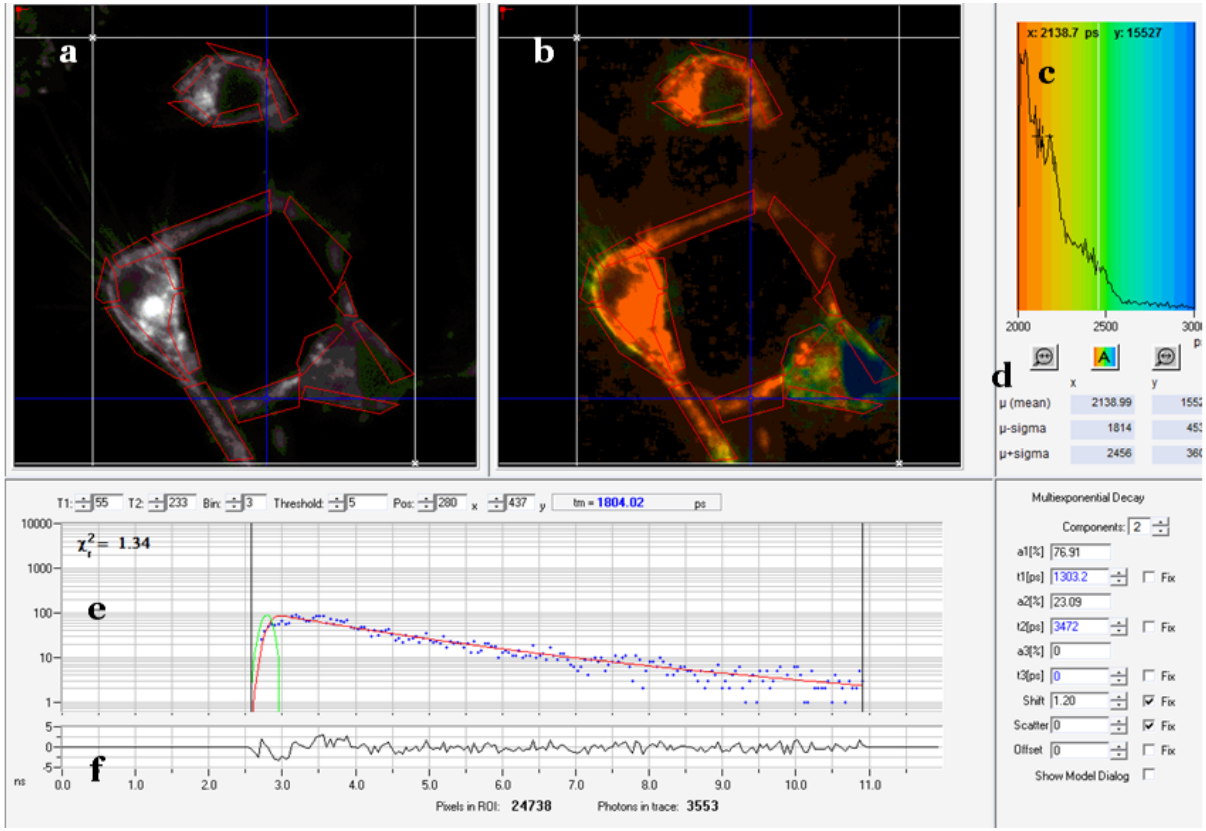

Figure S-5.6.2. Fluorescence lifetime image of N2A cells transfected with cerulean-VAMP-2 and citrine-SNAP25 (FRET or positive control system)at high potassium. Screen shot image of SPCImage software demonstrate **(a)** intensity image **(b)** spatially resolved lifetime image, followed by **(c)** frequency histogram of the lifetime in that ROI; color coded for the range 2000 (red) to 3000 (blue) picoseconds and quantified for **(d)** mean average lifetime and corresponding range. The decaying photons have been fit to **(e)** mono-exponential decay, that fits well, as checked by **(f)** random distribution of weighted residuals and chi square value < 2.5. The red regions in (a)intensity and (b) lifetime windows represent the region of interest (ROI) that have been used to depict the (c) frequency histogram. The mean lifetime at that point (vesicular fusion process) can be assessed by moving the cursor and obtaining the reading.

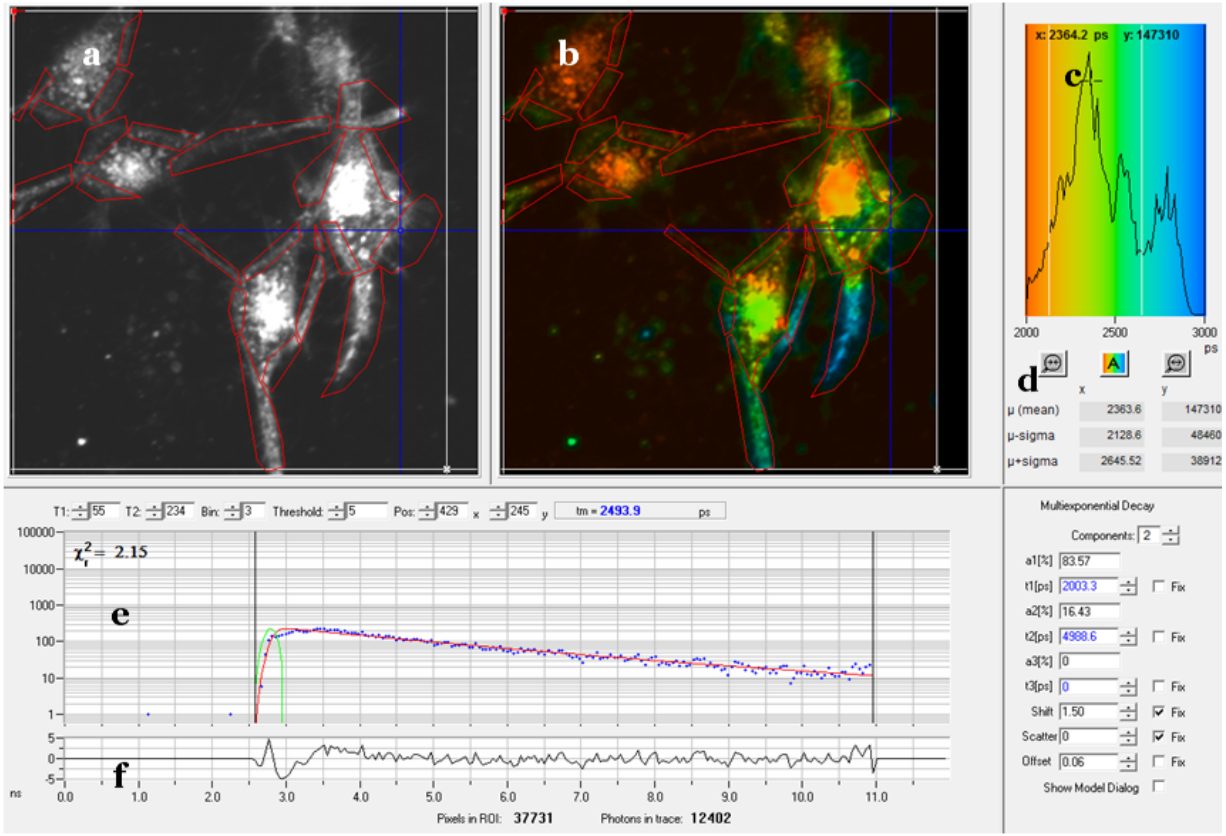

Figure S-5.6.3. Fluorescence lifetime image of N2A cells transfected with cerulean-VAMP-2 and citrine-SNAP25; that has been pretreated with Aβ40 at high potassium. Screen shot image of SPCImage software demonstrate **(a)** intensity image **(b)** spatially resolved lifetime image, followed by **(c)** frequency histogram of the lifetime in that ROI; color coded for the range 2000 (red) to 3000 (blue) picoseconds and quantified for **(d)** mean average lifetime and corresponding range. The decaying photons have been fit to **(e)** mono-exponential decay, that fits well, as checked by **(f)** random distribution of weighted residuals and chi square value < 2.5. The red regions in (a)intensity and (b) lifetime windows represent the region of interest (ROI) that have been used to depict the (c) frequency histogram. The mean lifetime at that point (vesicular fusion process) can be assessed by moving the cursor and obtaining the reading.

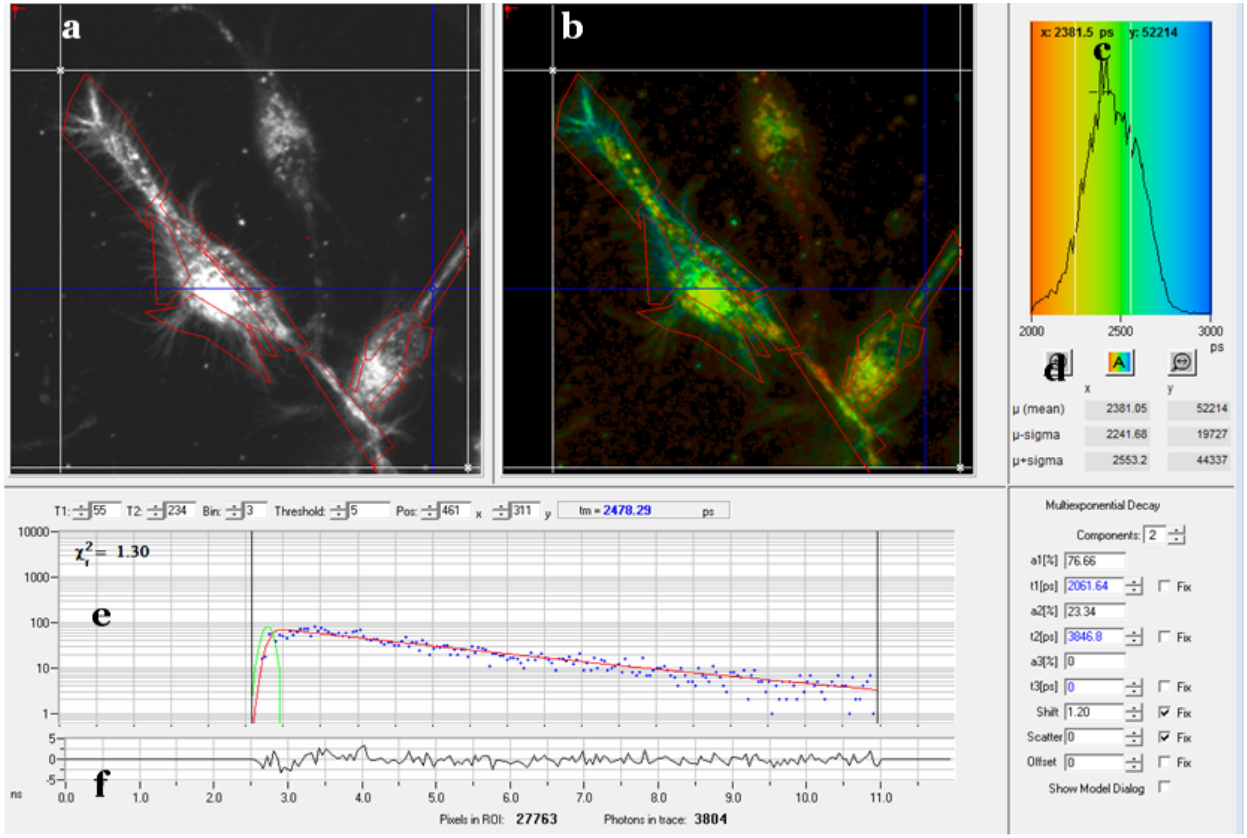

Figure S-5.6.4. Fluorescence lifetime image of N2A cells transfected with cerulean-VAMP-2 and citrine-SNAP25; that has been pretreated with Aβ42 at high potasium. Screen shot image of SPCImage software demonstrate **(a)** intensity image **(b)** spatially resolved lifetime image, followed by **(c)** frequency histogram of the lifetime in that ROI; color coded for the range 2000 (red) to 3000 (blue) picoseconds and quantified for **(d)** mean average lifetime and corresponding range. The decaying photons have been fit to **(e)** mono-exponential decay, that fits well, as checked by **(f)** random distribution of weighted residuals and chi square value < 2.5. The red regions in (a)intensity and (b) lifetime windows represent the region of interest (ROI) that have been used to depict the (c) frequency histogram. The mean lifetime at that point (vesicular fusion process) can be assessed by moving the cursor and obtaining the reading.

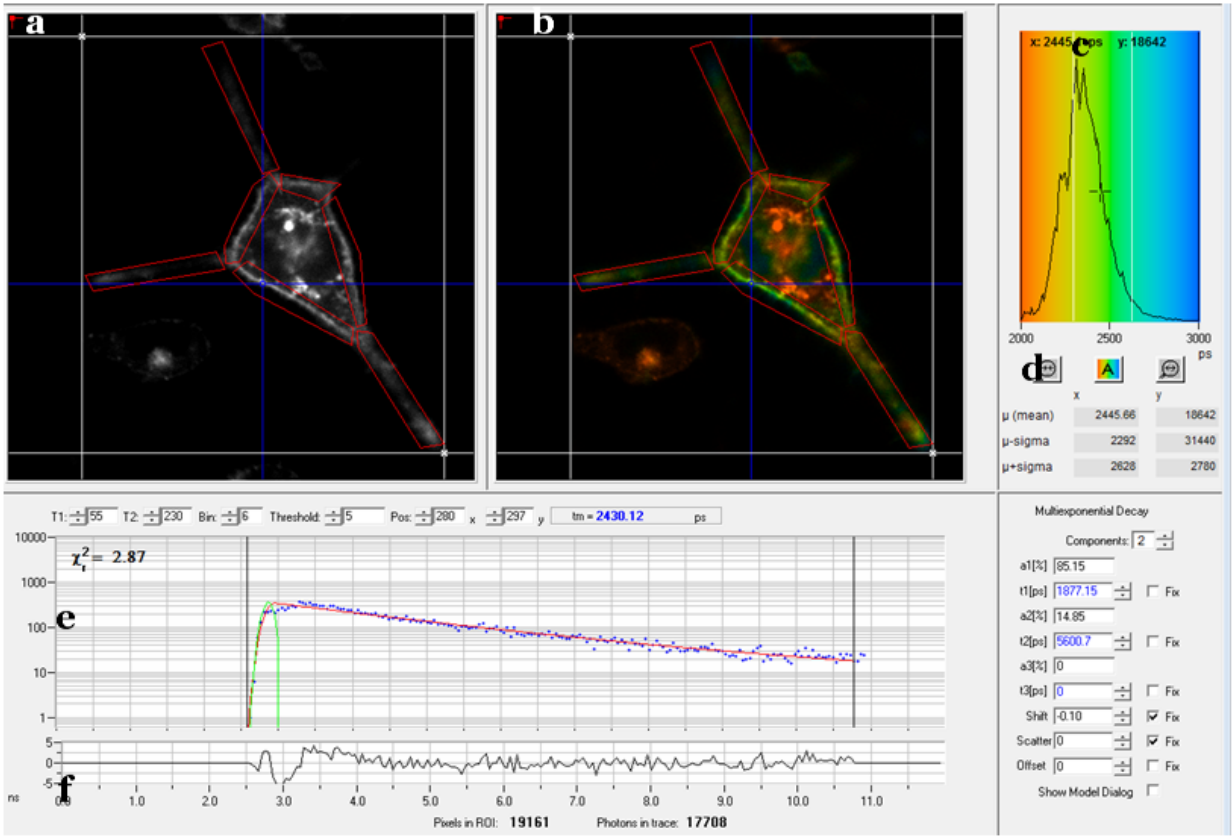

Figure S-5.6.5. Fluorescence lifetime image of N2A cells transfected with cerulean-VAMP-2 and citrine-SNAP25; that has been pretreated with TeNT at high potassium. Screen shot image of SPCImage software demonstrate **(a)** intensity image **(b)** spatially resolved lifetime image, followed by **(c)** frequency histogram of the lifetime in that ROI; color coded for the range 2000 (red) to 3000 (blue) picoseconds and quantified for **(d)** mean average lifetime and corresponding range. The decaying photons have been fit to **(e)** mono-exponential decay, that fits well, as checked by **(f)** random distribution of weighted residuals and chi square value < 2.5. The red regions in (a)intensity and (b) lifetime windows represent the region of interest (ROI) that have been used to depict the (c) frequency histogram. The mean lifetime at that point (vesicular fusion process) can be assessed by moving the cursor and obtaining the reading.

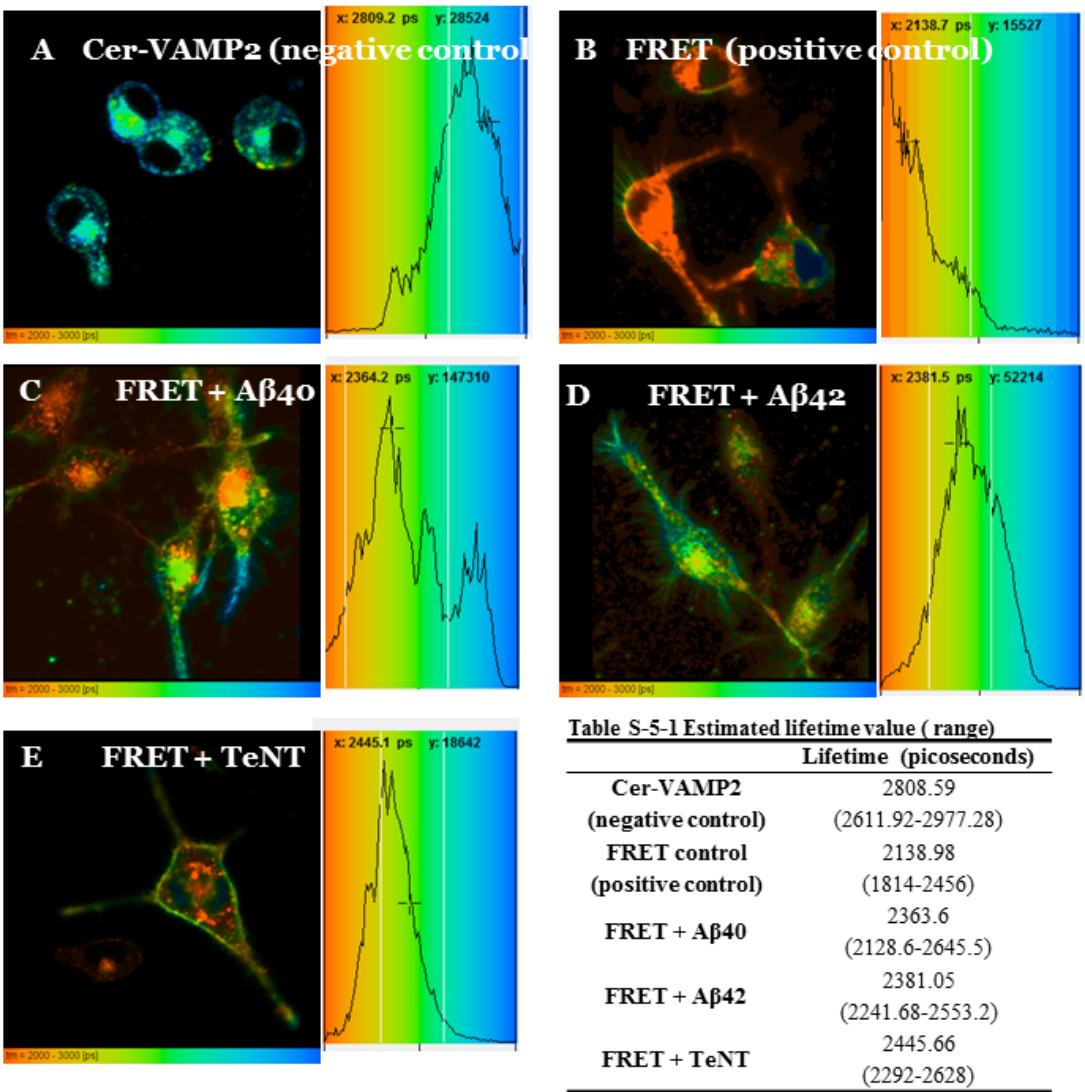

Table S-5-1 Estimated lifetime value (range)

	Lifetime (picoseconds)
Cer-VAMP2 (negative control)	2808.59 (2611.92-2977.28)
FRET control (positive control)	2138.98 (1814-2456)
FRET + Aβ40	2363.6 (2128.6-2645.5)
FRET + Aβ42	2381.05 (2241.68-2553.2)
FRET + TeNT	2445.66 (2292-2628)

Figure S-5.6.6. Spatial lifetime images of donor (cerulean) lifetime and corresponding frequency histograms in transfected N2A cells at high potassium. A-E Spatial lifetime images and frequency histograms obtained by measuring lifetime of cerulean (donor) by TCSPC in cells transfected with either **(A)** cer-VAMP2 only or **(B-E)** cerulean-VAMP2 and cit-SNAP25. Histogram represents lifetime frequency at the membrane. **A-B** Lifetime decreases from the blue range in **(A)** negative control cerulean-only transfected cell to yellow range in **(B)** dual transfected cells or FRET (positive control).**C-E** In the presence of **(C)** Aβ40; **(D)** Aβ42; and **(E)** TeNT; donor lifetime increases back from yellow to blue range . Color code represents lifetime from 2000 (red) to 2700 (blue) picoseconds. **Table S-5-1** shows changes in donor (cerulean) lifetime as estimated by B&H software for the membrane ROI in value (range)

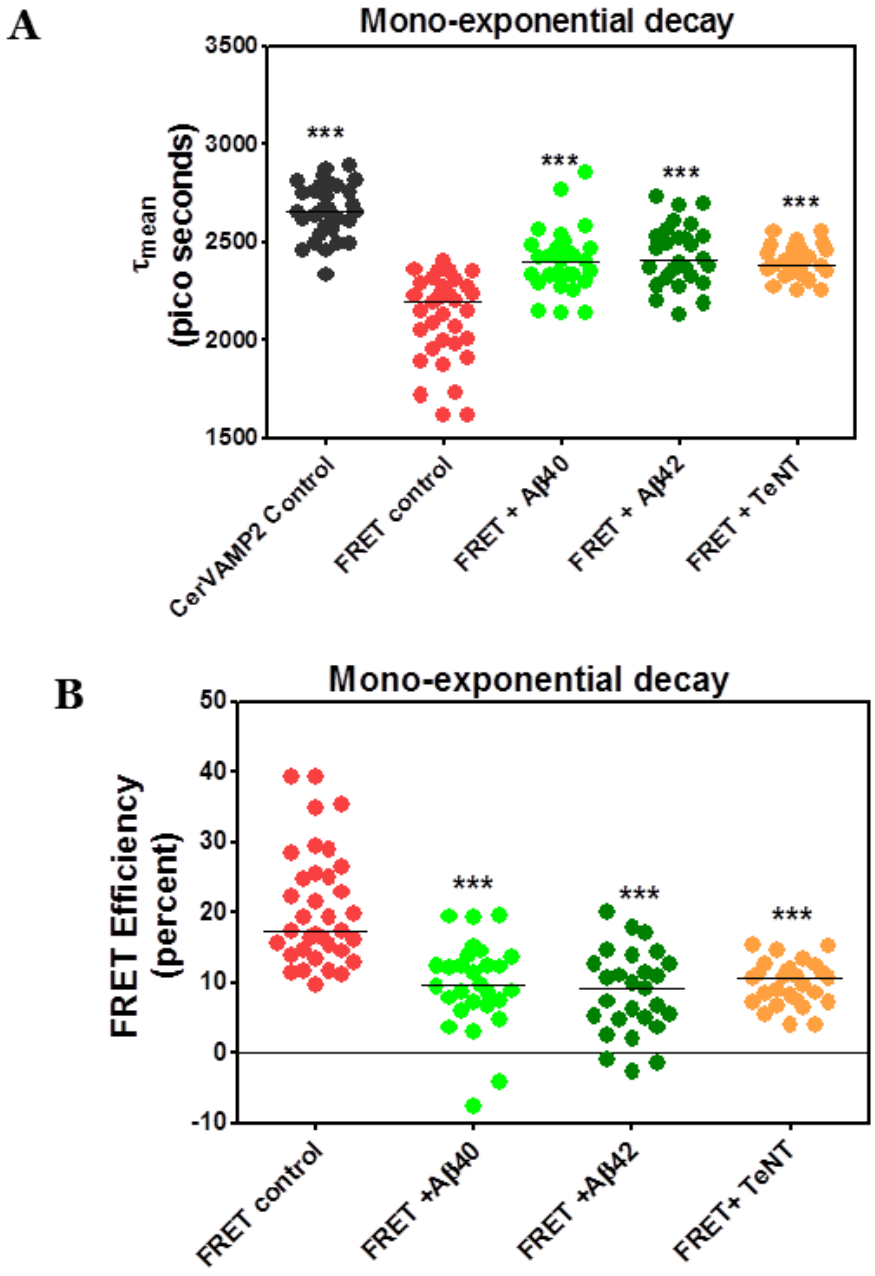

Figure S-5.6.7. Lifetime measurements and corresponding FRET efficiency of functional vesicular fusion processes in transfected N2A cells at high potassium by monoexponential decay model. A-B Changes in **(A)** τ_{mean} or mean lifetime of donor (cerulean) and **(B)** FRET efficiency in cells transfected with cer-VAMP2 only (Cer-VAMP2 control) or both cer-VAMP2 and Cit-SNAP25 (FRET) that are pretreated with Aβ40, Aβ42 or TeNT. 30-40 functional vesicular fusion processes at membrane are estimated using FM dye channel image. Data represented as scatter dot plot of individual measurement at mono-exponent decay plot and median. Significance determined using one-way ANOVA test. (*** $p<0.001$)

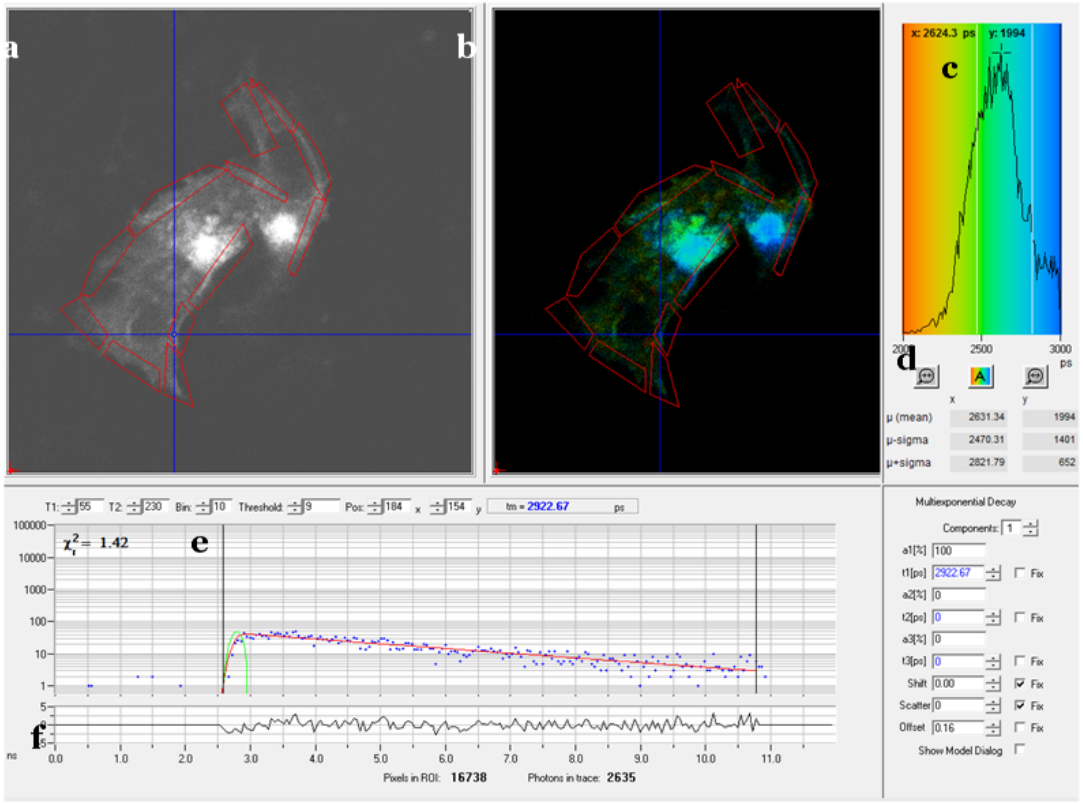

Figure S-5.7.1. Fluorescence lifetime image of D3 cells transfected with cerulean-VAMP2 (donor only) negative control system. Screen shot image of SPCImage software demonstrate **(a)** intensity image **(b)** spatially resolved lifetime image, followed by **(c)** frequency histogram of the lifetime in that ROI; color coded for the range 2000 (red) to 3000 (blue) picoseconds and quantified for **(d)** mean average lifetime and corresponding range. The decaying photons have been fit to **(e)** mono-exponential decay, that fits well, as checked by **(f)** random distribution of weighted residuals and chi square value < 2.5. The red regions in (a)intensity and (b) lifetime windows represent the region of interest (ROI) that have been used to depict the (c) frequency histogram. The mean lifetime at that point (vesicular fusion process) can be assessed by moving the cursor and obtaining the reading.

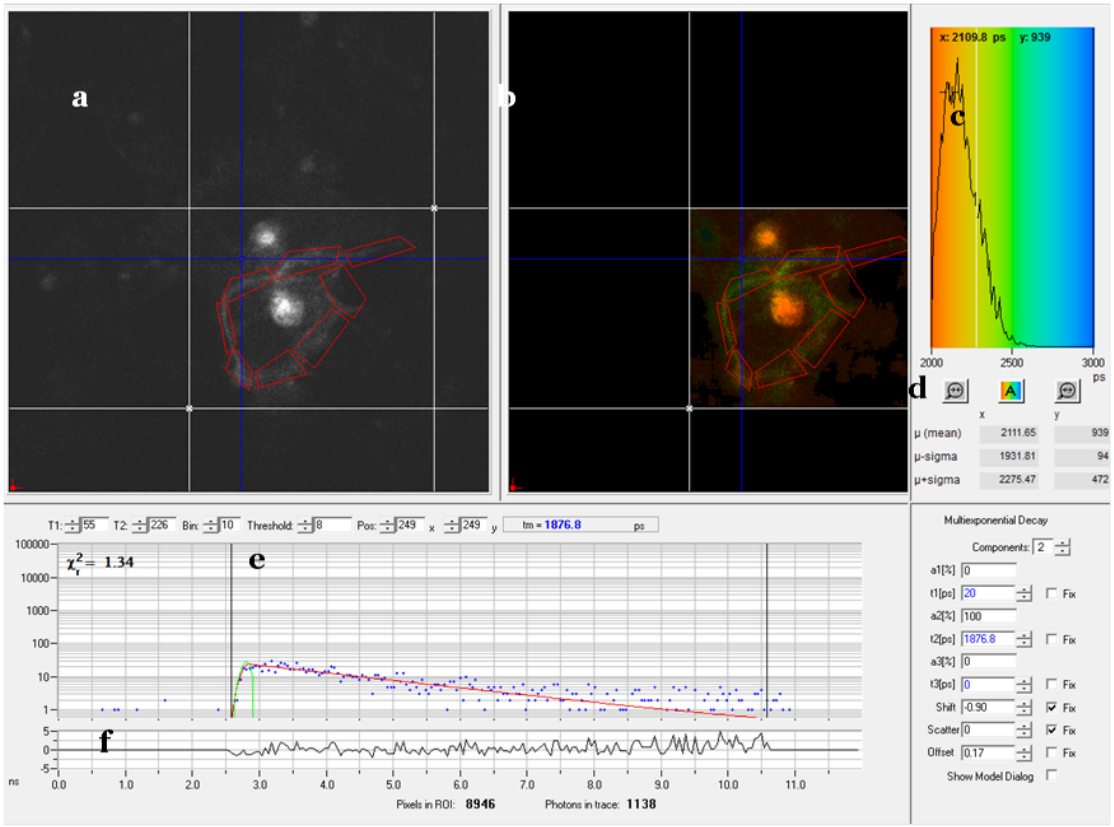

Figure S-5.7.2. Fluorescence lifetime image of D3 cells transfected with cerulean-VAMP-2 and citrine-SNAP25 (FRET or positive control system). Screen shot image of SPCImage software demonstrate **(a)** intensity image **(b)** spatially resolved lifetime image, followed by **(c)** frequency histogram of the lifetime in that ROI; color coded for the range 2000 (red) to 3000 (blue) picoseconds and quantified for **(d)** mean average lifetime and corresponding range. The decaying photons have been fit to **(e)** mono-exponential decay, that fits well, as checked by **(f)** random distribution of weighted residuals and chi square value < 2.5. The red regions in (a)intensity and (b) lifetime windows represent the region of interest (ROI) that have been used to depict the (c) frequency histogram. The mean lifetime at that point (vesicular fusion process) can be assessed by moving the cursor and obtaining the reading.

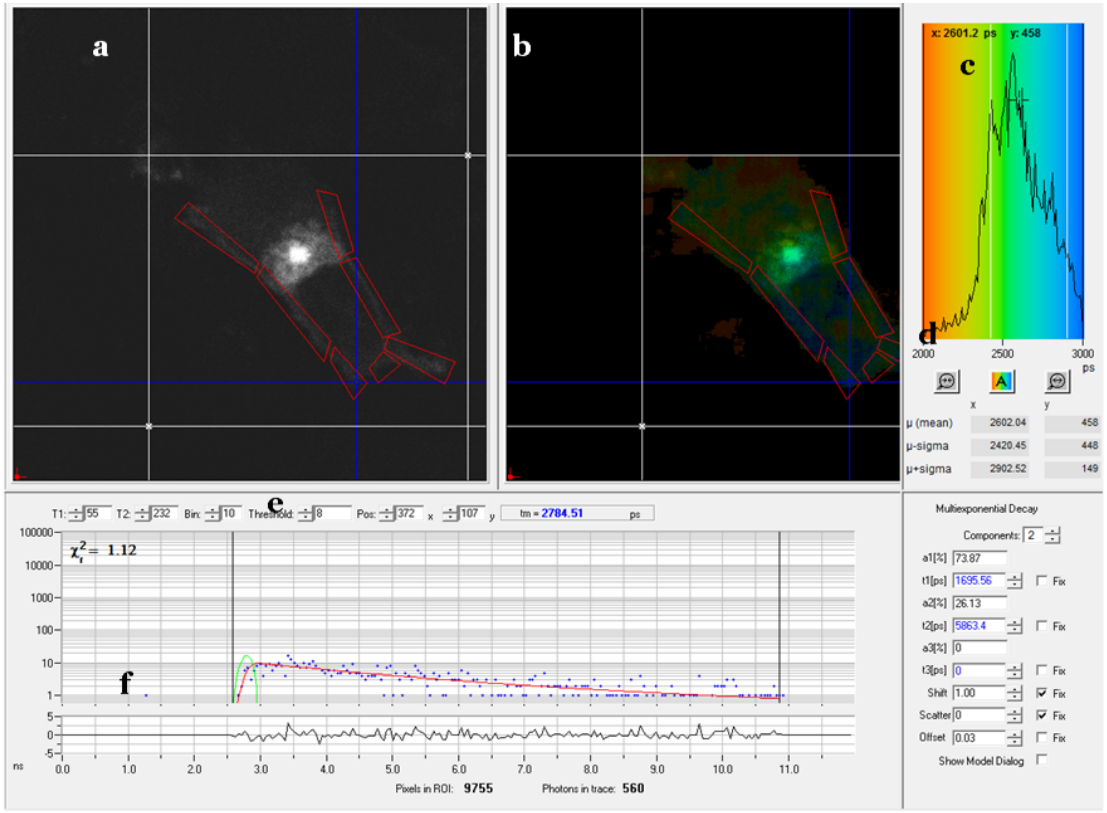

Figure S-5.7.3. Fluorescence lifetime image of D3 cells transfected with cerulean-VAMP-2 and citrine-SNAP25; that has been pretreated with Aβ40. Screen shot image of SPCImage software demonstrate **(a)** intensity image **(b)** spatially resolved lifetime image, followed by **(c)** frequency histogram of the lifetime in that ROI; color coded for the range 2000 (red) to 3000 (blue) picoseconds and quantified for **(d)** mean average lifetime and corresponding range. The decaying photons have been fit to **(e)** mono-exponential decay, that fits well, as checked by **(f)** random distribution of weighted residuals and chi square value < 2.5. The red regions in (a)intensity and (b) lifetime windows represent the region of interest (ROI) that have been used to depict the (c) frequency histogram. The mean lifetime at that point (vesicular fusion process) can be assessed by moving the cursor and obtaining the reading.

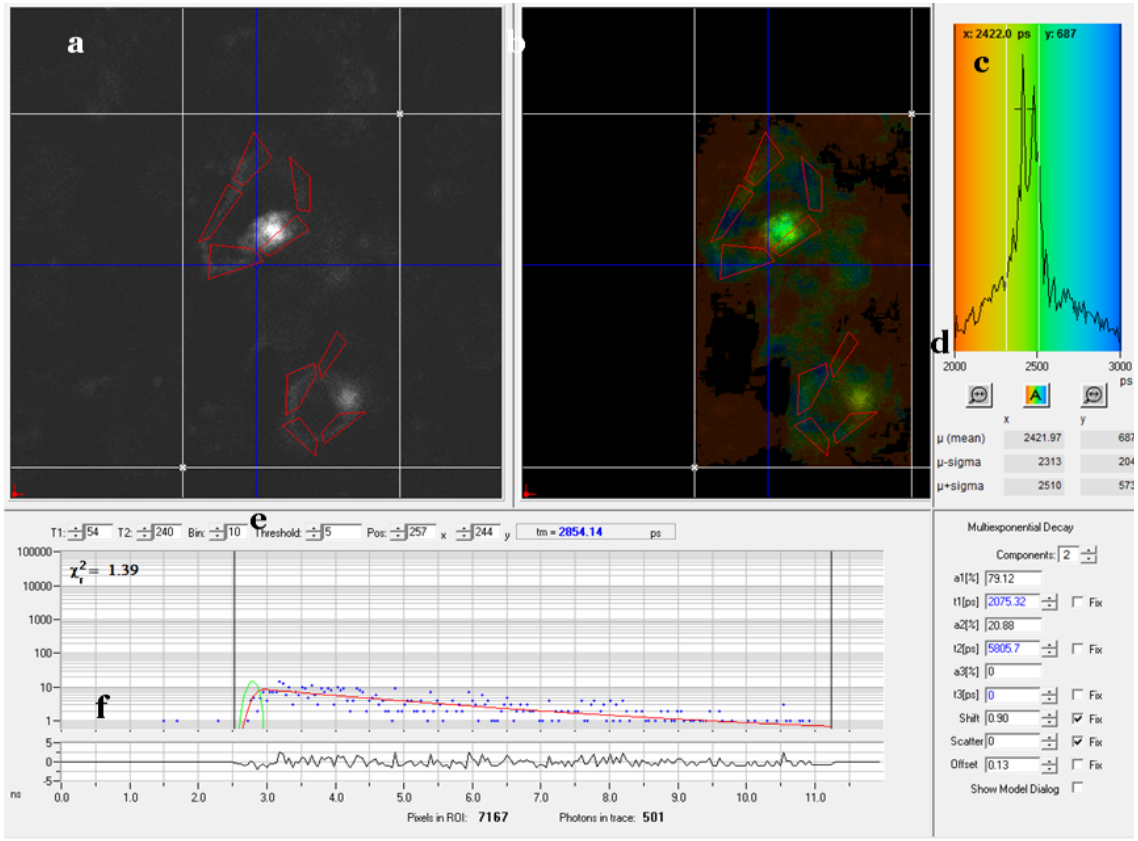

Figure S-5.7.4. Fluorescence lifetime image of D3 cells transfected with cerulean-VAMP-2 and citrine-SNAP25; that has been pretreated with Aβ42. Screen shot image of SPCImage software demonstrate **(a)** intensity image **(b)** spatially resolved lifetime image, followed by **(c)** frequency histogram of the lifetime in that ROI; color coded for the range 2000 (red) to 3000 (blue) picoseconds and quantified for **(d)** mean average lifetime and corresponding range. The decaying photons have been fit to **(e)** mono-exponential decay, that fits well, as checked by **(f)** random distribution of weighted residuals and chi square value < 2.5. The red regions in (a)intensity and (b) lifetime windows represent the region of interest (ROI) that have been used to depict the (c) frequency histogram. The mean lifetime at that point (vesicular fusion process) can be assessed by moving the cursor and obtaining the reading.

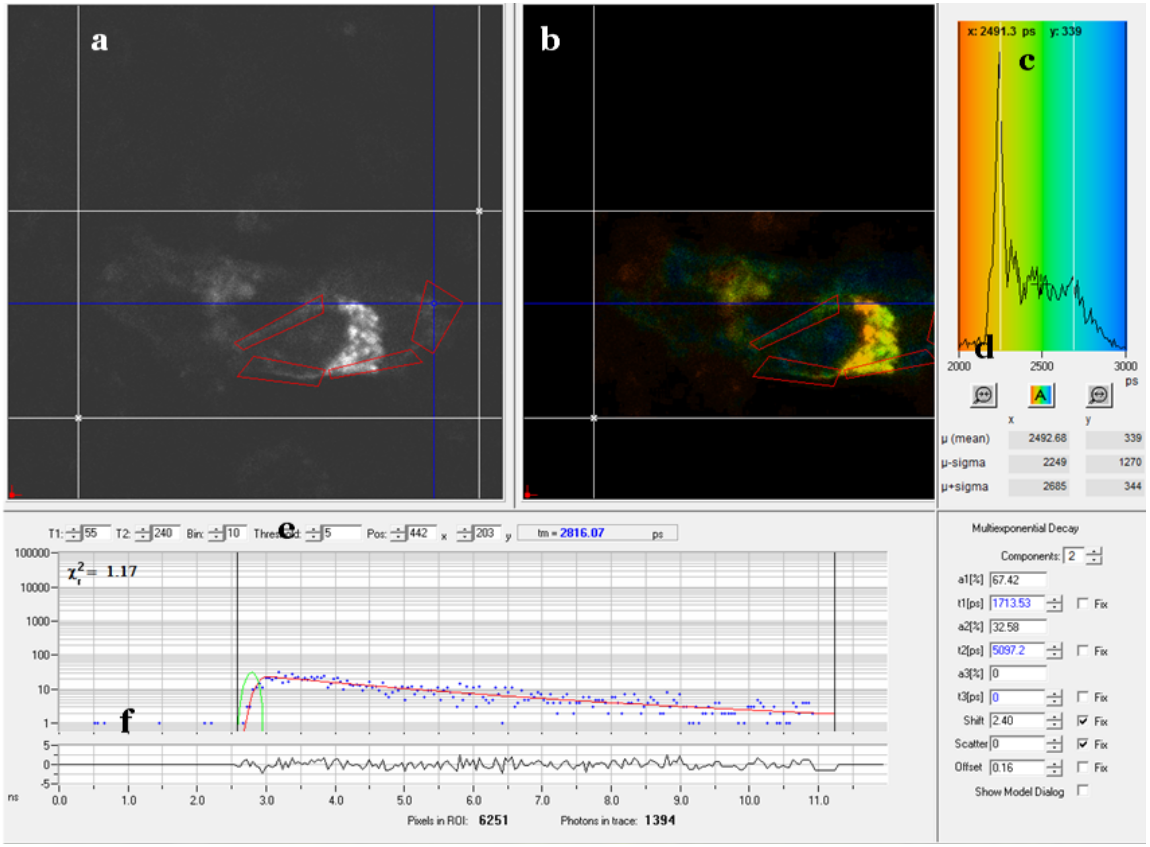

Figure S-5.7.5. Fluorescence lifetime image of D3 cells transfected with cerulean-VAMP-2 and citrine-SNAP25; that has been pretreated with TeNT. Screen shot image of SPC Image software demonstrate **(a)** intensity image **(b)** spatially resolved lifetime image, followed by **(c)** frequency histogram of the lifetime in that ROI; color coded for the range 2000 (red) to 3000 (blue) picoseconds and quantified for **(d)** mean average lifetime and corresponding range. The decaying photons have been fit to **(e)** mono-exponential decay, that fits well, as checked by **(f)** random distribution of weighted residuals and chi square value < 2.5. The red regions in (a)intensity and (b) lifetime windows represent the region of interest (ROI) that have been used to depict the (c) frequency histogram. The mean lifetime at that point (vesicular fusion process) can be assessed by moving the cursor and obtaining the reading.

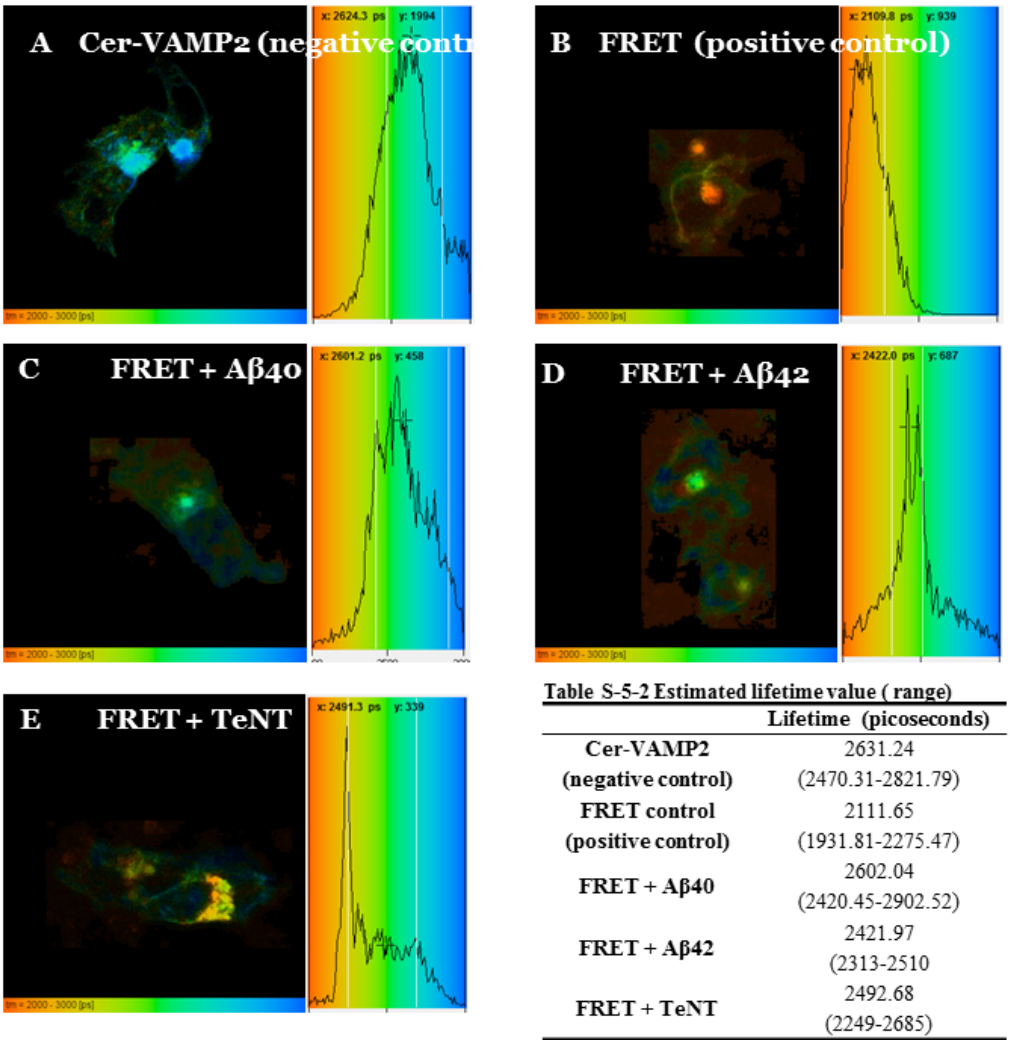

Table S-5-2 Estimated lifetime value (range)

	Lifetime (picoseconds)
Cer-VAMP2 (negative control)	2631.24 (2470.31-2821.79)
FRET control (positive control)	2111.65 (1931.81-2275.47)
FRET + Aβ40	2602.04 (2420.45-2902.52)
FRET + Aβ42	2421.97 (2313-2510
FRET + TeNT	2492.68 (2249-2685)

Figure S-5.7.6 Spatial lifetime images of donor (cerulean) lifetime and corresponding frequency histograms in transfected D3 Cells. A-E Spatial lifetime images and frequency histograms obtained by measuring lifetime of cerulean (donor) by TCSPC in cells transfected with either **(A)** cer-VAMP2 only or **(B-E)** cerulean-VAMP2 and cit-SNAP25. Histogram represents lifetime frequency at the membrane. **A-B** Lifetime decreases from the blue range in **(A)** negative control cerulean-only transfected cell to yellow range in **(B)** dual transfected cells or FRET (positive control).**C-E** In the presence of **(C)** Aβ40; **(D)** Aβ42; and **(E)** TeNT; donor lifetime increases back from yellow to blue range . Color code represents lifetime from 2000 (red) to 2700 (blue) picoseconds. **Table S-5-2** shows changes in donor (cerulean) lifetime as estimated by B&H software for the membrane ROI in value (range)

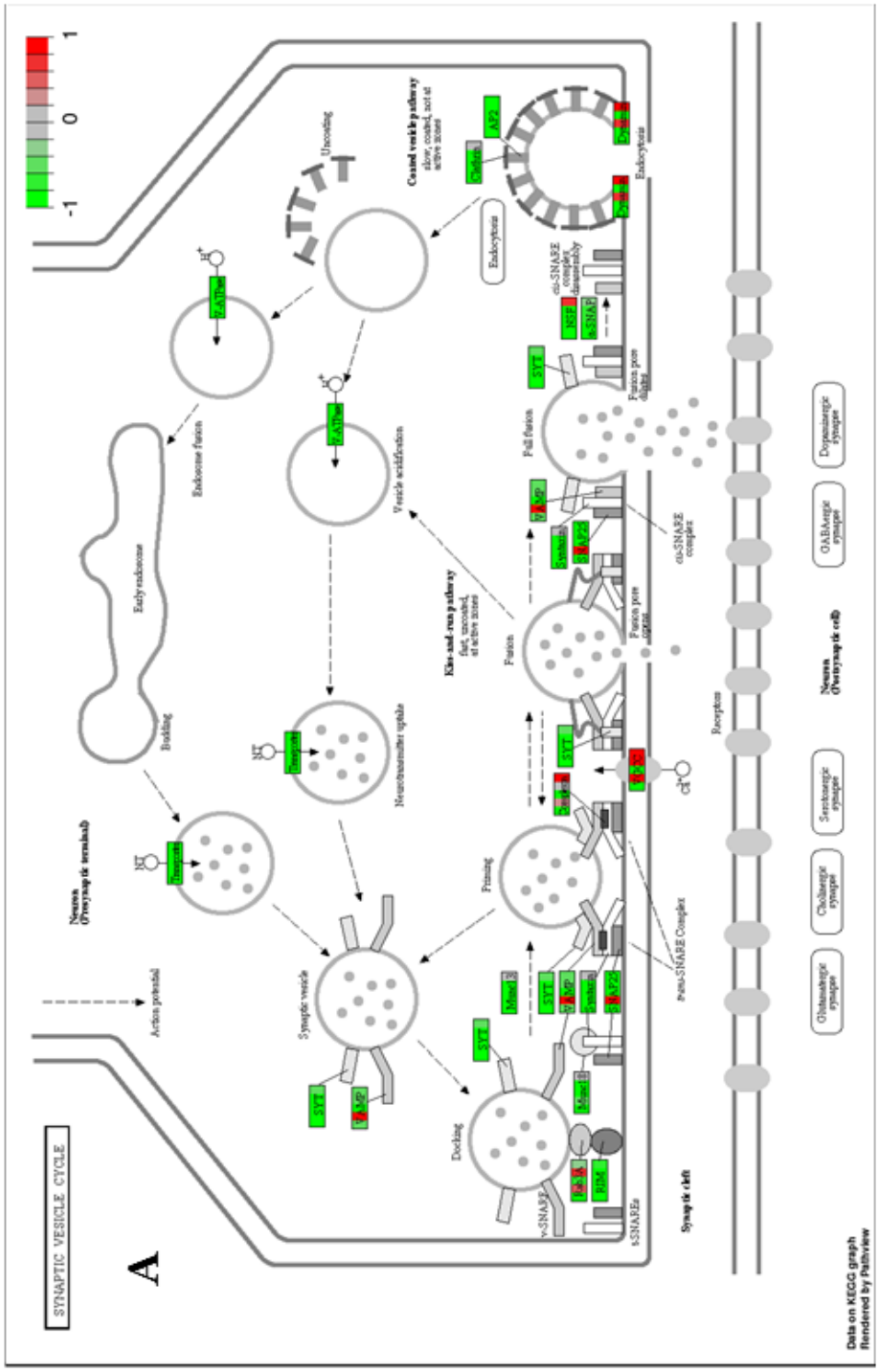
SYNAPTIC VESICLE CYCLE
A
Neuron (Presynaptic terminal)
Action potential
Synaptic vesicle
Docking
Priming
Fusion
Fusion pore
Fusion pore dilation
Full fusion
Endocytosis
Uncoating
Coated vesicle pathway
slow, coated, not at active zones
Vesicle acidification
Kiss-and-run pathway
fast, uncoated, at active zones
Endosome fusion
Endosome
Budding
Neurotransmitter uptake
Neurotransmitter
Receptors
Synaptic cleft
Neuron (Postsynaptic cell)
Glutamatergic synapse
Cholinergic synapse
Serotonergic synapse
GABAergic synapse
Dopaminergic synapse
v-SNARE
t-SNAREs
trans-SNARE Complex
cis-SNARE complex
Data on KEGG graph
Rendered by Pathview

B

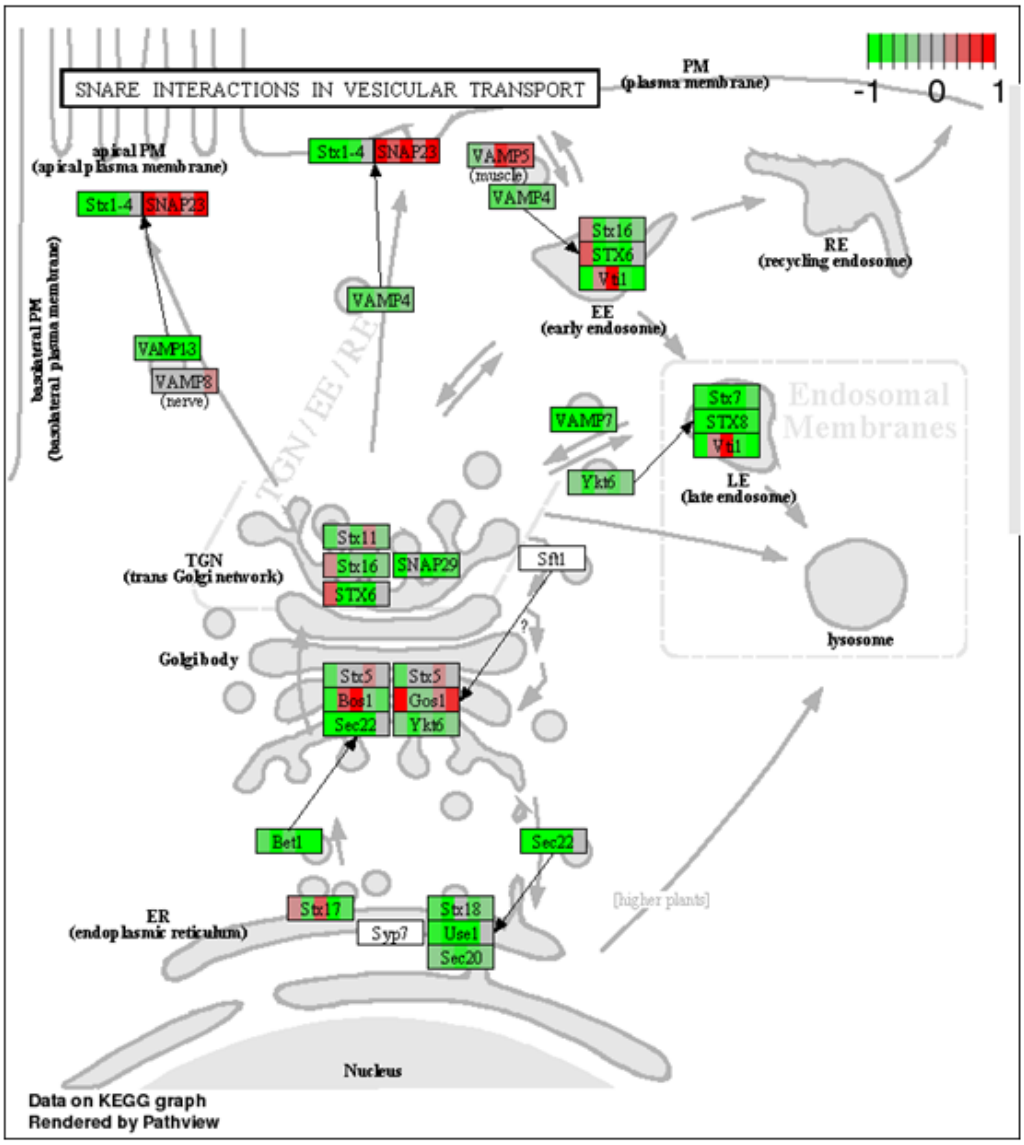

Figure S-5.8 KEGG Graph of synaptic vesiclular gene expression analysis in brains of AD patients compared to age matched normal individuals. Plot represents downregulation (green) of **(A)** SNARE assembly**,** in particular **(B)** VAMP2 SNARE protein.